Modelling and Simulation of the Laboratory Low Temperature Proton Exchange Membrane and Direct Methanol Fuel Cells

A Thesis Submitted By

Lei Xing

For the Degree of Doctor of Philosophy

School of Chemical Engineering and Advanced Materials

Newcastle University

April 2014

Abstract

Proton exchange membrane fuel cells (PEMFCs) are promising candidates as power sources due to their high energy conversion efficiency, power density and low pollutants emission. Water management is of vital importance to achieve maximum performance and durability from PEMFCs. The main object of this work was to develop a mathematic model to better understand the water transport in PEMFCs under practical conditions. The aim is to enhance the output power of fuel cells by establishing effective water removal and distribution strategies.

A single-phase flow, along the channel, isothermal model of a PEMFC is developed and validated against experimental data. Reactant flow and diffusion are simulated using the Navier-Stokes equation and Maxwell-Stefan equation, respectively. Water transport through the membrane is described by the combinational mechanism in which electro-osmotic drag, back diffusion and hydraulic permeation are all included. Agglomerate assumption is applied for the catalyst layer structure. This model is used to study the effects of the catalyst layer properties on cell performance. The model indicates that the rapid decrease in current density at lower cell voltage is due to an increased oxygen diffusion resistance through the ionomer film.

A two-phase flow, across the channel, isothermal model is developed. The water phase transfers between water vapour, dissolved water and liquid water are taken into account and liquid water formation and transport are introduced. Liquid water occupies the secondary pores of the cathode catalyst layer to form a liquid water film on the outer boundary of the ionomer film. This model is used to study the influence of catalyst layer parameters and operating conditions on the cell performance. The model provides useful guidance for optimisation of the ionomer volume fraction in the cathode catalyst layer and the relative humidity of the cathode gas inlet.

A two-phase flow, across the channel, non-isothermal model is developed. The model considered the non-uniform temperature distribution within the fuel cell. The modelling results show that heat accumulates within the cathode catalyst layer under the channel. Higher operating temperatures improved the fuel cell performance by increasing the kinetic rate, reducing the liquid water saturation on the cathode and

increasing the water carrying capacity of the anode gas. Applying higher temperature on the anode and enlarging the width ratio of the channel/rib could improve the cell performance.

A multi-variable optimisation of the cathode catalyst layer composition is represented by a surrogate modelling. Five design parameters, platinum loading, platinum mass ratio, ionomer volume fraction, catalyst layer thickness and agglomerate radius, are optimised by a multiple surrogate model and their sensitivities are analysed by a Monte Carlo method based approach. Two optimisation strategies, maximising the current density at a fixed cell voltage and within a specific range, are implemented for the optima prediction. At higher current densities, cell performance is improved by reducing the ionomer volume fraction and increasing the catalyst layer porosity.

The one-dimensional, isothermal, time dependent and steady state models for the anode of a direct methanol fuel cell (DMFC) are developed. The two models are based on the dual-site mechanism, in which the coverage of intermediate species of methanol, OH and CO on the surface of platinum and ruthenium are included. Both the effect of operating conditions and electrode parameters are investigated. The distributions of methanol concentration and overpotential inside the electrode are represented and the current densities predicted by the intrinsic and macro kinetics are compared.

From the analysis of the different models developed in this thesis, the main results can be summarised as: (1) Mass transport resistance resulted from the oxygen diffusion through the ionomer film surrounding the agglomerate is the main reason for the rapid fall of current density at lower cell voltage. (2) Ionomer swelling has a significant effect on fuel cell performance because it resulted in a decrease in the porosity and an increase in the ionomer film thickness, leading to an increase in the oxygen transport resistance. (3) Catalyst layer composition has a vital impact on the utilisation of the platinum catalyst and cell performance. (4) Heat accumulates within the cathode catalyst layer under the channel. Applying higher temperatures on the anode optimises the temperature distribution within the MEA and improves the cell performance. (5) Cell performance is improved by enlarging the width ratio of channel/rib. However, the improvement is limited by the sluggish oxygen reduction reaction. (6) For the methanol oxidation reaction in a Pt-Ru anode, the intrinsic current density is determined by the coverage ratios of the intermediate species. The structure and property of the electrode also play an important role in determining the anode performance of a DMFC.

Table of Content

List of Figures

List of Tables

Nomenclature

A	cross-sectional area, m^2
A_s	reaction surface area per unit platinum mass, $m^2\ kg^{-1}$
a	specific area, m^{-1}
C	dimensionless concentration
c	concentration, $mol\ m^{-3}$
$c_{p,i}$	specific heat capacity of species i, $J\ mol^{-1}\ K^{-1}$
D	diffusivity, $m^2\ s^{-1}$
D_c	capillary diffusion coefficient, $m^2\ s^{-1}$
D_{ij}	Maxwell-Stefan diffusion coefficient matrix, $m^2\ s^{-1}$
$\tilde{D}_i$	partial variance
d	pore diameters, m
E_r	effectiveness factor
$\hat{E}_r$	average effectiveness factor
E^0	open circle potential, V
E^{cell}	cell voltage, V
EW	equivalent weight of Nafion® membrane, $g\ mol^{-1}$
F	Farady's constant, 96485 $C\ mol^{-1}$
f	platinum mass ratio to *Pt/C*
$\mathbf{f}$	column vector of length n_s
H	Henry's constant, $Pa\ m^3\ mol^{-1}$
I	dimensionless current density
i	current density, $A\ m^{-2}$
i_0	exchange current density, $A\ m^{-2}$
$J(s)$	Leverett function
k	rate coefficient, s^{-1}
k_i	thermal conductivity of species i, $W\ m^{-1}\ K^{-1}$
k_r	relative permeability
k_p	hydraulic permeability, m^2
L	length of the flow channel, m
l	thickness, m
L_i	volume fraction of species i
M_j	molecular weight for specie j, $kg\ mol^{-1}$
M_n	mean molecular weight, $kg\ mol^{-1}$

M_T	Thieles's modulus
m_{Pt}	platinum loading, mg cm^{-2}
m_C	carbon loading, mg cm^{-2}
N	number per volume, m^{-3}
N_j	molar flux of specie j, mol m^{-2} s^{-1}
n	number
p	pressure, Pa
Q	reactant gas flow rates, m^3 s^{-1}
R	symmetric correlation matrix
R	reaction rate, mol m^3 s^{-1}
R_g	ideal gas constant, 8.314 J mol^{-1} K^{-1}
R_M	membrane resistance, Ω m^{-2}
RH	relative humidity
r	radius, m
S	source term
s	liquid water saturation
T	temperature, K
t	time, s
u	velocity vector, m s^{-1}
V	mole volume, m^3
w	mass fraction
X	normalised distance (x/l_{CL})
x	design matrix of sample
x	mole fraction
$\tilde{x}_i$	design variable i
Y	normalised distance (y/L)
y	column vector
$\%M$	volume fraction of primary pores occupied by ionomer

Greek letters

α	charge transfer coefficient
α_w	water activity
β	$(1-\beta_3)F/R_gT = (1-\beta_4)F/R_gT$
λ	water content
μ	viscosity, Pa s
ρ	density, kg m^{-3}

ε	porosity
δ	thickness of ionomer/liquid water coating, m
γ	oxygen diffusion rate through the coating, s^{-1}
η	overpotential, V
σ	surface tension, N m^{-1}
θ	coverage ratio
θ_c	contact angel, °
σ_s	electronic conductivity, S m^{-1}
σ_M	ionic conductivity, S m^{-1}
φ	potential, V
Ψ_w	association parameter for water (the value is 2.6)
ς	dimensionless modulus, $\varsigma = a_{CL} i_0 l^2 / nFD_e c_M^0$
ζ	dimensionless modulus, $\zeta = a_{CL} i_0 l^2 \beta / \sigma_s^{eff}$
ν	D_{O_2-M} / δ_M , m s^{-1}

Superscripts

0	intrinsic
d	dissolved
eff	effective
ref	reference
eq	equilibrium
l	liquid
g	gas

Subscripts

a	anode
ads	adsorption
agg	agglomerate
C	carbon
c	cathode
CL	catalyst layer
des	desorption
GDL	gas diffusion layer
i	species i
j	species j
Kn	Knudsen diffusion

loc	local
M	Membrane/ionomer in PEMFCs and methanol in DMFCs
P	void space
Pt	platinum
Pt/C	platinum dispersed carbon
p	primary pores
r	relative
S	GDL penetration
s	secondary pores
T	temperature or total
w	liquid water
sat	saturation
tot	total
vl	vapour to liquid
vd	vapour to dissolved
dl	dissolved to liquid

Mathematical operators

∇	Nabla operator
$\frac{\partial}{\partial t}$	time derivative
$\sum$	summation
$\lvert\ \rvert$	modulus
exp	exponential function
ln	natural logarithm function
log	10 base logarithm function

Abbreviations

1D	one dimensional
2D	two dimensional
3D	three dimensional
AFC	alkaline fuel cell
ACL	anode catalyst layer
ANN	artificial neural network
B-V	Bulter-Volmer
CCD	charge coupled device

CCL	cathode catalyst layer
CFD	computational fluid dynamics
CL	catalyst layer
CHP	combined heat and power
DC	direct electricity
DHE	dynamic hydrogen electrode
DMFC	direct methanol fuel cell
EOD	electro-osmotic drag
FCV	fuel cell vehicles
FEM	finite element method
HOR	hydrogen oxidation reaction
GDL	gas diffusion layer
GSA	global sensitivity analysis
KRG	Kriging model
LB	Lattice Boltzmann
M^2	multi-phase mixture
MC	Monte Carlo
MCFC	molten carbonate fuel cell
MEA	membrane electrode assembly
MOR	methanol oxidation reaction
NMR	nuclear magnetic resonance
OCP	open circuit potential
ORR	oxygen reduction reaction
PAFC	phosphoric acid fuel cell
PDE	partial differential equation
PEMFC	proton exchange membrane fuel cell
RBF	radial basis function
RTD	residence time distribution
SHE	standard hydrogen electrode
SPE	solid polymer electrolyte
SOFC	solid oxide fuel cell
TPB	triple phase boundary
VHLC	variable heating and load control
VRE	voltage reversal effect
VOF	volume of fluid
WCC	water carrying capacity

Acknowledgements

I would like to take this opportunity to thank my supervisor, Prof. Keith Scott, for the precious opportunity of working on this project. I will never forget the inspiration, guidance, support and encouragement he provided during the last three and half years.

Thanks a lot for every friend and colleague in the Fuel Cell Lab, especially Dr. M. Mamlouk. Everything becomes easier with his help. I would like to thank all the PhD students who joined in this group in the same year as me, Asier, Ukrit, Ravi, Vinod. We met here from different countries, thank you guys for the friendship and encouragement. We will be friends forever. Many thanks to Dr. Xu Wang and Dr. Chenxi Xu. I still remember the first day I came to UK and met you at the airport of Newcastle. During the last two years, we shared ideas, discussed experiments and drank beer. Life is not easy, but it becomes better with you, my friends. During my three-year study, Dr. Yuancheng Cao, Dr. Xiaoteng Liu and Dr. Kui Zhang also provide massive help. I appreciate all of your kindness and your interesting talk in the Buttery on the fourth floor of Merz Court.

I would like to acknowledge the financial support from EPSRC through the Supergen; fuel cell consortium award.

I would like to thank my father, mother, younger sister and uncle for supporting my decisions.

Last but not least, I dedicate this thesis to my wife, Mrs. Yue Wang, and our forthcoming baby. We met in Newcastle and fell in love in this magic city. I am grateful for having you always by my side as you continuously make me better.

Chapter 1. Introduction

1.1 Hydrogen, the next generation energy source

Energy is vitally important to every aspect of modern society. The entire industrialised infrastructure of the world would collapse without energy. The rapid industrialisation and urbanisation lead to an increasing consumption of energy. As shown in Figure 1-1, the world's primary energy consumption increases more than ten times from 1900 to 2000. Today, the global energy requirements are mostly dependent on fossil fuels, which is about 80% of the present world energy demand [2]. This will eventually result in the depletion of limited fossil energy resources (for example coal and oil) and the environmental pollution. By 2050, oil and gas supply is unlikely to be able to meet the global energy demand [3]. The CO_2 content in the atmosphere has increased 30% since the industrial era begin, leading to a global warming [4]. In order to prevent the depletion of fossil fuels and decrease their negative effect on climate change, increasing focus is being placed on renewable energy to satisfy the growing energy demand [5]. According to the report of 2013 from the Renewable Energy Policy Network [6], the renewable power capacity (excluding the hydropower) worldwide has exceeded 1470 Giga watt (GW) in 2012, up about 8.5% from the previous year.

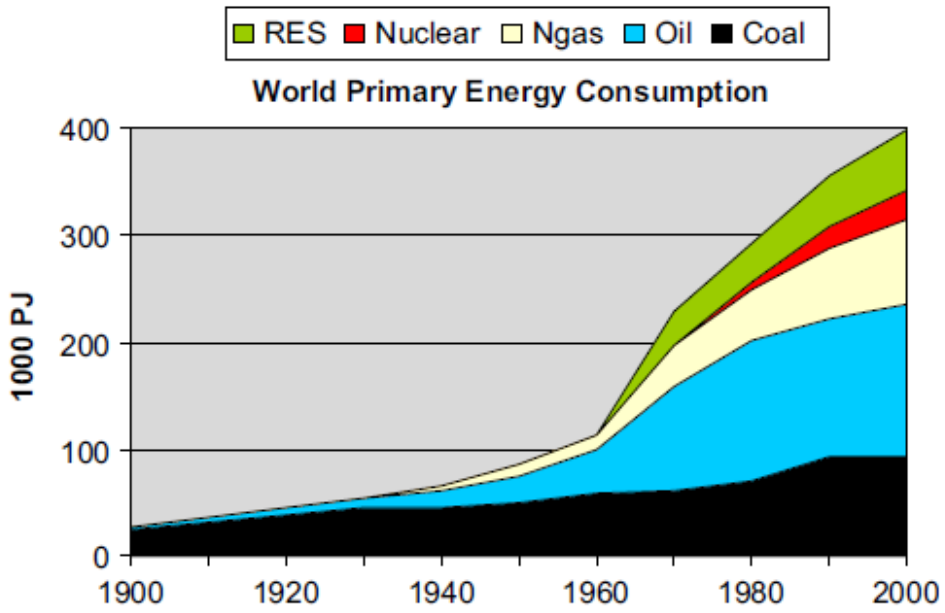

Figure 1-1 World primary energy consumption from 1900 to 2000 [1]

(RES: Renewable Energy Source; Ngas: Natural gas)

Hydrogen is suggested as the ideal energy carrier for the future. This is because hydrogen can be obtained from several resources, in particular, fossil, renewable and nuclear resources. Hydrogen is the lightest and one of the most plentiful elements in nature. Hydrogen makes up approximate 75% of all the matter in the universe and its density is 7.5% of air. Hydrogen has a range of excellent properties over the conventional power sources. However, hydrogen is not a primary energy source. It must be produced by other energy sources before using as a clean energy [6]. Figure 1-2 illustrates how hydrogen can be produced as an energy carrier by multiple hydrogen production methods and how hydrogen can be used as various end-user applications.

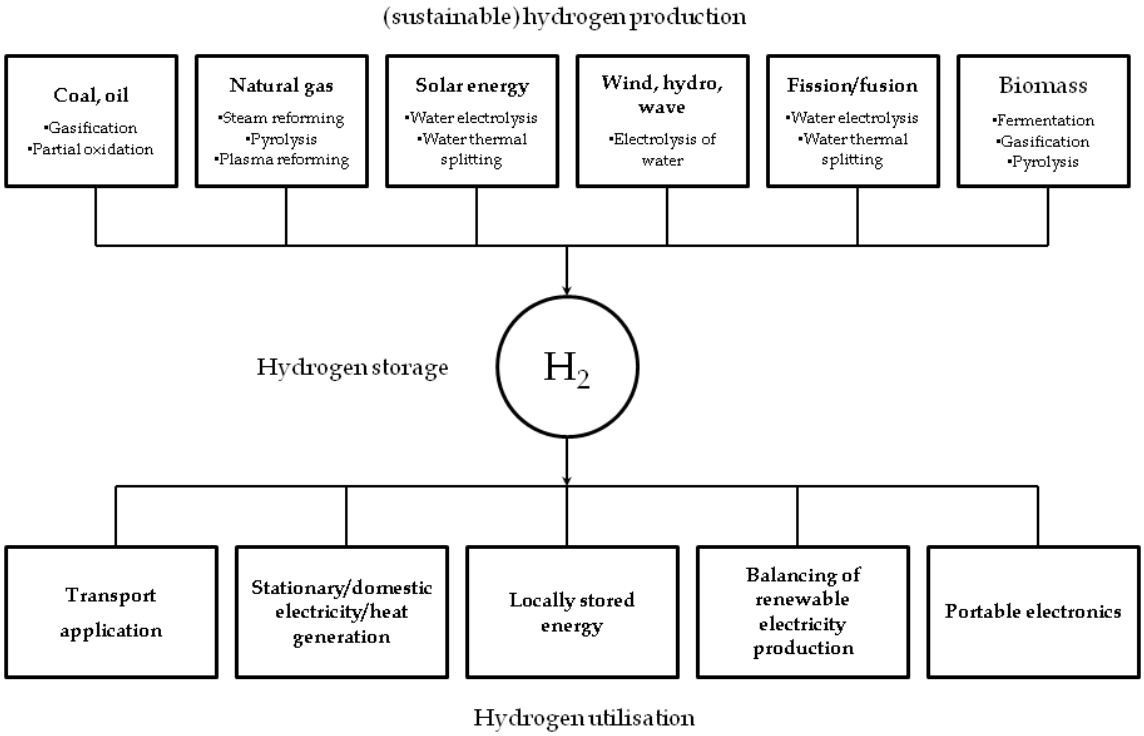

Figure 1-2 Hydrogen as an energy carrier linking multiple hydrogen production methods, through storage to various end-users [5]

Obviously, hydrogen can be produced from a variety of resources, contributing significant security to energy supply. Hydrogen will be in the long-term produced from renewable energy sources by developed technology, such as water electrolysis. However, in the short-term, hydrogen is produced in large quantities from fossil fuels reformation [7]. For example, in 2007, the annual production of hydrogen is about 0.1 Giga ton (Gton), 98% from the reforming of fossil fuels, such as oil refining and ammonia and methanol production [8]. The portion of hydrogen produced by renewable energy sources has increased in recent years. Renewable energy contributed 2.0% of

total global energy consumption in 2005 [9], and it increased to 19% in 2012[6]. For instant, renewable energy met 27% of the electricity demand of Italy in 2012 [6]. The expansion of combined heat and power (CHP) plants helps Denmark maintaining the same primary fuel consumption more than 30 years, which has so far saved 14 % of fossil fuels [10]. The European roadmap for the development of hydrogen and fuel cell technologies has now set a target of 1 GW of distributed power generation capacity from fuel cells by 2015 [3].

Researchers believed that the strong relationship between hydrogen and electricity provided an opportunity of achieving the sustainable use of energy. Fuel cells are considered as ideal devices capable of replacing traditional internal combustion engines as the primary way to convert chemical energy into electricity [11].

1.2 Fuel cells

A fuel cell is an electrochemical device that converts chemical energy of fuel (e. g. hydrogen or methanol) directly into direct current (DC) electricity. Unlike the traditional internal combustion engine, fuel cell produces electrical energy through electrochemical reaction, rather than through combustion. A single fuel cell consists of a pair of anode and cathode, and an electrolyte in between. Individual fuel cells can be connected in series to form a fuel cell stack, which can generate higher power for portable and stationary application.

The first observation of a fuel cell effect was made by Shoenberin in 1838 [12]. Based on this work, the first fuel cell was demonstrated and developed by Grove in 1839 [13] and 1822 [14]. The fuel cell used platinum strips and sulphuric acid as the electrodes and electrolyte, respectively. Electrical energy was produced by combing hydrogen and oxygen. In the following one hundred years, fuel cells were not practically used until the U.S. space program, Gemini and Apollo program, in 1960s. The first practical fuel cell applications were in the Gemini Program. In the following Apollo Program, fuel cells were used to provide electricity for life support, guidance and communications. In spite of the continued successful application in the U. S. space program, fuel cells were “forgotten” for terrestrial applications until the early 1990s. In 1993, Energy Partners demonstrated the first passenger car running on PEM fuel cells [15].

A typical process of electricity generation from fuels involves several energy conversion steps. The efficiency of the traditional combustion engines is limited by the Carnot efficiency because the energy conversion steps are not 100% efficient [16]. Fuel cells circumvent all the energy conversion steps and generate electricity in a single step. This makes fuel cells more efficient than the combustion systems. Moreover, fuel cell operating on hydrogen is zero emission; the only exhausts are water and heat. A variety of advantages make them promising candidates as power sources for portable and stationary applications.

Although fuel cells have a variety of advantages, some disadvantages, such as high cost and low durability, remain big barriers that slow down their commercialisation [16]. In order to make the fuel cells economically competitive, new technological solutions must be developed.

1.2.1 Types of fuel cells

Depending on the different electrolyte used, fuel cells can be categorised in five groups, namely:

a. Alkaline fuel cells (AFC)
b. Proton exchange membrane or polymer electrolyte membrane fuel cells (PEMFC)
c. Phosphoric acid fuel cells (PAFC)
d. Molten carbonate fuel cells (MCFC)
e. Solid oxide fuel cells (SOFC)

AFCs adopt an immobilised liquid KOH, while PEMFCs use a perfluorinated membrane, such as Nafion®, and PAFCs apply an immobilised liquid H_3PO_4 as the electrolyte, respectively. Hydrogen and oxygen (air) are the fuel and oxidant used in AFCs, PEMFCs and PAFCs, which are typically operated under 220 °C. MCFCs are high-temperature (approximate 600 °C) fuel cells that use an electrolyte composed of a molten carbonate salt mixture suspended in a porous, chemically inert ceramic matrix. MCFCs use natural gas, biogas as well as hydrogen as the fuel. The operating temperature of SOFCs (800-1000 °C) is higher than that of MCFCs. SOFCs use a solid oxide materials, such as ceramic, as the electrolyte which conducts negative oxygen

ions from the cathode to anode. Oxygen or air is used at cathode while hydrogen or hydrocarbon, such as methane, is used as the fuel at anode. Note that in the PEMFC group, fuel cells used methanol as the fuel is categorised as another type of fuel cell, direct methanol fuel cell (DMFC). Although all types of fuel cells are based on the same electrochemical principles, they all operate at different temperature ranges, incorporate different materials, and differ in the performance characteristics and fuel tolerance. The main characteristics of each types of fuel cell are shown in Table 1-1 [17, 18].

Table 1-1 Description of major fuel cell types

	AFC	PEMFC	PAFC	MCFC	SOFC	DMFC
Electrolyte	Liquid KOH (immobilised)	Polymer membrane (e.g. Nafion®)	Liquid H_3PO_4 (immobilised)	Molten carbonate	Ceramic (usually Y_2O_3-stabilised ZrO_2)	Polymer membrane (e.g. Nafion®)
Charge carrier	OH^-	H^+	H^+	CO_3^{2-}	O^{2-}	H^+
Operating temperature	60-220 °C	80-220 °C	150-220 °C	600-700 °C	800-1000 °C	50-120 °C
Catalyst	Ni, Ag, metal oxides and noble metals	Platinum	Platinum	Nickel	Perovskites (ceramic)	Platinum and Ruthenium
Cell components	Carbon based	Carbon based	Carbon based	Stainless based	Ceramic based	Carbon based
Fuel compatibility	Hydrogen	Hydrogen	Hydrogen	Hydrogen, methane	Hydrogen, methane, carbon monoxide	Methanol

The research reported in this thesis is focused on PEMFC and DMFC operating with Nafion® as electrolyte. Their operation, performance, design and application will be described in the next sections.

1.2.2 Proton exchange membrane fuel cell (PEMFC)

The first practical fuel cell was developed by General Electric Company (GE) in the 1950s. GE was awarded the contract for the Gemini space program in 1962. The fuel cell in the Gemini program is a 1 kW PEMFC system with a platinum loading of 35 mg Pt cm^{-2}. The observed current density was 37 mA cm^{-2} at 0.78 V [19]. In the 1960s, improvements were made by incorporating Teflon in the catalyst layer directly adjacent to the electrolyte. Considerable improvements were made from the early 1970s onward with the adoption of the fully fluorinated Nafion® membrane [20].

A typical PEMFC unit (see Figure 1-3) consists of a membrane electrode assembly (MEA) sandwiched between the flow field plates of the anode and cathode in which flow channels are machined. The MEA includes three parts, gas diffusion layer (GDL) and catalyst layer (CL) on anode and cathode, respectively, and polymer electrolyte membrane in between. At anode, hydrogen flows into the anode flow channel and transport to the CL through the GDL, and then oxidises into protons and electrons in the anode CL (reaction 1-1). The protons pass through the polymer electrolyte membrane and reach to the cathode CL, while the electrons travel via an external circuit to the cathode. At the same time, at cathode, air or oxygen flows into the cathode flow channel and transport to the CL through the GDL. In the cathode CL, oxygen combines with the protons and electrons, which generated in the anode CL, to produce water (reaction 1-2).

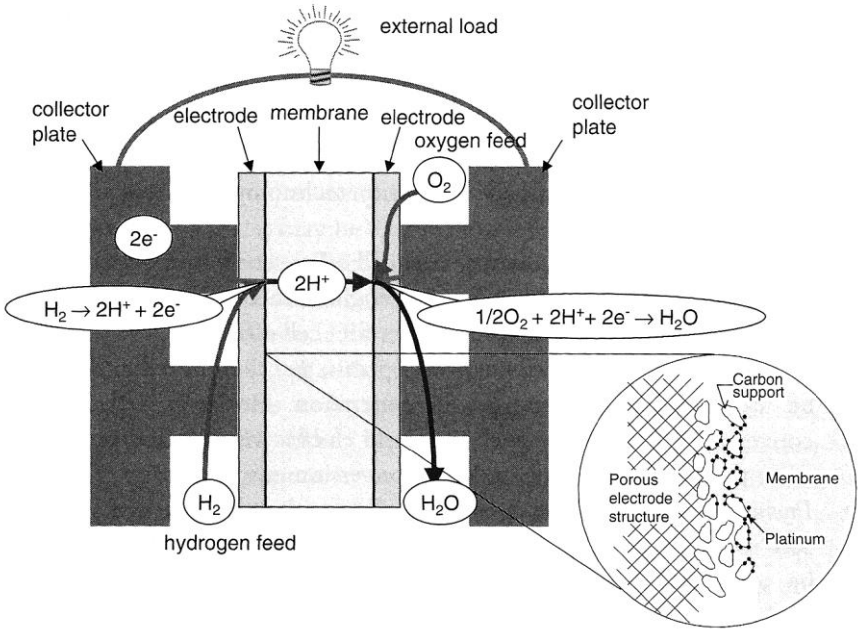

Figure 1-3 Schematic diagram and basic principle of operation of a PEMFC

$$\text{Anode reaction:} \quad H_2 \rightarrow 2H^+ + 2e^- \tag{1-1}$$

$$\text{Cathode reaction:} \quad \frac{1}{2}O_2 + 2H^+ + 2e^- \rightarrow H_2O \tag{1-2}$$

$$\text{Net cell reaction:} \quad H_2 + \frac{1}{2}O_2 \rightarrow H_2O \tag{1-3}$$

The thermodynamic potential for the reaction (1-2) calculated from the standard chemical potentials at 25 °C and 1.0 atm is 1.23 V versus standard hydrogen electrode (SHE).

In the case of a fuel cell supplied with reactants gases without the closed electrical circuit, the observed practical cell potential is called the open circuit potential (OCP). The OCP is lower than the theoretical potential due to the activation losses, especially at the cathode, in the fuel cell even when no external current is generated [16]. The relationship between fuel cell potential and current density is called the polarisation curves, which is obtained by subtracting the activation polarisation losses, ohmic losses, and concentration polarisation losses from the equilibrium potential. Figure 1-4 shows the polarisation curve and different voltage losses in a PEMFC. Note that a majority of the voltage losses occur at the cathode due to the sluggish oxygen reduction reaction (ORR) [21].

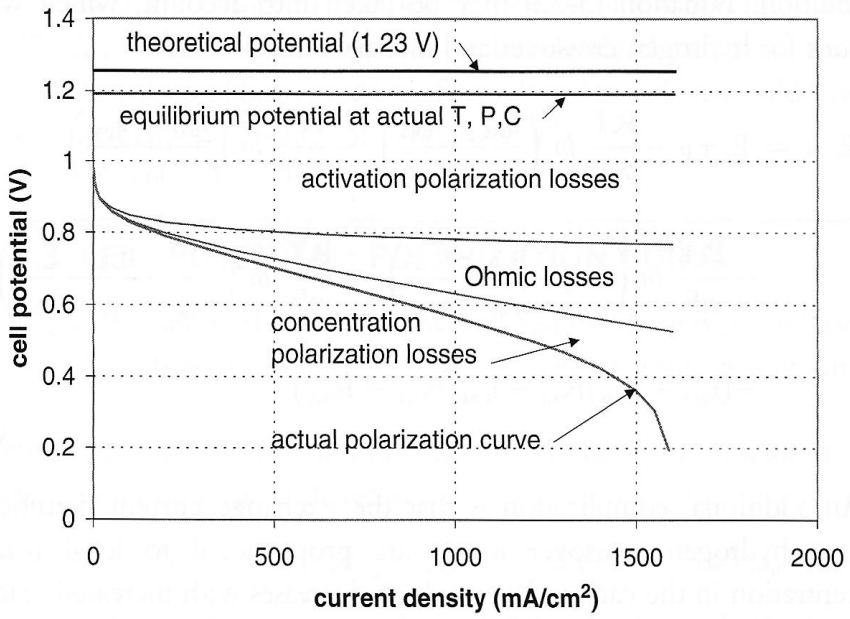

Figure 1-4 Voltage losses in the fuel cell and the resulting polarisation curves [17]

The major application of PEMFCs focuses on transportation due to their potential impact on the environment, e.g. the low emission. Stationary electricity plants and portable power sources are the other important applications. In the last decade, the interest and involvement of the scientific and engineering communities and companies in the PEMFC technology have continuously increased. The total number of the granted fuel cell patents increased approximate 350% during 2000 to 2010. In 2010, 1801 granted fuel cell patents were published by the U.S. and European patent offices, and this number increased to 2732 in 2011 [22, 23]. Automakers such as General Motors (GM), Honda, Toyota, have paid considerable attention on developing their fuel cell vehicles (FCV) and announced plans of commercialising their FCV by 2015 [24].

Intelligent Energy, an intellectual property rich company in UK, launched its first commercial off-grid hydrogen fuel cell, Upp^{TM}, in 2013. Upp^{TM} is a smart PEMFC device that can conveniently power and charge all the compatible hand-held electronic devices via universal serial bus (USB) [25].

1.2.3 Direct methanol fuel cell (DMFC)

Direct methanol fuel cells (DMFCs) are a subcategory of proton exchange membrane fuel cells in which methanol solution is used as the fuel. Because the liquid fuel is used, DMFCs have a variety of excellent features over hydrogen PEMFC. The main advantage is the ease of transport of methanol, stable energy output at all environmental conditions. In DMFCs, methanol is directly electro-oxidised on the catalyst surface, resulting in a standard electromotive force of 1.20 V [26].

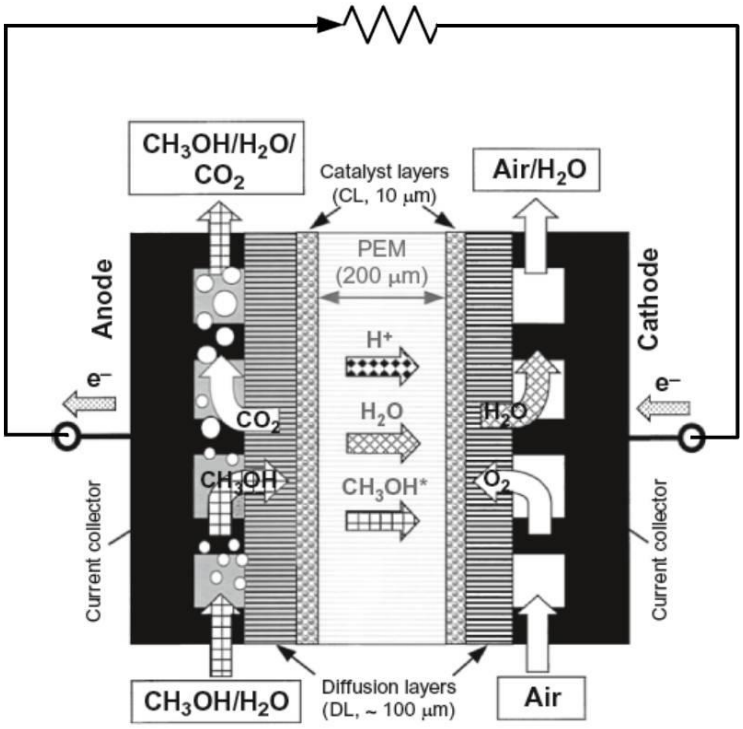

Figure 1-5 Schematic diagrams and operating principle of a typical DMFC

DMFCs have a similar configuration and operating principle in comparsion with PEMFCs. In a DMFC employing an acid electrolyte, methanol is directly oxidised to carbon dioxide at the anode. The thermodynamic potential for the anode reaction (reaction 1-4) calculated from the standard chemical potentials at 25 °C and 1.0 atm is 0.03 V versus standard hydrogen electrode (SHE). At the cathode, oxygen combines with the proton and electrons and is reduced to water. The thermodynamic potential for

the cathode reaction (reaction 1-5) is 1.23 V (vs. SHE). Finally, a standard electromotive force of 1.20 V is generated according to the net cell reaction (reaction 1-6). The schematic diagram of a typical DMFC with proton conducting membrane and the operating principle are demonstrated in Figure 1-5.

Anode reaction: $CH_3OH + H_2O \rightarrow CO_2 \uparrow + 6H^+ + 6e^-$ (1-4)

Cathode reaction: $\frac{3}{2}O_2 + 6H^+ + 6e^- \rightarrow 3H_2O$ (1-5)

Net cell reaction: $CH_3OH + \frac{3}{2}O_2 \rightarrow 2H_2O + CO_2 \uparrow$ (1-6)

Although the thermodynamic potential for reaction (1-4) is 0.03 V (vs. SHE), because of the number of electrons involved, the equilibrium value is not readily realisable, even with the best possible catalysts. Furthermore, because of the high degree of irreversibility of reaction (1-5), even under open-circuit conditions, the overpotential at the oxygen electrode is about 1.2 V which represents a loss of about 20% from the theoretical efficiency.

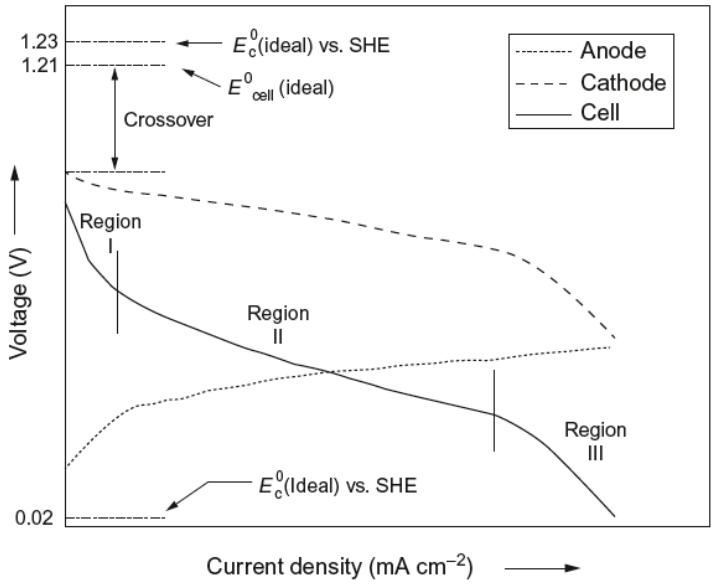

Figure 1-6 Polarisation curves for a DMFC and its constituent electrodes [26]

A main drawback of DMFCs is the very sluggish methanol oxidation reaction in the anode, which coupled with the inefficient cathode reaction, leads to a low overall performance, particularly at low temperatures [27]. Due to the property of the Nafion® membrane, methanol is able to migrate through the membrane from anode to cathode, which not only causes loss of fuel but also deteriorates cathode performance. Methanol

crossover is therefore considered to be another drawback in DMFC operation [28]. In short, the kinetics and mass transport process within the DMFCs are more complex than those from hydrogen PEMFCs [29, 30]. Consequently, the output cell voltage in a solid polymer electrolyte (SPE) DMFC is much lower than the ideal thermodynamic value, and it decreases with increasing current density [31]. A typical polarisation curve for a DMFC is schematically shown in Figure 1-6, which illustrates the limitations to the performance of the DMFC.

DMFC is an appropriate alternative to rechargeable battery technology and an ideal solution as the auto motive and portable power sources. Several research communities and companies have developed the DMFC stack for practical application [32]. For example, Sony developed a DMFC system combined with a Li-ion secondary battery in 2008. This hybrid system improved the peak output of the single DMFC from 1 W to 3 W [33]. In 2009, Toshiba launched its first commercial DMFC product: Dynario^{TM}, which can be used as an external power source for mobile digital products use [34]. Oorja Protonics, a U.S. manufacturer of methanol fuel cells, announced the installation of the OorjaPac^{TM} Model III units in 2011. The energy output capacity is 29 kWh day^{-1} and it can work 12-16 hours without refuelling [35].

1.3 Fuel cells modelling

Modelling plays a significant role in the process of fuel cell design and development. Normally, the fuel cell design and development process begins with a set of requirements, including power output, operating conditions, size limitation, safety specifications, and others. Based on the knowledge of materials and processes involved in the fuel cells, modelling is performed to predict the fuel cell performance. The modelling helps the designer to determine the best candidate designs or improve the existing designs that satisfy the requirement.

Modelling can provides a better understanding on the electrochemical reactions and mass transport occurred within the fuel cells, for example, the reactants profiles [36], temperature distribution [37], and polarisation curves obtained [38]. It can give a quick prediction of the fuel cell performance under various given operating conditions, material properties and fuel cell geometries. Modelling reduces the time, effort and cost associated with the experimental studies and provides a theoretical guidance on the development and optimisation of the fuel cells [39].

Even though numerous fuel cell models are available, the complicate chemical and physical processes inside fuel cells are not fully coupled. In other words, specific models normally focus on particular aspects. The thesis fills the knowledge gap between the previous fuel cell models and improves the simulation accuracy by fully coupling the following six processes simultaneously occurres, namely, agglomerate model for oxygen reduction reaction (ORR) within the cathode catalyst layer, two-phase flow model for liquid water saturation and transport within the cathode electrode, non-isothermal model for heat generation and transport, combinational mechanism for water transport through the membrane, water phase transfer and membrane/ionomer swelling.

1.4 Project objectives and thesis structure

A main objective of this programme is to develop a better understanding of water transport in PEMFCs under a variety of load conditions. The aim is to develop a computational model which is capable of analysing and predicting the behaviour of a PEMFC equipped with a Nafion® membrane. This model will give guidance to enhance the PEMFC output by optimising the composition of the electrode and operating conditions.

The research programme is comprised of the following targets:

a. A review of PEMFC modelling approaches.

b. Developing a mathematical relationship for the composition of the catalyst layers of the anode and cathode.

c. Developing a single-phase flow model to analyse the mass transport along the flow channel and within the porous media.

d. Developing a two-phase flow model to study the dissolved water transport through the membrane and the liquid water distribution in cathode.

e. Developing a non-isothermal model to analyse the temperature distribution within the MEA.

f. Optimising the composition of the cathode catalyst layer based on surrogate modelling.

g. Developing a time dependent isothermal model for the DMFC anode to study the macro kinetic of methanol oxidation, in which methanol transport process and oxidation reaction are coupled.

This thesis is divided into eight chapters as follow:

Chapter 1. An overview of the hydrogen energy and fuel cell technology.

Chapter 2. A literature review of the different fuel cell modelling approaches.

Chapter 3. A detailed description of the fundamentals, principles and governing equations.

Chapter 4. A single-phase flow isothermal model is developed to analyse the distribution of the reactant species in flow channel and porous electrode. This model is used to study the water content distribution within the membrane and the effect of catalyst layer parameters on fuel cell performance.

Chapter 5. A two-phase flow isothermal model is developed to study the water phase transfer, dissolved water transport through the membrane and ionomer, and liquid water distribution in cathode catalyst layer and gas diffusion layer is represented.

Chapter 6. A two-phase flow non-isothermal model is developed to investigate the temperature distribution in MEA, and the influence of temperature on membrane water content, liquid water saturation, and cell performance.

Chapter 7. A multiple surrogate model is developed to optimise the cathode catalyst layer composition. Five design parameters are optimised and their sensitivities are analysed by a Monte Carlo method based approach.

Chapter 8. The time dependent and steady state macro kinetic models for methanol oxidation in a porous anode of a DMFC are presented. These models are used to investigate the effect of operating conditions on the transient response and the effect of electrode parameters on the anode performance.

Chapter 9. Conclusions of the study are summarised and future research trends and directions are recommended.

Chapter 2. Overview of water management, optimisation and performance of PEMFCs and DMFCs

2.1 Introduction

By now, research and development in fuel cell technology have resulted in a broad range of insights on aspects to material, design, manufacturing and operating of PEMFCs and DMFCs [40-43]. These variations indicate that there are a multitude of factors governing the performance of the PEMFCs and DMFCs, of which some physical design or operation can be optimised to improve the fuel cell performance, for example, the platinum and ionomer loadings of the catalyst layer [44-47], the relative humidity of the reactant gas inlet [48, 49], as well as the flow field configuration [50-55].

This chapter reviews the state-of-art research and development on the modelling, design and optimisation of the PEMFCs and DMFCs. As a vital important issue of fuel cell operation, water management including water transport and liquid water flooding are reviewed. Following the review of modelling approach and experimental study for water transport, the overview of the PEMFCs optimisation is represented. At the end of this chapter, the anode behaviour of the DMFCs is reviewed.

2.2 Overview of water transport and flooding in the PEMFC

For PEMFCs, the perfluorinated membranes, such as Nafion®, are typically used as the electrolyte. Ionomer is required in the catalyst layers preparation for the purpose of proton transport from the anode catalyst layer, through the membrane, to the cathode catalyst layer. As shown in Figure 2-1, on the membrane-catalyst layer boundary, Nafion® membrane is connected with the ionomer in the catalyst layers, for both the anode and cathode. Water in PEMFCs acts as the lubricant which makes the fuel cell system running smoothly [56]. It can be fed into the PEMFCs system by the gas inlet or/and generated by the oxygen reduction reaction (ORR) at cathode. Water existes as water vapour in the gas mixture, which is absorbed by the Nafion® membrane as well as the ionomer in the catalyst layer becoming the dissolved water. When current is generated, the proton migration through the membrane is associated with a drag of water molecules from the anode to the cathode. This so-called electro-osmotic drag

(EOD), together with the electrochemical water production, leads to a water accumulation at the cathode.

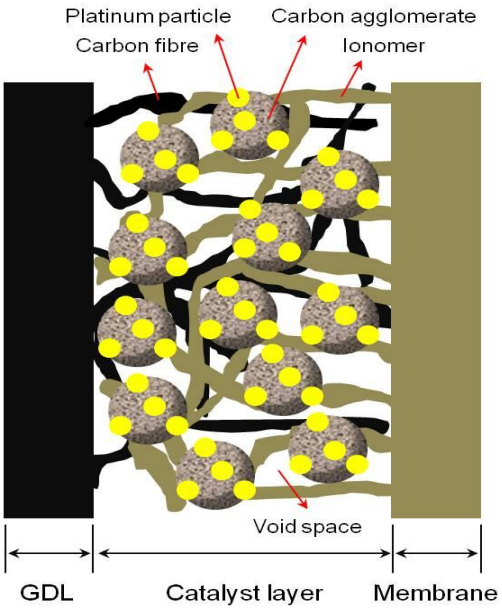

Figure 2-1 Structure of catalyst layers in PEMFCs

Due to the generated gradient of water concentration between the anode and cathode, a certain amount of water could diffuse back from the cathode to the anode, which is an opposite direction against the EOD. In addition, the pressure difference between the anode and cathode could drive a water transport through the membrane, which is called hydraulic permeation. The water transport occurred in a PEMFC is schematically shown in Figure 2-2.

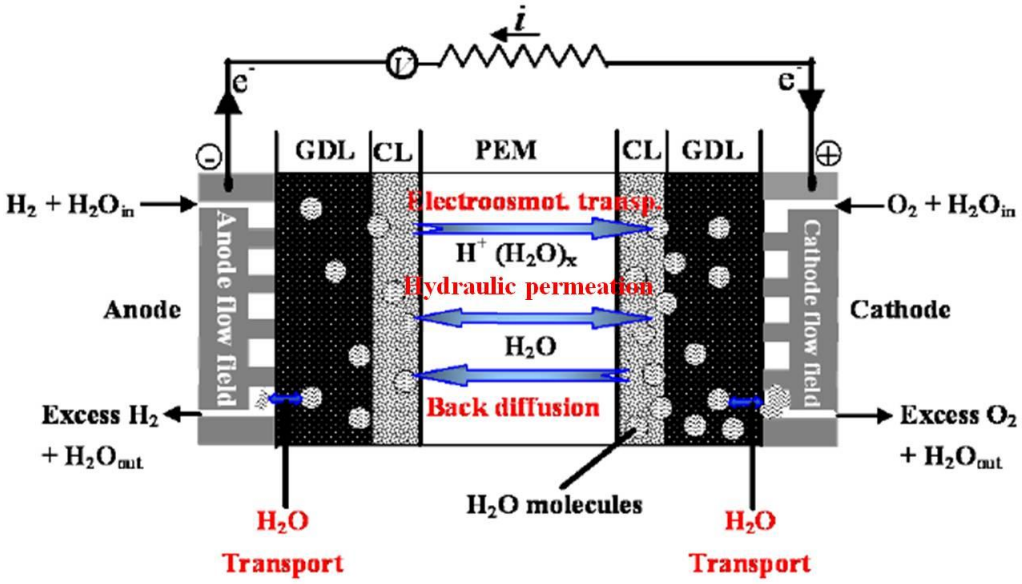

Figure 2-2 Water transport mechanism inside the PEMFCs [56]

Maintaining a subtle equilibrium between membrane dehydration and liquid water flooding is the key issue to achieve maximum performance and durability for PEMFCs [57, 58]. On one hand, water is required to guarantee the good proton conductivity of the proton exchange membrane, where protons move in the hydrated parts of the ionomer via dissociation of sulfonic acid bonds. The protons cannot migrate in dry proton exchange membrane, where the sulfonic acid bond cannot be dissociated, lead to a decrease of ionic conductivity [59]. Furthermore, lower ionic conductivity hinders the access of protons to the active sites of catalyst layer, resulting in an increase in activation polarisation [60]. On the other hand, excess water formed within catalyst layers needs to be transported to flow channels through gas diffusion layers and removed by reactant gas out of the PEMFC system (see Figure 2-3) or else excess water will block the flow channel and the pores of the porous electrodes and then increase the mass transport resistance. This phenomenon, which can be considered as one of the most important limiting factor of PEMFC performance, is known as "flooding".

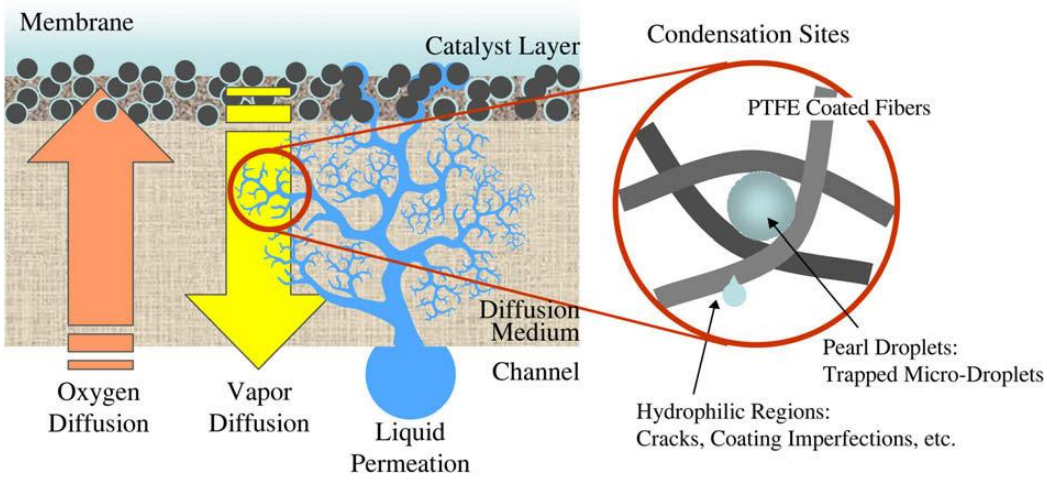

Figure 2-3 Converging capillary tree water transport mechanism [126]

Cathode flooding, anode flooding and flow channel flooding are the three main types of flooding included in the PEMFC system. They are determined by temperature, gas flow rate, pressure and humidity of the reactant gases. Generally, flooding of the cathode and the anode are linked to high current density that results in a greater water formation rate than the removal rate. Moreover, even if liquid water floods into both side of the electrodes [61, 62], water flooding is more prone to occur at the cathode, because water formed within the catalyst layer of the cathode, especially at higher current density [63]. The accumulation of liquid water in the channels is observed only after complete saturation of the gas with water vapour because the evaporation and

water vapour transport are relatively faster than liquid water transport [62]. The thickness of the membrane, water content of the membrane and humidity of the reactant gases in turn determine the concentration gradient of water between anode and cathode. Furthermore, membrane water content and reactant gas humidity are dependent on the gas inlet humidification and the temperature and pressure in the gas channels [63]. Besides, back diffusion prevails over electro-osmotic drag at lower current density; and electro-osmotic drag prevails over back diffusion while higher current density is achieved, thus the anode (including the membrane) tends to dry out, even the cathode is well hydrated at high current density [64].

Membrane dehydration is the most serious negative influence on the fuel cell performance. It is more likely to occur at the anode side of the membrane due to the dry reactant gas inlet and the effect of electro-osmotic drag. The pores of membrane shrink under the dehydrated condition, leading to lower water back diffusion, especially for the operating conditions such as higher temperature and higher current density. Consequently, the proton exchange membrane dehydrates, resulting in a remarkable decrease in the conductivity and a big increase in the ionic resistance [58, 64, 65]. In addition, severe drying condition leads to irreversible degradation of the membrane [66, 67]. All types of flooding lead to instant increase in mass transport losses, gas starvation and immediate drop of cell potential. As shown in Figure 2-4, the time dependent performance of current density at 0.6 V vs. SHE (standard hydrogen electrode) is observed [68]. The gas flow path can be temporarily blocked by liquid water, giving rise to a sharp reduction in current density.

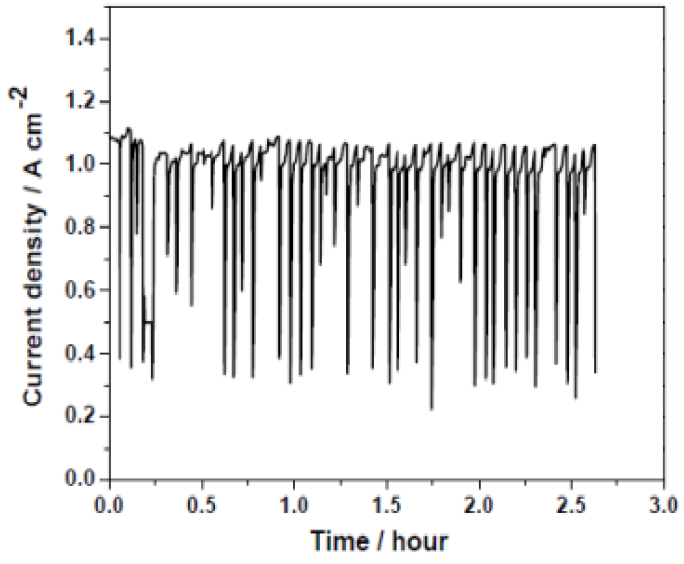

Figure 2-4 A typical water flooding pattern in a PEMFC operated at constant cell voltage [56]

It is important to note that one of the most serious negative effects of cathode flooding is the voltage reversal effect (VRE). In the case of oxygen starvation, not enough oxygen supplied at cathode. H_3O^+, which generated by water molecule and proton at cathode according to Eq. (2-1), would be reduced by electron instead of oxygen, resulting in a significant drop of potential.

$$H_2 + 2H_2O \rightarrow 2H_3O^+ + 2e^- \quad (\phi^0 = 0.00\text{V}) \tag{2-1}$$

The original electron consuming process of oxygen reduction reaction (Eq. 2-2) would be replaced by the new electron consuming process (Eq. 2-3) as follow:

$$O_2 + 4H^+ + 4e^- \rightarrow 2H_2O \qquad (\phi^0 = 1.23\text{V}) \tag{2-2}$$

$$2H_3O^+ + 2e^- \rightarrow H_2 + 2H_2O \quad (\phi^0 = 0.00\text{V}) \tag{2-3}$$

Consequently, the cathode potential decreases from 1.23 V to 0.00 V at current off and from 0.80 V to -0.1 V at current on.

Polarisation occurs while current flows through the electrode. The cathode polarisation causes potential to change more negative and anode polarisation more positive [68], for example 0.1 V. As a result, the output voltage of the cell decreases from 0.7 V to -0.2 V under the effect of VRE (see Figure 2-5).

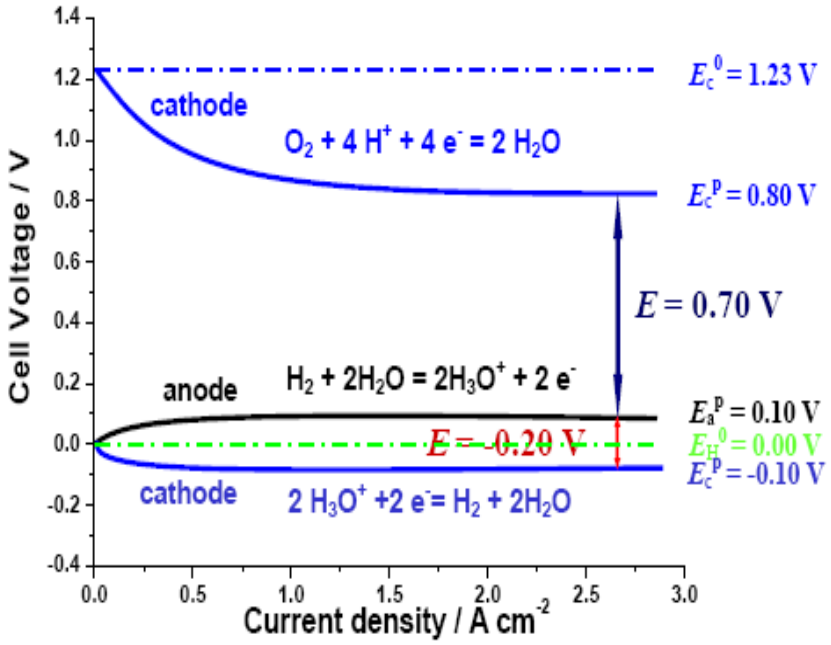

Figure 2-5 Voltage reversal effect (VRE) in PEMFC [56]

2.3 Overview of modelling of water transport in PEMFC

Numerical modelling of PEMFC is important for better understanding of the transport processes in PEMFC because of the experimental drawbacks such as difficulty of performing the different experimental measurements simultaneously, unrealistic operating conditions, and high cost of materials and testing instruments. Numerous models have been developed to describe water management and liquid water transport in PEMFCs over the last decade [69-73]. Depending on different descriptions on water formation and transport, the models can be mainly categorised into four groups: dynamic models, lumped models, flooding models and other models associated with the effect of geometrical configuration.

In early 1990s, some simple models have been developed. These models were all simplified models which all applied the assumption that the reactant and charge only transport along one direction. The numerical models developed by Springer *et al.* [74, 75] and Bernardi and Verbrugge [21, 76] are usually considered as the pioneering modelling works for PEMFC. These models are essentially one dimensional models considering the membrane, catalyst layer and gas diffusion layer based on solving the conservations equations by assuming homogeneous materials and using effective transport properties. After that, Nguyen and White [77] and Fuller and Newman [78] developed pseudo two dimensional models by further considering the flow channels, which considered the effect of water humidity inlet and temperature distributions, providing more detailed water and thermal management capability. However, the models developed in this period are too simple to simulate the very complex PEMFC system although they laid the foundation for PEMFC modelling.

More numerical models were developed in the late 1990s. Yi and Nguyen [79, 80] and Gurau *et al.* [36] developed two dimensional models to explore more detailed transport phenomena in PEMFCs. These models illustrated the utility of multi-dimensional models in the understanding of the internal conditions of PEMFC, such as the reactant and water distribution. Gloaguen and Durand [81], Bultel *et al.* [82-84] and Marr and Li [85] developed the agglomerate models. These models applied simplified catalyst layer structures by assuming that the large agglomerates were formed by ionomer and platimum/carbon particles on the level of micrometre. Compared to the models developed earlier, more detailed mass and charge transport phenomena were

analysed more accurately because these models extended the one dimensional or pseudo two dimensional to the two dimensional. It is important to note that all the models developed were based on the single phase assumption, which treated the water as vapour, including the water formed in the cathode catalyst layer and supplied along with the humidified gas inlet. The water condensation within the porous electrodes and the flow channels was not considered. Although there was not sufficient evidence to conform that water could be condensed in catalyst layers and gas diffusion layers while the PEMFC system operated in normal condition. However, condensed water in the flow channels has been observed by some instruments such as high-resolution camera [86, 87]. Generally, ideal single phase assumption is applied when reactant gases are oxidised or reduced at the surface of solid catalyst (Pt-Ru and other binary or ternary alloy). In reality, the condensed water could change the single-phase flow problem to a two-phase flow problem.

In the 2000s, multi-dimensional models have been developed by many researchers to solve a complete set of conservation equations (such as continuity and Navier-Stokes) coupled with electrochemical reactions (for example the kinetics of oxygen reduction at cathode). Computational fluid dynamics (CFD) code and some commercial software (such as Fluent, COMSOL) based on finite volume methods were adopted to develop such models, and more complicated geometry and transport phenomena were investigated. In the area of three dimensional geometry, the models developed by Dutta *et al.* [88, 89], Zhou and Liu [90], Berning *et al.* [91], Mazumder and Cole [92], Lee *et al.* [93], Um and Wang [94] and Wang and Wang [95] were considered as the pioneering works in this field, these models mainly considered a single flow channel with the major components of reactant gases. Large scale simulations considering multi-channel or small stacks were also carried out [96-99]. Without doubt, these models give more accurate and more specific analysis on the distribution of reactant gases (H_2 and O_2), water vapour, and pressures. The main impediment to the widespread use of these multi-dimensional models is the requirement for the computer hardware.

In fact, reasonable simplification of the complex multi-dimensional models is considered as the practical way of modelling the complicate transportation and reaction inside of the PEMFC with lower computational requirement. In order to simplify the models and reduce the amount of computation for conservation equations, some modelling works neglected liquid water formation by assuming liquid water as super saturated water vapour [77-79]. The real two-phase flow models, which give more

accurate prediction than the previous models with single-phase assumption, have also been developed by Nguyen *et al.* [100-103], Djilali *et al.* [104-106], Mazumber and Cole [107], and Wang *et al.* [108, 109]. These two-phase flow models solved the mass, momentum and species transport conservation equations for the gas mixture, with an extra conservation equation for liquid water transport. However, the accurate and detailed water transport behaviour cannot be studied in these models because the interface tracking between liquid water and gas is not permitted. As a result, the volume of fluid (VOF) model, based on liquid water dynamics in order to investigate water flow in single serpentine flow channel, was developed by Quan *et al.* [110].

Overall, a large number of numerical models have been developed by researches around the world. The main difference between the models developed in different period is presented in Table 2-1. In short, the development of these models is from simple to complex, from general to specific. In spite of the great changes of the equation forms in the models, all the processes are described based on some basic laws, for example, the laws of conservation of energy and momentum. Developing a comprehensive and comparatively simple model for the PEMFCs under practical load conditions by reasonably simplify the complex multi-dimensional models is our main objective of the modelling work. Furthermore, the experimental data will be obtained to validate the simulation results.

Table 2-1 Development of modelling work on the PEMFC

Models	Period of development	Dimensions of reactant, products and charge transportation	Accuracy of modelling process comparing to practical fuel cell	Complexity of the models and computer hardware requirement
1D and pseudo 2D	Early 1990s	One dimension	Crude	Simple and low
2D	Later 1990s	Two dimensions	Medium	Medium
3D and multi-dimensional	2000s	Three dimensions	Precise	Complex and high

2.3.1 Modelling of water transport through the membrane

The previous modelling efforts on water transport through the membrane can be classified into three types: diffusive, chemical potential and hydraulic models. The diffusive model can be explained with dilute solution theory by considering the

membrane as solvent while water and proton as solute. This theory assumes that the interaction between different solute species can be neglected, and only the interaction between solute (water and proton) and solvent (membrane) is considered. Then the flux of solute species in solvent can be described by using the Nernst-Planck equation. Nernst-Planck equation is a conservation of mass describing the flux of ions under the influence of both an ionic concentration gradient and an electric field. The general form of Nernst-Planck equation is:

$$\frac{dc_i}{dt} = \nabla(D_i \nabla c_i - \mathbf{u}c_i + \frac{D_i z_i e}{k_B} c_i \nabla \phi) \tag{2-4}$$

where t (s) is time, D_i (m^2 s^{-1}) is the diffusivity of the solute specie i, c_i (mol m^{-3}) is the concentration of the solute specie i, $\mathbf{u}$ (m s^{-1}) is the velocity of the fluid, z_i is the valence of ionic specie i, e (1.60218×10^{-19} C) is elementary charge, k_B (1.3806505×10^{-23} J K^{-1}) is the Boltzmann constant, T (K) is temperature.

For water transport, $\frac{D_i z_i e}{k_B} c_i \nabla \phi$ becomes zero because water is in zero valence. For proton transport, $D_i \nabla c_i$ becomes zero by assuming constant concentration of proton through the membrane. Furthermore, $\mathbf{u}c_i$ becomes zero for both the water and proton transport due to the fact that the membrane does not move. Therefore, the Nernst-Planck equation for proton transport is simplified to Ohm's law [111],

$$i = -\sigma_M \nabla \phi \tag{2-5}$$

By further considering the effect of electro-osmotic drag, the water transport is simplified to [112]:

$$J_w = D_M \nabla c_w + n_{drag} \frac{i}{F} \tag{2-6}$$

where σ_M (Ω^{-1}) is the membrane conductivity, $\nabla \phi$ (V) is the potential, D_M (m^2 s^{-1}) is the diffusivity of water through the membrane, n_{drag} is electro-osmotic drag coefficient through membrane, c_w (mol m^{-3}) is water concentration, F (C mol^{-1}) is Faraday's constant, i (A m^{-2}) is the current density.

The diffusive model is the most successful model for water transport through membrane since its initial application by Springer *et al.* [74, 75]. By further considering the interaction between different solute species, the chemical potential model is developed. The proton and water transport through membrane therefore can be explained by concentrated solution theory [112, 113] as

$$i = -\sigma_M \nabla \phi - \frac{n_{drag}\sigma_M}{F} \nabla \prod_H \tag{2-7}$$

$$J_w = -\alpha_w \nabla \prod_w + n_{drag} \frac{i}{F} \tag{2-8}$$

where $\prod_H$ (J mol^{-1}) and $\prod_w$ (J mol^{-1}) are the chemical potential of proton and water, respectively. α_w is water transport coefficient through membrane.

Comparing Eq. (2-5) with Eq. (2-7) and Eq. (2-6) with Eq. (2-8), it can be noticed that the concentration (c) is replaced by chemical potential ($\prod$), the diffusion coefficient (D) is replaced by transport coefficient (α), and one more term is added in Eq. (2-7) to account for the multi-component interaction. The biggest obstacle of the widespread use of the chemical potential model is the difficulty in obtaining the transport parameters. As a result, the chemical potential model is less popular than the diffusive model.

In the diffusive and chemical potential models, the convective transport caused by pressure gradient across membrane is not considered. However, the convective transport could happen when water enlarges the pores of the membrane. To fill the gap, the hydraulic model is developed [21, 76] according to two assumptions:

(1) The membrane is assumed to be fully hydrated to allow the maximum possible convective transport.

(2) Constant gas volume fraction in membrane is assumed.

Consequently, water flux due to pressure gradient and electro-osmotic drag can be calculated by Nernst-Planck equation. Generally, the hydraulic model neglects the diffusive transport, and the water flux can be represented by the following equation:

$$J_w = -c_w \frac{k_p}{\mu_w} \nabla p_w + n_{drag} \frac{i}{F} \tag{2-9}$$

where k_p (m^2) and μ_w (Pa s) are the permeability and dynamic viscosity of water in membrane. Due to the effect of electro-osmotic drag, the anode side of the membrane is often prone to dry out. Therefore, the fully hydrated membrane assumption remains questionable. In fact, water convective transport is only considerable while the pressure gradient exists between the anode and cathode. If the inlet gas pressure of anode is as same as that of cathode, the water convective transport could be neglect because diffusive transport and electro-osmotic drag have bigger influence on the water transport. The merits and demerits of these three types of models are summarised in Table 2-2.

Table 2-2 Comparison between the water transport models

Model	*Merits*	*Demerits*
Diffusion model-Springer *et al.* [74, 75]	1. Membrane conductivity was associated with water content. 2. Capable of determining the membrane conductivity in moderate and high hydration cases.	1. Lack of accuracy at very low membrane water content. 2. Failed to describe the water concentration through the membrane in case of saturation. 3. Restricted to Nafion® membrane.
Chemical potential model-Weber and Newman [112]	1. The frictional forces on species motion were considered. 2. The electrostatic interactions were taken into account. 3. Both the pressure and activity are incorporated as the driving force. 4. Bridging the gap between the single-phase and two-phase models	1. A multitude of parameters. 2. Difficulty in obtaining the values of the parameters. 3. Complicated boundary conditions. 4. Only works on Nafion® membrane.
Hydraulic model-Bernardi and Verbrugge [21, 76]	1. Both the pressure and electric potential forces were included in the driving force. 2. Electro-osmotic drag, back diffusion and hydraulic permeation were all considered for water transport through the membrane.	1. Requiring the values of the membrane parameters. 2. Impossible to account for the membrane structure. 3. The chemical interaction between water and membrane materials was not considered.

2.3.2 Modelling of water transport in porous electrodes

A variety of different models have been developed for modelling the water transport in the porous electrodes, including gas diffusion layers and catalyst layers. Depending on the assumption of the morphology of the porous electrodes, the models can be categorised into two groups, namely homogenous and non-homogenous models. In the homogenous models, the porous electrodes are assumed to be constructed by

homogeneous materials, while the non-homogenous model applies real or simplified micro-structure of the porous electrodes. When the porous electrodes are assumed as homogeneous, the entire computational domain shares the same properties, such as conductivity, permeability and porosity. The overall effect of micro-structure is usually reflected by the effective coefficient. Thus, the geometry generation and model solving process are greatly simplified and result in an easier model development and lower requirement of the computer hardware. The drawback of this assumption is the lack of precision about the detailed process within the porous electrodes, such as nucleation water. The modelling works before 2000s usually adopts the homogeneous assumption [21, 72-84].

The gas diffusion layer is typically made up of three-dimensional random carbon fibre and its real structure is highly anomalous [114-116]. In order to accurately simulate the electrochemical reactions and transport processes occurred in a real or simplified gas diffusion layer, e.g. the liquid water formation and transport, numerous models have been developed [55, 63, 66, 94, 95, 108, 109, 117-121]. The volume of fluid (VOF) model [63, 66, 94, 95, 108, 109, 117] and Lattice Boltzmann (LB) model [55, 118, 119, 120, 121] are the two types of the most popular models for liquid water transport in the gas diffusion layers. In this literature review, the VOF model is presented as an example. Under isothermal condition, by omitting the phase change and electrochemical reaction, the VOF model with two phases, reactant gas and liquid water, can be presented by the following conservation equations.

Conservation of mass for the two-phase mixture:

$$\frac{\partial}{\partial t}\rho + \nabla(\rho\vec{u}) = 0 \tag{2-10}$$

Conservation of momentum for the two-phase mixture:

$$\frac{\partial}{\partial t}(\rho\vec{u}) + \nabla(\rho\vec{u}\vec{u}) = -\nabla p + \mu\nabla(\nabla\vec{u} + \nabla\vec{u}^{T}) - \frac{2}{3}\mu\nabla(\nabla\vec{u}) + S_u \tag{2-11}$$

Conservation of momentum for the liquid water only:

$$\frac{\partial}{\partial t}(\rho s_l) + \nabla(\rho s_l\vec{u}) = 0 \tag{2-12}$$

where ρ (kg·m^{-3}) and μ (kg·m^{-1}·s^{-1}) are the density and dynamic viscosity of the two-phase mixture, respectively, and they are the volume averaged values. The volume averaged density and viscosity can be described as follow:

$$\rho = s_g \rho_g + s_l \rho_l \tag{2-13}$$

$$\mu = s_g \mu_g + s_l \mu_l \tag{2-14}$$

$$s_g + s_l = 1 \tag{2-15}$$

where s is the volume fraction, and the subscript l and g represent the liquid and gas phases, respectively.

In the momentum equation Eq. (2-11), S_u (kg m^{-2} s^{-2}) is the source term accounting for the surface tension effect, which can be calculated as

$$S_u = \gamma \frac{2\chi\rho\nabla s_g}{(\rho_g + \rho_l)} \tag{2-16}$$

where γ (N·m^{-1}) is the surface tension coefficient between the two phases, and χ (m^{-1}) is the surface curvature defined as

$$\chi = \nabla[\vec{\nu}_w \cos(\theta) + \vec{\tau}_w \sin(\theta)] \tag{2-17}$$

where $\vec{\nu}_w$ and $\vec{\tau}_w$ (m s^{-1}) are the unit vectors normal and tangential to the wall surface, and θ (°) is the contact angel.

Note that the shape of the interface between the two phases at the wall depends on the wettability of the wall. By using the VOF model in a micro-structure of the gas diffusion layers, the movement of liquid water under the effect of pressure gradient and contact angel can be observed [117]. Figure 2-6 shows the transient liquid water discharging from the gas diffusion layer with the pressure gradient of 6.5×10^5 Pa m^{-1} and contact angel of 135°. It can be observed that liquid water is removed under a pressure gradient and finally only a small amount of liquid water is left in the GDL.

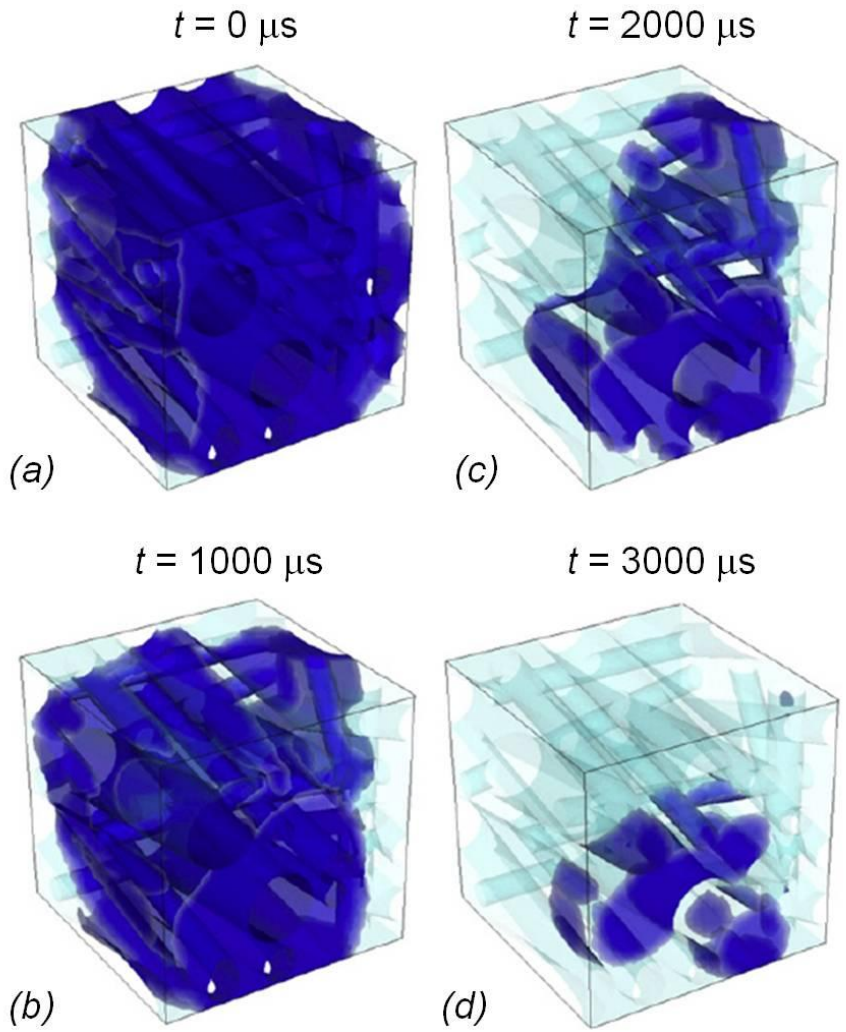

Figure 2-6 Transient liquid water discharging from GDL obtained from VOF model [117]
(Pressure gradient is 6.5×10^5 Pa m^{-1} and the contact angel is 135°)

Catalyst layer is the core of the PEMFC in which electrochemical reaction occurred. The catalyst layers are prepared by spraying the catalyst particle (such as Pt-Ru alloy) contained ink onto the carbon paper. The difference between the catalyst layer and gas diffusion layer is that the catalyst particle is surrounded by the carbon fibre in the catalyst layers and result in much small pores than that of the gas diffusion layers. Therefore, the VOF model is hard to be applied to the micro-structure of the catalyst layers [114]. The general process of the electrochemical reaction includes two steps, diffusion and reaction. First of all, the reactants must transport through the porous media and reach the surface of the catalyst particles. Then the reactants are absorbed on the surface of the catalyst particle where products are generated via chemical reactions. Finally, the products generated on the surface of the catalyst particle must move away.

The models mentioned previously applied a variety of approaches to describe the catalyst layer. Depending on the degree of complexity, these approaches can be categorised into three groups. In the simplest approach, the catalyst layers are treated as reactive boundaries between the gas diffusion layer and membrane [91, 122]. For example, Jeng *et al.* [122] developed a simple two dimensional across-the-channel model to study the mass transport of the reactant gases through the gas diffusion layers. The effectiveness of the gas diffusion layers was evaluated under different current densities and an optimal thickness of the cathode gas diffusion layer was suggested. Berning *et al.* [91] developed a three dimensional, non-isothermal model to investigate the temperature distribution in the MEA. However, the catalyst layers were treated as one-dimensional boundaries in this model. It is important to notice that this kind of approach always over estimate the current density due to the ignorance of the mass transport resistance in the catalyst layer.

The second approach assumes the catalyst layer as a thin film fully flooded with liquid water or ionomer. This approach is adopted in the model developed by Marr and Li [85], in which the void space within the cathode catalyst layer was fully occupied by liquid water. This model can give a reasonable simulation on the cell performance during higher current densities. However, it underestimated the cell performance during lower current densities due to an increase in mass transport within the catalyst layer.

In the last approach, the catalyst layer is assumed as a porous two or three dimensional domain filled with catalyst particles agglomerate. The void spaces within the agglomerates (inter-agglomerate space) and between the agglomerates (outer-agglomerate space) are defined as the primary and secondary pores, respectively. Both the primary and secondary pores can be filled with ionomer, liquid water, and reactants. The models applied this approach is called the agglomerate models, which can be further subcategorised into three sub-groups namely slab, cylindrical and spherical agglomerate models [115] as shown in Figure 2-7.

In order to give a more accurate simulation on the diffusion-reaction process occurred in the catalyst layer, agglomerate models are usually preferred. In the agglomerate models, the catalyst particles, ionomer and void space are assumed to be homogeneously mixed to form the micrometre agglomerates. In the spherical agglomerate model, the diameter of the agglomerate is less than 10 μm [116].

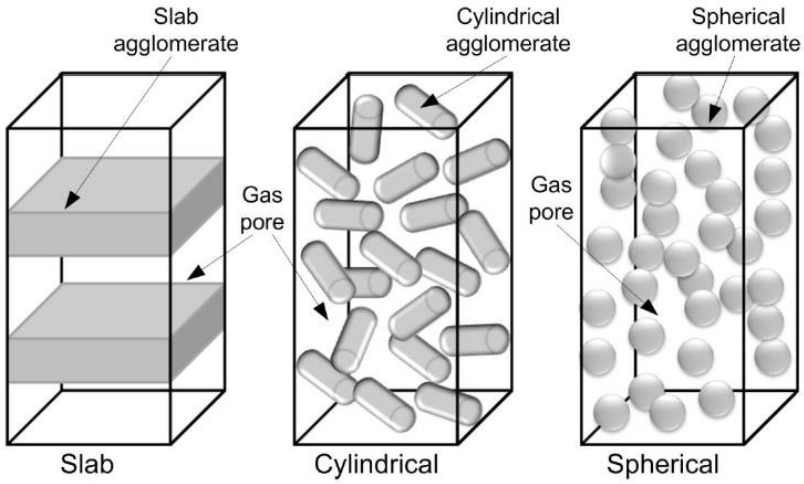

Figure 2-7 Schematic representation of the agglomerate catalyst layer

Due to the fact that the sluggish oxygen reduction reaction (ORR) occurred at the cathode, the agglomerate models are therefore usually adopted in the cathode catalyst layer. At cathode, the rate expression of oxygen reduction can be presented as:

$$R_{O_2} = k_{O_2} c_{O_2} \tag{2-18}$$

In order to account for the mass transport from the outer boundary to the centre of the agglomerates, the effectiveness factor, E_r, is introduced into Eq. (2-18) as follow:

$$R_{O_2} = E_r k_{O_2} c_{O_2} \tag{2-19}$$

where

$$E_r = \frac{1}{\Phi_L}\left(\frac{1}{\tanh(3\Phi_L)} - \frac{1}{\Phi_L}\right), \qquad \Phi_L = \frac{R_{agg}}{3}\sqrt{\frac{k_{O_2}}{D_{eff}}} \tag{2-20}$$

The effectiveness factor can be considered as an indicator of catalyst utilisation.

By the effort of the agglomerate model, the ORR kinetics is simulated quantitatively. As the production of ORR, the amount of water can be therefore calculated.

2.4 Flow field design

There are mainly four types of typical flow fields, namely parallel (conventional), serpentine, interdigitated and pin-type, employed in the practical applications. The features and differences are shown in Figure 2-8 as follow:

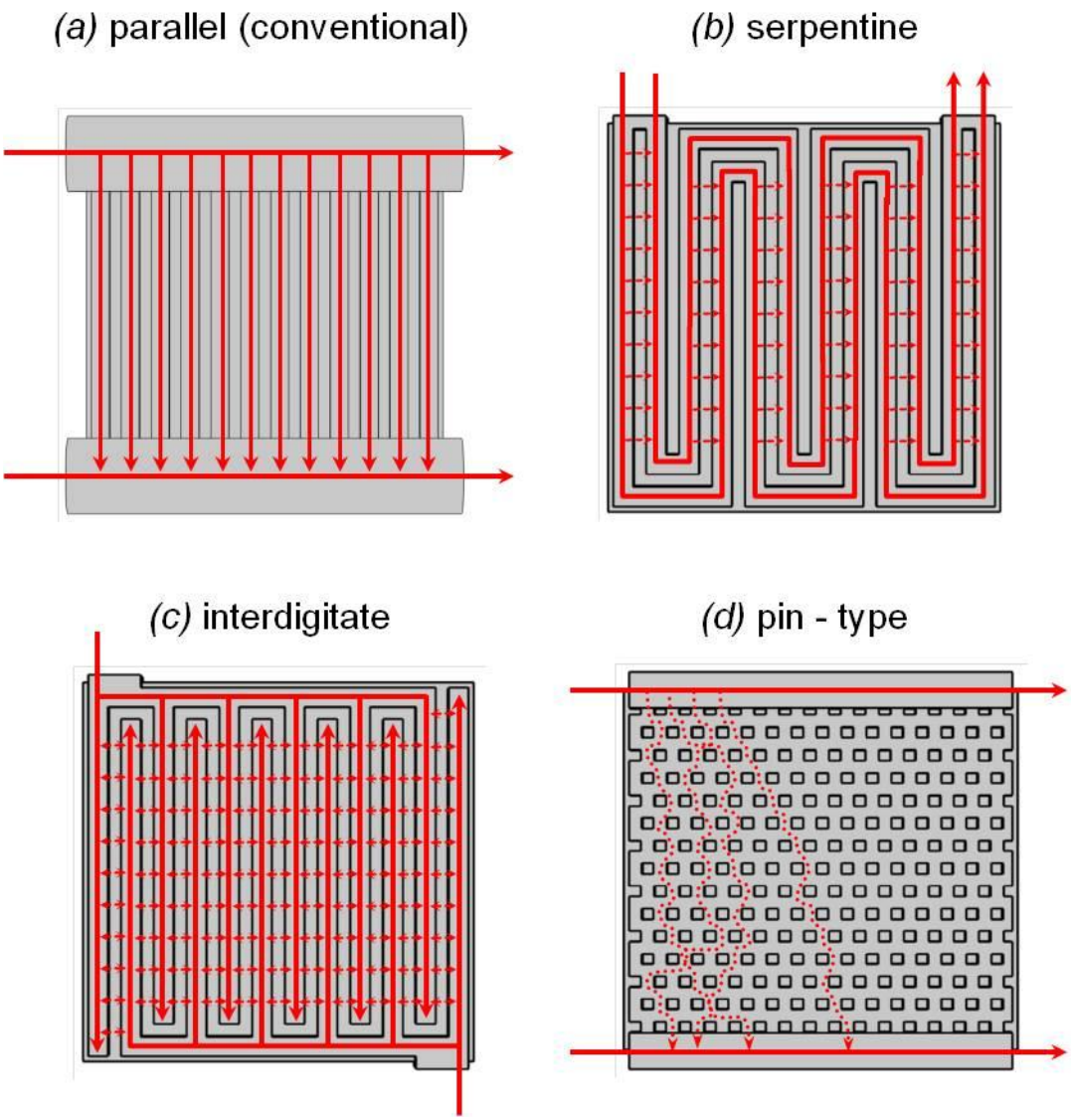

Figure 2-8 Four types of typical flow field designs [53]

In the parallel flow field, diffusion is the dominant mechanism for the transport of reactants and products. The conventional flow field is an energy saving design because very low inlet pressure is required for the gas flow at the inlet. However, the accumulation of reactant gas and liquid water are prone to occur because the transport rate is limited by diffusion. The parallel flow field is popular due to its simple mass transport mechanism and low inlet pressure requirement.

In the serpentine flow field, the pressure and concentration of the reactant gas decrease along the flow channel from the inlet to the outlet. If the channel cross-section is small while the channel length is very long, the pressure drop between the adjacent channels becomes substantial, significant pressure gradient is therefore set up across the porous electrode, much larger than the pressure gradient along the flow channel,

resulting in a considerable cross leakage flow between the adjacent channels. This significant cross leakage flow through the porous electrode induces a strong convection in the electrode, resulting in a reinforced transport of the reactant gas to the catalyst layer for electrochemical reaction and an accelerated moving of product water from the active sites of catalyst layer to the flow channels. Therefore, this flow field design with a convective feature is most widely used and shows the most interesting of industrial collaboration. However, serpentine flow channel design is not the ideal flow field configuration due to a number of problems. For example, the substantial pressure drop due to the relatively long reactant flow path in the serpentine flow channel, which is considered as a significant power loss.

The flow channel design is a dead-end mode in the interdigitated flow field. When the reactant gases feed into the flow channel, they cannot flow out along the channel directly but flow through the porous gas diffusion layers. Therefore, the transport mechanism is converted from a diffusion mechanism to a forced convection mechanism. The shear force resulted from the gas flow helps to flush liquid water out of the electrode, thus effectively reducing the water flooding and significantly improving the cell performance [123]. However, higher inlet pressure is needed for gas flowing through the gas diffusion layers, which leads to a significant power loss.

The pin-type flow filed is a commonly utilised configuration, which provides random and multiple flow paths to the reactant gases. Therefore, one of the outstanding advantages of the pin-type flow filed is the low pressure drop between the inlet and the outlet. However, non-uniform flow and stagnant areas tend to occur at various places of the channels [124]. This significantly decreases the reactants transport efficiency and thus the overall fuel cell performance.

As stated by Liu *et al.* [50], an appropriate flow field design improves the reactant transport and the efficiency of the thermal and water management. The optimised flow filed is capable of reducing the activation polarisation and internal ohmic losses. The fuel cells with a parallel and an interdigitated flow fields were firstly experimentally compared by Nguyen [51] in 1996 and numerically compared by Kazim *et al.* [52] in 1999, respectively. They found that, as a new flow filed design, the interdigitated flow fields improve the fuel cell performance by enhancing the oxygen transport and reinforcing the water removal from the catalyst layer under forced gas convection. Four different flow filed designs including parallel, interdigitated, serpentine and pin-type,

were numerically compared by a three dimensional model developed by Sousa *et al.* [53]. The serpentine flow fields with different dimensions were further studied and optimised by the experiment and model of Liu *et al.* [50]. The effect of different channel shapes on pressure drop, oxygen distribution, liquid water formation and transport, as well as fuel cell performance were studied in recent years [44, 45].

2.5 Experimental measurement and visualisation of liquid water

Liquid water formation and transport can be observed directly or indirectly by experimental measurement including direct visualisation, nuclear magnetic resonance (NMR) imaging, beam interrogation and fluorescence microscopy.

Direct visualisation has the advantage of providing high resolution image of water transport in flow channels. Transparent flow channels are required when optical devices, such as high-speed camera [86, 87], infrared cameras [125] and charge-coupled device (CCD) cameras [126], are applied. It is useful to observe the effect of operating conditions on the formation, growth and movement of the droplet. For example, as shown in Figure 2-9, Hussaini and Wang [127] applied an operating fuel cell with a transparent flow channel of cathode to observe the liquid water flooding on the surface of the gas diffusion layer and in the flow channel. The two-phase transport, in the form of droplet, film and slug, is occurred in micro-channels of the PEMFC. However, the direct visualisation technique always provides images of liquid water in flow channels only because of the opaque materials of the gas diffusion layers and catalyst layers.

NMR is widely used in water visualisation by measuring the emitted signal from the excited H nuclei in an external magnetic field in PEMFC with opaque structures. This technique has successfully detected liquid water in the flow channels of an operating PEMFC. For example, Minard *et al.* [128] observed the dehydration of the membrane by employing the NMR technique. However, the NMR technique can only be used to observe water in the membrane rather than within paramagnetic materials like carbon. As a result, water content in the gas diffusion layers and catalyst layers is impossible to be detected by this technique.

Neutron imaging, electron microscopy and X-rays are the three frequently employed techniques included in the beam interrogation. The principle of neutron imaging is based on the sensitive response of neutrons to hydrogen-containing compounds such as water [129].This technique provides in-situ analysis on an operating PEMFC, such as

visualisation of water accumulation and distribution of water in the cathode porous electrodes and flow channels. The drawback of this technique, which limites the widespread application, is the high cost and the availability of radiation equipment that provides a neutron source. As shown in Figure 2-10, electron microscopy can be used to observe vapour condensation and liquid water morphology in porous gas diffusion layers and catalyst layers [114, 130]. Moreover, the X-ray image technique can give the temporal and spatial resolution of water formation and transport inside a PEMFC. These two techniques all show strong potential for the visualisation of water.

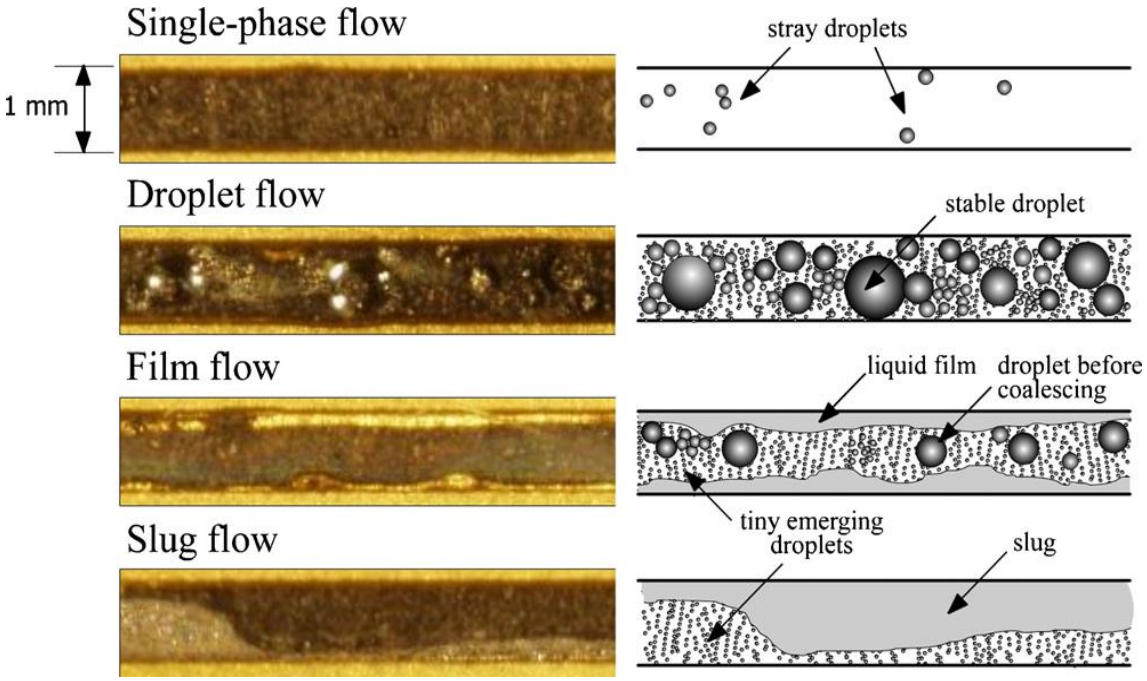

Figure 2-9 Magnified view of flow patterns in channels captured by the high resolution Olympus video microscope and the illustrations of liquid water generation and distribution [127]

Fluorescence microscopy is one of the important techniques for detecting the water in a PEMFC. This technique is based on the phenomenon that certain material, such as H nuclei, emits energy detectable as visible light when irradiated with the light of a specific wavelength. Fluorescence microscopy in conjunction with optical photography provides a method to visualise the micro-scale transport of liquid water on the surface of gas diffusion layers [131] and the dynamic water droplet behaviour emerging from the gas diffusion layers into flow channels [132].

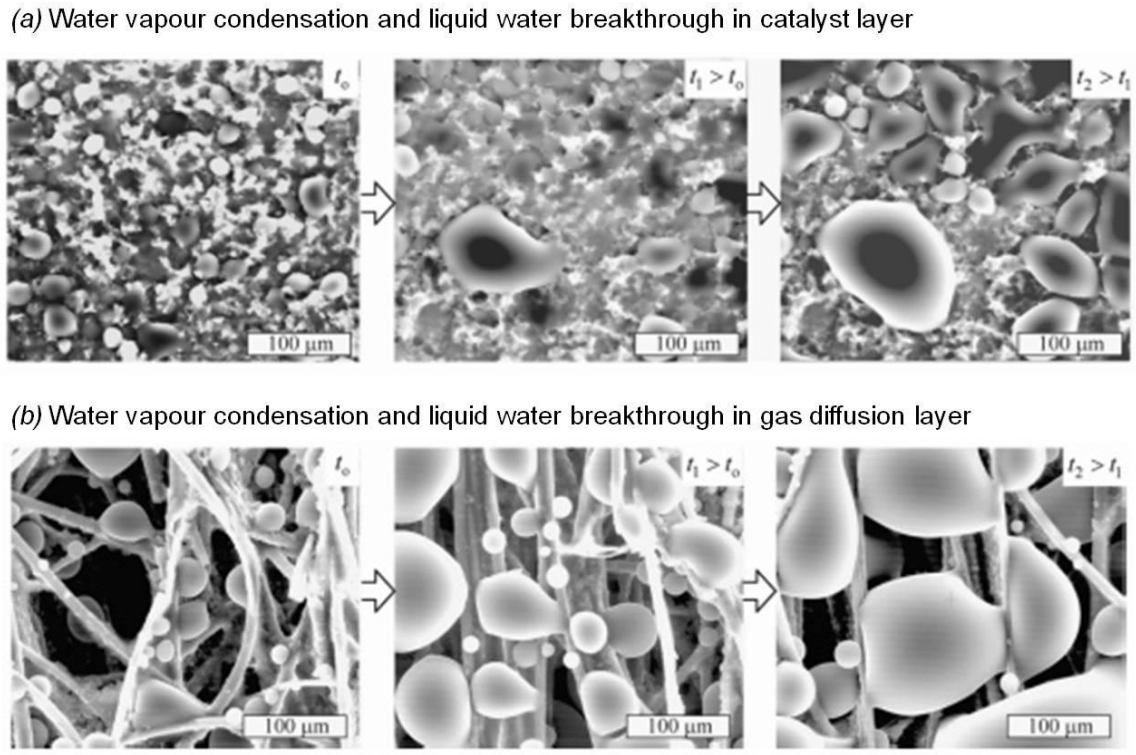

Figure 2-10 ESEM micrographs of vapour condensation and liquid water breakthrough in electrode [114]

The overview of the different visualisation techniques is summarised in Table 2-3.

Table 2-3 Water visualisation techniques and their applications

Water visualisation techniques	Type of visualisation	Basic principle	Scope of application
Direct visualisation	Direct	Optical photography	Transparent flow channels
NMR	Indirect	The spin of nuclei in an external magnetic field	Flow channels and membrane
Beam interrogation	Indirect	The sensitive response of neutrons to hydrogen-containing compounds	GDL, CL and membrane
Fluorescence microscopy	Indirect	Certain material emits energy detectable as visible light when irradiated with the light of a specific wavelength	GDL

2.6 Overview of PEMFC numerical optimisation

Numerical optimisation has been an active research area since 1960s [133]. It has been used in many applications, such as, structural [134], aerospace [135] and automotive engineering [136]. The common principle of the numerical optimisation is

to efficiently search for an optimal design in a coupled mathematical algorithm with the aid of a computational analysis tool. Only a few designs need to be evaluated using the optimisation algorithm, the computational time is therefore reduced. Optimal design helps the researchers to create a new design or improve an existing one. In order to account for the inter-relationship between various parameters and optimise several objectives simultaneously in a fuel cell design, a multi-objective optimisation is always used. A mathematical formulation of such a problem is given by:

$$\begin{aligned} &\text{Maximise or minimise} && \mathbf{J(x)} = [J_1, J_2, J_3, ..., J_n]^T \\ &\text{W.R.T} && x_k \quad \text{for } k = 1, 2, 3, \ldots\ldots, n \\ &\text{Subject to:} && h_i(\mathbf{x}) = 0 \quad \text{for} \quad i = 1, 2, 3, \ldots\ldots, p \\ & && g_i(\mathbf{x}) \le 0 \quad \text{for} \quad i = 1, 2, 3, \ldots\ldots, q \\ & && \mathbf{x}_L \le \mathbf{x} \le \mathbf{x}_U \end{aligned} \tag{2-22}$$

where **J(x)** is the vector of objectives. In fuel cell design, the objective can be cost, performance, durability and others, which is represented by J_i individually. x_k is known as the design variables, which are related to objective vector, **J(x)**. $\mathbf{x}_L$ and $\mathbf{x}_U$ are the lower and upper bounds of design variable x_k. $h_i(\mathbf{x})$ and $g_i(\mathbf{x})$ are the design constraints.

Design of fuel cells is a challenging endeavour because a multitude of physical and chemical phenomena need to be optimised simultaneously to achieve the best performance. Normally, it requires the evaluation of a set of possible designs. Due to the fact that the number of possible designs increases sharply as the number of design variables increase. For example, the number of possible designs is 10^5 for a design with ten variables and five possibilities per variable. It is impossible to evaluate all possible designs. As a result, some design variables have to be constrained as constants to reduce the number of possible designs. This is the so-called sub-optimal design. The sub-optimal designs in fuel cell optimisation mainly focus on the following aspects: flow field design, electrode design, operating condition optimisation and fuel cell stack optimisation. Similarly, the optimisation has to mainly concentrate on limited important objectives, while ignoring other design objectives.

The first efforts in the flow field design and optimisation were published in 2004 by Grujicic *et al.* [137]. The unique optimisation objective was to maximise the current density at a cell voltage of 0.7 V with an interdigitated flow field. The design parameters included cathode pressure inlet, cathode gas diffusion layer thickness, the width and ratio of gas channel and current collector. However, all design variables reached the bounds in the optimal design. In 2006, Lin *et al.* [138] optimised the channel width ratio, porosities of gas diffusion layers and catalyst layers using a gradient-based optimisation algorithm (simplified conjugate gradient method). The optimal channel width ratio of 0.54, GDL porosity of 0.6 and CL porosity of 0.3 were obtained in the optimisation results.

Song *et al.* [44, 45] are considered as the pioneers of optimisation of the fuel cell electrode using numerical optimisation approach. The catalyst layer composition was optimised in order to achieve the maximum current density at the cell voltage of 0.6 V. The design variables were ionomer volume fraction, platinum loading and the thickness of the catalyst layer. The optimal distributions of Nafion® ionomer and platinum were obtained. The optimisation results indicated that the optimal ionomer loading was around 30 wt. % [44], and the electrode performance was improved by placing more ionomer and platinum near the membrane [45]. Secanell *et al.* optimised both platinum loading and performance of a complete MEA [46] based on the previously developed optimisation framework [139]. The design variables included platinum loading, ionomer loading, GDL porosity and platinum mass ratio. Figure 2-11 shows that the cell performance was improved using the parameters obtained from the optimal design. The optimisation results showed that the platinum loading had to be controlled within the range of 0.1 to 0.5 mg cm^{-2}, as higher loading resulted in a waste of platinum rather than an increase in current density.

The improved cell performance can be achieved with higher operating temperature, inlet pressure and stoichiomeric flow ratio [140-142]. Consequently, both an accurate fuel cell model and a complete fuel cell system model have to be coupled in the optimisation of operating conditions. Otherwise, the optimisation algorithm would always choose the higher values of the operating parameters [143]. The pioneering efforts in the operating conditions optimisation can be found in 2000 by Mawardi *et al.* [144]. The objective was to maximise the power density at a fixed current density. The design variables included operating temperature, pressures of anode and cathode, mole

fractions of the gas inlet, stoichimomerty and relative humidity. Minimising membrane hydration, maximising temperature rise and cell voltage were the additional constraints. The optimisation results indicated that the optimal operating conditions strongly depend on the current densities. Wu *et al.* [145] optimised the efficiency of the fuel cell system at low, medium and high current densities. The design variables used were the operating temperature, pressure of cathode gas inlet, stoichiometry and relative humidity. The optimisation results suggested that, for a realistic system, the optimal cathode stoichiometry was between 1.25 and 2, cathode pressure between 1.5 and 3 atm, and cathode relative humidity between 10% and 15%.

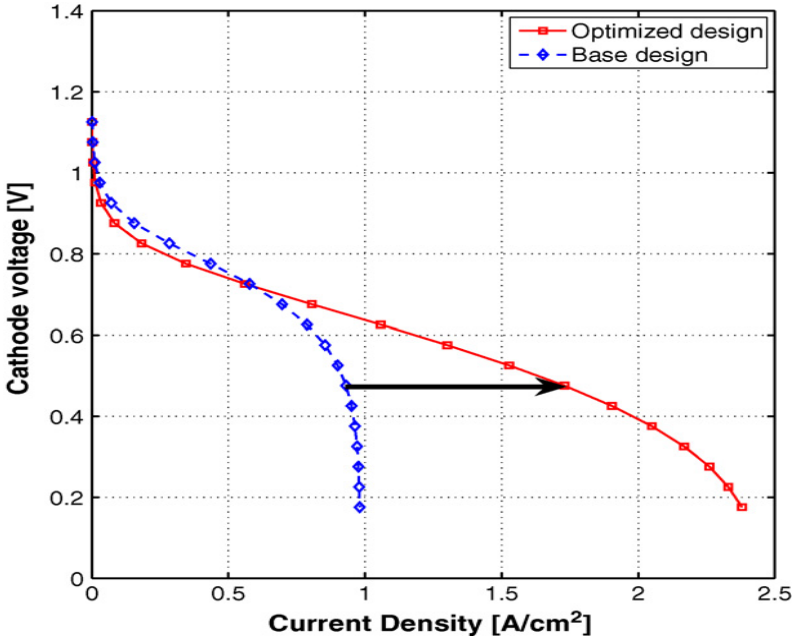

Figure 2-11 Polarisation curves of the base design and optimal design at the cell voltage of 0.476 V [139]

Fuel cell stack optimisation has received little attention compared with the flow field design, electrode design and operating condition optimisation. In the fuel cell stack, the clamping load applied to a PEM fuel cell stack is considered as the most important effect on fuel cell performance due to the influence on electron transfer, mass and thermal transport [146]. Zhou *et al.* [147] proposed a finite element method (FEM) in a developed two-phase flow model to study the effect of cathode gas diffusion layer deformation on the fuel cell polarisation curves. The modelling results showed that an optimal compression deformation exists when the contact resistance was considered. Mohamed and Jenkins [148] optimised the number of cells in series based on a simplified zero dimensional, isothermal fuel cell stack model, in which the optimisation objective was to maximise the power output. Recently, Zhou *et al.* [149] developed a

cold start model for PEM fuel cells aimed at optimising the start-up methods. As a novel method, the variable heating and load control (VHLC) was proposed.

Numerical optimisation is able to provide insight for fuel cell design including cost reduction, performance improvement, and efficiency increase. As a relative new research area, numerical optimisation of needed fuel cells has attracted the growing interest.

2.7 Overall review of DMFC

Modelling the DMFC can lead to a greater understanding of the cell and its interactions with other components in the system. Because of the similarities with the PEMFC, modelling of the DMFC using polymer electrolyte membranes (PEMs) can follow similar approaches to hydrogen PEM fuel cells, although there are of course some crucial differences as will be discussed.

Overall modelling of the DMFC can be carried out at various levels focusing on one or more different aspects or components in the cell as below:

1. Anode catalysis. The mechanism of methanol oxidation is not known, but it is known that simple Butler-Volmer expressions are not appropriate.
2. PEM transport and conductivity. As well as facilitating proton transfer from anode to cathode the crossover of methanol and water is important in determining performance.
3. Cathode catalysis. Oxygen reduction is kinetically a faster process than methanol oxidation, but its overpotential behaviour will have a significant influence on overall cell behaviour. In addition, methanol oxidation at the cathode which through a mixed potential has severe repercussions on cell voltage.
4. Fluid transport in porous backing layers. This influences the transport of reactants methanol and oxygen to the catalysts and the transport of products carbon dioxide and water away from the catalysts.
5. Fluid mechanics in the flow channels. This impacts on the local variation of methanol in the cell and is influenced by variations in velocity and pressure as also is the associated equilibrium between the methanol and water and carbon dioxide gas. This and many other factors will influence the current distribution over individual cells.

6. Current and potential distribution in the catalyst layers. The electrodes in the DMFC are essentially three dimensional to provide a high specific area. The current is thus distributed in a direction normal to overall current flow and this distribution should be determined for both the anode and the cathode.

7. Thermal energy and heat transfer. The electrochemical inefficient use of methanol leads to significant amounts of heat generation in the cell and thus local variations in temperature and heat transfer rates may influence cell behaviour.

8. Cell stacking. The practical application of multi-cell units requires, in principle, an integration of all the above factors. In addition, due regard must be taken of the variation in temperature in the cells and in the requirements of feeding air and methanol to the many compartments in the cell, i.e. cell manifolds. Such behaviour can see variations in performance from one cell to the other.

9. Dynamics. The application of the DMFC will inevitably impose a varied load demand on the unit and the ability or not of the cell to respond effectively to the load demand will be crucial.

The types of models can vary from simple analytical and empirical models to detailed physicochemical models to stochastic models which cover single environments, such as electrodes, to complete fuel cell systems.

Scott *et al.* [150] developed a simple cell performance model describing mass transport in the porous electrode structures and the potential and concentration distributions in the electrode regions. The model incorporated the influence of methanol crossover based on a combination of diffusion, electro-osmotic drag and pressure. Cruickshank and Scott [151] presented a simplified DMFC model to predict the cell voltage characteristics depending on some key parameters obtained from measured permeation rates of methanol and water through Nafion® 117 membranes. Sundmacher and Scott [152] developed a steady state, isothermal cell model accounting for mass transfer and charge transport processes in the different fuel cell layers. Kulikovsky [153-155] reported analytical models employing a semi-empirical approach to account for the limiting current behaviour. The general expression for the voltage-current curve was based on exact solution for the catalyst layer reaction and includes the overpotentials due to transport limitation in diffusion backing layer and due to methanol crossover.

The simplest DMFC performance models combine theoretical differential and algebraic equations with empirical determined parameters. However the estimated parameters from the experimental data are normally specific to certain types of cells and valid for a limited range of operating conditions. The advantage of these models is their simple structure and the low computational effort to perform predictions for existing designs [156-161].

Kauranen and Skou [156] reported a DMFC model describing both the oxygen reduction and the crossed-over methanol oxidation in the cathode and showed that the oxygen reduction current is reduced in the presence of methanol oxidation due to surface poisoning. Argyropoulos *et al.* [160] presented a liquid feed DMFC model to predict the cell voltage versus current density. The model was based on a semi-empirical approach in which methanol oxidation and oxygen reduction kinetics were combined with effective mass transport coefficients for the fuel cell electrodes. Dohle and Wipperman [161] developed a DMFC model to predict polarisation curves and the permeability of methanol based on a set of parameters adjusted from experiments performed in a wide range of operating conditions.

Methanol oxidation in anode porous electrode plays a vital role in determining the fuel cell performance [156, 162-167]. There have been a range of studies of the mechanism of methanol oxidation and several rate/kinetic models were proposed. It is generally thought that the rate determining step is surface reaction between CO_{ads} and OH_{ads}. It has been proposed that methanol and hydroxyl groups are adsorbed on different parts of the surface on carbon supported platinum. Kaurenan and Skou [156] developed a model for methanol oxidation on carbon supported platinum in which the rate of the surface reaction was limiting and that the hydroxyl adsorption was assumed in Nernstian equilibrium and followed a Langmuir adsorption. The rate of adsorption of the intermediate CO was expressed by a Temkin adsorption rate equation. -CO and -OH adsorption were assumed to occur at different sites of the supported catalyst. Observed experimental limiting currents were accredited to the adsorbed OH-groups reaching saturation coverage. The model overall gave reasonable agreement with experimental observed anode polarisation although aspects of methanol mass transport were not considered.

Nordlund and Lindbergh [162] developed an agglomerate model for the porous DMFC anode using kinetic expressions for methanol oxidation based on the formation

of adsorbed methanol, CO and OH species. The transport of methanol in the spherical agglomerate was described by radial (Fick's) diffusion. It was shown that the mass transport did not limit cell performance but that liquid phase mass transport was of importance at lower methanol concentrations.

However, despite significant research on methanol oxidation, the mechanism is not fully known and the adsorption of the various reactive intermediates may involve a combination of single site and dual site processes. These species may include those proposed in the mechanism of Freelink [163] for Pt alloys. Mayer and Newmann [164, 165] have presented modeling and data analysis of transport phenomena in a SPE (solid polymer electrolyte)-DMFC. In contrast to most of the earlier models, which employed a simple Butler-Volmer (B-V) relationship for describing the electrode kinetics for methanol oxidation at the anode, the model due to Mayer and Newmann follows the reaction mechanism proposed by Gasteiger *et al.* [166]. Scott and Argyropoulos [167] proposed a one dimensional potential distribution model which used a kinetic model derived from the adsorption model of Nordlund and Lindbergh [162]. This model provided an analytic solution for the current density at various overpotentials and methanol concentrations shown in Figure 2-12.

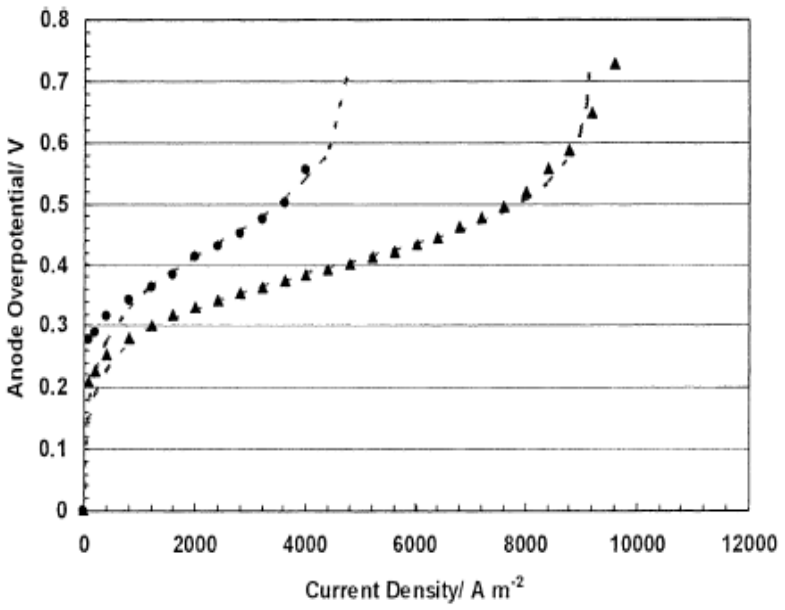

Figure 2-12 Experimental data and modelling results of the methanol oxidation at a DMFC anode at 60 °C (left) and 90 °C (right) [167]

However, it is important to state that the mechanistic model alone cannot generally be substantiated for porous high surface area electrodes because of influences of current

distribution, variable geometry and mass transport. Thus for modelling, electrode structure and ionic and electronic conduction within, mass transport effects together with a kinetic model of the oxidation, are required to predict electrode polarisation and thereby cell voltage vs. current density behaviour.

There has been useful information published on the time varying performance of the DMFC with regard to stability studies. The effect of current pulsing on performance has been reported [168]. More detailed studies of the dynamic voltage response under varied current loads have been also reported for small and large scale cells [169 ,170] under a range of different operating conditions (see Figure 2-13). The cell responded rapidly and reversibly to changes in magnitude and rate of change of load.

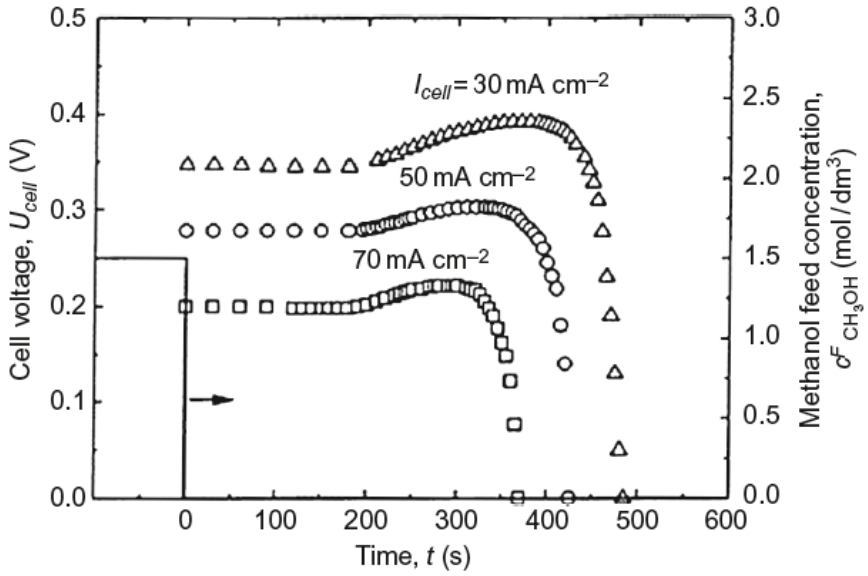

Figure 2-13 Effect of pulsed methanol solution flow on DMFC performance [170]

Modelling of the dynamic behaviour of the DMFC has been limited to only a few studies, although, in principle, most steady state models can be readily adopted for dynamic simulation by introducing time derivatives. Dynamics are important from the point of assessing cell and system stability to fluctuation in variables as well as for control purpose. Schultz *et al.* [171, 172] have extended their steady state models to simulate dynamic operation. Through simulation of the pulsing of methanol feed solution concentration, it was shown that an enhanced cell output was maintained. This enhancement, confirmed experimentally, was due to the reduction in the impact of methanol crossover on oxygen reduction. The dynamic model was also used to simulate the operation of the DMFC in a vehicular application. Gerteisen [173] presented a

dynamic model to investigate the coupled reaction mechanisms in a DMFC and therein associated voltage losses in the catalyst layers. The model accounted for the crossover of methanol from anode to cathode and oxygen from cathode to anode. The reactant crossover results in parasitic internal currents that were finally responsible for high overpotentials in both electrodes, so-called mixed potentials. A simplified and general reaction mechanism for the methanol oxidation reaction (MOR) was selected, that accounted for the coverage of active sites by intermediate species occurring during the MOR. The simulation of the anode potential relaxation after current interruption showed an undershoot behaviour as seen in the experiment data. The model help explain that this phenomenon was due to the transients of reactant crossover in combination with the change of CO and OH coverage ratios on Pt and Ru, respectively.

When direct methanol fuel cells are used for portable power sources, it is impossible to keep the cell temperature constant and thus it is important to know the cell performance at varying cell temperatures. In the DMFC there can be an increase in the transient cell temperature, driven by the waste heat that is generated for DMFC operation. This can be beneficial for cell performance through increased kinetics and mass transport, but the temperature rise also increases the amount of methanol crossover from the anode to the cathode, which causes high mixed cathode overpotential and ultimately lowers the overall DMFC efficiency. A transient-thermal model based on a lumped system was developed and implemented in a one dimensional (1D), two phase DMFC model [174]. The main focus was investigation of the transient thermal behaviour of DMFCs and its influence on methanol crossover, cell performance, and efficiency. This model indicated that insufficient cooling of DMFCs can eventually lead to thermal runaway, particularly under high methanol-feed concentrations. Hence an efficient cooling system was needed to safeguard DMFC operations and enhance the performance of DMFCs for portable DMFC applications. A dynamic non-linear circuit model for passive methanol fuel cells was presented by Guarnieri *et al.* [175]. The model considered mass transport, electronic and proton conduction, methanol adsorption and electrochemical kinetics into account. Adsorption and oxidation rates, which mostly affect the cell dynamics, were modelled by a detailed two-step reaction mechanism. A fully coupled equivalent circuit was solved by assembling first-order differential equations into a nonlinear state-variable system in order to simulate the electrical evolution of the fuel cell from its initial conditions. The runtime of a DMFC can be predicted from the current load and the initial methanol concentration. The

model showed that the fuel cell dynamics over short and long time scales is dominated by mass transport in the diffusion layers and in the membrane and by electrochemical effects in the triple phase boundaries (TPBs) inside the catalyst layers.

2.8 Conclusions

Water formation and transport mechanisms and the negative effect of liquid water flooding on the fuel cell performance are overviewed and the mathematical models for water formation and transport are chronologically summarised in this chapter. Based on the water formation mechanism and the water transport processes described, the models for water transport through the Nafion® membrane are mainly categorised as three types: diffusion models, chemical potential models and hydraulic models. The merit and demerit of each type of models are compared in this chapter. For the water transport through the Nafion® membrane, a model accounted for the electro-osmotic drag (EOD), back diffusion and hydraulic permeation will be developed.

The oxygen oxidation reaction (ORR) at the cathode is one of the main sources for liquid water generation. In order to accurately simulate the ORR inside the porous catalyst layer, the agglomerate model has to be adopted. Liquid water movement through the porous electrodes, including catalyst layers and gas diffusion layers, can be simulated by the volume of fluid (VOF) model and Lattice Boltzmann (LB) model. The VOF model and the agglomerate model will be combined in this thesis to provide an effective way for modelling the liquid water formation and transport through the porous electrodes.

Liquid water formation and movement can be experimentally detected and observed. The basic principles and scopes of each visualisation techniques are concluded and compared. In addition, different flow field designs are introduced and compared.

The fuel cell performance can be improved by optimising the composition of the electrode and operating conditions. Fuel cell optimisations in terms of flow field design, electrode design, operating condition optimisation and fuel cell stack optimisation are overviewed. The property of the cathode catalyst layer plays an important role in determining the fuel cell performance. Therefore, an optimal composition of the cathode catalyst layer will be studied in this thesis.

The methanol oxidation behaviour within the porous anode of the DMFC is overviewed. For the purpose of appropriately modelling the methanol oxidation reaction (MOR), a dual-site mechanism of methanol oxidation on Pt-Ru binary catalyst is adopted instead of the simple Butler-Volmer kinetics. The steady state and time dependent performance of the DMFC are dominated by both the MOR kinetics in the catalyst layer and the mass transport in the gas diffusion layer and in the membrane.

Chapter 3. Fundamentals, principles and governing equations

3.1 Introduction

The electrochemical and physical phenomena occurred in PEMFCs, including the polarisation curves, profiles of the reactant and product species, velocities of species, as well as the temperature distributions, can be described by coupling the electrode kinetics with the conservation equations of mass, momentum, energy and charge. In this chapter, the fundamentals, principles are given and the governing equations used in the model are presented.

3.2 Electrode kinetics

3.2.1 Butler-Volmer kinetics

Fuel cells operation is based on the electrochemical reactions occurring simultaneously at the anode and cathode, which have been presented by Eq. (1-1) to Eq. (1-6) in Chapter 1. The reaction rate of an electrochemical reaction is defined as the speed of the electrochemical reaction proceeds on the electrode surface. Electrical current is generated by the electrons released and consumed in the electrochemical reaction processes. Current density is the current per unit surface area. According to Faraday's law, current density is proportional to the charge transferred and the consumption of reactants per unit area:

$$i = nFN_i \tag{3-1}$$

where n is the amount of substance, F (96385 C mol^{-1}) is the Faraday's constant, N_i (mol m^{-2} s^{-1}) is the flux of reactant per unit area, i (A m^{-2}) is the current density.

An electrochemical reaction involves either oxidation or reduction of reactant species. Typically, the oxidation process produces electrons while the reduction process consumes the electrons as follow:

$$Rd \leftrightarrow Ox + ne^- \tag{3-2}$$

On an electrode at equilibrium conditions (no external current is generated), both the oxidation and reduction processes occur at equal rates. The net current density generated is the difference between the electrons released and consumed:

$$i = nF(k_f c_{Ox} - k_b c_{Rd}) \tag{3-3}$$

where k_f and k_b (s^{-1}) are the forward (reduction) and backward (oxidation) reaction rate coefficient, c_{Ox} and c_{Rd} (mol m^{-2}) are the surface concentration of the oxidised and reduced species, respectively. The reaction rate coefficient for an electrochemical reaction is a function of the Gibbs free energy as follow:

$$k_{f/b} = \frac{k_B T}{h} \exp(\frac{-\Delta G}{R_g T}) \tag{3-4}$$

where k_B (1.38×10^{-23} J K^{-1}) is the Boltzmann's constant, h (6.626×10^{-34} J s) is the Planck's constant, R_g (8.314 J mol^{-1} K^{-1}) is the universal gas constant, T (K) is the temperature, and ΔG (J mol^{-1}) is the Gibbs free energy, which is considered to consist of both chemical and electrical terms. Consequently, for a reduction reaction:

$$\Delta G = \Delta G_{ch} + \alpha_{Rd} F\phi \tag{3-5}$$

and for an oxidation reaction:

$$\Delta G = \Delta G_{ch} - \alpha_{Ox} F\phi \tag{3-6}$$

where ΔG_{ch} (J mol^{-1}) is the Gibbs free energy of the chemical component, ϕ (V) is the potential, and α_{Rd} and α_{Ox} are the transfer coefficient for reduction and oxidation reactions, respectively.

Note that in the case of multi-step electrochemical reactions, α_{Rd} + α_{Ox} is generally equal to n/v, where n is the number of electrons transferred in the overall reaction and v is the stoichiometric number. The forward and backward reaction rate coefficients in Eq. (3-3) are represented, respectively:

$$k_f = k_{0,f} \exp(\frac{-\alpha_{Rd} F\phi}{R_g T}) \tag{3-7}$$

$$k_b = k_{0,b} \exp(\frac{\alpha_{Ox} F\phi}{R_g T}) \tag{3-8}$$

Therefore, from Eq. (3-3) to Eq. (3-8), the net current density expression is obtained:

$$i = nF[k_{0,f} c_{Ox} \exp(\frac{-\alpha_{Rd} F\phi}{R_g T}) - k_{0,b} c_{Rd} \exp(\frac{\alpha_{Ox} F\phi}{R_g T})] \quad (3\text{-}9)$$

At equilibrium, the forward and backward reactions proceed simultaneously, generating zero net current. In this case, the current densities for both forward and backward reaction are equal.

$$i_0 = nFk_{0,f} c_{Ox} \exp(\frac{-\alpha_{Rd} F\phi_{eq}}{R_g T}) = k_{0,b} c_{Rd} \exp(\frac{-\alpha_{Ox} F\phi_{eq}}{R_g T}) \quad (3\text{-}10)$$

where i_0 (A m^{-2}) is the exchange current density, $k_{0,f}$ and $k_{0,b}$ (s^{-1}) are the reaction rate constant of the forward and backward reaction at standard conditions (25 °C and atmospheric pressure), ϕ_{eq} (V) is the equilibrium or reversible potential.

As described in Chapter 1, the equilibrium potential for a hydrogen PEMFC anode is 0 V and for a DMFC is 0.03V, while the equilibrium potential for the cathode operated with oxygen is 1.229 V at standard conditions. By combing Eq. (3-9) and Eq. (3-10), a relationship between the current density and the overpotential is obtained, which is known as the Butler-Volmer (B-V) equation.

$$i = i_0[\exp(\frac{-\alpha_{Rd} F\eta}{R_g T}) - \exp(\frac{\alpha_{Ox} F\eta}{R_g T})] \quad (3\text{-}11)$$

where η (V) is the overpotential, defined as the difference between the electrode potential and the equilibrium potential. The B-V equation is valid for both anode and cathode reaction in a PEMFC:

$$i_a = i_{0,a}[\exp(\frac{-\alpha_{Rd,a} F\eta_a}{R_g T}) - \exp(\frac{\alpha_{Ox,a} F\eta_a}{R_g T})] \quad (3\text{-}12)$$

$$i_c = i_{0,c}[\exp(\frac{-\alpha_{Rd,c} F\eta_c}{R_g T}) - \exp(\frac{\alpha_{Ox,c} F\eta_c}{R_g T})] \quad (3\text{-}13)$$

The anode overpotential is positive, which makes the first term in the bracket of Eq. (3-12) negligible and results in a negative sign of the anode current density obtained. Similarly, the cathode overpotential is negative, which makes the second term in the

bracket of Eq. (3-13) negligible and leads to a positive sign of the cathode current density.

3.2.2 Agglomerate kinetics

The electrochemical reactions, in which electrons, protons and gas are involved, only take place on the surface of the catalyst. Reactant gas transport through the micro pores within the catalyst layer, electrons travel through the electrically conductive solid, and protons migrate through the electrolyte. According to the functions of different component within the catalyst layer, the existence of triple phase boundaries (TPB) is needed [176], where the content of electrolyte (for proton transfer), void space (for gas transport) and platinum dispersed carbon (for catalysis and electron transfer) interact (see Figure 3-1).

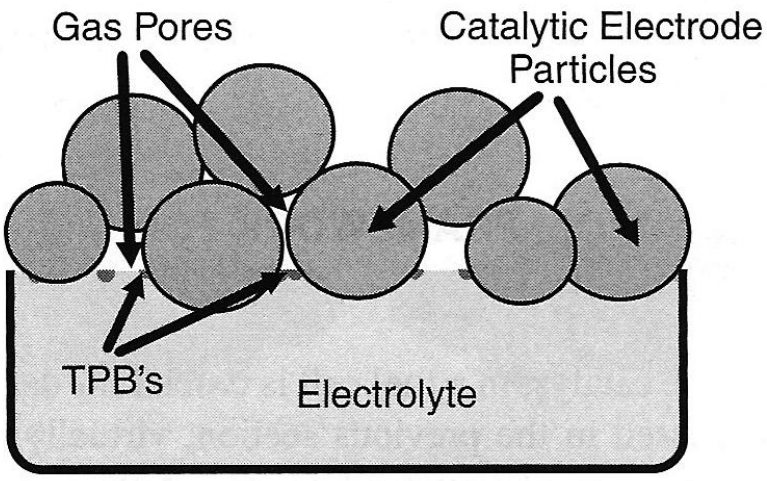

Figure 3-1 A simplified schematic diagram of the triple phase boundary (TPB) in a catalyst-electrolyte-pores interacted electrode [176]

In order to provide a more accurate description of the catalyst layer structure, the spherical agglomerate model is adopted, in which each agglomerate is assumed to consist of three components: platinum dispersed on carbon (*Pt/C*), ionomer and void space. The void space within the agglomerate is defined as the primary pores and the void space between the agglomerate is defined as the secondary pores. The primary pores are partially occupied by the ionomer, whereas the secondary pores are partially occupied by the ionomer and liquid water surrounding the agglomerate. The structure of the catalyst layer is schematically represented in Figure 3-2. Reactant gas has to dissolve in the ionomer/water film before reaching the catalyst particles. Thus, the

simple Butler-Volmer relationship can't describe the kinetics, as the transport of the dissolved species in the ionomer/water film should be taken into account.

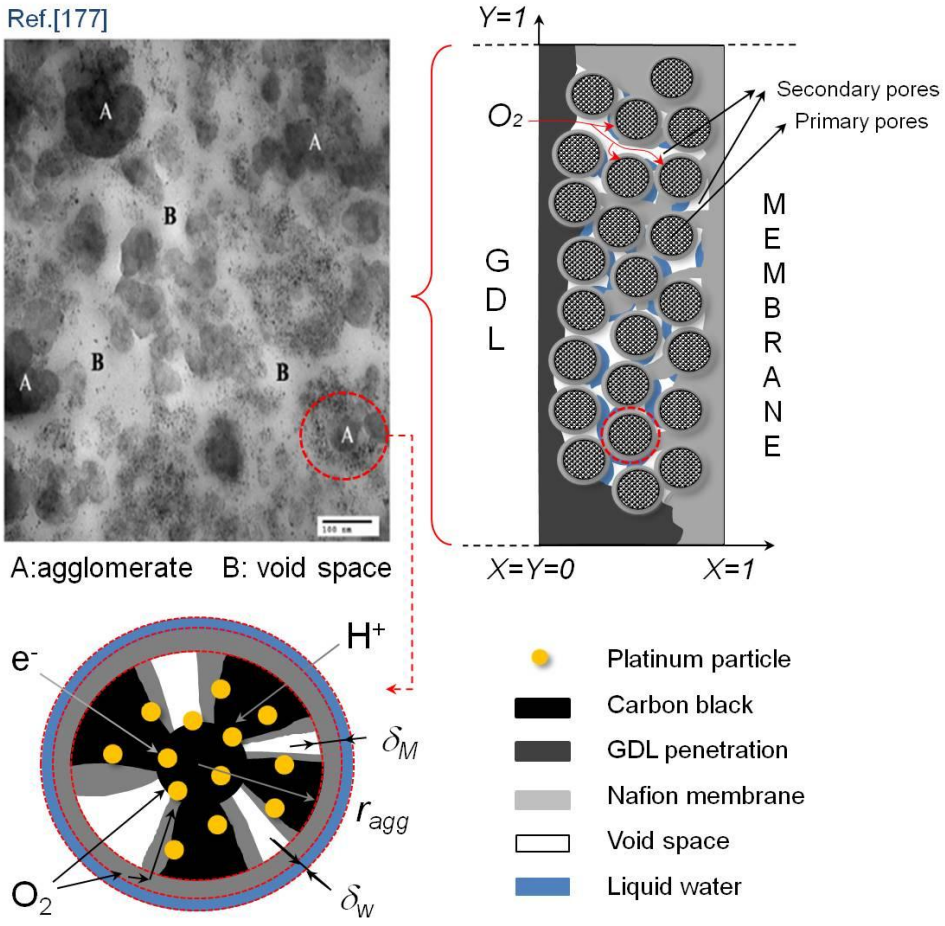

Figure 3-2 Sketch of the catalyst layer based on agglomerate assumption [177]

In the agglomerate assumption, six key processes were included:

a. Multicomponent diffusion of reactant gases;

b. Reactant gases dissolution at the electrolyte/water film outer boundary;

c. Diffusion of dissolved reactant gases through the electrolyte/water film;

d. Diffusion of dissolved reactant gases within the agglomerate;

e. Electrochemical reactions occurred on the *Pt/C* surface;

f. Electrons and proton transport through the solid and electrolyte phases, respectively.

As shown in Figure 3-3, the concentration of the dissolved species at the outer and inner boundary of the ionomer/water film are represented by $c_{i,out}$ and $c_{i,in}$ (mol m^{-3}),

respectively. The concentration of the dissolved species at the outer interface is described by Henry's law as:

$$c_{i,out} = \frac{p_i}{H_i} \tag{3-14}$$

where p_i (Pa) and H_i (Pa m^3 mol^{-1}) are the partial pressure and Henry's constant of reactant species *i*, respectively.

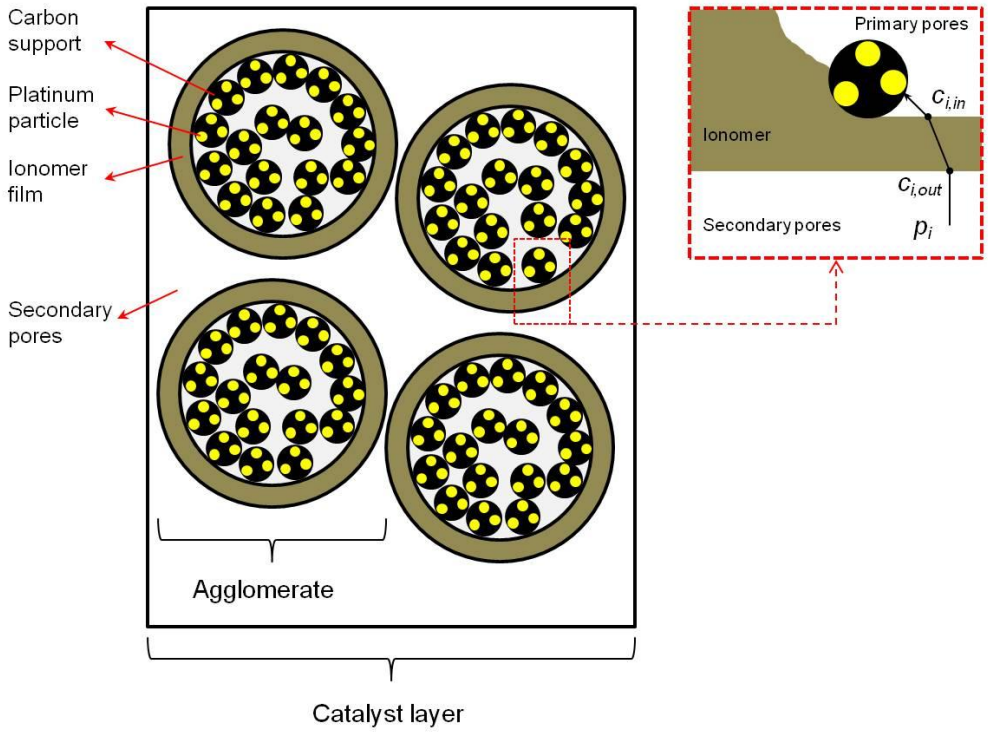

Figure 3-3 Schematic representation of reactant gas diffusion through the ionomer film surrounding the agglomerate

By postulating that the species flux goes from regions of high concentration to regions of low concentration, with a magnitude that is proportional to the concentration gradient. The diffusion of reactant through the ionomer/water film therefore can be described by Fick's law:

$$N_i = -D_i^{eff} \frac{\partial c_i}{\partial r} \tag{3-15}$$

where N_i (mol m^{-2} s^{-1}) is the reactants mole flux through the ionomer/water film, D_i^{eff} (m^2 s^{-1}) is the effective diffusion coefficient of reactants, c_i (mol m^{-3}) is the reactant concentration, and r (m) is the radius.

It is assumed that the ionomer/water film is present in the agglomerate evenly, and the film is much thinner than the size of the agglomerate, and the molar rate is conserved in the ionomer/water film, namely the molar rate is constant at the outer boundary of the ionomer/water film. Thus, the reactants mole flux through the ionomer/water film can be derived as follow:

$$C = -(4\pi r^2) D_i^{eff} \frac{\partial c_i}{\partial r} \tag{3-16}$$

Boundary conditions: $r = r_{agg}, \quad c_i = c_{i,in}$

$$r = r_{agg} + \delta, \quad c_i = c_{i,out} \tag{3-17}$$

where C (mol s^{-1}) is a constant. Integrating Eq. (3-16) and applying the boundary conditions in Eq. (3-17) leading to:

$$C = -D_i^{eff} \left(\frac{c_{i,out} - c_{i,in}}{\delta}\right) 4\pi r_{agg}(r_{agg} + \delta) \tag{3-18}$$

where r_{agg} (m) is the radius of the agglomerate, δ (m) is the thickness of the ionomer/water film. Combing Eq. (3-16) and Eq. (3-18), the reactants mole flux is obtained as follow:

$$N_i = D_i^{eff} \frac{r_{agg}}{(r_{agg} + \delta)} \frac{c_{i,out} - c_{i,in}}{\delta} \tag{3-19}$$

According to mass balance, at steady state, the amount of the species consumed equals to the species diffusion to the active surface.

$$a_{agg} N_i = R_i \tag{3-20}$$

where a_{agg} (m^{-1}) is the specific area of the agglomerate, defining as the surface area per agglomerate volume, and R_i (mol m^{-3} s^{-1}) is the reaction rate.

Assuming the reactions of either hydrogen oxidation, oxygen reduction or methanol oxidation as the first-order kinetics with respect to the reactant concentration [115, 178, 179] gives:

$$R_i = k_{agg} c_i \tag{3-21}$$

where k_{agg} (s^{-1}) is the reaction rate coefficient representing the reactions occurred in the agglomerate. By introducing the effectiveness factor into Eq. (3-21), the overall reaction rate only depends on the reactant concentration at the outer boundary of the agglomerate, obtained as:

$$R_{i,agg} = E_{agg} k_{agg} c_{i,out} \tag{3-22}$$

where $R_{i,agg}$ (mol m^{-3} s^{-1}) is the reaction rate based on the agglomerate volume and, E_{agg} is the effectiveness factor of the agglomerate, which represents the geometry of the agglomerate and the reactant mass transport resistance within the agglomerate. For the spherical agglomerates, the effectiveness factor can be described as follow [115]:

$$E_{agg} = \frac{1}{M_{T,agg}} \left[\frac{1}{\tanh(3M_{T,agg})} - \frac{1}{3M_{T,agg}} \right] \tag{3-23}$$

where $M_{T,agg}$ is the Thiele's modulus, a dimensionless parameter [115].

$$M_{T,agg} = \frac{r_{agg}}{3} \sqrt{\frac{k_{agg}}{D_{i,agg}^{eff}}} \tag{3-24}$$

where $D_{i,agg}^{eff}$ (m^2 s^{-1}) is the reactant effective diffusion coefficient inside the agglomerate.

According to Faraday's law, the volumetric current density is related to the reactants consumption rate via the following equation:

$$i_{i,agg} = nFE_{agg} k_{agg} c_{i,in} \tag{3-25}$$

$i_{i,agg}$ (A m^{-3}) is the volumetric current density based on the agglomerate volume, and the subscript i refers to anode or cathode, respectively. Combining equations from Eq. (3-19) to Eq. (3-22) the concentration of the dissolved species at the inner boundary of the ionomer/water film is obtained as:

$$c_{i,in} = [1 + \frac{E_{agg} k_{agg} (r_{agg} + \delta)\delta}{a_{agg} r_{agg} D_i^{eff}}]^{-1} c_{i,out} \tag{3-26}$$

Substituting Eq. (3-26) into Eq. (3-25), gives

$$i_{i,agg} = nF[\frac{1}{E_{agg}k_{agg}} + \frac{(r_{agg}+\delta)\delta}{a_{agg}r_{agg}D_i^{eff}}]^{-1}c_{i,out} \quad (3\text{-}27)$$

Substituting Eq. (3-14), the Henry's law, into Eq. (3-27):

$$i_{i,agg} = nF\frac{p_i}{H_i}[\frac{1}{E_{agg}k_{agg}} + \frac{(r_{agg}+\delta)\delta}{a_{agg}r_{agg}D_i^{eff}}]^{-1} \quad (3\text{-}28)$$

The current density obtained from Eq. (3-11) could transfer to volumetric current density after corrected by the specific area of the electrode. The agglomerate volumetric current therefore can be related to the Butler-Volmer kinetics as:

$$i_{i,agg} = a_{agg}i_0[\exp(\frac{-\alpha_{Rd}F\eta}{RT}) - \exp(\frac{\alpha_{Ox}F\eta}{RT})] \quad (3\text{-}29)$$

On the inner boundary of the agglomerate, the intrinsic volumetric current density is obtained as:

$$i_{i,agg} = nFk_{agg}c_{i,in} \quad (3\text{-}30)$$

Comparing Eq. (3-29) with Eq. (3-30), the reaction rate is obtained:

$$k_{agg} = \frac{a_{agg}i_0}{nFc_{i,in}}[\exp(\frac{-\alpha_{Rd}F\eta}{RT}) - \exp(\frac{\alpha_{Ox}F\eta}{RT})] \quad (3\text{-}31)$$

Thus the volumetric current densities generated inside the electrodes of anode and cathode can be calculated by Eq. (3-29).

3.3 Catalyst layer property

3.3.1 Porosity of the catalyst layer

Most previous works assume the agglomerate as a solid nucleus in which no primary pores exist. However, in practice, both primary pores and secondary pores exist within the agglomerate and between agglomerate, respectively [180, 181].

The total volume of the catalyst layer consists of five components including ionomer (M), platinum (Pt), carbon black (C), void space (P) and solid portion(S).

$$V_{tot} = V_M + V_{Pt} + V_C + V_P + V_S \quad (3\text{-}32)$$

where the volume of the void space consists of two parts: primary pores ($V_{P,p}$) and secondary pores ($V_{P,s}$).

As shown in Figure 3-2, the primary pores are the void space within the agglomerates and the secondary pores are the void space between the agglomerates, thus we have:

$$V_P = V_{P,p} + V_{P,s} \tag{3-33}$$

The platinum dispersed carbon (*Pt/C*) is constructed by platinum and carbon, thus

$$V_{Pt/C} = V_{Pt} + V_C \tag{3-34}$$

Dividing both sides of Eq. (3-34) by the total volume of catalyst layer (V_{tot}), the sum of volume fractions of all components is equal to unity. Eq. (3-32) and Eq. (3-33) becomes, respectively, to

$$1 = L_M + L_{Pt} + L_C + L_S + \varepsilon_{CL} \tag{3-35}$$

$$\varepsilon_{CL} = \varepsilon_p + \varepsilon_s \tag{3-36}$$

where the terms on the right side of Eq. (3-35) represent the volume fraction of ionomer (L_M), platinum (L_{Pt}) carbon (L_C), solid portion (L_S), primary pores (ε_p), and secondary pores (ε_s), respectively, which are written as:

$$L_M = \frac{V_M}{V_{tot}},\quad L_{Pt} = \frac{V_{Pt}}{V_{tot}},\quad L_C = \frac{V_C}{V_{tot}},\quad L_S = \frac{V_S}{V_{tot}},\quad \varepsilon_p = \frac{V_{P,p}}{V_{tot}},\quad \varepsilon_s = \frac{V_{P,s}}{V_{tot}} \tag{3-37}$$

The volume fraction of platinum, carbon and ionomer were related to their mass loading and densities and the thickness of the catalyst layer as

$$L_{Pt} = \frac{m_{Pt}}{\rho_{Pt} l_{CL}},\quad L_C = \frac{m_C}{\rho_C l_{CL}},\quad L_M = \frac{m_M}{\rho_M l_{CL}} \tag{3-38}$$

Normally, platinum is dispersed in carbon black to construct the catalyst particles. Therefore, the volume fraction of platinum dispersed on carbon (*Pt/C*) is the sum of the volume fractions of platinum and carbon, which is given as follow:

$$L_{Pt/C} = \frac{m_{Pt}}{l_{CL}}\left(\frac{1}{\rho_{Pt}} + \frac{1-f}{f}\frac{1}{\rho_C}\right) \tag{3-39}$$

where the platinum mass ratio to that of carbon (abbreviated as platinum mass ratio) is introduced as:

$$f = \frac{m_{Pt}}{m_{Pt} + m_C} \tag{3-40}$$

Due to the clamping force of the membrane electrode assembly (MEA), the gas diffusion layer can penetrate into the catalyst layer. The volume fraction of the solid portion of the catalyst layer is defined as:

$$L_S = L_{GDL}(1-\varepsilon_{GDL}) \tag{3-41}$$

where L_{GDL} is the percentage of gas diffusion layer penetrating into catalyst layer and, ε_{GDL} is the porosity of the gas diffusion layer. The porosity of the catalyst layer is therefore being written as:

$$\varepsilon_{CL} = 1 - L_M - L_{GDL}(1-\varepsilon_{GDL}) - \frac{m_{Pt}}{l_{CL}}\left(\frac{1}{\rho_{Pt}} + \frac{1-f}{f}\frac{1}{\rho_C}\right) \tag{3-42}$$

3.3.2 Agglomerate density

The iomomer firstly partially fills up the primary pores within the agglomerate then covers the agglomerate to form a thin film. The total volume of ionomer is:

$$V_M = V_{M,agg} + V_{M,\delta} \tag{3-43}$$

where $V_{M,agg}$ (m^3) is the volume of ionomer within the agglomerate and, $V_{M,\delta}$ (m^3) is the volume of ionomer existed as the thin film surrounding the agglomerate. Due to the fact that the agglomerate particles consists of platinum dispersed carbon (*Pt/C*), ionomer and primary pores, the total volume of the agglomerate is:

$$V_{agg,tot} = V_{Pt/C} + V_{M,agg} + V_{P,p} \tag{3-44}$$

The volume fraction of ionomer within the agglomerate ($\varepsilon_{agg,M}$) and the volume fraction of primary pore space within the agglomerate ($\varepsilon_{agg,p}$) are introduced as:

$$\varepsilon_{agg,M} = \frac{V_{M,agg}}{V_{agg,tot}}, \quad \varepsilon_{agg,p} = \frac{V_{P,p}}{V_{agg,tot}} \tag{3-45}$$

By substituting Eq. (3-45) into Eq. (3-44), the total volume of the agglomerate becomes to:

$$V_{agg,tot} = \frac{V_{Pt/C}}{1-\varepsilon_{agg,M}-\varepsilon_{agg,p}} \tag{3-46}$$

The volume of the individual agglomerate particle (without the ionomer film) is

$$V_{agg,i} = \frac{4}{3}\pi r_{agg}^3 \tag{3-47}$$

Dividing Eq. (3-47) by Eq. (3-46), the total number of the agglomerate particles can be calculated as follow:

$$n_{agg} = \frac{3V_{Pt/C}}{4(1-\varepsilon_{agg,M}-\varepsilon_{agg,p})\pi r_{agg}^3} \tag{3-48}$$

Assuming the platinum is homogenously dispersed in carbon black, the volume fraction of the primary pores of the agglomerate (before filled with ionomer) equals to the volume fraction of the total void space (including primary and secondary pores) of the entire catalyst layer, leading to:

$$\varepsilon_{agg,M} + \varepsilon_{agg,p} = \varepsilon_{CL} \tag{3-49}$$

Substituting Eq. (3-49) into Eq. (3-48) and dividing Eq. (3-48) by the total volume (V_{tot}), the agglomerate density can be obtained, which is defined as the number of agglomerate particles per volume of catalyst layer, as follow:

$$N_{agg} = \frac{3L_{Pt/C}}{4(1-\varepsilon_{CL})\pi r_{agg}^3} \tag{3-50}$$

3.3.3 Thicknesses of the ionomer and liquid water films

The volume of agglomerate with the ionomer film is equal to the volume of platinum dispersed carbon, ionomer and primary pores, leading to:

$$n_{agg}\frac{4}{3}\pi(r_{agg}+\delta_M)^3 = V_M + V_{Pt/C} + V_{P,p} \tag{3-51}$$

Substituting Eq. (3-51) into Eq. (3-32):

$$V_{tot} = n_{agg}\frac{4}{3}\pi(r_{agg}+\delta_M)^3 + V_{P,s} + V_S \tag{3-52}$$

Substituting Eq. (3-48) into Eq. (3-52) then dividing both side by V_{tot} gives

$$1 = \frac{L_{Pt/C}(r_{agg}+\delta_M)^3}{(1-\varepsilon_{CL})r_{agg}^3} + \varepsilon_s + L_S \tag{3-53}$$

From Eq. (3-37) and Eq. (3-45), we have

$$\frac{\varepsilon_p}{\varepsilon_{agg,p}} = \frac{V_{agg,tot}}{V_{tot}} \tag{3-54}$$

Substituting Eq. (3-46) and Eq. (3-49) into Eq. (3-54) gives

$$\frac{\varepsilon_p}{\varepsilon_{CL}-\varepsilon_{agg,M}} = \frac{L_{Pt/C}}{1-\varepsilon_{CL}} \tag{3-55}$$

Then the volume fractions of the primary and secondary pores can be obtained as:

$$\varepsilon_p = \frac{L_{Pt/C}(\varepsilon_{CL}-\varepsilon_{agg,M})}{1-\varepsilon_{CL}} \tag{3-56}$$

$$\varepsilon_s = \varepsilon_{CL} - \frac{L_{Pt/C}(\varepsilon_{CL}-\varepsilon_{agg,M})}{1-\varepsilon_{CL}} \tag{3-57}$$

By substituting Eq. (3-57) into Eq. (3-53), the thickness of the ionomer thin film can be calculated by the following equation:

$$\delta_M = r_{agg}\left[\sqrt[3]{\frac{(1-\varepsilon_{CL})(1-\varepsilon_{CL}-L_S)+L_{Pt/C}(\varepsilon_{CL}-\varepsilon_{agg,M})}{L_{Pt/C}}}-1\right] \tag{3-58}$$

Defining the volume fraction of the primary pores occupied by the ionomer as:

$$\%M = \frac{\varepsilon_{agg,M}}{\varepsilon_{agg,M}+\varepsilon_{agg,p}} \tag{3-59}$$

Then Eq. (3-58) becomes to:

$$\delta_M = r_{agg}[\sqrt[3]{\frac{(1-\varepsilon_{CL})(1-\varepsilon_{CL}-L_S)+L_{Pt/C}\varepsilon_{CL}(1-\%M)}{L_{Pt/C}}}-1] \tag{3-60}$$

If the primary pores are completely occupied by the ionomer ($\%M=1$), Eq. (3-60) changes to:

$$\delta_M = r_{agg}[\sqrt[3]{\frac{(1-\varepsilon_{CL})(1-\varepsilon_{CL}-L_S)}{L_{Pt/C}}}-1] \tag{3-61}$$

It is important to note that the volume fraction of the ionomer with the agglomerate ($\varepsilon_{agg,M}$) is impossible to bigger than the porosity of the catalyst layer (ε_{CL}).

Assuming that the ionomer is hydrophilic, any liquid water is assumed to coat the entire surface of the individual agglomerate to generate a liquid water film adjacent to the outer boundary of the ionomer film. The total volume of the liquid water generated can be obtained as:

$$V_w = s\varepsilon_{CL}V_{tot} \tag{3-62}$$

where s is the liquid water saturation, which is defined as the volume fraction of the void space occupied by liquid water.

Averaging the total volume of the liquid water to each individual agglomerates, the volume of the liquid water surrounding each agglomerate is:

$$V_{w,i} = \frac{s\varepsilon_{CL}}{N_{agg}} \tag{3-63}$$

Then the liquid water film thickness is given as:

$$\delta_w = \sqrt[3]{(r_{agg}+\delta_M)^3+\frac{3s\varepsilon_{CL}}{4\pi N_{agg}}}-(r_{agg}+\delta_M) \tag{3-64}$$

Substituting Eq. (3-50) into Eq. (3-64):

$$\delta_w = \sqrt[3]{(r_{agg}+\delta_M)^3+\frac{s'\varepsilon_{CL}(1-\varepsilon_{CL})r_{agg}^3}{L_{Pt/C}}}-(r_{agg}+\delta_M) \tag{3-65}$$

where s' is the corrected liquid water saturation, defined as the volume fraction of the secondary pores occupied by the liquid water.

3.3.4 Specific area

The reaction surface area per unit platinum mass (m^2 kg^{-1}) can be calculated by an empirical equation as follow [182, 183]:

$$A_s = (227.79 f^3 - 158.57 f^2 - 201.53 f + 159.5) \times 10^3 \tag{3-66}$$

The specific area of the catalyst layer (m^{-1}), defined as the total active area per volume of catalyst layer, can be written as [182, 183]:

$$a_{CL} = \frac{m_{Pt}}{l_{CL}} A_s \tag{3-67}$$

The specific area of the agglomerate, defined as the total active area per volume of agglomerate, is

$$a_{agg} = \frac{a_{CL} V_{tot}}{V_{agg,tot}} \tag{3-68}$$

Substituting Eq. (3-46) and Eq. (3-49) into Eq. (3-68) leads to:

$$a_{agg} = \frac{m_{Pt} A_s}{l_{CL}} \frac{3}{4\pi r_{agg}{}^3 N_{agg}} \tag{3-69}$$

The specific area of the agglomerate covered by the ionomer is:

$$a'_{agg} = a_{agg} \left(1 + \frac{\delta_w}{r_{agg}}\right)^2 \tag{3-70}$$

3.4 Water phase transfer and transport through the membrane

3.4.1 Phase transfer and transport through the membrane

Water exists as three different phases in different solvents [184-186] including the dissolved water in the membrane and ionomer, water vapour and liquid water in the porous media and flow channels. The dissolved water is the membrane and ionomer absorbed water, which enters the membrane and ionomer from the water vapour during water uptake and leaves the membrane and ionomer in the liquid phase when the water

content of membrane and ionomer reaches complete saturation. The main phase transfer mechanisms include: phase transfer between liquid water and water vapour via condensation and evaporation, phase transfer between dissolved water and water vapour by membrane and ionomer absorption or water uptake, and phase transfer between liquid water and dissolved water during the process of membrane and ionomer desorption.

Water transport in the membrane plays an important role in determining the water content in the membrane/ionomer [184-188]. During fuel cell operation, water transport through the membrane occurs via three mechanisms: electro-osmotic drag (EOD) of water molecules carried by protons migrating from anode to cathode, back diffusion driven by the concentration gradient of water, and convection generated by the pressure gradient.

In order to mathematically describe the dissolved water transport through the membrane, a second order partial differential equation (PDE) is developed by following the traditional diffusive approach as follow:

$$\frac{\partial}{\partial t}(L_M c_w^d) + \nabla \cdot (n_d \frac{i_M}{F}) - \nabla \cdot (D_{w-M} \nabla c_w^d) - \nabla \cdot (\frac{k_{p,M} c_w^d}{\mu_w} \nabla p) = S_w^d \qquad (3\text{-}71)$$

The term on the left hand side of the equation refers to the water accumulation, water migration by electro-osmotic drag (EOD), the back diffusion and the hydraulic permeation, respectively. L_M is the volume fraction of ionomer (L_M =1 in membrane, 0 < L_M <1 in catalyst layer), c_w^d (mol m^{-3}) is the concentration of the dissolved water, n_d is the EOD coefficient, which is expressed as $2.5\lambda/22$ [184-189], D_{w-M} (m^2 s^{-1}) is the diffusion coefficient of water through the membrane, $k_{p,M}$ (m^2) is the hydraulic permeability of water in the membrane, μ_w (Pa s) is the water viscosity, p (Pa) is the pressure. S_w^d (mol m^{-3} s^{-1}) is the source term. The concentration of the dissolved water depends on the water content of the membrane and ionomer, which can be calculated by the following equation [188]:

$$c_w^d = \frac{\rho_M}{EW} \frac{\lambda}{1 + k_s \lambda} \qquad (3\text{-}72)$$

where ρ_M (kg m^{-3}) is the density of dry membrane, EW (g mol^{-1}) is the equivalent weight of membrane, and k_s is the swelling coefficient, representing the volume increase of the membrane and ionomer.

Dissolved water is absorbed by the membrane and ionomer when the concentration of the dissolved water is smaller than the equilibrium concentration, which is the maximum dissolved water being carried by the membrane and ionomer. After reaching the equilibrium concentration, the dissolved water move away from the membrane and ionomer in the liquid water phase, during the process of membrane and ionomer desorption. The source terms regarding the process above are expressed as:

$$S_{vd} = k_{ads}(c_w^{eq} - c_w^d) \qquad c_w^d < c_w^{eq} \tag{3-73}$$

$$S_{dl} = k_{des}(c_w^d - c_w^{eq}) \qquad c_w^d \geq c_w^{eq} \tag{3-74}$$

The subscripts *vd* and *dl* in the source term represent the water phase change from vapour to dissolved water and from dissolved water to liquid water, respectively. k_{ads} and k_{des} (s^{-1}) are the adsorption and desorption rate coefficient, calculated by [189, 190]:

$$k_{ads} = \frac{1.14\times10^{-5} f_w}{\delta_{CL}} \exp\left[2416\left(\frac{1}{303} - \frac{1}{T}\right)\right] \tag{3-75}$$

$$k_{des} = \frac{4.59\times10^{-5} f_w}{\delta_{CL}} \exp\left[2416\left(\frac{1}{303} - \frac{1}{T}\right)\right] \tag{3-76}$$

$$f_w = \frac{\lambda V_w}{V_w + \lambda V_w} \tag{3-77}$$

where V_W and V_M (m^3 mol^{-1}) are the partial molar volume of water and the dry membrane, respectively. c_w^{eq} (mol m^{-3}) is the equilibrium dissolved water concentration, which is determined by the equilibrium water content according to Eq. (3-72). The equilibrium water content is determined by empirical correlations based on water uptake measurements [184], given as:

$$\lambda^{eq} = \begin{cases} 0.3 + 6\alpha_w[1 - \tanh(\alpha_w - 0.5)] + 3.9\sqrt{\alpha_w}[1 + \tanh(\frac{\alpha_w - 0.89}{0.23})] & s \leq 0 \\ 16.8s + 14.0(1 - s) & s > 0 \end{cases} \tag{3-78}$$

The actual water content is proposed as a function of water activity:

$$\lambda = 0.043 + 17.81\alpha_w - 39.85\alpha_w^2 + 36.0\alpha_w^3 \qquad \alpha_w \le 1 \tag{3-79}$$

where α_w is a function of both water vapour partial pressure and liquid water saturation [186], expressed as:

$$\alpha_w = x_w \frac{p}{p_{sat}} + 2s \tag{3-80}$$

3.4.2 Liquid water transport in the porous electrode

At a steady state condition, applying the continuity equation on liquid water and gas phase, respectively, the following equations are obtained:

$$\nabla \cdot (\rho_w^l \mathbf{u}_w^l) = M_w S_l \tag{3-81}$$

$$\nabla \cdot (\rho_w^g \mathbf{u}_w^g) = M_w S_g \tag{3-82}$$

where M_w (kg mol^{-1}) is the molecular weight of water and, ρ (kg m^{-3}), $\mathbf{u}$ (m s^{-1}) and S (mol m^{-3} s^{-1}) are the density, velocity and source term of liquid water and water vapour, respectively. The subscript *w* represents water, and the superscripts *l* and *g* represent the liquid water and gas phase, respectively.

According to the Darcy's law, the velocity of the liquid water and gas phase can be related to their partial pressure as:

$$\mathbf{u}_w^l = -\frac{K^l}{\mu_w^l} \nabla p^l \tag{3-83}$$

$$\mathbf{u}_w^g = -\frac{K^g}{\mu_w^g} \nabla p^g \tag{3-84}$$

where K (m^2), μ (Pa s) and p (Pa) are the permeability, viscosity and partial pressure of the liquid water and gas phase, respectively.

The pressure difference between the wetting and non-wetting phase within the porous media is defined as the capillary pressure (p^c), which is expressed as:

$$p^c = p^g - p^l \tag{3-85}$$

Substituting Eq. (3-85) into Eq. (3-83), the liquid water velocity becomes to:

$$\mathbf{u}_w^l = \frac{K^l}{\mu_w^l}\nabla p^c - \frac{K^l}{\mu_w^l}\nabla p^g \tag{3-86}$$

Introducing the liquid water saturation into the expression above, gives

$$\mathbf{u}_w^l = \frac{K^l}{\mu_w^l}\frac{dp^c}{ds}\nabla s - \frac{K^l}{\mu_w^l}\nabla p^g \tag{3-87}$$

where s is the liquid water saturation, defined as the volume fraction of the liquid water in the porous media.

Capillary pressure can be related to the liquid water saturation via [191]:

$$p^c = \sigma\cos(\theta_c)(\frac{\varepsilon}{K})^{1/2}J(s) \tag{3-88}$$

where $J(s)$ is the Leverett function, and is given by [191]:

$$J(s) = \begin{cases} 1.417(1-s) - 2.120(1-s)^2 + 1.263(1-s)^3 & \theta_c < 90° \\ 1.417s - 2.120s^2 + 1.263s^3 & \theta_c > 90° \end{cases} \tag{3-89}$$

Normally, the porous electrode is hydrophobic, therefore the Leverett function is expressed in terms of the liquid water saturation and the contact angel, θ_c, is between 90° and 180°. The surface tension σ, for liquid water - air system, is taken as 0.0625 N/m. Combing Eq. (3-87) and Eq. (3-88), the liquid water velocity is expressed in terms of liquid water saturation as:

$$\mathbf{u}_w^l = \sigma\cos(\theta_c)\frac{K^l}{\mu_w^l}(\frac{\varepsilon}{K})^{1/2}\frac{dJ(s)}{ds}\nabla s - \frac{K^l}{\mu_w^l}\nabla p^g \tag{3-90}$$

The permeability of liquid water and gas phase can be associated with the permeability of the porous media via:

$$K^l = k_r^l K \ , \quad K^g = k_r^g K \tag{3-91}$$

where k_{rl} and k_{rg} are the relative permeability of liquid water and gas phase, which are proportional to the cube of liquid water saturation as:

$$k_r^l = s^3 , \quad k_r^g = (1-s)^3 \tag{3-92}$$

Substituting Eq. (3-84) and Eq. (3-91) into Eq. (3-90) leads to:

$$\mathbf{u}_w^l = \frac{\sigma\cos(\theta_c)k_r^l}{\mu_w^l}(\varepsilon K)^{1/2}\frac{dJ(s)}{ds}\nabla s - \frac{k_r^l\mu_w^g}{k_r^g\mu_w^l}\mathbf{u}_w^g \tag{3-93}$$

Substituting Eq. (3-93) into Eq. (3-81) and taking the liquid water accumulation into account, the liquid water saturation can be calculated by the as follow:

$$\frac{\partial}{\partial t}(\varepsilon\rho_w^l s) + \nabla\cdot(\rho_w^l D_c\nabla s - \frac{\rho_w^l k_r^l\mu_w^g}{k_r^g\mu_w^l}\mathbf{u}^g) = M_w S_w^l \tag{3-94}$$

where D_c (m^2 s^{-1}) is the capillary diffusion coefficient, which is calculated using the following expression:

$$D_c = \frac{\sigma\cos(\theta_c)k_r^l}{\mu_w^l}(\varepsilon K)^{1/2}\frac{dJ(s)}{ds} \tag{3-95}$$

At a steady state, if the velocity of the gas phase can be neglected, Eq. (3-94) becomes a second order partial differential equation with respect to the liquid water saturation, shown as follow:

$$\nabla^2 s = \frac{M_w}{\rho_w^l D_c}S_w^l \tag{3-96}$$

The source term, S_{vl} (mol m^{-3} s^{-1}), is introduced for the interfacial mass transfer rate of water by condensation and evaporation, which is defined as:

$$S_{vl} = \begin{cases} k_{con}\dfrac{\varepsilon(1-s)x_w^g}{RT}(x_w^g p^g - p_{sat}) & x_w^g p^g \geq p_{sat} \\ k_{eva}\dfrac{\varepsilon s\rho_w^l}{M_w}(p_{sat} - x_w^g p^g) & x_w^g p^g < p_{sat} \end{cases} \tag{3-97}$$

where k_{con} (s^{-1}) and k_{eva} (atm^{-1} s^{-1}) are the condensation and evaporation rate coefficient, respectively.

3.4.3 Water vapour transport in porous electrode

The transport of all involved gas species, including water vapour, within the porous electrode is described by the Maxwell-Stefan equation shown as follow:

$$\rho^g\mathbf{u}^g\cdot\nabla w_i^g - \nabla\cdot[-\rho^g\sum_{j=1}^{N}(1-s')D_{ij}(\nabla x_j^g - w_j^g)\frac{\nabla p}{p} + D_i^T\frac{\nabla T}{T}] = M_i S_i^g \tag{3-98}$$

where w_i^g, w_j^g and M_i (kg mol^{-1}) are the mass fraction, mole fraction and molecular weight of species *i*, respectively. D_{ij} (m^2 s^{-1}) and D_i^T (m^2 s^{-1}) are the multi-component diffusion coefficient and the thermal diffusion coefficient, which will be discuss in detail in Section 3.6.5 and Section 3.6.9, respectively, T is the temperature, S_i^g (mol m^{-3} s^{-1}) is the source terms, which account for the electrochemical reactions taken place within the porous catalyst layer shown as follow:

$$S_{H_2}^g = \frac{i_a}{2F},\ S_{O_2}^g = -\frac{i_c}{4F},\ S_w^g = \frac{i_c}{2F} \tag{3-99}$$

Note that ρ^g (kg m^{-3}) is the density of the gas mixture, which is given by the ideal gas law:

$$\rho^g = \frac{p^g M_n}{RT} \tag{3-100}$$

where p^g (Pa) is the pressure of the gas mixture and M_n (kg mol^{-1}) is the mean molecular weight of the gas mixture, which can be related to the mole fraction of the component as follow:

$$M_n = \sum_{i=1}^{n} x_i M_i \tag{3-101}$$

where *n* is the number of component gas in the gas mixture and, M_i (kg mol^{-1}) is the molecular weight of the species *i*.

In the practical condition, the fuel cell anode typically dehydrates. Therefore, assuming no liquid water exists at the anode [184]. The water phase transfer mechanism is only from vapour to dissolved water in the anode catalyst layer. The relationship between the sources terms of water in different phase within different region of the fuel cell are listed in Table 3-1, shown as follow:

Table 3-1 Source terms of water vapour, liquid water and dissolved water

	Anode GDL	Anode CL	Cathode CL	Cathode GDL
Water vapour	$S_w^v = 0$	$S_w^v = -S_{vd}$	$S_w^v = S_w^g - S_{vd}$ -	$S_w^v = -S_{vl}$
Liquid water	$S_w^l = 0$	$S_w^l = 0$	$S_w^l = S_{dl} + S_{vl}$	$S_w^l = S_{vl}$
Dissolved water	$S_w^d = 0$	$S_w^d = S_{vd}$	$S_w^d = S_{vd} - S_{dl}$	$S_w^d = 0$

Note: The unit for every source term is (mol m^{-3} s^{-1})

3.4.4 Membrane and ionomer swelling

The polymeric matrix of the membrane and ionomer expands leading to an increase in their volume when membrane/ionomer water absorption (water uptake) occurs. Normally a dry Nafion® membrane/ionomer swells approximately 20% when fully hydrated by water vapour [188, 192]. The membrane penetrates into the gas diffusion layer combined with the platinum catalyst to form the catalyst layer. The membrane in the catalyst layer co-exists with the ionomer. Membrane and ionomer swellings have two effects on fuel cell performance. For the membrane, higher swelling increases the ionic conductivity and the water diffusion coefficient, while for the ionomer higher swelling increases the thickness of the iomomer film surrounding the agglomerate and decreases the void space within the catalyst layer leading to an increase in species transport resistance, specifically oxygen diffusion [188].

Depending on the directions of membrane swelling, there are two types of membrane deformation: the through-plane membrane thickness increasing and the in-plane membrane buckling. The through-plane membrane thickness increase is caused by the zero or low fastening force from gas flow fields to the MEA [193]. Due to the fact that the membrane is fixed between the bipolar plates under a relative high clamping force, the thickness of the portion of the membrane under the current collector ribs is impossible to change during membrane water absorption (water uptake). However, the in-plane buckling occurs within channel portions at grooved gas flow field as shown in Figure 3-4. Compared to the through-plane thickness increasing, the in-plane buckling is more important as the in-plane stress is the major stress component in the membrane [194]. The in-plane buckling could have a significant impact on the channel flow as the MEA bulges into the channel. The bulged gas diffusion layer into the flow channels increases the mass transport resistance and can lead to pinhole formation of the membrane under the channel [195].

Because the catalyst layer is very thin compared with the gas diffusion layer and membrane, the volume increase of the catalyst layer therefore can be neglected while the ionomer swelling occurres. It is reasonable to assume that ionomer swelling only increases the thickness of the ionomer film surrounding the agglomerate and decreases the volume fraction of the void space.

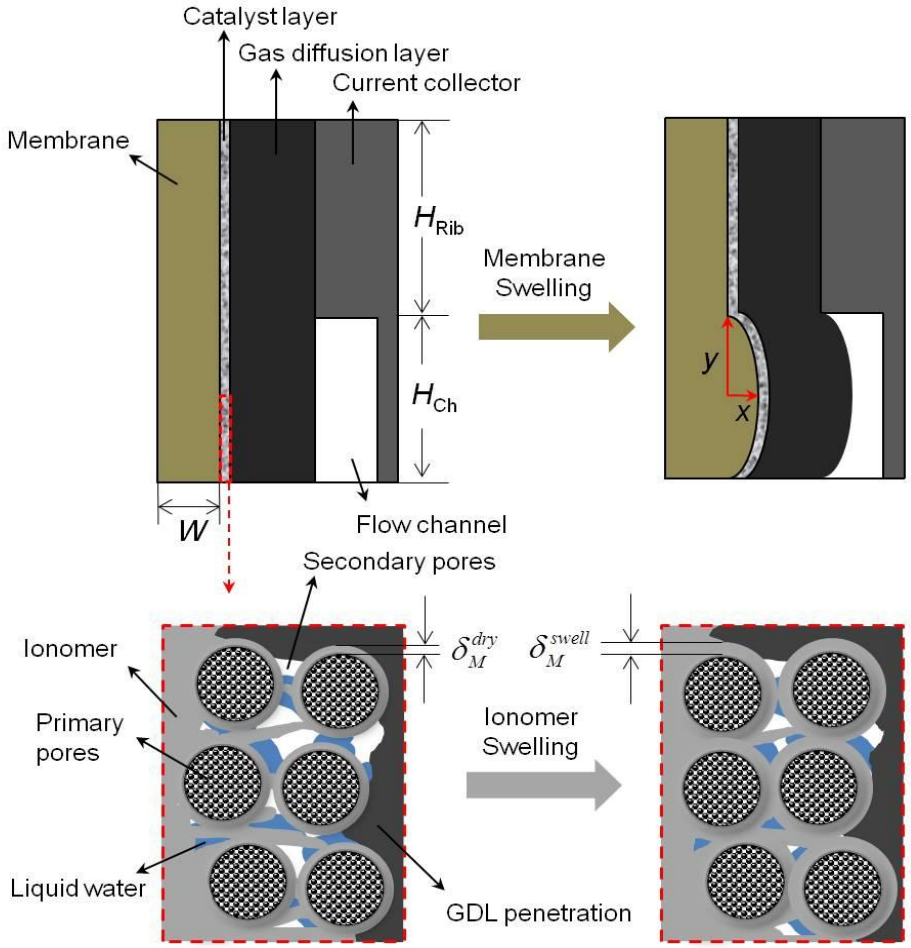

Figure 3-4 Sketch of the membrane and ionomer swelling and the bulged MEA into flow channel

By further assuming the shape of the swelled membrane is a half ellipse as shown in Figure 3-4, the major radius and the minor radius can be calculated as follow:

$$\frac{\pi xy}{2} = A_M^{swell} \tag{3-102}$$

where x (m) and y (m) are the major radius and the minor radius, respectively. A_M^{swell} (m^2) is the increased area of the swelled membrane, which is related to the membrane water content by:

$$A_M^{swell} = (H_{Rib} + H_{Ch}) \cdot W \cdot (1 + k_s \lambda) \tag{3-103}$$

Note that the major radius of the ellipse is equal to the half height of the flow channels, gives:

$$y = \frac{H_{Ch}}{2} \tag{3-104}$$

By combing Eq. (3-102) and Eq. (3-104), the minor radius of the ellipse is obtained as:

$$x = \frac{4(H_{Rib} + H_{Ch}) \cdot W \cdot (1 + k_s \lambda)}{\pi H_{Ch}} \tag{3-105}$$

And the volume fraction of the ionomer after swelling is calculated by the following equation:

$$L_M^{swell} = L_M (1 + k_s \lambda) \tag{3-106}$$

3.5 Governing equations

By coupling the conservation equations of mass, momentum, species, energy and charge, the complicate physical and chemical phenomena occurred within the fuel cells can be described in details. The general forms of the governing equations used in Chapter 4 to Chapter 7 are represented in detail in Appendix A.

3.6 Constitutive relations and model parameters

It is necessary and important to estimate and select the parameters rigorously in a particular model as the parameters input may have a strong influence on the final simulation results. Sometimes, the unreasonable parameters make errors in the simulation process. The parameters represent the physical and chemical properties of the materials and reactants involved, therefore it is important to fully understand the relationships between every parameter and the operating conditions, such as temperature, pressure and relative humidity. The model can be simplified by defining some insensitive parameters as constants. In this section a detailed description on the parameters obtained is presented.

3.6.1 Kinetic parameters

The electrochemical reaction kinetics described by both the Butler-Volmer equation and the agglomerate model have been given in Section 3.1. Two important kinetic parameters, the transfer coefficient and exchange current density, are investigated in this section. At this point, it is important to highlight that the kinetics parameters used in this work are identical to that in an acid system.

Transfer coefficient

The transfer coefficients are first shown in Eq. (3-5) and Eq. (3-6) to account for the electrical effects on the change of Gibbs free energy in an electrochemical reaction. As shown in Eq. (3-12) and Eq. (3-13), forward and backward reactions co-exist in the

oxidation reaction on anode and the reduction reaction on cathode. The transfer coefficient for reduction reaction, α_{Rd}, is assumed to be equal to the transfer coefficient for oxidation reaction, α_{Ox} , for both anode and cathode by Sousa *et al.* [202], leading to $\alpha_{Rd,a} = \alpha_{Ox,a} = \alpha_a$ and $\alpha_{Rd,c} = \alpha_{Ox,c} = \alpha_c$. In this study, $\alpha_{Rd} + \alpha_{Ox}$ is set to unity according to the assumption in the paper of Sun *et al.* [115]. For oxygen reduction reaction on cathode: $\alpha_{Rd,c} = \alpha_c$, $\alpha_{Ox,c}$ =1- α_c; for hydrogen oxidation reaction on anode: $\alpha_{Ox,a} = \alpha_a$, $\alpha_{Rd,a}$ =1- α_a.

It is well known that the transfer coefficient have a significant influence on the current density. However, it is very difficult to predict the accurate value of the transfer coefficient for a particular system as it is a function of numerous conditions, such as temperature, pressure, catalyst structure, and reactant impurity. Parthasarathy *et al.* [203] found that the Tafel slope is lower at higher cell voltages and higher at lower at lower cell voltages. Based on the experimental measurement of Parthasarathy *et al.* [203], the cathode transfer coefficient was regressed by Sun *et al.* [115] as follow:

$$\alpha_c = 0.495 + 2.3\times10^{-3}(T - 300) \tag{3-107}$$

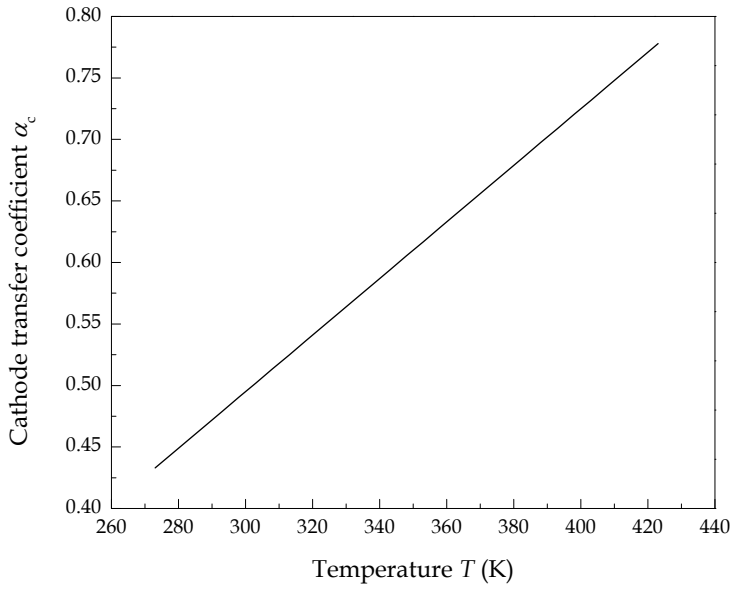

Figure 3-5 Temperature dependent transfer coefficient of anode and cathode

In comparison with the cathode transfer coefficient, the anode transfer coefficient changes slightly as the operating condition changed. Therefore, we applied the value reported by Bernardi and Verbrugge [21] of α_a = 0.5. The effect of temperature on the cathode transfer coefficient is plotted in Figure 3-5.

Exchange current density

As shown in Section 3.1.1, the exchange current density is the current densities for anode and cathode in case of both the forward and backward reactions are equal. It is analogous to the rate constant in chemical reactions and is a function of operating temperature and partial pressure of the reactant. The exchange current density can be expressed by the following equation [17]:

$$i_0 = i_0^{ref} a_{CL} \left(\frac{p_r}{p_r^{ref}}\right)^{\gamma} \exp\left[-\frac{E}{R_g T}\left(1-\frac{T}{T^{ref}}\right)\right] \quad (3\text{-}108)$$

where i_0^{ref} (A m^{-2}) is the reference exchange current density per unit catalyst surface area obtained at the reference temperature of 25 °C and pressure of 1.0 atm, a_{CL} (m^{-1}) is the specific area of the catalyst layer, which was given in Section 3.2.3, p_r (kPa) is the reactant partial pressure, p_r^{ref} (kPa) is the reference pressure, γ (0.5 for hydrogen oxidation reaction and 1.0 for oxygen reduction reaction [204, 205, 206]) is the pressure dependency coefficient, T^{ref} (298K) is the reference temperature, E (kJ mol^{-1}) is the activation energy, it was found to be 72.4 kJ mol^{-1} for oxygen reduction on cathode [207], and 16.9 kJ mol^{-1} for hydrogen oxidation on anode [205].

Exchange current density is a reflection of the activity of the surface of the electrode. Higher exchange current density means lower energy barrier that the charge must overcome in moving from electrolyte to the catalyst surface. In a hydrogen/oxygen fuel cell, the exchange current density of the anode is several orders of magnitude larger than that of the cathode. In other words, more current is generated at a fixed overpotential with a higher exchange current density, and the cathode overpotential is much larger than the anode overpotential. For this reason, the polarisation curve is mainly determined by the oxygen reduction reaction (ORR) at cathode. According to the literatures [21, 85, 208], the reference exchange current density (i_0^{ref}) for anode is 1.0 A cm^{-2} whereas it is much small for cathode and can be related with temperature as follow:

$$i_0^{ref} = 10^{\left(3.507-\frac{4001}{T}\right)} \quad (3\text{-}109)$$

The relationship between the operating temperature and cathode reference exchange current density is shown in Figure 3-6.

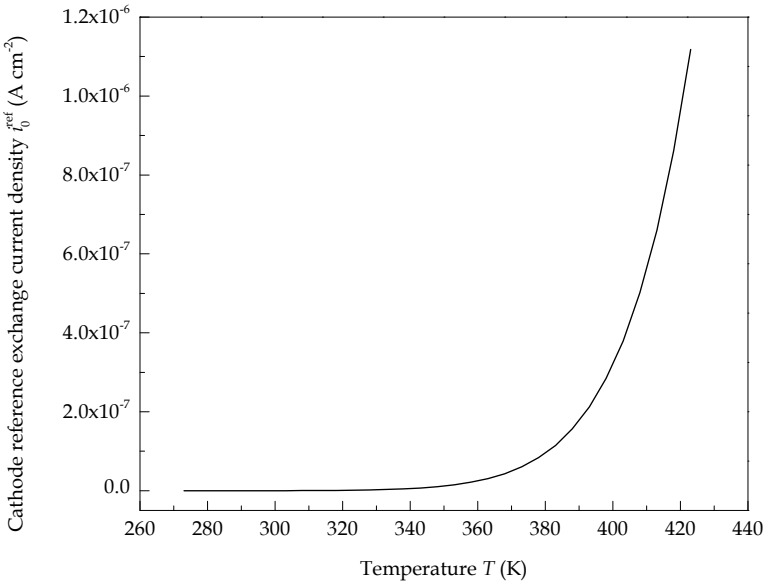

Figure 3-6 Temperature dependent cathode reference exchange current density

3.6.2 Open circuit potential

The open circuit potential is the theoretical or equilibrium potential of an electrode in absence of external current flow to or from the electrode, which can be calculated based on the knowledge of thermodynamics shown as follow. The portion of the reaction enthalpy that can be converted to electricity in a fuel cell corresponds to Gibbs free energy given by the following equation:

$$\Delta G = \Delta H - T\Delta S \tag{3-110}$$

As demonstrated in the equation above, Gibbs free energy ΔG is not equal to the total reaction enthalpy ΔH because there are some irreversible losses in energy conversion due to creation of entropy ΔS. According to the stoichiometry of the reactions, the changes of enthalpy and entropy are calculated as follow:

$$\Delta H = \Delta H^0 + \int_{T_{ref}}^{T} c_{p,H_2O} dT - \int_{T_{ref}}^{T} c_{p,H_2} dT - \frac{1}{2}\int_{T_{ref}}^{T} c_{p,O_2} dT \tag{3-111}$$

$$\Delta S = \Delta S^0 + \int_{T_{ref}}^{T} \frac{1}{T} c_{p,H_2O} dT - \int_{T_{ref}}^{T} \frac{1}{T} c_{p,H_2} dT - \frac{1}{2}\int_{T_{ref}}^{T} \frac{1}{T} c_{p,O_2} dT \tag{3-112}$$

where ΔH^0 (J mol^{-1}) and ΔS^0 (J mol^{-1} K^{-1}) are the enthalpy and entropy at standard conditions (1.0 atm, 25 °C), respectively. In general, electrical work is a product of charge and potential:

$$W_{el} = qE \tag{3-113}$$

where W_{el} (J mol^{-1}) is the electrical work, q is the charge (C mol^{-1}) and E (V) is the potential.

The total charge transferred in a fuel cell reaction per mole of H_2 consumed is equal to:

$$q = nNq_{el} \tag{3-114}$$

where n is the number of electrons per molecule of hydrogen ($n = 2$), N is the Avogadro's number ($N = 6.022 \times 10^{23}$ molecules mol^{-1}), q_{el} is the charge per electron ($q_{el} = 1.602 \times 10^{-19}$ C electron^{-1}). Because $q_{el} N = 9.65 \times 10^{23}$ C mol^{-1} is the Faraday's constant F , the electrical work is therefore becomes to:

$$W_{el} = nFE \tag{3-115}$$

As mentioned previously, the maximum amount of electrical energy generated in a fuel cell is equal to the Gibbs free energy.

$$W_{el} = -\Delta G \tag{3-116}$$

The theoretical potential of fuel cell is then changed to:

$$E = -\frac{\Delta G}{nF} \tag{3-117}$$

The temperature dependent theoretical cell potential can be calculated by substituting Eq. (3-110) into Eq. (3-117) yields:

$$E = -\frac{\Delta H - T\Delta S}{nF} \tag{3-118}$$

The theoretical cell potential also varies with reactant pressure. Assuming the reactants and product behave like ideal gas, the change in Gibbs free energy in an isothermal condition is expressed by the following equation:

$$dG = RT\frac{dp}{p} \tag{3-119}$$

After integration:

$$G = G^0 + RT\ln(\frac{p}{p^0}) \tag{3-120}$$

where G^0 (J mol^{-1}) is the Gibbs free energy at standard condition (25 °C and 1.0 atm), and p^0 (1.0 atm) is the reference or standard pressure. For any chemical reaction:

$$jA + kB \rightarrow mC + nD \tag{3-121}$$

The change in Gibbs free energy is the change between products and reactants:

$$\Delta G = mG_C + nG_D - jG_A - kG_B \tag{3-122}$$

Substituting the equation above into Eq. (3-120):

$$G = G^0 + RT\ln[\frac{(\frac{p_C}{p^0})^m(\frac{p_D}{p^0})^n}{(\frac{p_A}{p^0})^j(\frac{p_B}{p^0})^k}] \tag{3-123}$$

This is the known as the Nernst equation. Assuming the water produced in gas phase in Eq. (1-3), for the hydrogen/oxygen fuel cell, the open circuit potential (OCP) can be calculated as:

$$E^{OCP} = -\frac{(\Delta H - T\Delta S)}{nF} + RT\ln[\frac{p_{H_2}p_{O_2}^{0.5}}{p_{H_2O}}] \tag{3-124}$$

For the hydrogen oxidation process, the enthalpy is the difference between the heats of formation of products and reactants, which can be expressed as follow:

$$\Delta H = h_{f,H_2O} - h_{f,H_2} - 1/2\,hh_{f,O_2} \tag{3-125}$$

Similarly, the entropy is the difference between entropies of products and reactants:

$$\Delta S = s_{f,H_2O} - s_{f,H_2} - 1/2\,sh_{f,O_2} \tag{3-126}$$

where h_{f,H_2O}, h_{f,H_2} and h_{f,O_2} (J mol^{-1}) are the enthalpies of water, hydrogen and oxygen, and s_{f,H_2O}, s_{f,H_2} and s_{f,O_2} (J mol^{-1} K^{-1}) are the entropies of water, hydrogen and oxygen respectively. The values of enthalpies and entropies for reaction reactants and products at standard condition (25 °C, 1.0 atm) are shown in Table 3-2.

Table 3-2 Enthalpies and entropies of formation for reactants and products at standard condition [17]

	h_f^0 (kJ mol^{-1})	s_f^0 (kJ mol^{-1} K^{-1})
Hydrogen	0	0.13066
Oxygen	0	0.20517
Liquid water	-286.02	0.06996
Water vapour	-241.98	0.18884

Assuming water is generated as liquid, the enthalpy and entropy for hydrogen oxidation reaction at standard condition are $\Delta H^0 = -286.02$ kJ mol^{-1} and $\Delta S^0 = -0.1633$ kJ mol^{-1} K^{-1} according to Eq. (3-125) and Eq. (3-126).

The open circuit potential changes with temperature. The enthalpies and entropies of reaction reactants and products are functions of temperature, which are shown as:

$$h_f = h_f^0 + \int_{29815}^{T} c_p dT \tag{3-127}$$

$$s_f = s_f^0 + \int_{29815}^{T} \frac{1}{T} c_p dT \tag{3-128}$$

The specific heat of gas reactant and product can be calculated by the following empirical relationship [17]:

$$c_p = a + bT + cT^2 \tag{3-129}$$

where *a*, *b*, and *c* are the empirical coefficients as shown in Table 3-3.

Table 3-3 Empirical coefficients for temperature dependent specific heat [17]

	a	*b*	*c*
Hydrogen	28.914	-0.00084	2.01×10^{-6}
Oxygen	25.845	0.01298	-3.90×10^{-6}
Water vapour	30.626	0.00962	1.18×10^{-6}

Note: the unit of the specific heat is (J mol^{-1} K^{-1})

The open circuit potential is therefore can be calculated by Eq. (3-124). As shown in Figure 3-7, the open circuit potential (OCP) decreases with temperature and the OCP is higher when the production generated as liquid water in comparison with water vapour.

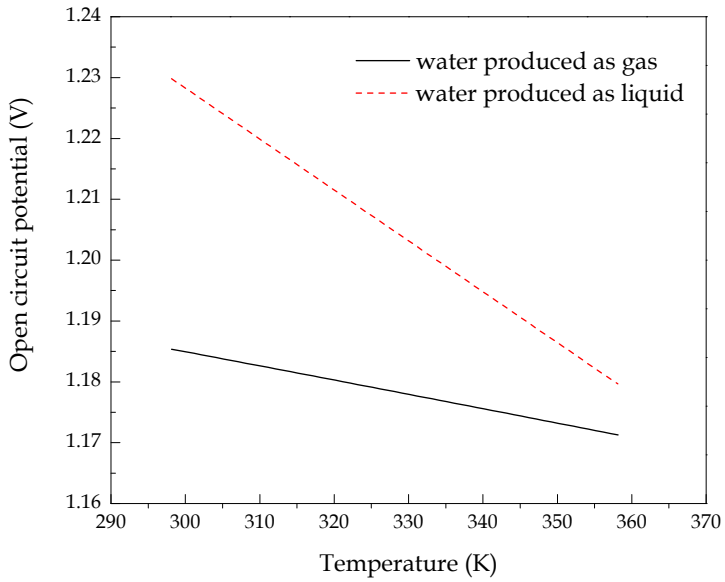

Figure 3-7 Temperature dependent open circuit potential (OCP) for hydrogen oxidation reaction

3.6.3 Reactant solubility and diffusivity in Nafion®

As described in Section 3.1.2, reactant gases must transport through the ionomer film surrounding the agglomerate before reacted on the surface of platinum catalyst particles inside the agglomerate. Due to the fact that the solubility and diffusivity of hydrogen through Nafion® is several times larger than that of oxygen, oxygen solubility and diffusivity through Nafion® therefore attracts more attentions [21, 85]. For oxygen diffusivity through the Nafion® membrane and ionomer, Marr and Li [85] developed a temperature dependent equation by fitting the experimental data published by Parthasarathy *et al.* [203]. Suzuki *et al.* [209] reported that the oxygen diffusion coefficient is proportional to the power of the membrane water content. Combining these two equations will account for both the effects of temperature and water content of membrane and ionomer. Therefore, we have adopted an equation to obtain the oxygen diffusion coefficient as follow:

$$D_{O_2-M} = 1.3926\times10^{-10}\lambda^{0.708}\exp\left(\frac{T-273.15}{106.65}\right) - 1.6461\times10^{-10}\lambda^{0.708} + 5.2\times10^{-10} \quad (3\text{-}130)$$

The oxygen diffusion coefficient obtained by Eq. (3-130) is validated by the experimental data by Takamura *et al.* [210] in Figure 3-8.

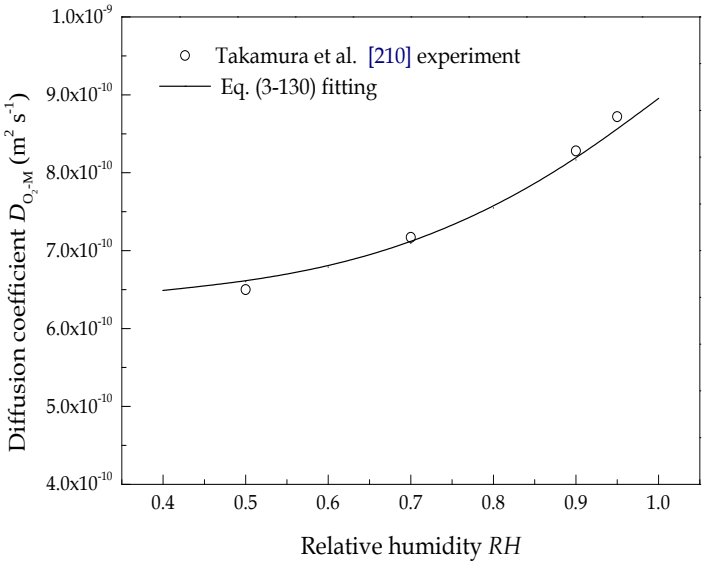

Figure 3-8 Relative humidity dependent oxygen diffusivity through Nafion® membrane/ ionomer

Nonoyama *et al.* [211] found that the Henry's constant for oxygen solubility in the Nafion® ionomer depends on the relative humidity. In order to investigate the effect of water content on the Henry's constant, we develop an equation by fitting the results of Suzuki *et al.* [209] based on the equation of Marr and Li [85].

$$H_{O_2} = 0.11552 \exp(14.1 + 0.0302\lambda - \frac{666}{T}) \tag{3-131}$$

The Henry's constant for oxygen dissolving in Nafion® ionomer, which is calculated by Eq. (3-131), is validated by the simulation results of Suzuki *et al.* [209] in Figure 3-9.

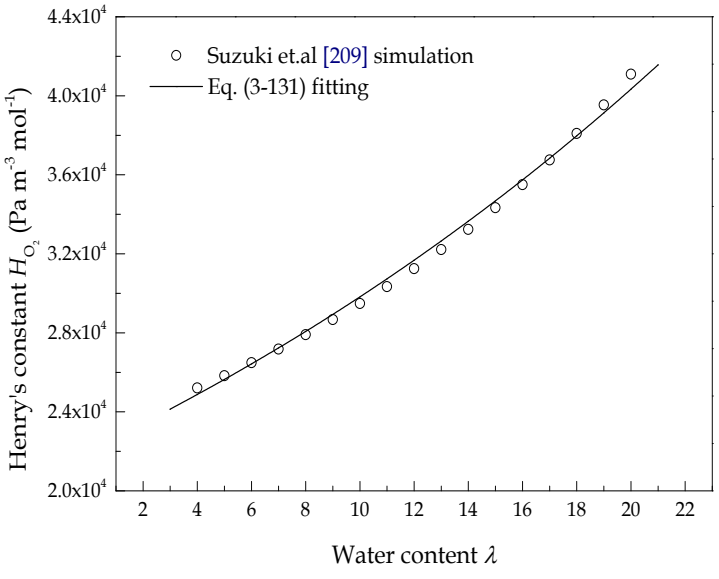

Figure 3-9 Water content dependent Henry's constant for oxygen solubility in Nafion® membrane/ ionomer

3.6.4 Oxygen diffusion coefficient in liquid water

The intrinsic diffusion coefficient of oxygen diffusing through the liquid water is calculated by the following empirical equations [211, 212]:

$$D_{O_2-w} = 7.4\times10^{-8} T \frac{\sqrt{\psi_w M_w}}{\mu_w (V_{O_2})^{0.6}} \tag{3-132}$$

V_{O_2} (cm^3 mol^{-1}) is the mole volume of the solute (dissolved oxygen) as liquid at its normal boiling point, ψ_w is the association parameter for the solvent (2.6 for water), μ_w (mPa s) is the temperature dependent viscosity of the solvent, T (K) is the operating temperature, M_w is the molar mass of the solvent (18 g mol^{-1} for water).

Figure 3-10 shows the oxygen diffusion coefficient in liquid water in comparison with that in Nafion® membrane and ionomer. It is clear that oxygen diffusion coefficient increases as the temperature increases. Oxygen diffusing in liquid water is much faster than in Nafion® membrane and ionomer, for example at 340 K, the oxygen diffusion coefficient in liquid water is almost ten times larger than that in Nafion® membrane and ionomer. As a result, the thickness of the ionomer film has a greater impact on oxygen transport than the liquid water film.

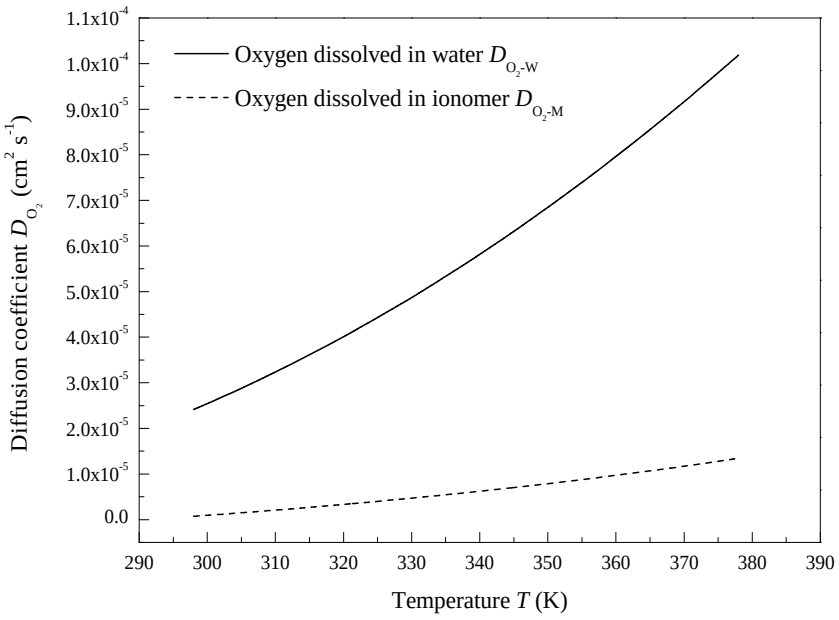

Figure 3-10 Temperature dependent oxygen diffusion coefficients in liquid water and Nafion® membrane/ ionomer

3.6.5 Multicomponent diffusivity

The intrinsic binary diffusion coefficients for all pairs of gas species D_{ij} (m^2 s^{-1}) can be calculated using the equation developed by Bird *et al.* [196] as follow:

$$D_{ij}^{0} = 1.8583\times10^{-7}\sqrt{T^3\left(\frac{1}{M_i}+\frac{1}{M_j}\right)}\frac{1}{p\sigma_{ij}^2\Omega_{ij}} \tag{3-133}$$

where

$$\sigma_{ij} = \frac{1}{2}(\sigma_i+\sigma_j),\ \varepsilon_{ij} = \sqrt{\varepsilon_i\varepsilon_j} \tag{3-134}$$

Ω_i and Ω_{ij} are functions of the reduced temperature T_i^* and T_{ij}^*.

$$T_i^* = \frac{\kappa}{\varepsilon_i}T,\ T_{ij}^* = \frac{\kappa}{\varepsilon_{ij}}T \tag{3-135}$$

There are empirical expressions for calculating Ω_i and Ω_{ij} written as:

$$\Omega_i = A/(T_i^*)^B + C/\exp(T_i^*D) + E/\exp(T_i^*F) \tag{3-136}$$

$$\Omega_{ij} = A/(T_{ij}^*)^B + C/\exp(T_{ij}^*D) + E/\exp(T_{ij}^*F) + G/\exp(T_{ij}^*H) \tag{3-137}$$

The parameters are listed in Table 3-4.

Table 3-4 Lennard-Jones potential parameters [196]

Species *i*	M_i	σ_i	ε_i/κ
H_2	2.016	2.915	38.0
O_2	32.000	3.433	113.0
N_2	28.013	3.667	99.8
H_2O	18.000	2.641	809.1
Ω_i	A=1.16145; B=0.14874; C=0.52487; D=0.77320; E=2.16178; F=2.43787		
$\Omega_{i,j}$	A=1.06036; B=0.15610; C=0.19300; D=0.47635; E=1.03587; F=1.52996; G=1.76474; H=3.89411		

The temperature dependent binary diffusion coefficients for all pairs of gas species at 1.0 atm are shown in Figure 3-11.

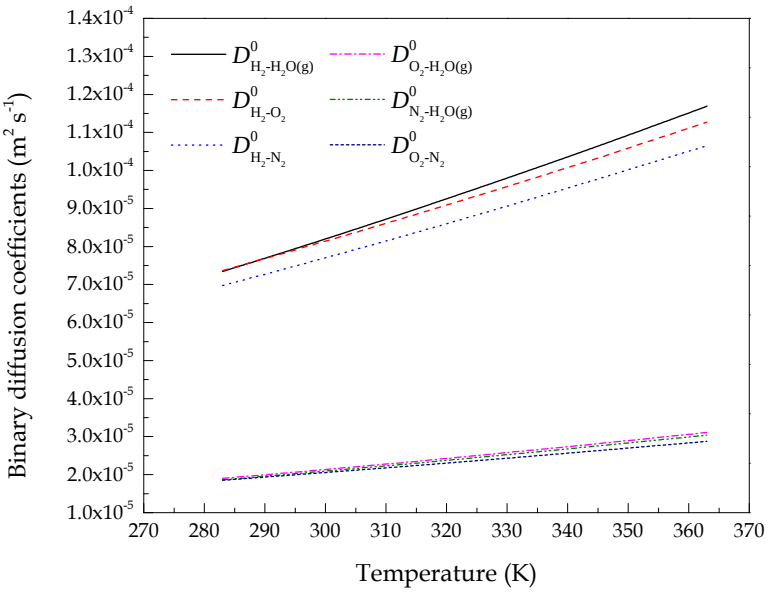

Figure 3-11 Temperature dependent binary diffusion coefficients for all pairs of gas species at 1.0 atm

3.6.6 Knudsen diffusion

Knudsen diffusion is a means of diffusion that occurs when the scale length of a system is comparable to or smaller than the mean free path of the particles involved. Knudsen effect on reactant gas diffusion is taken into account when the Knudsen number (K_n) is greater than 0.1 [213, 214]. The Knudsen number and Knudsen diffusion coefficient of oxygen diffusion in porous media is [181, 183]:

$$K_n = \frac{k_B T}{\sqrt{2}\pi p \sigma_{ii} d_{avg}} \tag{3-138}$$

$$D_{K_n,O_2} = \frac{d_{avg}}{3}\sqrt{\frac{8RT}{\pi M_{O_2}}} \tag{3-139}$$

where k_B (1.38065×10^{-23} J K^{-1}) is the Boltzmann constant, σ_{ii} (m) is the particle diameter, and d_{avg} (m) is the average pore diameter in the catalyst layer, which can be calculated as [181, 183]:

$$d_{avg} = \frac{4}{3}\frac{\varepsilon_{CL}}{1-\varepsilon_{CL}} r_{agg} \tag{3-140}$$

where ε_{CL} and r_{agg} (m) are the porosity of the catalyst layer and the radius of the agglomerate, respectively.

The intrinsic oxygen diffusion coefficient in the gas mixture is:

$$D_{O_2-g}^0 = \frac{1-x_{O_2}}{\frac{x_{N_2}}{D_{O_2-N_2}^0} + \frac{x_{H_2O}}{D_{O_2-H_2O}^0}} \tag{3-141}$$

where the intrinsic binary diffusion coefficients $D_{O_2-N_2}^0$ and $D_{O_2-H_2O}^0$ are shown in Section 3.5.5. Then the equivalent diffusion coefficient of oxygen in the porous media is:

$$\frac{1}{D_{O_2-g,e}^0} = \frac{1}{D_{O_2-g}^0} + \frac{1}{D_{K_n,O_2}} \tag{3-142}$$

The oxygen diffusion coefficients through the void space of porous electrode at various temperatures, which is obtained from Eq. (3-142), are shown in Figure 3-12. It is clear the Knudsen effect cannot be neglected, especially at higher temperature.

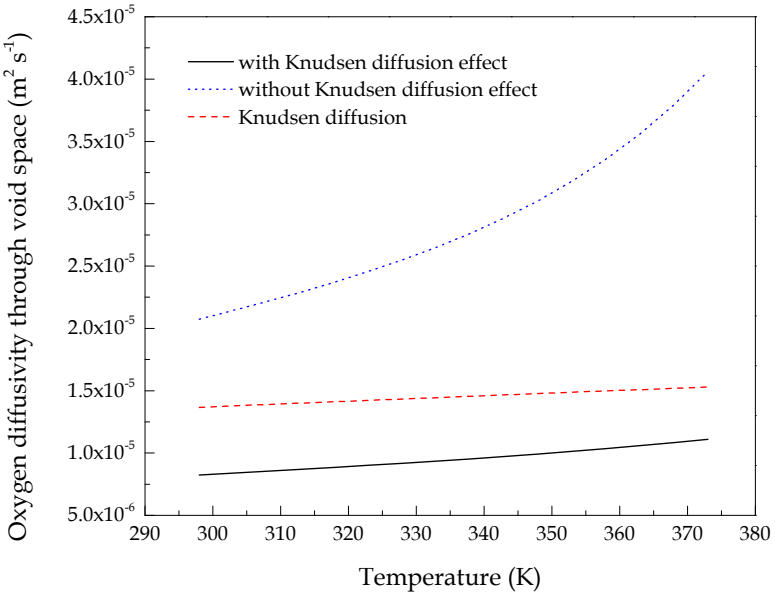

Figure 3-12 Temperature dependent oxygen diffusion coefficients through void space of porous electrode

3.6.7 Ionic conductivity

Proton transport between agglomerate requires sufficient ionomer films surrounding agglomerates. As the thickness of the ionomer film decreases, the contact between agglomerates decreases, which leads to a decrease in proton transport. The effective ionic conductivity of the catalyst layer, σ_M^{eff} (S m^{-1}), can be obtained using the equation of Kamarajugadda *et al.* [215] instead of Bruggeman correction shown as follow:

$$\sigma_M^{eff} = (1-\varepsilon_{CL})\left[1+\frac{(\varepsilon_{agg,M}-1)}{(1+\delta_M/r_{agg}+a_0)^3}\right]\sigma_M \tag{3-143}$$

where $\varepsilon_{agg,M}$ is the volume fraction of ionomer in agglomerate, δ_M (m) is the thickness of the ionomer film, r_{agg} (m) is the radius of agglomerate. The values of the parameters of $\varepsilon_{agg,M}$, δ_M and r_{agg} are associated with the structure of catalyst layer, which are shown in Section 3.2. Note that Eq. (3-143) is developed by improving the previous equation of Jaouen *et al.* [213, 214]. In order to capture the trend of the relationship between δ_M and σ_M^{eff} ($\delta_M \to 0$, $\sigma_M^{eff} \to 0$), the dimensionless parameter a_0 is added, which is given by:

$$a_0 = \min[0, (\frac{\delta_M}{r_{agg}} + \sqrt[3]{(1-\varepsilon_{agg,M})} - 1)] \tag{3-144}$$

The intrinsic ionic conductivity, σ_M (S m^{-1}), strongly depends on temperature and water content, which is expressed as:

$$\sigma_M = \exp\left[1268(\frac{1}{303}-\frac{1}{T})\right](0.5139\lambda - 0.326) \tag{3-145}$$

The dimensionless effective ionic conductivity of cathode catalyst layer with different ionomer film thicknesses is shown in Figure 3-13.

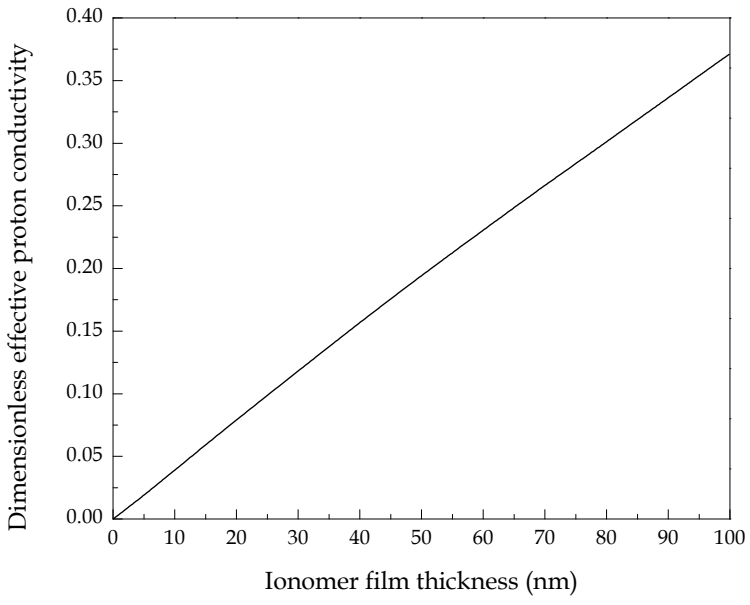

Figure 3-13 Effect of ionomer film thickness on dimensionless effective ionic conductivity of cathode catalyst layer (m_{Pt} = 0.4 mg cm^{-2}, f = 0.3, l_{CL} = 15μm, r_{agg} = 1.0 μm)

3.6.8 Electronic conductivity

The electronic conductivities for gas diffusion layer and catalyst layer are given in this section. For gas diffusion layer, a constant value of 1250 S m^{-1} is adopted [216]. For catalyst layer, the electronic conductivity depends on the composition, e.g. the volume fractions of the components responsible for the conductivity. The effective electronic conductivity is therefore obtained using the following equation [217]:

$$\sigma_s^{eff} = \sigma_s \frac{2-2\varepsilon_e}{\varepsilon_e + 2} \tag{3-146}$$

where σ_s (S m^{-1}) is the electronic conductivity of the solid phase (platinum dispersed carbon in the catalyst layer), ε_e is the volume fraction of the non-conductor materials, e.g. ionomer and void space in the catalyst layer.

The electronic conductivity of Vulcan XC-72 carbon black is 450 S m^{-1} reported by Pantea *et al.* [218], and the electronic conductivity of platinum is regressed from the experimental data provide by Powel and Tye [219] shown as follow:

$$\sigma_{Pt} = 1.7209 \times 10^9 T^{(-0.9259)} \tag{3-147}$$

The electronic conductivity calculated by Eq. (3-147) is validated by the experimental data in Figure 3-14.

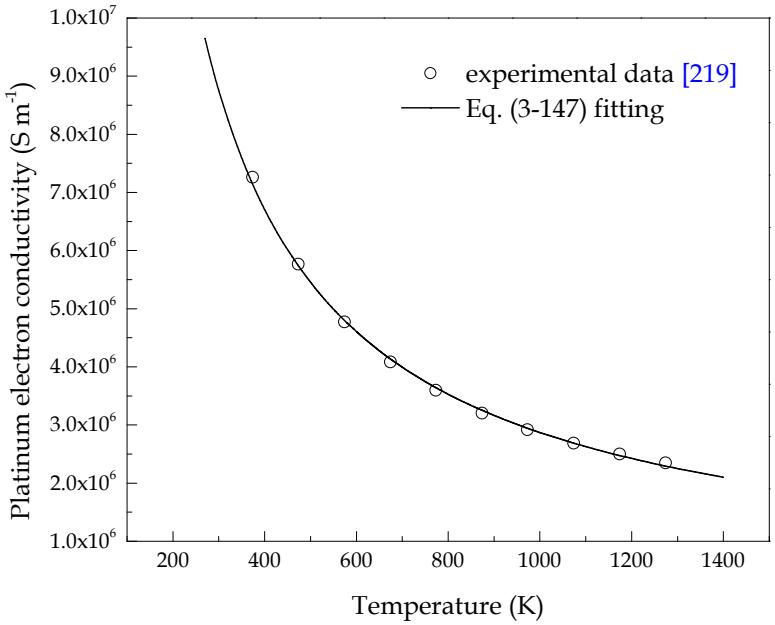

Figure 3-14 Temperature dependent platinum electronic conductivity

3.6.9 Specific heat capacity and thermal conductivity

The specific heat capacity and the thermal conductivity of the gas mixture are obtained by using an empirical equation developed by Wike [220],

$$c_p^g = \sum_i x_i c_{p,i}^g, \quad k^g = \sum_i \frac{x_i k_i}{\sum_j x_j \Phi_{ij}} \tag{3-148}$$

in which

$$\Phi_{ij} = \frac{1}{\sqrt{8}}\left(1+\frac{M_i}{M_j}\right)^{-0.5}\left[1+\left(\frac{k_i}{k_j}\right)^{0.5}\left(\frac{M_j}{M_i}\right)^{0.25}\right]^2, \quad \Phi_{ji} = \frac{k_j}{k_i}\frac{M_i}{M_j}\Phi_{ij} \tag{3-149}$$

where c_p^g (J mol^{-1} K^{-1}) is the specific heat capacity of the gas mixture, x_i is the mole fraction of species i in gas mixture, $c_{p,i}^g$ (J mol^{-1} K^{-1}) is the specific heat capacity of species i in gas mixture, k^g (W m^{-1} K^{-1}) is the thermal conductivity of the gas mixture, k_i (W m^{-1} K^{-1}) is the thermal conductivity of species i in gas mixture, M_i (kg mol^{-1}) is the molecular weight of species i.

The expressions for the specific heat capacities of each gas component including hydrogen, oxygen, nitrogen and water vapour are obtained by fitting the experimental data, which are compared in Figure 3-15.

$$c_{p,H_2}^g = 1.914\times10^{-6}T^2 - 8.314\times10^{-4}T + 28.890 \tag{3-150}$$

$$c_{p,O_2}^g = -4.281\times10^{-6}T^2 + 1.371\times10^{-2}T + 25.431 \tag{3-151}$$

$$c_{p,N_2}^g = 1.788\times10^{-5}T^2 + 2.924\times10^{-3}T + 27.848 \tag{3-152}$$

$$c_{p,H_2O}^g = 1.180\times10^{-6}T^2 + 9.621\times10^{-3}T + 30.326 \tag{3-153}$$

The specific heat capacities of solid and liquid phases changes slightly with temperature. Consequently, the specific heat capacities of platinum, carbon black, liquid water and membrane/iomomer are assumed as temperature independent constants shown in Table 3-5.

Also, the expressions for the thermal conductivities of hydrogen, oxygen, nitrogen and water vapour are obtained by fitting the experimental data shown in Figure 3-16.

$$k_{H_2} = 3.777\times10^{-4}T + 7.444\times10^{-2} \tag{3-154}$$

$$k_{O_2} = 6.204\times10^{-5}T + 8.83\times10^{-3} \tag{3-155}$$

$$k_{N_2} = 5.453\times10^{-5}T + 1.088\times10^{-2} \tag{3-156}$$

$$k^{g}_{H_2O} = 1.188\times10^{-4}T - 2.404\times10^{-2} \tag{3-157}$$

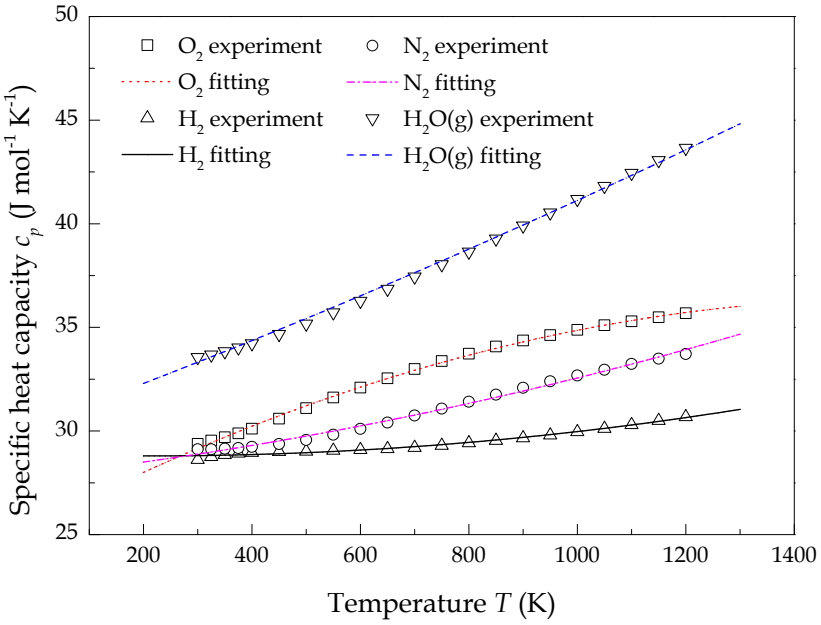

Figure 3-15 Temperature dependent specific heat capacities of hydrogen, oxygen, nitrogen and water vapour [221]

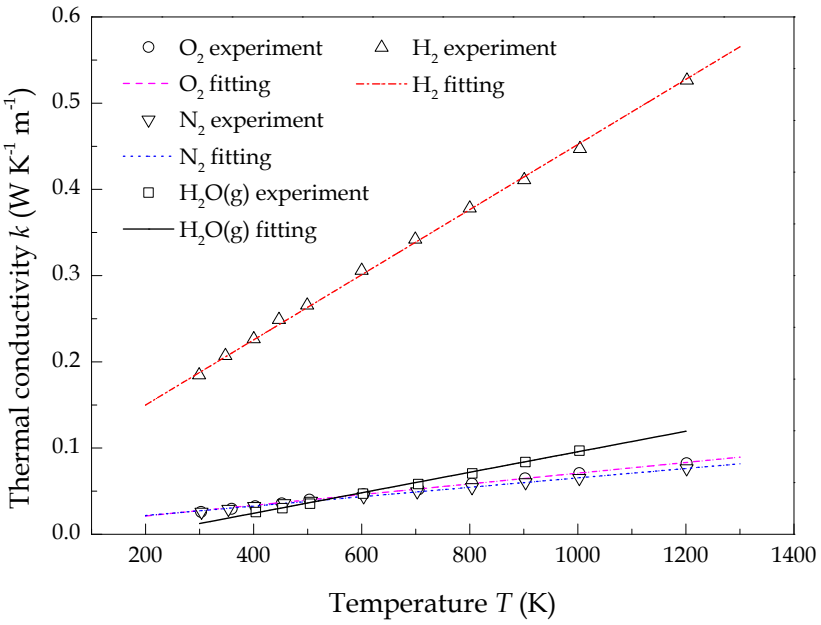

Figure 3-16 Temperature dependent thermal conductivities of hydrogen, oxygen, nitrogen and water vapour [221]

For the solid components, e.g. platinum, carbon black and liquid water, the expressions for the thermal conductivities are also obtained by fitting the experimental data.

$$k_{Pt} = -5.037\times10^{-9}T^3 + 2.483\times10^{-5}T^2 - 2.282\times10^{-2}T + 77.80 \quad (3\text{-}158)$$

$$k_C = 1.048\times10^{-6}T^2 - 2.869\times10^{-3}T + 2.979 \quad (3\text{-}159)$$

$$k^l_{H_2O} = -1.118\times10^{-5}T^2 + 8.388\times10^{-3}T - 0.9004 \quad (3\text{-}160)$$

Table 3-5 Specific heat capacities of platinum, carbon black, membrane/iomomer and liquid water [188]

	c_p (J kg^{-1} K^{-1})
platinum	1.3×10^2
carbon black	894.4
membrane/iomomer	1090.0
liquid water	4187.0

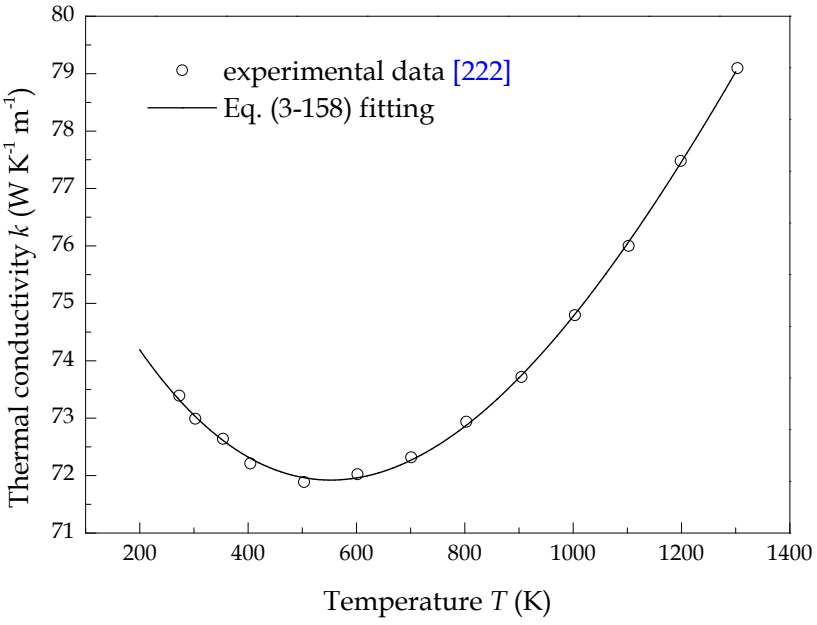

Figure 3-17 Temperature dependent platinum thermal conductivity

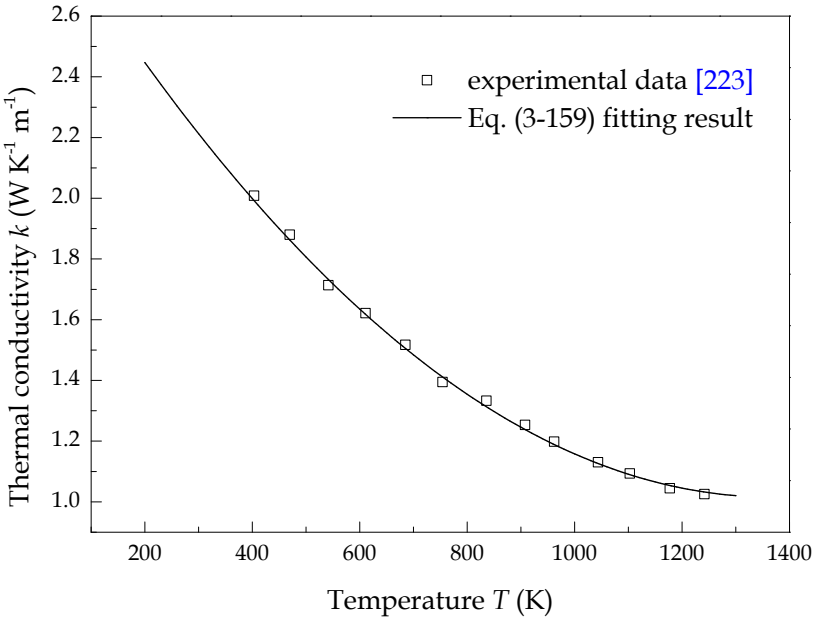

Figure 3-18 Temperature dependent carbon black thermal conductivity

The thermal conductivity of membrane/ionomer is assumed to be a temperature independent constant of 0.25 W m^{-1} K^{-1} [186, 192]. The thermal diffusion coefficient of species i in gas mixture, D_i^T (m^2 s^{-1}), in Section 3.3.3 can be expressed as the quotient of the thermal conductivity and specific heat capacity as follow:

$$D_i^T = M_i k_i / c_{p,i} \tag{3-161}$$

Figure 3-15 to Figure 3-18 show that the fitted expressions agree very well with the experimental data. The effective thermal conductivity and specific heat capacity depend on the volume fractions of the species within a chosen domain. Without a doubt, the cathode catalyst layer is the most complicated domain in which gas mixture, liquid water, ionomer, platinum dispersed carbon, gas diffusion layer penetration are all involved. The detailed expressions for the effective thermal conductivity, specific heat capacity of gas diffusion layer, catalyst layer and membrane/ionomer are listed in Table 3-6. The volume fractions of the component can be known from Section 3.2.

Table 3-6 Effective specific heat capacity and thermal conductivity of gas diffusion layer, catalyst layer and membrane

	Gas diffusion layer	*Catalyst layer*	*Membrane*
c_p^{eff}	$\varepsilon_{GDL}c_{p,C} + s\varepsilon_{GDL}c_{p,w}^{l} + (1-s)\varepsilon_{GDL}c_p^{g}$	$L_{Pt}c_{p,Pt} + (L_C + L_S)c_{p,C} + L_M c_{p,M} + s\varepsilon_{CL}c_{p,w}^{l} + (1-s)\varepsilon_{CL}c_p^{g}$	$c_{p,M}$
k^{eff}	$\varepsilon_{GDL}k_C + s\varepsilon_{GDL}k_w^{l} + (1-s)\varepsilon_{GDL}k_p^{g}$	$L_{Pt}k_{Pt} + (L_C + L_S)k_C + L_M k_M + s\varepsilon_{CL}k_w^{l} + (1-s)\varepsilon_{CL}k_p^{g}$	k_M

3.6.10 Water diffusivity through the membrane

Nafion® membrane is an ideal media for dissolved water transport, the diffusion coefficient of water through the membrane is a piecewise function which is determined by both temperature and membrane water content as follow [21, 181-188, 191, 192]:

$$D_{w-M} = \begin{cases} D_0(2.563 - 0.33\lambda + 0.0264\lambda^2 - 0.000671\lambda^3) & \lambda > 4 \\ D_0(-1.25\lambda + 6.65) & 3 < \lambda \le 4 \\ D_0(2.05\lambda - 3.25) & 2 \le \lambda \le 3 \end{cases} \quad (3\text{-}162)$$

$$D_0 = 1.0\times10^{-10}\exp[2416(\frac{1}{303} - \frac{1}{T})] \quad (3\text{-}163)$$

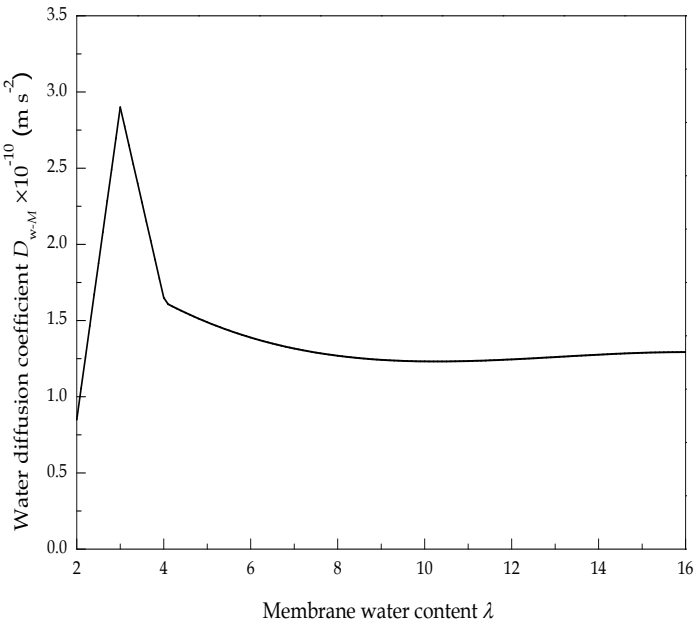

Figure 3-19 Water content dependent diffusion coefficient of water through Nafion® membrane

As shown in Figure 3-19, when the membrane water content increasing, the diffusion coefficient initially increases then decrease to a constant. In Eq. (3-162), the membrane

water content (λ) is defined as the number of water molecules per sulfonic acid site, which can be expressed as a function of water vapour activity (α_w) as follow:

$$\lambda = \begin{cases} 0.043 + 17.81\alpha_w - 39.85\alpha_w^{\,2} + 36.0\alpha_w^{\,3} & \alpha_w < 1 \\ 14.0 + 1.4(\alpha_w - 1) & 1 \le \alpha_w \le 3 \\ 16.8 & \alpha_w > 3 \end{cases} \tag{3-164}$$

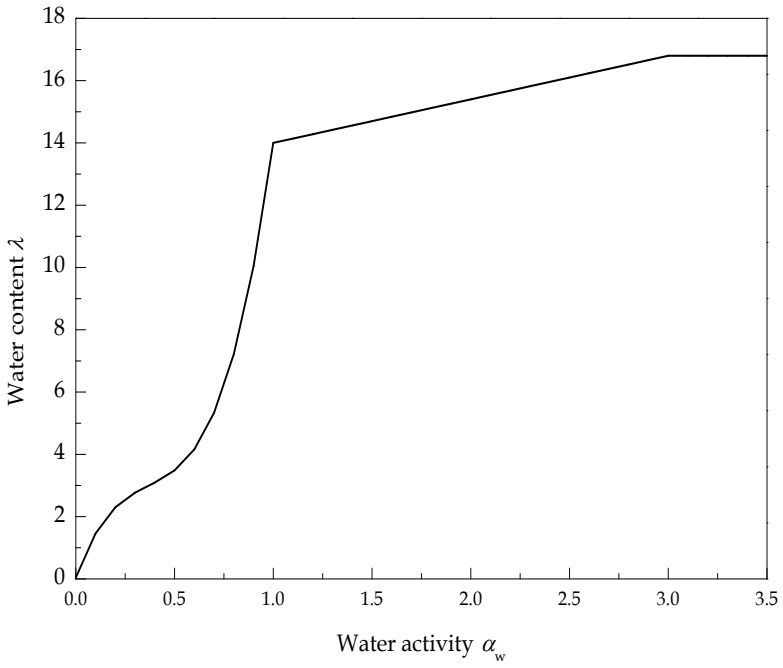

Figure 3-20 Relationship between water activity and membrane water content

As shown in Figure 3-20, the membrane water content increases up to 16.8 as water activity increases. Water activity can be associated with the partial pressure of water vapour as follow [224]:

$$\alpha_w = \frac{p_w}{p_w^{sat}} = RH \tag{3-165}$$

where p_w (Pa) is the partial pressure of water vapour, p_w^{sat} (Pa) it the saturated water vapour pressure, which is the water vapour pressure at saturation temperature, and RH is the relative humidity.

As shown in Figure 3-21, the saturated water pressure is obtained by fitting the experimental data as follow:

$$p_w^{sat} = 9.531\times10^{-4}(T-237)^4 - 3.123\times10^{-2}(T-237)^3 + 3.451(T-237)^2 + 20.96(T-237) + 611.0 \quad (3\text{-}166)$$

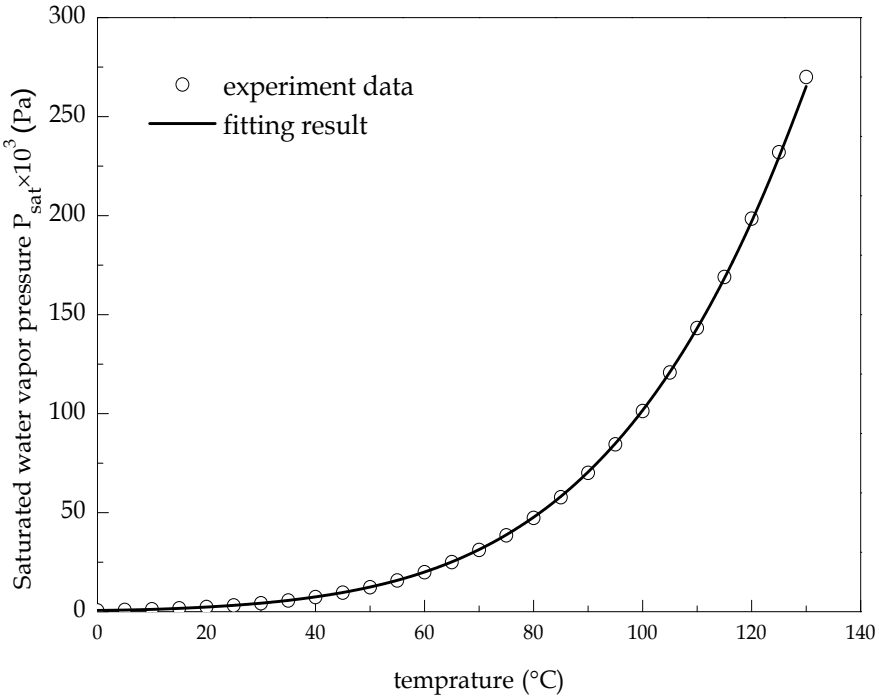

Figure 3-21 Comparison of the fitted saturated water vapour pressure with the experimental data [221]

3.6.11 Gas permeability in porous electrode and through membrane

Water could diffuse through the Nafion® membrane under a pressure force. The hydraulic permeability of water through Nafion® membrane is associated with the membrane water content as follow [21]:

$$k_{p,M} = 2.86\times10^{-20}\lambda \quad (3\text{-}167)$$

The through-plane and in-plane permeability of gas diffusion in porous gas diffusion layer is obtained by the studies of Ismail *et al.* [225, 226], which is given in Table 3-7.

Table 3-7 Gas permeability of gas diffusion layer and catalyst layer [225, 226]

	Gas diffusion layer	Catalyst layer
Through-plane permeability (m^2)	4.97×10^{-13}	$4.97\times10^{-13}(\varepsilon_{CL}/\varepsilon_{GDL})^{1.5}$
In-plane permeability (m^2)	1.87×10^{-12}	$1.87\times10^{-12}(\varepsilon_{CL}/\varepsilon_{GDL})^{1.5}$

3.6.12 Viscosity

According to Bird [196], the viscosity of single species i can be calculated by the following equation:

$$\mu_i = 2.669\times10^{-6}\frac{\sqrt{M_i T}}{\sigma_i^2\Omega_i} \tag{3-168}$$

The viscosities of hydrogen, oxygen, nitrogen and water vapour are shown in Figure 3-22. As studied by Yaws [227], the viscosity of gas mixture μ_m (Pa s) at anode and cathode are given as:

$$\mu_m = \frac{\sum_{i=1}^{n} x_i\mu_i M_i^{0.5}}{\sum_{i=1}^{n} x_i M_i^{0.5}} \tag{3-169}$$

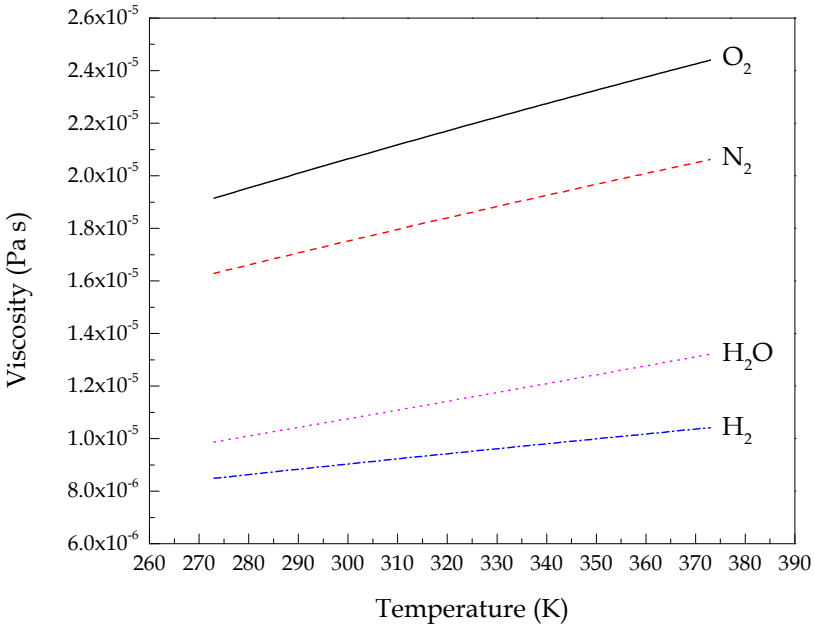

Figure 3-22 Temperature dependent gas viscosity

The temperature dependent viscosity of liquid water can be calculated by the empirical equation developed by Kestin *et al.* [228] as follow:

$$\log\left[\frac{\mu_w}{\mu_w(293K)}\right] = \frac{293-T}{T-177}\left[1.2378-1.303\times10^{-3}(293-T) + 3.06\times10^{-6}(293-T)^2 + 2.55\times10^{-8}(293-T)^3\right] \tag{3-170}$$

where $\mu_w(293K) = 1.002$ mPa s.

$\mu_w(T)/\mu_w(293K)$ obtained by Eq. (3-170) is shown in Figure 3-23. It is clear that the effect of temperature on liquid water viscosity is apparent.

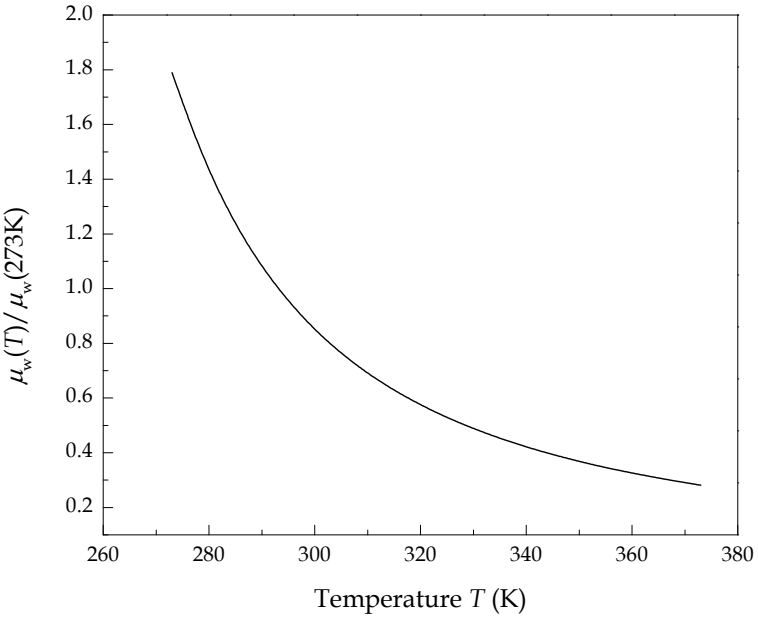

Figure 3-23 Temperature dependent liquid water viscosity [228]

3.7 Conclusions

All chemical and physical processes involved in the fuel cell can be described by proper differential and algebraic equations. In this chapter, the fundamentals and principles of a typical fuel cell are represented and the governing equations are derived.

A series of equations are developed to represent the properties of the catalyst layer, in which the porosity, agglomerate density, thicknesses of ionomer film and liquid water film, specific area can be quantitatively obtained. Both the Butler-Volmer and agglomerate structure based equations are developed for the reaction kinetics. For the most important transport process in PEMFC operation, the water phase transfer and transport processes are described by a second order partial differential equation (PDE). The membrane and ionomer swelling is associated with their water content.

The majority of the parameters used are treated as dependent variables, which expand the model limits of applicability as the model will be valid at different operating conditions.

Chapter 4. Single-phase flow isothermal model

In this chapter, the aim is to develop a two dimensional, along the channel, single-phase flow, isothermal, steady state model based on a spherical-agglomerate catalyst structure combined with the comprehensive water transport mechanism, to investigate the effect of catalyst layer parameters and operating conditions on the effectiveness factor of the catalyst layer and the performance of the fuel cell. This model can give guidance for optimisation of the catalyst layer composition.

4.1 Introduction

Proton exchange membrane fuel cells (PEMFCs) are promising candidates for automotive and small stationary applications due to their high electrical efficiency, power density and durability [16, 229, 230]. Although significant improvements with respect to cell performance, stability and cost have been achieved over the past decade, some barriers still hamper the commercial use of PEMFCs. The relatively poor oxygen reduction reaction (ORR) in the cathode catalyst layer is one of the biggest obstacles holding back the PEMFC performance [182, 231-233, 239-242].

Numerous models have been developed to investigate the effect of cathode catalyst layer on the fuel cell performance, for example, ultra-thin layer [79, 91], pseudo-homogeneous [85, 236] and agglomerate [115, 232] models. The ultra-thin layer model is the simplest model requiring the least computational resource because the catalyst layer is assumed to behave as merely an interface between the gas diffusion layer and the membrane. This model gives limited insight into the effect of composition on the performance of the catalyst layer. Due to the significant difference between the ultra-thin layer structure and the real three dimensional structure of the catalyst layer, the ultra-thin layer model typically overestimates the current density output of the fuel cells.

An improved model developed by Marr and Li [85], based on the work of Bernardi and Verbrugge [21], applied a pseudo-homogeneous thin layer as the cathode catalyst structure and investigated the composition of the cathode catalyst layer, such as platinum and ionomer loading, on performance. This model indicated that good utilisation of the thin layer catalyst layer is difficult to achieve due to the greater ORR rate relative to the oxygen diffusion rate. However, this model, by assuming the void

space of the catalyst layer was fully occupied by liquid water, failed to simulate the fuel cell performance accurately under a wide range of operating condition. Broka and Ekdunge [232] compared the pseudo-homogeneous model with the agglomerate model and concluded that the latter gave a superior representation of the catalyst layers. Sun *et al.* [115] developed an improved two dimensional, across the channel, spherical agglomerate model for the PEMFC cathode. They showed that in this model both electron and proton transport were important in determining the local cathode overpotential and the electrochemical reaction rate, and that the oxygen transport resistance through the ionomer film surrounding the agglomerates was the main factor controlling the observed limiting current density. However, the presence of liquid water was not considered in this model.

Water management is an important issue in PEMFCs that use perfluorinated membrane such as Nafion®. The earliest water management models were developed by Springer *et al.* [231], Bernardi and Vebrugge [21], and Nguyen and White [77]. The first one dimensional steady state model, developed by Springer *et al.* [231], described water diffusion coefficients, electro-osmotic drag coefficients and membrane conductivity as function of water content in the Nafion® 117 membrane. The model developed by Bernardi and Vebrugge [21] used a porous electrode instead of the ultrathin film electrode which was applied by Springer *et al.* [231]. Water transport through the membrane was associated with hydraulic pressure and the potential gradients. This model gave comprehensive profiles of concentration, pressures and water velocity through the membrane electrode assembly (MEA) including the catalyst layers and membrane. Heat management was combined with water management in the model developed by Nguyen and White [77]. The model focused on the effect of gas inlet humidity on the cell performance in which water migration and back diffusion accounted for the net water flux through the membrane. However, the effect of hydraulic permeation through the membrane was not included. Ge and Yi [234] developed a two dimensional steady state model to describe water transport through the membrane with fuel and oxidant gases in co-flow and counter-flow modes. In this model, three water transport mechanisms: electro-osmotic drag, back diffusion and hydraulic permeation were all considered. This so-called combinational model was successfully applied in previous work [79, 108, 235-237].

Although previous models have given several important insights for optimisation of the electrode composition and operating conditions, in order to improve the accuracy and reliability of the simulation results under various practical conditions, the hydrogen oxidation reaction (HOR) at anode need to be introduced into the model simultaneously when investigating the cathode.

4.2 Model description

4.2.1 Computational domain and assumption

The three dimensional representation of a typical PEMFC unit is shown in Figure 4-1(a), which includes the bipolar plates, gas flow channels (domain 1), gas diffusion layers (domain 2) and catalyst layers (domain 3) on both the anode and cathode and a electrolyte membrane (domain 4) in between. The two dimensional computational domain in this model, plane Z1 in Figure 4-1(a), is represented in detail in Figure 4-1(b). This plane is located in the middle of flow channels, on which the reactant flow direction is counter-flow. The geometric parameters and material properties of each layer are listed in Table 4-1.

In addition to the general assumption discussed in Chapter 3, the model features and main assumptions in this particular model are listed as follows:

1. Reactant gases at both anode and cathode are treated as ideal gases and transport is by diffusion and convection.

2. The membrane is non-permeable to hydrogen, oxygen and nitrogen. Only dissolved water and protons for species transport are accounted for in the membrane.

3. Liquid water is not included in this model. The product water in the cathode catalyst layer is generated as water vapour.

4. Catalyst layers are constructed from spherical agglomerates, which are covered by ionomer films only.

5. Membrane/ionomer swelling is not addressed.

6. Counter-flow mode of reactant gases is applied.

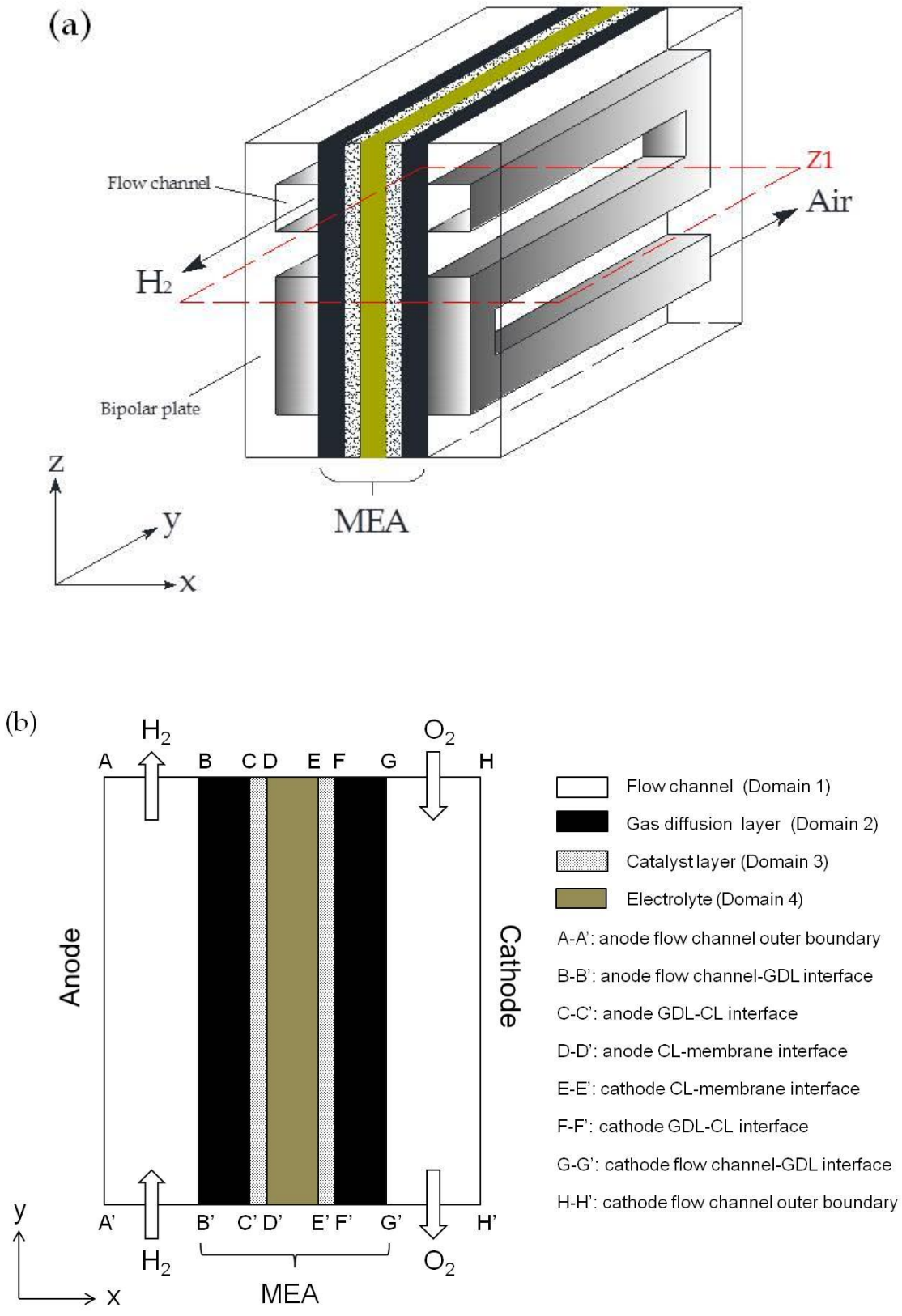

Figure 4-1 Sketch of a typical PEMFC (a) 3D representation (b) 2D computational domain Z1

Table 4-1 Geometric parameters and material properties of a PEMFC

Parameters	*Value*	*Reference*
Flow channels (Domain 1)		
Width, w (mm)	1.0	assumed
Depth, d (mm)	1.0	assumed
Length, l (mm)	10.0	assumed
Gas diffusion layer (Domain 2)		
Thickness, l_{GDL} (μm)	380	assumed
Porosity, ε_{GDL}	0.4	[182, 239]
Conductivity, σ_{GDL} (Ω^{-1} m^{-1})	1250	[216]
Permeability, $k_{p,GDL}$ (m^2)	4.97×10^{-13}	[226]
Platinum density, ρ_{Pt} (kg m^{-3})	2.145×10^{4}	[182]
Carbon density, ρ_C (kg m^{-3})	1800	[182]
Equivalent weight of ionomer, EW (g mol^{-1})	1100	[77]
Density of the dry membrane, ρ_M (kg m^{-3})	2.0×10^{3}	[77]
Catalyst layer (Domain 3)		
Thickness, l_{CL} (μm)	15.0	assumed
Porosity, ε_{CL}	Eq. (3-42)	calculated
Specific area, a_{agg} (m^{-1})	Eq. (3-68)	calculated
Conductivity, σ_M^{eff} (Ω^{-1} m^{-1})	Eq. (3-143)	calculated
Permeability, $k_{p,CL}$ (m^2)	$4.97\times10^{-13}(\varepsilon_{CL}/\varepsilon_{GDL})^{1.5}$	[181, 226]
Membrane (Domain 4)		
Thickness, l_M (μm)	120	assumed
Conductivity, σ_M (Ω^{-1} m^{-1})	Eq. (3-190)	calculated
Permeability, $k_{p,M}$ (m^2)	Eq. (3-212)	calculated

4.2.2 Governing equations

By taking all assumptions above into consideration, the governing equations described in Chapter 3 can be specified as follow to account for the particular processes in the selected domains (see Table 4-2).

Table 4-2 Governing equations used in the single-phase flow and isothermal model

Flow channels (Domain 1)		
Conservation of mass	$\nabla\cdot(\rho^g\mathbf{u}^g)=0$	(4-1)
Conservation of momentum	$-\nabla\cdot(\rho^g\mathbf{u}^g\mathbf{u}^g)-\nabla\cdot p-\nabla\cdot\boldsymbol{\tau}+\rho^g\mathbf{g}=0$	(4-2)
Conservation of species	$\rho^g\mathbf{u}^g\cdot\nabla w_i^g-\nabla\cdot[-\rho^g\sum_{j=1}^{N}D_{ij}(\nabla x_j^g-w_j^g)\frac{\nabla p}{p}]=0$	(4-3)
Gas diffusion layers (Domain 2)		
Conservation of mass	$\nabla\cdot(\rho^g\mathbf{u}^g)=0$	(4-4)
Conservation of momentum	$-\mathbf{u}^g\frac{\mu^{eff}}{K}-\nabla\cdot p-\nabla\cdot\boldsymbol{\tau}+\rho^g\mathbf{g}=0$	(4-5)
Conservation of species	$\rho^g\mathbf{u}^g\cdot\nabla w_i^g-\nabla\cdot[-\rho^g\sum_{j=1}^{N}D_{ij}(\nabla x_j^g-w_j^g)\frac{\nabla p}{p}]=0$	(4-6)
Conservation of charge	$\nabla(-\sigma_s^{eff}\nabla\phi_s)=\nabla(-\sigma_M^{eff}\nabla\phi_M)=0$	(4-7)
Catalyst layers (Domain 3)		
Conservation of mass	$\nabla\cdot(\rho^g\mathbf{u}^g)=0$	(4-8)
Conservation of momentum	$-\mathbf{u}^g\frac{\mu^{eff}}{K}-\nabla\cdot p-\nabla\cdot\boldsymbol{\tau}+\rho^g\mathbf{g}=0$	(4-9)
Conservation of species	$\rho^g\mathbf{u}^g\cdot\nabla w_i^g-\nabla\cdot[-\rho^g\sum_{j=1}^{N}D_{ij}(\nabla x_j^g-w_j^g)\frac{\nabla p}{p}]=M_iS_i^g$	(4-10)
Conservation of charge	$\nabla(-\sigma_s^{eff}\nabla\phi_s)=Q_s$	(4-11)
	$\nabla(-\sigma_M^{eff}\nabla\phi_M)=Q_M$	(4-12)
Membrane (Domain 4)		
Conservation of charge	$\nabla(-\sigma_M^{eff}\nabla\phi_M)=0$	(4-13)

4.2.3 Electrochemical reactions kinetics

Butler-Volmer kinetics

The volumetric current densities of both the anode and cathode based on the Butler-Volmer kinetics are obtained by substituting Eq. (3-108) into Eq. (3-12) and Eq. (3-13) as follow:

$$i_a = a_{CL} i_{0,a}^{ref} \left(\frac{p_{H_2}}{H_{H_2} c_{H_2}^{ref}}\right)^{0.5} \left[\exp\left(\frac{-(1-\alpha_a)F\eta_a}{R_g T}\right) - \exp\left(\frac{\alpha_a F \eta_a}{R_g T}\right)\right] \tag{4-14}$$

$$i_c = a_{CL} i_{0,c}^{ref} \frac{p_{O_2}}{H_{O_2} c_{O_2}^{ref}} \left[\exp\left(\frac{-\alpha_c F\eta_c}{R_g T}\right) - \exp\left(\frac{(1-\alpha_a)F\eta_c}{R_g T}\right)\right] \tag{4-15}$$

where $c_{H_2}^{ref}$ $c_{O_2}^{ref}$ (mol m^{-3}) are the reference molar concentration of hydrogen and oxygen, respectively. a_{CL} (m^{-1}) is the specific area of the catalyst layer, $i_{0,i}^{ref}$ (A m^{-2}) is the exchange current density, α_i is the transfer coefficient, and η_i (V) is the overpotential. The subscript $i = a$ or c, refer to the anode and cathode, respectively.

Agglomerate kinetics

The volumetric current densities based on the agglomerate kinetics are obtained by applying Eq. (3-28) for both the anode and cathode:

$$i_{a,agg} = 2F \frac{p_{H_2}}{H_{H_2}} \left[\frac{1}{E_{agg,a} k_{agg,a}} + \frac{(r_{agg} + \delta_M)\delta_M}{a_{agg} r_{agg} D_{H_2-M}^{eff}}\right]^{-1} \tag{4-16}$$

$$i_{c,agg} = 4F \frac{p_{O_2}}{H_{O_2}} \left[\frac{1}{E_{agg,c} k_{agg,c}} + \frac{(r_{agg} + \delta_M)\delta_M}{a_{agg} r_{agg} D_{O_2-M}^{eff}}\right]^{-1} \tag{4-17}$$

The first terms in the brackets of Eq. (4-16) and Eq. (4-17) represent the effect of mass transport within the agglomerate and the second terms represent the mass transport resistance resulting from the ionomer film surrounding the agglomerate. If no ionomer film is formed, the second terms are ignored then Eq. (4-16) and Eq. (4-17) can be simplified to:

$$i_{a,agg} = 2F E_{agg,a} k_{agg,a} \frac{p_{H_2}}{H_{H_2}} \tag{4-18}$$

$$i_{c,agg} = 4F E_{agg,c} k_{agg,c} \frac{p_{O_2}}{H_{O_2}} \tag{4-19}$$

Due to the weak dependence of the anode charge transfer coefficient, anode reference exchange current density and hydrogen solubility on temperature, these parameters are assumed as constant over the operating temperature range. The electrochemical parameters used in this model are listed in Table 4-3.

Table 4-3 Electrochemical parameters used in this model

Parameters	*Anode*	*Cathode*	*Reference*
Charge transfer coefficient	$\alpha_a = 0.5$	Eq. (3-107)	[21, 115, 208]
Reference exchange current density (A cm^{-2})	$i_{0,a}^{ref} = 1.0$	Eq. (3-109)	[21, 85, 208]
Equilibrium potential (V)	$\varphi_a^{eq} = RT \ln[\frac{p_{H_2}}{c_{H^+}^2}]$	Eq. (3-124)	[208, 226]
Henry's constant (Pa m^3 mol^{-1})	$H_{H_2} = 4.56 \times 10^3$	Eq. (3-131)	[21, 85]
Hydrogen reference concentration (mol cm^{-3})	$c_{H_2}^{ref} = 5.64 \times 10^{-5}$	----------	[21]
Oxygen reference concentration (mol cm^{-3})	----------	$c_{O_2}^{ref} = 3.39 \times 10^{-6}$	[21]

4.2.4 Polarisation curves

The overpotential η_i (V) for each electrode is defined as:

$$\eta_i = \phi_s - \phi_M - E_i^{eq} \tag{4-20}$$

where ϕ_s (V) is the solid phase potential, ϕ_M (V) is the electrolyte phase (ionomer) potential and E_i^{eq} (V) is the reference potential of the electrode. E_a^{eq} is zero at standard condition (T = 25 °C, $p_{H_2} = 1.0$ atm, $c_{H^+} = 1.0 \times 10^{-7}$ M) for the anode and E_c^{eq} equals the equilibrium cell potential for the cathode. Due to the relative high current conductivity of the electrode, the ohmic resistance is neglected. Therefore, the cell voltage E^{cell} (V) is obtained from the membrane resistance, current density and overpotential shown as follow:

$$E^{cell} = E^0 - \eta_a - |\eta_c| - i_M R_M \tag{4-21}$$

where E^0 (V) is the open circuit potential (OCP) of the fuel cell.

4.2.5 Gas transport within the catalyst layers

As described in Section 3.1.2, reactant gases firstly transport through the secondary pores to the outer boundary of the ionomer films surrounding the agglomerate. The

effective diffusion coefficient of species *i* through the secondary pores, corrected by the Bruggman relationship [85, 231, 232, 239], is:

$$D_{i,s}^{eff} = \varepsilon_s^{1.5} D_{i-P}^0 \tag{4-22}$$

Secondly, reactant gases must diffuse through the ionomer films and reach the inner boundary of the films. Finally, reactant gases transport through the primary pores inside the agglomerates to the surface of the platinum particles. As assumed in Section 3.2, the agglomerates inside the catalyst layers consist of three components namely, platinum dispersed carbon (*Pt/C*), ionomer and primary pores. As a consequence of the fact that ionomer and primary pores are the media for gas transport, the overall transport coefficient of gas species *i* within the agglomerates is:

$$D_{i,p}^{eff} = (\varepsilon_{agg,M})^{1.5} D_{i-M}^0 + (\varepsilon_{agg,p})^{1.5} D_{i-P}^0 \tag{4-23}$$

In Eq. (4-20) and Eq. (4-21), ε_s is the porosity of the secondary pores, $\varepsilon_{agg,M}$ and $\varepsilon_{agg,p}$ are the volume fractions of ionomer and primary pores within the agglomerate, respectively. Their expressions were given in Section 3.2. By taking the Knudsen diffusion into account, the equivalent diffusion coefficient of species *i* in the void space is:

$$\frac{1}{D_{i-P}^0} = \frac{1}{D_{i-g}^0} + \frac{1}{D_{Kn,i}} \tag{4-24}$$

where the intrinsic diffusion coefficient D_{i-g}^0 and Knudsen diffusion coefficient $D_{Kn,i}$ of species *i* were described in detail in Section 3.5.6.

4.2.6 Property of the catalyst layer

The properties of the catalyst layer were studied in Section 3.2. In this section, the catalyst layer porosity (ε_{CL}), agglomerate density (N_{agg}), volume fraction of secondary pores (ε_s), thickness of the ionomer film (δ_M), catalyst layer specific area (a_{CL}) and agglomerate specific area (a_{agg}) are summarised as follows:

$$\varepsilon_{CL} = 1 - L_M - L_{GDL}(1-\varepsilon_{GDL}) - \frac{m_{Pt}}{l_{CL}}\left(\frac{1}{\rho_{Pt}} + \frac{1-f}{f}\frac{1}{\rho_C}\right) \tag{4-25}$$

$$N_{agg} = \frac{3L_{Pt/C}}{4(1-\varepsilon_{CL})\pi r_{agg}^3} \tag{4-26}$$

$$\varepsilon_s = \varepsilon_{CL} - \frac{L_{Pt/C}(\varepsilon_{CL} - \varepsilon_{agg,M})}{1-\varepsilon_{CL}} \tag{4-27}$$

$$\delta_M = r_{agg}[\sqrt[3]{\frac{(1-\varepsilon_{CL})(1-\varepsilon_{CL}-L_S)+L_{Pt/C}\varepsilon_{CL}(1-\%M)}{L_{Pt/C}}}-1] \tag{4-28}$$

$$a_{CL} = \frac{m_{Pt}}{l_{CL}}(227.79f^3 - 158.57f^2 - 201.53f + 159.5)\times 10^3 \tag{4-29}$$

$$a_{agg} = \frac{m_{Pt}(1-\varepsilon_{CL})}{L_{Pt/C}l_{CL}}(227.79f^3 - 158.57f^2 - 201.53f + 159.5)\times 10^3 \tag{4-30}$$

4.2.7 Water transport through the membrane

In this single-phase flow model, the source term in Eq. (3-71), which is responsible for water phase transfer, is zero. In addition, membrane swelling is neglected. At a steady state condition, Eq. (3-71) is therefore simplified to:

$$\nabla\cdot(\frac{2.5\lambda}{22}\frac{i_M}{F}) - \nabla\cdot(\frac{\rho_M D_{w-M}}{EW}\nabla\lambda) - \nabla\cdot(\frac{k_{p,M}\rho_M}{\mu_w EW}\frac{p_{c,M}-p_{a,M}}{\delta_M}\lambda) = 0 \tag{4-31}$$

where $p_{a,M}$ and $p_{c,M}$ (Pa) are the pressures at the anode side (boundary D-D' in Figure 4-1(b)) and cathode side (boundary E-E' in Figure 4-1(b)) of the membrane, respectively. Other parameters were discussed in Chapter 3. Eq. (4-31) is used to describe the dissolved water transport through the membrane under the driving forces of electro-osmotic drag, back diffusion and hydraulic permeation.

4.2.8 Stoichiometric flow ratio

The stoichiometric flow ratio is defined as the amount of supplied reactants divided by the amount that is required by the electrochemical reaction. For the reactant gases at the anode and cathode, the stoichiometric flow ratios are given as follow:

$$\xi_a = \frac{p_a x_{H_2} Q_a}{R_g T}\frac{2F}{i^{ref}A} \tag{4-32}$$

$$\xi_c = \frac{p_c x_{O_2} Q_c}{R_g T}\frac{4F}{i^{ref}A} \tag{4-33}$$

where Q_a and Q_c ($m^3\ s^{-1}$) are the reactant flow rate of anode and cathode, respectively. i^{ref} ($A\ cm^{-2}$) is the reference current density.

4.2.9 Boundary conditions and source terms

The stoichiometric flow ratios at the anode and cathode inlet are defined as ξ_a and ξ_c at a reference current density of 1.0 A cm^{-2} while the inlet pressures at the anode and cathode are defined as p_a (Pa) and p_c (Pa), respectively. The water content on the catalyst layer-membrane boundaries of anode and cathode (D-D' and E-E' in Figure 4-1(b)) are defined as Dirichlet boundaries with the values according to Eq. (3-164). At the outlets, the species transport is assumed by convection only. The exterior boundaries of the domain are treated as solid walls. The detailed boundary conditions and source terms are defined in Tables 4-4.

4.2.10 Numerical solution

The commercial software COMSOL Multiphysics 4.2 is used to implement the fully coupled equations in the mathematical model. The key issue of successfully solving of this model is the water content (λ) due to its strong effect on all critical parameters, such as electro-osmotic drag coefficient, membrane ionic conductivity and water diffusion coefficient through the membrane. The numerical solution of all equations is based on the finite element method (FEM). The computational geometry consists of 19,672 elements, the distance between each element is known as the step. At each step, the equations accounting for different phenomena are fully coupled and computed following the schematic as shown in Figure 4-2. The calculating error is controlled lower than 10^{-5}.

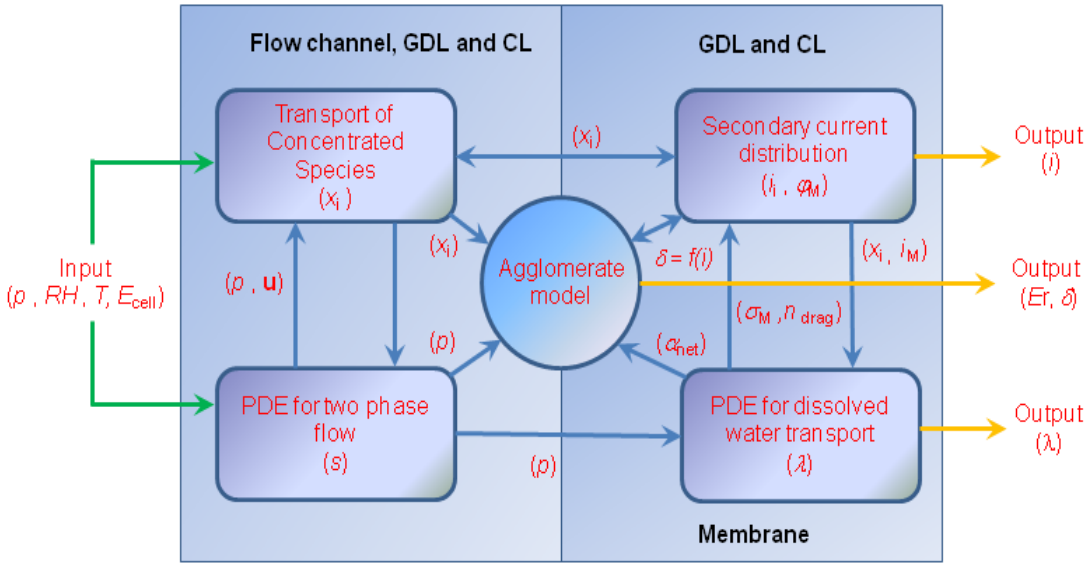

Figure 4-2 Schematic of the computational process

Table 4-4 Boundary conditions and source terms in the single-phase flow and isothermal model

Boundary or domain in Figure 4-1(b)	*Condition expressions*
Anode inlet (Boundary A'-B')	$x_{H_2O,a}=\frac{p_{sat}}{p_a}RH_a$, $x_{H_2,a}=1-x_{H_2O,a}$, $RH_a=1.0$, $\xi_a=2.0$, $p_a=1.0\,\text{atm}$
Cathode inlet (Boundary G-H)	$x_{H_2O,c}=\frac{p_{sat}}{p_c}RH_c$, $x_{O_2,c}=0.21(1-x_{H_2O,c})$, $x_{N_2,c}=0.79(1-x_{H_2O,c})$, $RH_c=1.0$, $\xi_c=2.0$, $p_c=1.0\,\text{atm}$
Gas diffusion layers (Domain 2)	$S_{H_2}=0$, $S_{O_2}=0$, $S_{H_2O}=0$
Catalyst layer (Domain 3)	$S_{H_2}=\frac{i_a}{2F}$, $S_{O_2}=-\frac{i_c}{4F}$, $S_{H_2O}=\frac{i_c}{2F}$
Anode flow channel- gas diffusion layer interface (Boundary B-B')	$\phi_s=0$
Cathode flow channel- gas diffusion layer interface (Boundary G-G')	$\phi_s=E^{cell}$
Anode outlet (Boundary A-B)	$w_{H_2}\rho u\cdot\mathbf{n}=0$
Cathode outlet (Boundary G'-H')	$w_{O_2}\rho u\cdot\mathbf{n}=0$

Note: $\mathbf{n}$ is the normal vector to the boundary.

4.3 Results and discussion

4.3.1 Experiment

The anode is made from 20% Pt/C (VulcanXC-72) with a Pt loading of 0.1 mg cm^{-2} and the cathode is made from 50% Pt/C with a Pt loading of 0.4 mg cm^{-2}, respectively. 5% Nafion® solution in di-ionised water (Sigma-Aldrich, Dorset, U.K.) is used as binder. The ionomer mass ratios are 20% in the catalyst layers of the anode and cathode. The gas diffusion layer is made of carbon paper. Taking the anode preparation as an example, the ink is made by adding a small amount of de-ionized water into Nafion® and mixing in a glass sample holder, followed by ultra-sonication for 15 min. The required amount of Pt/C catalyst and isopropanol are added to the above solution, the suspension is then placed in the ultrasonic bath for a further 30 min. The preparation is carried out at room temperature. The carbon paper is heated on a hot plate to maintain the temperature at 80 °C to 100 °C for good liquid evaporation. The ink is sprayed evenly onto the surface of the carbon paper using a Badger Model 100™ spray gun fed

by N_2 gas. The Nafion® 112 membrane is sandwiched between the cathode and the anode, and then hot pressed for 3 min at a pressure of 500 kg and temperature of 100 °C. The cell body is made of stainless steel with the active areas for both the anode and cathode of 1.0 cm × 1.0 cm. The cell is thermostatically controlled by cartridge heaters. Pure hydrogen and air are supplied as the reactants which are humidified by passing through an external humidifier. The operating conditions are fuel cell and gas inlet temperatures of 60 °C and 80 °C, gas pressure of 1.0 atm, anode and cathode gas humidity of 100%, hydrogen flow rate of 0.2 standard liters per minute (slpm), air flow rate of 0.5 slpm. Polarisation curves are recorded during at a scan rate of 10 mV s^{-1}.

4.3.2 Model validation

Figure 4-3 compares the experimental data with the results simulated by three models: the simple Butler-Volmer, agglomerate without a film and agglomerate with a film models. The parameters used for model validation and base case are listed in Table 4-5.

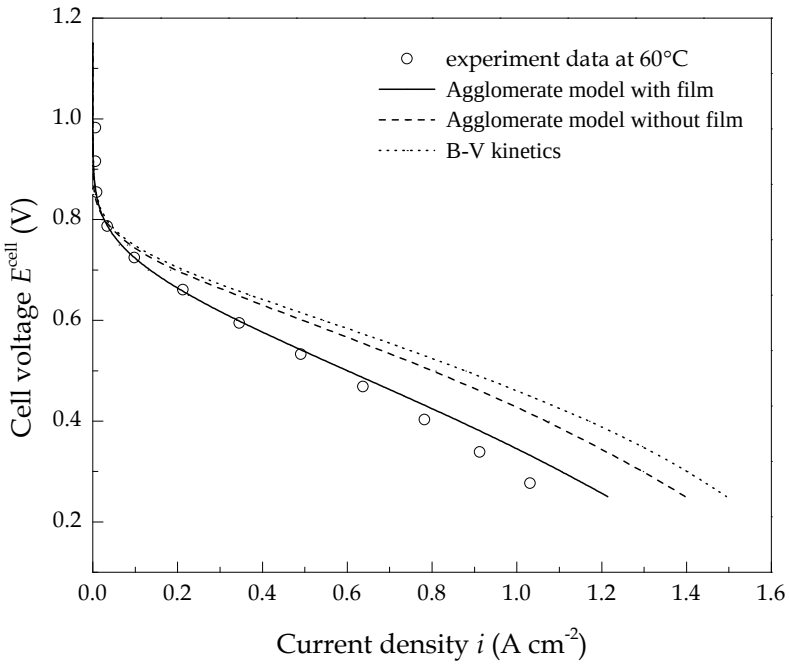

Figure 4-3 Validation of the modelling results to the experimental data
($m_{Pt,a}$ = 0.1 mg cm^{-2}, $m_{Pt,c}$ = 0.4 mg cm^{-2}, f_a = 20%, f_c = 20%, L_S = 6%, l_{CL} = 15 μm, ε_{GDL} = 40%, L_M = 13.3%, T = 60°C, p = 1.0 atm, RH = 100%, ξ_a = 19.6, ξ_c = 20.6)

It is apparent from Figure 4-3 that, due to weak mass transport resistance at higher cell voltages, all three models gives very close simulation in agreement with the experimental data. With increasing current density there is the typical fall in cell voltage.

At higher current densities there is a more rapid decrease in current density which is caused by the increase in mass transport resistance.

By accounting for the resistance of oxygen transport to the platinum surface, the agglomerate with a film model gives more accurate predictions of the polarisation curve whilst the other two models overestimate the current density.

Table 4-5 Physical parameters used in the model

Electrode parameters	*Validation*	*Base case*
Anode platinum loading, $m_{Pt,a}$ (mg cm^{-2})	0.1	0.4
Cathode platinum loading, $m_{Pt,c}$ (mg cm^{-2})	0.4	0.4
Anode platinum mass ratio, f_a	0.2	0.4
Cathode carbon loading, f_c	0.2	0.4
Agglomerate radius, r_{agg} (μm)	1.0	0.5
Catalyst layer thickness, l_{CL} (μm)	15.0	15.0
GDL thickness, l_{GDL} (μm)	300	380
Membrane thickness, l_M (μm)	55	120
GDL porosity, ε_{GDL}	40%	40%
Ionomer volume fraction, L_M	13.3%	30%
Volume fraction of solid portion, L_S	6%	6%
Cathode transfer coefficient, α_c	0.85	$0.495+2.3\times10^{-3}(T-300)$
Operating conditions	*Validation*	*Base case*
Operating temperature, T (K)	333	343
Anode pressure, p_a (atm)	1.0	1.0
Cathode pressure, p_c (atm)	1.0	1.0
Relative humidity, RH (%)	100	100
Anode stoichiometric flow ratio, ξ_a	19.6	1.2
Cathode stoichiometric flow ratio, ξ_c	20.6	2.0

4.3.3 Property of the catalyst layer

Following the model validation, the effect of the composition of the catalyst layer without ionomer swelling is studied. Three important parameters of the catalyst layer are investigated, namely porosity (ε_{CL}), agglomerate density (N_{agg}), ionomer film

thickness (δ_M). During this study, the thickness of the catalyst layer (l_{CL}), agglomerate radius (r_{agg}), ionomer volume fraction (L_M), volume fraction of ionomer in primary pores ($\%M$), and volume fraction of gas diffusion layer penetration (L_S) are held constant at 15 μm, 0.5 μm, 40%, 50% and 6%, respectively.

Porosity and agglomerate density

Figure 4-4 shows the porosity and Figure 4-5 shows the agglomerate density of the catalyst layer with varying platinum loading from 0.2 to 0.8 mg cm^{-2} and platinum mass ratio from 0.1 to 1.0, respectively. It is clear that the porosity and agglomerate density of the catalyst layer are diametrically opposed with respect to how they change with platinum loading and platinum mass ratio. At a fixed platinum loading, since the catalyst layer thickness is constant, the porosity increases as the platinum mass ratio increases. On the contrary, the agglomerate density decreases as the platinum mass ratio increases. The increase in porosity can be explained by the densities of the platinum particles with respect to the carbon particles. According to Eq. (3-39), the volume fraction of the solid phase ($L_{Pt/C}$) is determined by two parts: the volume fraction of platinum and carbon, which are expressed as the quotient of their mass loadings and densities ($m_{Pt}/(l_{CL}\rho_{Pt})$ and $(1-f)m_{Pt}/(l_{CL}\rho_C f)$). As shown in Table 4-1, the density of platinum is approximate twelve times bigger than carbon. The volume fraction of the solid phase is therefore mainly determined by the volume fraction of carbon. If the catalyst layer consists of the platinum particles only ($f=1$), the volume fraction of the solid phase decreases to $m_{Pt}/(l_{CL}\rho_{Pt})$. For example, the increase in platinum mass ratio from 0.3 to 0.8 decreases the volume fraction of the solid phase from 35.8% to 5.0% when the platinum mass loading and the catalyst layer thickness are fixed at 0.4 mg cm^{-2} and 15 μm, respectively. In this condition, the decrease in volume fraction of the solid phase leads to an increase in the porosity from 18.2% to 49.1% and results in a decrease in the agglomerate density from 8.4×10^{17} m^{-3} to 2.7×10^{17} m^{-3}. On the other hand, at a fixed platinum mass ratio, the porosity of the catalyst layer decreases and the agglomerate density increases as the platinum loading increases. This is because, the volume of the solid phase varies linearly with the platinum loading when the platinum mass ratio and catalyst layer thickness are fixed as constant in Eq. (3-39). For example, the increase in the platinum loading from 0.2 to 0.8 mg cm^{-2} results in the volume fraction of the solid phase increasing from 11.7% to 46.9% at fixed platinum mass ratio

and catalyst layer thickness of 0.4 and 15 μm, respectively. In this condition, the increase in the volume fraction of the solid phase result in a decrease in the porosity from 42.3% to 7.1% according to Eq. (4-25) and an increase in the agglomerate density from 3.9×10^{17} m^{-3} to 9.6×10^{17} m^{-3} according to Eq. (4-26).

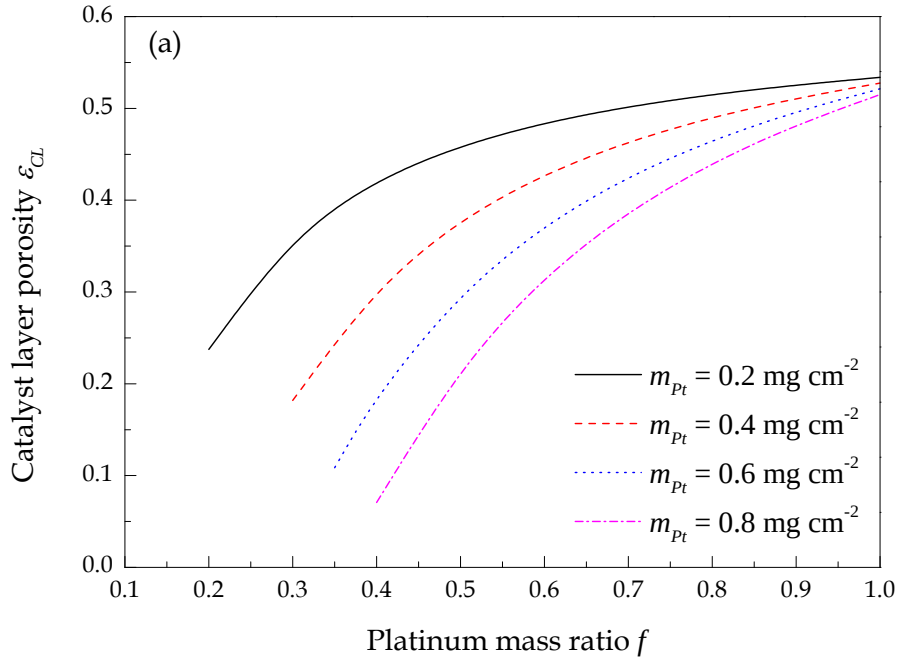

Figure 4-4 Porosities of the catalyst layer with different platinum mass ratios in base case condition

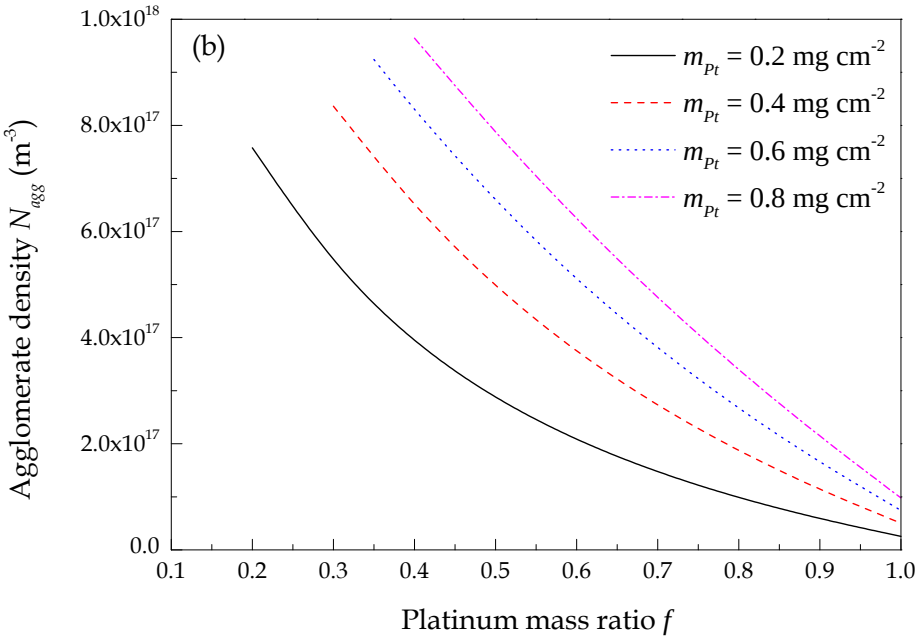

Figure 4-5 Agglomerate densities with different platinum mass ratios in base case condition

Ionomer film thickness

Figure 4-6 shows the variation of the ionomer film thicknesses with the platinum loading from 0.2 to 0.8 mg cm^{-2} and platinum mass ratio from 0.2 to 0.9, respectively. The ionomer film thickness increases as the platinum loading decreases and the platinum mass ratio increases. For example, the increase in platinum mass ratio from 0.2 to 0.8 increases the ionomer film thickness from 0.1 to 0.5 μm when the platinum loading and the catalyst layer thickness are fixed at 0.4 mg cm^{-2} and 15 μm, respectively. On the other hand, the increase in the platinum loading from 0.2 to 0.8 mg cm^{-2} decreases the ionomer film thickness from 0.7 μm to 0.3 μm when the platinum mass ratio and the catalyst layer thickness are fixed at 0.8 and 15 μm, respectively. As mentioned above, the increase in platinum mass ratio and the decrease in platinum loading result in an increase in porosity then a decrease in the volume fraction of the solid phase of the catalyst layer. It is assumed that, the ionomer firstly fills part of the primary pores of the agglomerate then the remainder covers the agglomerate forming a thin film surrounding the agglomerates. The decrease in the volume of solid phase means a decrease in the volume of primary pore. Consequently, more ionomer will occupy the secondary pores, resulting in an increase in the ionomer film thickness. Moreover, according to Eq. (4-28), the ionomer film thickness varies linearly with the agglomerate radius. The value of agglomerate radius therefore has an important influence on the ionomer film thickness and the oxygen transport resistance.

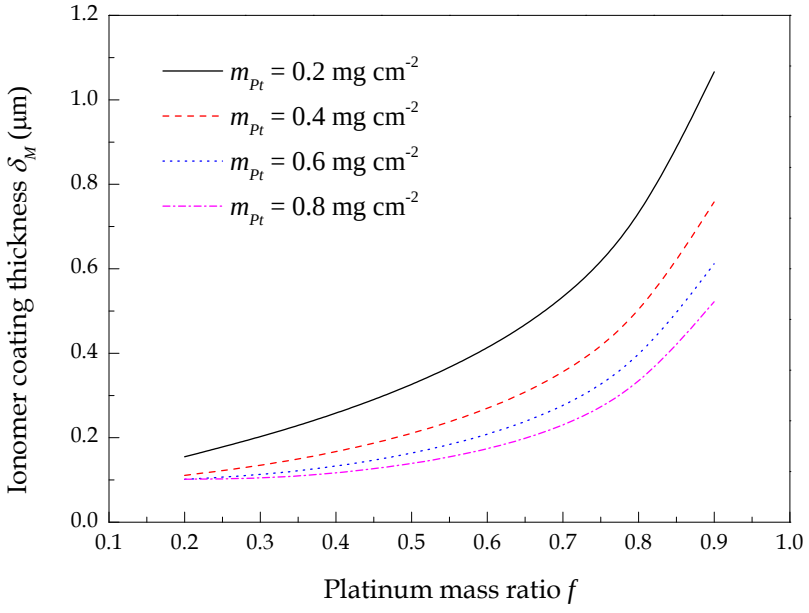

Figure 4-6 Ionomer film thicknesses with different platinum mass ratios in base case condition

4.3.4 Reactant gas distribution

The distribution of the concentration of oxygen, hydrogen and water vapour are given in the following sections. Note that the concentrations of all reactant gases are corrected by dividing by their inlet concentration.

Distribution of dimensionless oxygen concentration

The dimensionless oxygen concentration profiles in the gas diffusion layer and catalyst layer are shown in Figure 4-7. In Figure 4-7(a), the boundaries of $X = 0$ and $X = 1$ refer to the distances from CL-GDL interface (F-F') to GDL-channel interface (G-G'), while in Figure 4-7(b), the boundaries of $X = 0$ and $X = 1$ refer to the distances from membrane-CL interface (E-E') to CL-GDL interface (F-F'), respectively. In both Figure 4-7(a) and Figure 4-7(b), the boundaries of $Y = 0$ and $Y = 1$ refer to the outlet and inlet of the cathode, respectively.

Oxygen remains at a very high concentration (close to the inlet concentration) in the flow channel in the full range of cell voltages from 0.3 V to 0.9 V due to the fact that oxygen in the feed air is supplied above stoichiometric requirements. It is clear in Figure 4-7(a) that along the diffusion direction (X coordinate) through the gas diffusion layer, the dimensionless concentration of oxygen decreases from 1.0 to 0.6 as the cell voltage decreases from 0.9 V to 0.3 V. Along the flow direction (Y coordinate) through the gas diffusion layer, although the decrease of dimensionless concentration of oxygen can be neglected at higher cell voltages, it decreases from 0.6 to 0.4 at the cell voltage of 0.3 V. The decrease in oxygen concentration along both the diffusion and flow directions, especially at lower cell voltages, can be explained by the increase in oxygen consumption due to the accelerated oxygen reduction reaction (ORR) as the cell voltage decreases and the presence of oxygen transport resistance through the gas diffusion layer. Oxygen transport resistance is determined by the micro structure of the porous media only, and therefore can be considered as constant during a full range of cell voltages. As described in Section 3.1.2, the overall rate of an electrochemical reaction is determined by the rate of the slowest process involved in the coupled diffusion-reaction processes. At higher cell voltage, the rate of oxygen consumption is lower. In this condition, the oxygen transport resistance almost has no effect on the overall rate. However, at lower cell voltages, the rate of oxygen consumption becomes faster. In this condition, the oxygen transport from the flow channel to the active surface of the

catalyst particles is constrained due to the transport resistance. The overall rate of the ORR is determined by oxygen diffusion rate rather than the oxygen reaction rate in this condition.

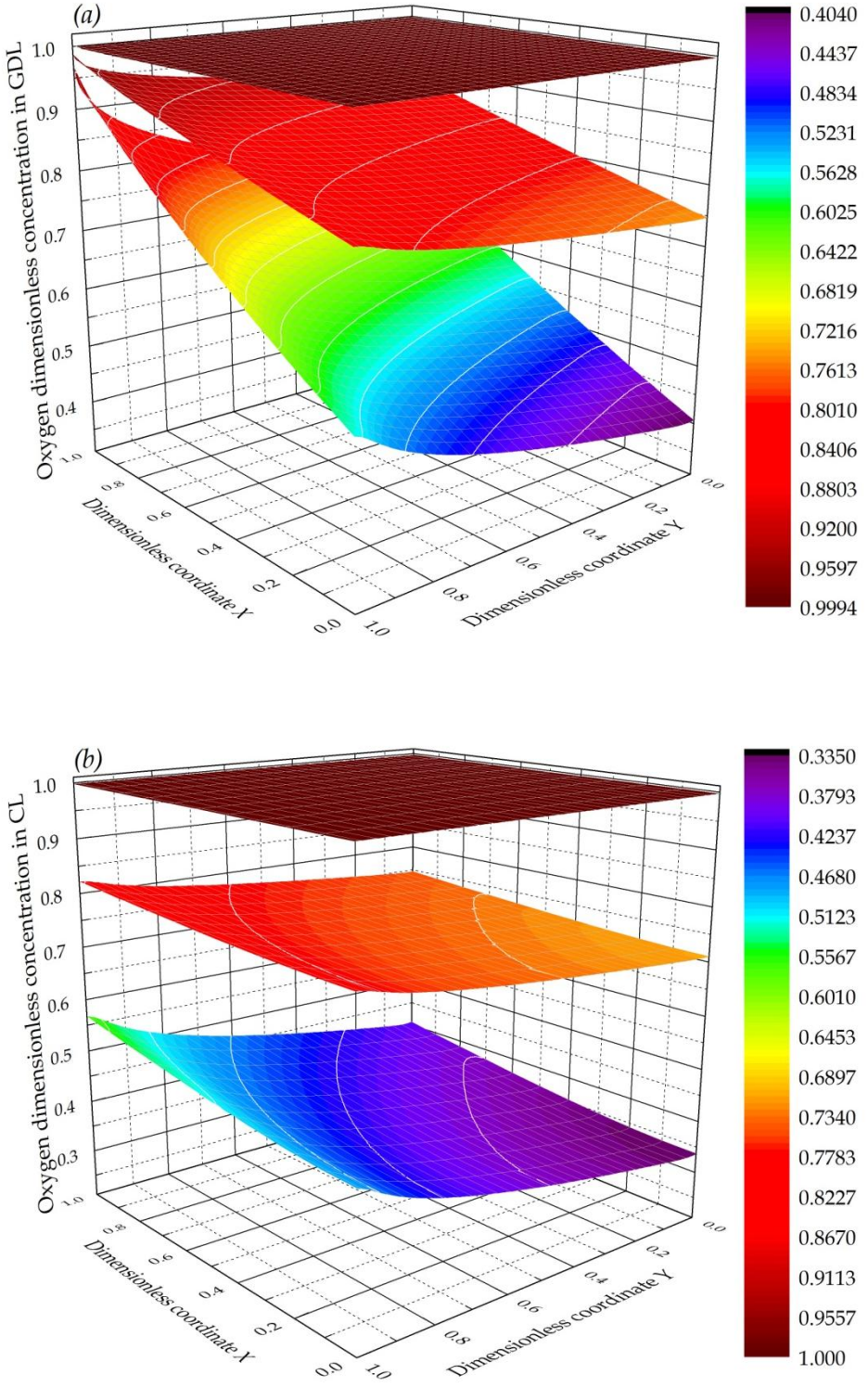

Figure 4-7 Dimensionless concentration of oxygen in gas diffusion layer (a) and catalyst layer (b) in base case condition (E^{cell} = 0.3, 0.6 and 0.9 from down up)

Figure 4-7(b) shows that oxygen concentration decreases along the diffusion direction from the boundary of GDL-CL (F-F') to CL-membrane (E-E') resulting in a lower utilisation of the active sites in the catalyst layer located near the membrane (away from the gas diffusion layer). The lower oxygen concentration near the membrane is due to two reasons: firstly, oxygen consumption by electrochemical reaction, and secondly, the oxygen diffusion resistance. At higher cell voltages, e.g. larger than 0.6 V, the oxygen concentration is mainly determined by the electrochemical reaction rate, which is lower at higher cell voltages, leading to a relative higher concentration (approximate 70%) near the membrane. However, the oxygen concentration is determined by the diffusion rate instead of the reaction rate at lower cell voltage, e.g. lower than 0.4 V. When the cell voltage decreases to 0.3 V, only 30% of the oxygen could reach the active sites located near the membrane.

Distribution of dimensionless hydrogen concentration

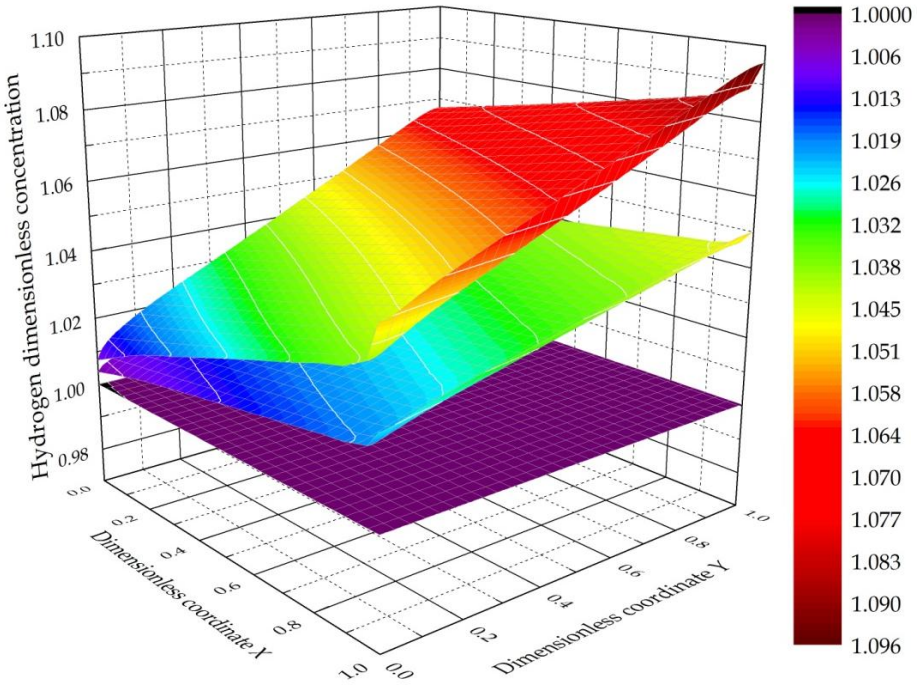

Figure 4-8 Dimensionless concentration of hydrogen in anode gas diffusion layer and catalyst layer in base case condition (E^{cell} = 0.3, 0.6 and 0.9 from up down)

The dimensionless hydrogen concentration profile in gas diffusion layer and catalyst layer are shown in Figure 4-8, in which X = 0 and X = 1 refer to the distances from channel-GDL interface (B-B') to CL-membrane interface (D-D') while Y = 0 and Y = 1 refer to the inlet and outlet of cathode, respectively. Surprisingly, rather than decreases in concentration, the hydrogen concentration remains almost at the inlet concentration at

the cell voltage of 0.9 V, and increases approximately 10% at the cell voltage of 0.3 V along the flow direction. This is because water transport through the membrane from anode to cathode increases the hydrogen fraction of the anode reactant. Especially near the anode outlet (Y=1) the greater current density takes more water molecules from anode to cathode. Although hydrogen is consumed along the flow direction by the hydrogen oxidation reaction (HOR), the decrease in hydrogen concentration is compensated by the decrease in water concentration which results in a slight increase in hydrogen concentration along the flow direction.

Distribution of dimensionless water vapour concentration

Figure 4-9 shows the dimensionless water vapour concentration profiles in the gas diffusion layer and catalyst layer of anode and cathode. The dimensionless coordinate X and Y in Figure 4-9(a) refers to the same geometry as shown in Figure 4-8. In Figure 4-9(b), coordinate Y refers to the same geometry as shown in Figure 4-7 and the boundary X=0 and X=1 refer to the distance from membrane-CL interface (E-E') to GDL-channel interface (G-G'). It is clear in Figure 4-9(a) that, as expected, the anode water vapour concentration decreases along the flow and diffusion directions as the cell voltage decreases, which dehydrates the membrane at the anode side and increases the proton transport resistance.

However, as shown in Figure 4-9(b), the water vapour concentration is higher than the inlet value in full range of cell voltages, and the maximum concentration is observed in the cathode catalyst layer near the membrane. This can be explained by two reasons. Firstly, water is produced by the oxygen reduction reaction inside the cathode catalyst layer. Secondly, water is carried by protons from anode to cathode due to the effect of electro-osmotic drag. It is important to note that water vapour will condense when it reaches the saturation level. However, water phase transfer is not included in this single-phase flow model, which will be taken into account in the two-phase flow model in Chapter 5.

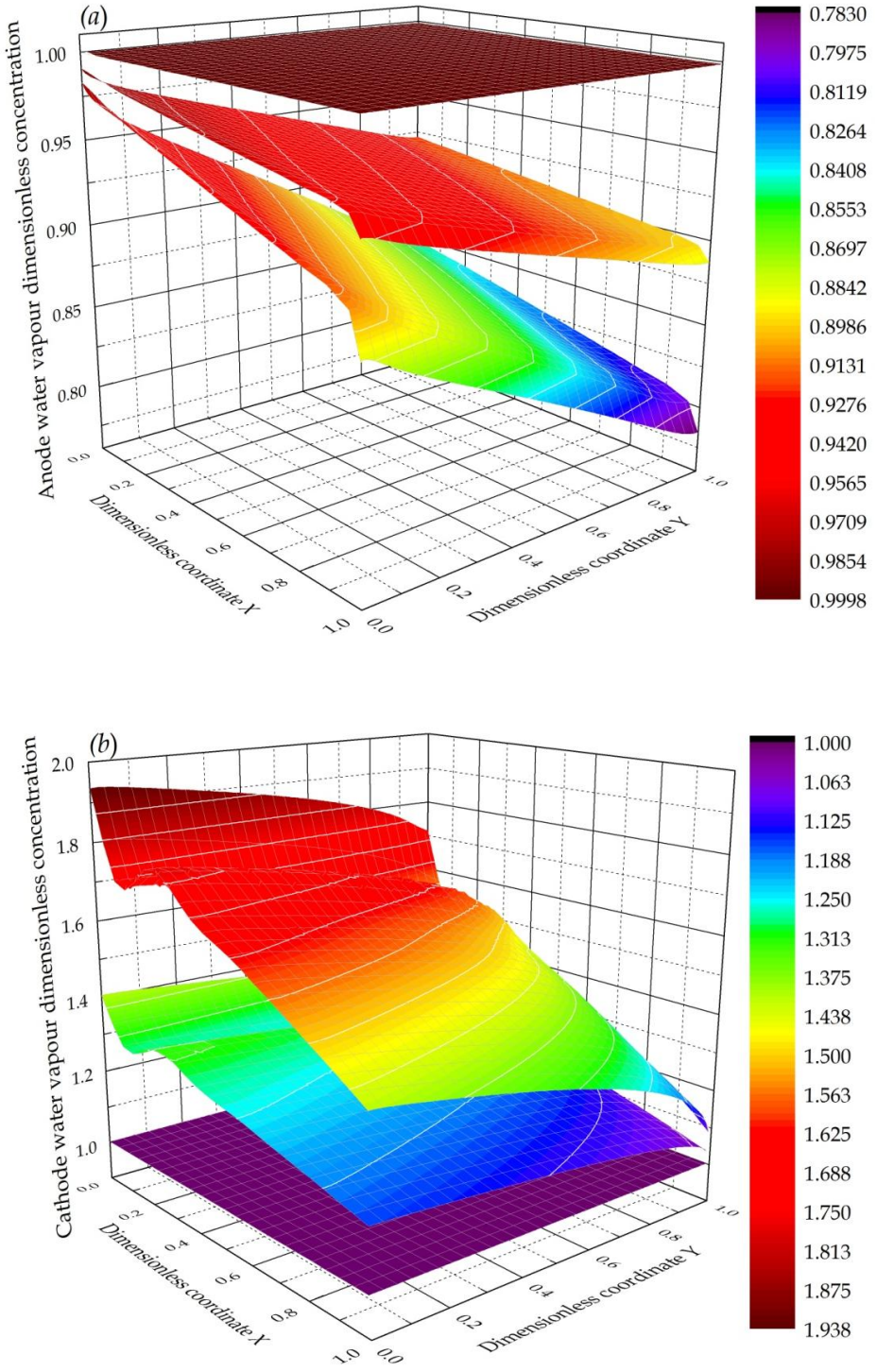

Figure 4-9 Dimensionless concentration of water vapour in the gas diffusion layer and catalyst layer of anode (a) and cathode (b) in base case condition (E^{cell} = 0.3, 0.6 and 0.9 from down up for case (a) and from up down for case (b))

4.3.5 Effectiveness factor

The distribution of the effectiveness factor of the cathode catalyst layer (E_r) at different cell voltages is presented in Figure 4-10. The coordinates *X* and *Y* refer to the same geometry as shown in Figure 4-7(b). The highest effectiveness factor

(approximately equal to 1.0) is observed at 0.9 V, and it decreases with the decrease of cell voltage from 0.9 to 0.3 V. The decrease in effectiveness factor is due to the higher reaction rate at lower cell voltages. At the cell voltage of 0.9 V, the overall rate of oxygen reduction reaction is determined by the rate of electrochemical reaction rather than the rate of oxygen diffusion. The platinum catalyst is therefore almost fully utilised leading to a very high effectiveness factor.

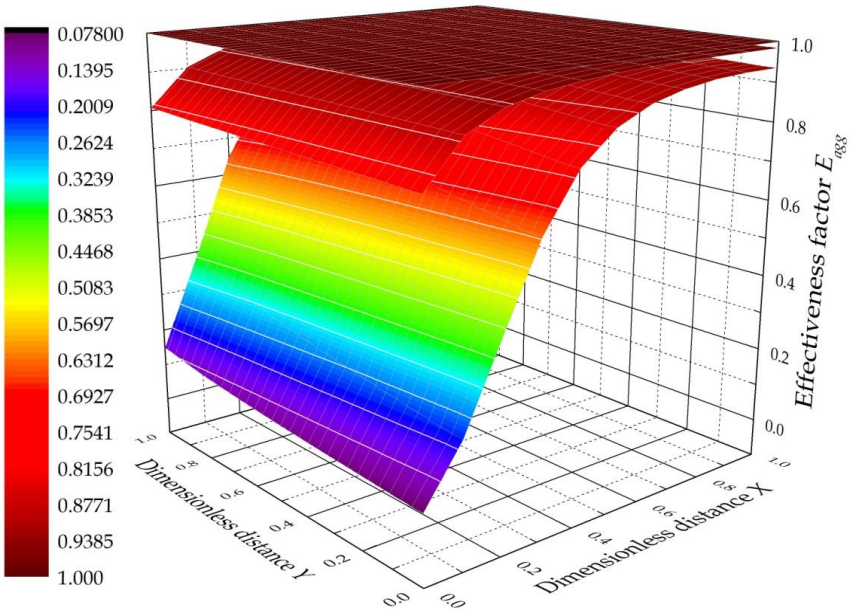

Figure 4-10 Effectiveness factor of cathode catalyst layer at three cell voltages in base case condition (E^{cell} =0.3, 0.6 and 0.9 V from down up)

As the cell voltage decreases, the increase in electrochemical reaction rate leads to faster oxygen consumption relative to the oxygen diffusion rate to the catalyst surface. The rate determining process therefore changes from electrochemical reaction to oxygen diffusion. Consequently, along the oxygen diffusion direction through catalyst layer, the catalyst utilisation is higher near the GDL-CL boundary (X=1) than that of the CL-membrane boundary (X =0). For a cell voltage of 0.3 V, corresponding to a current density of approximate 1.4 A cm^{-2}, the dimensionless effectiveness factor decreases from 0.9 at the GDL-CL boundary to 0.08 at the CL-membrane boundary. It is important to note that the change of the effectiveness factor is not pronounced along the reactant flow direction (Y direction). At 0.3 V, it only decreases from 0.15 to 0.08 along the CL-membrane boundary. This is because the geometric effect, i.e. the land and channel effect, is omitted in this the along channel model. In other words, oxygen is considered to be distributed uniformly everywhere within the cathode catalyst layer

along the flow direction in this along the channel model. In order to simplify the figure, the two dimensional effectiveness factor (E_r) can be replaced by the one dimensional average effectiveness factor ($\widehat{E}_r$).

4.3.6 Distribution of membrane water content

The distribution of membrane water content at different cell voltages is presented in Figure 4-11. At a higher cell voltage, e.g. 0.9 V, the water content distribution is almost uniform. The water content within the membrane at both the anode and cathode side is equal to their initial values, which are determined by the relative humidity of the gas inlet according to Eq. (3-164). With the decrease in cell voltage, the current density increases and leads to a water transport through the membrane from anode to cathode. As shown in Figure 4-11, the decrease in cell voltage from 0.9 to 0.6 V results in a slight water content distribution along the reactant flow direction (Y direction). However, the cell voltage decreases from 0.6 to 0.3 V leads to a non-uniform water content distribution along both the diffusion and flow directions. This indicates more water transport through the membrane from anode (X = 0) to cathode (X = 1) and more water movement from cathode inlet (Y = 1) to the cathode outlet (Y = 0) along the air flow direction as the cell voltage decreases from 0.6 V to 0.3 V. The increase in water flux through the membrane can be explained by the increase in current density within the membrane.

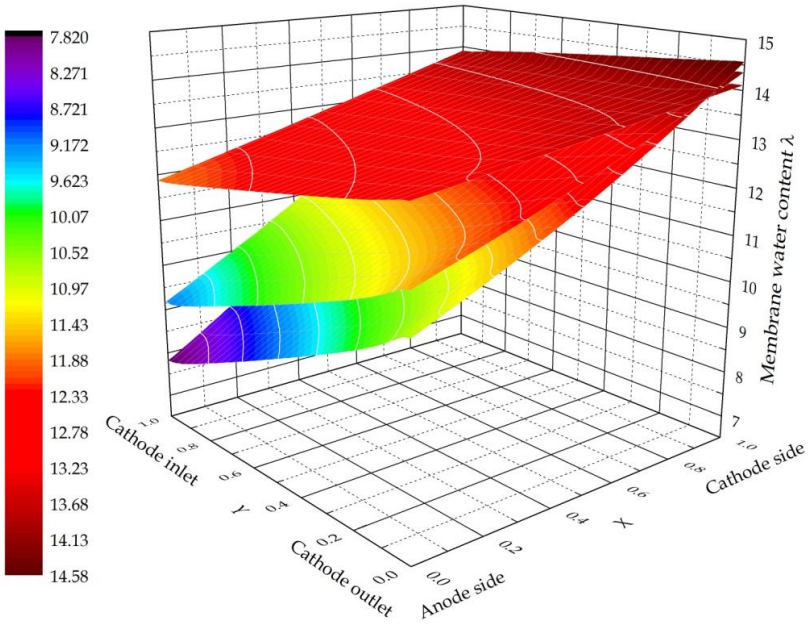

Figure 4-11 Water content distribution within the membrane at three cell voltages in base case condition (E^{cell} =0.3, 0.6 and 0.9V from down up)

The current density within the membrane is uniform when the cell voltage is higher, e.g. at 0.8 V. However, as shown in Figure 4-12, it becomes higher at the cathode outlet (Y = 0) than that at the cathode inlet (Y = 1) when the voltage decreases, e.g. from 0.6 V to 0.3 V. This is because water back diffusion from cathode to anode cannot compensate for the electro-osmotic drag at the cathode inlet (Y = 1), resulting in dehydration of the membrane on the anode side, which leads to an increase in the membrane resistance. The electro-osmotic drag flux is therefore reduced by the decreased current density within the membrane near the cathode inlet.

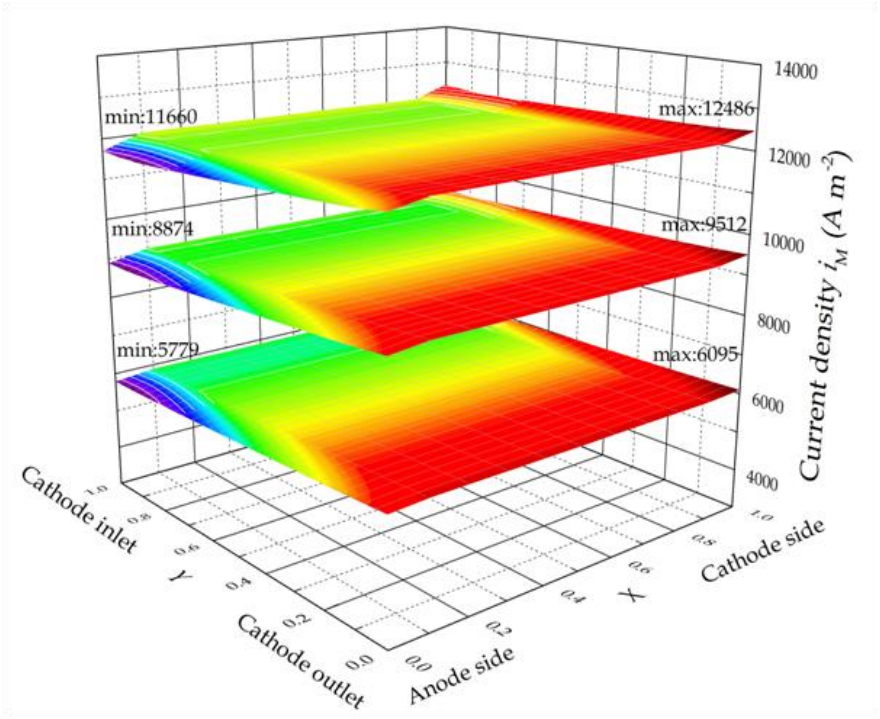

Figure 4-12 Current density distribution within the membrane with different cell voltages in base case condition (E^{cell} =0.4, 0.5 and 0.6 from up down)

4.3.7 Distribution of current density

Figure 4-13 shows the current density distributions with the catalyst layers of anode and cathode with the cell voltage varying from 0.7 to 0.3 V. These figures illustrate where the current density generated inside the catalyst layers. It is clear that the current densities in both catalyst layers of the anode and cathode increase, in other words, more current is extracted from the cell, as the cell voltage decreases. Moreover, both the current densities of the anode and cathode decrease along the reactant diffusion

direction, leading to an insufficient utilisation of the catalyst near the CL-membrane boundary ($X = 0$ for cathode and $X = 1$ for anode). On the contrary, the current densities almost maintain constants along the reactant flow direction. It is apparent that the current density distribution in the anode catalyst layer is more uniform than that in the cathode catalyst layer. In the region near the CL-membrane boundary, the anode current density is higher than the cathode current density at a fixed cell voltage. This can be explained by the relative slow oxygen reduction reaction (ORR) in the cathode. Due to the slower ORR in the cathode, the interior of the cathode catalyst layer is not fully utilised, especially in case of higher current densities are produced.

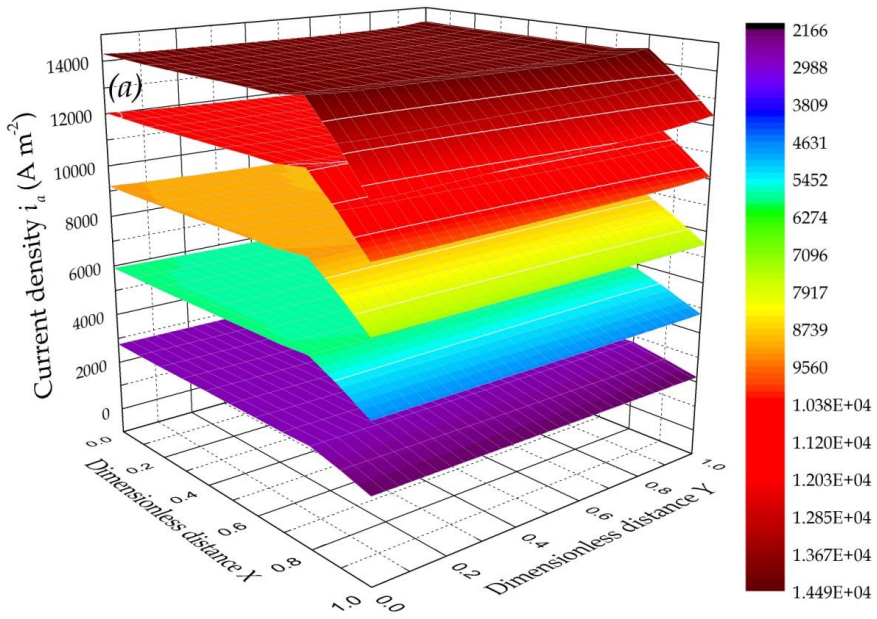

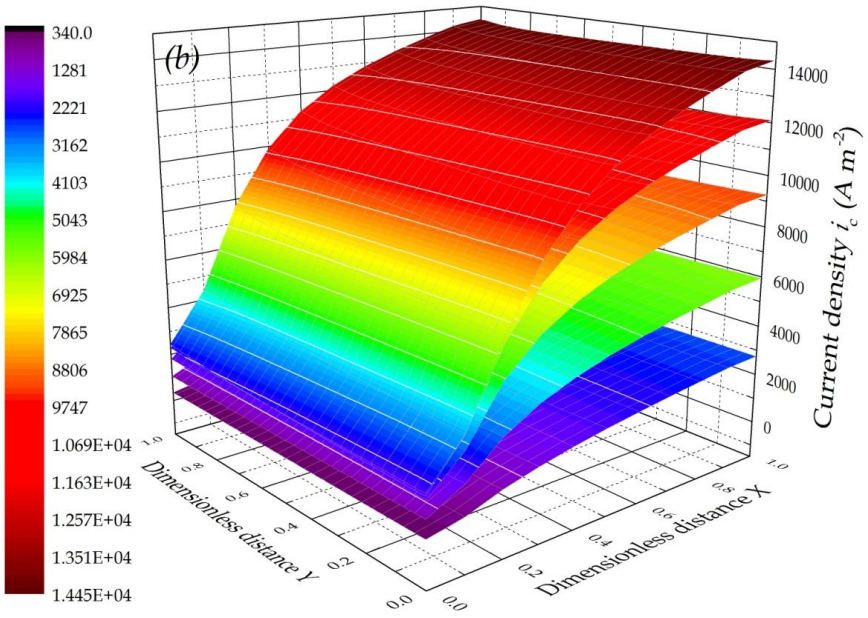

Figure 4-13 Current density distributions with the catalyst layers of anode and cathode in base case condition (E^{cell} = 0.3, 0.4, 0.5, 0.6, 0.7 from up down)

4.3.8 Effect of platinum and carbon loading

As shown in Figure 4-14, the cell performance is improved by increasing the cathode platinum loading. This improvement can be explained by the increase in reaction rate and the increase in effective specific area of the catalyst layer which can be calculated according to Eq. (3-31) and Eq. (4-30), respectively. However, this improvement is limited because, according to Eq. (3-23) and Eq. (3-24), the effectiveness factor decreases dramatically as the reaction rate increases. In other words, the increase in reaction rate leads to faster reactant consumption near the GDL-CL boundary (F-F') inside the catalyst layer, which results in insufficient utilisation of the catalyst layer near the CL-membrane boundary (E-E').

Simultaneously, the increase in platinum loading leads to a decrease in catalyst layer porosity, which is shown in Figure 4-4. The effective oxygen diffusion coefficient decreases due to the loss of void space, resulting in an increase in the mass transport resistance. As shown in Figure 4-14, the fuel cell performance improves very slightly when the platinum loading is doubled, especially at higher current densities. It is apparent that the increase in platinum loading from 0.4 to 0.8 mg cm^{-2} makes a slight contribution to the current density improvement. The optimal catalyst layer porosity, approximate 20%, is suggested by the previous numerial study of Bernardi *et al.* [21].

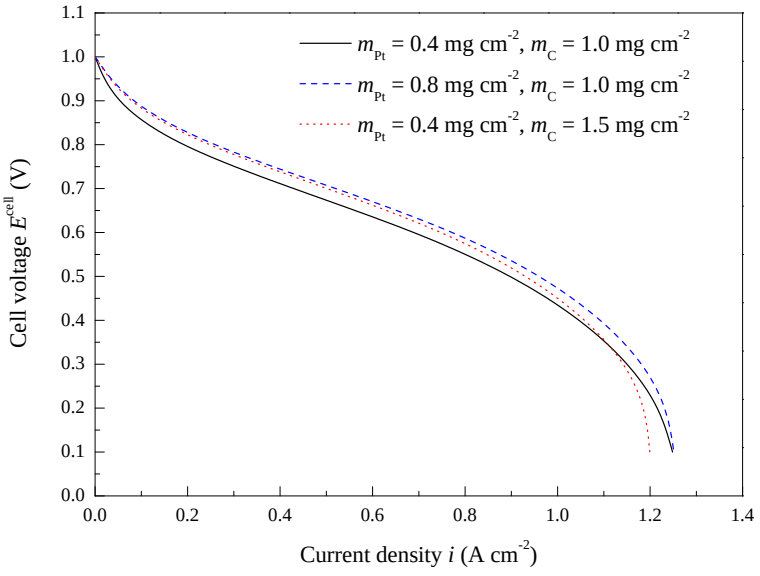

Figure 4-14 Polarisation curves for different platinum and carbon loadings in base case condition

Figure 4-15 shows the average effectiveness factors of the cathode catalyst layer with different platinum loadings. It is clear that, due to the slower transport rate of oxygen to the platinum surface, the catalysts in the interior of the catalyst layer cannot be fully utilised, which results in a decrease in effectiveness factor and thus a waste of platinum.

The effect of cathode carbon loading can be also seen in Figure 4-14. Similar to the effect of platinum loading, the increase in effective specific area and decrease in catalyst layer porosity are observed as the carbon loading increases according to Eq. (4-30) and Figure 4-4. Unlike the effect of the platinum loading, the increase in carbon loading increases the specific area rather than the reaction rate. As shown in Figure 4-14, the fuel cell performance is improved at lower current densities as the carbon loading increases from 1.0 to 1.5 mg cm^{-2}. However, it is also clear in Figure 4-4 that the increase in carbon loading decreases the catalyst layer porosity, which leads to a decrease in effective oxygen diffusion coefficient. Consequently, the cell performance is decreased at higher current densities, e.g. larger than 1.1 A cm^{-2}. In this condition, the improved fuel cell performance resulting from the increased catalyst layer specific area is offset by the decreased oxygen diffusion coefficient.

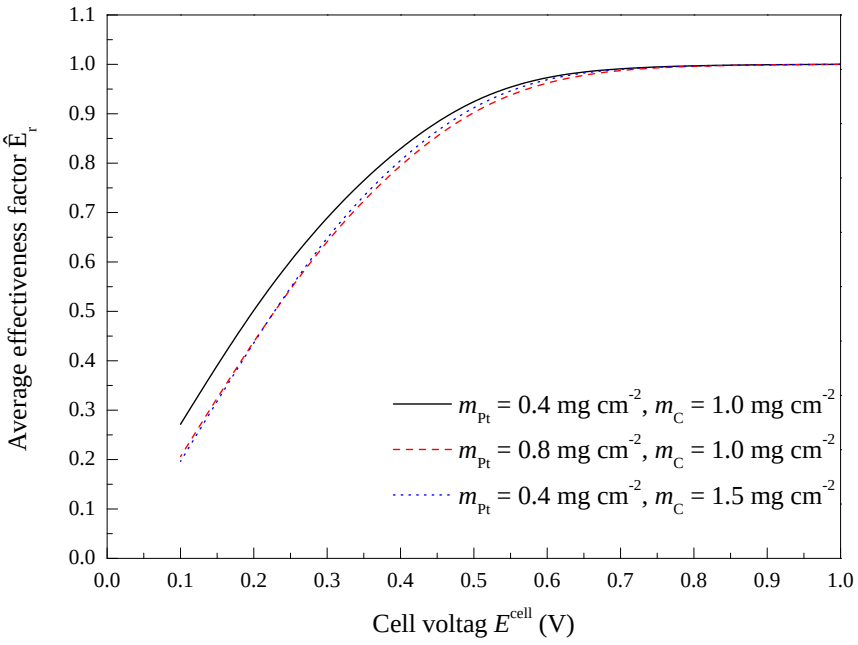

Figure 4-15 Average effectiveness factors for different platinum and carbon loadings in base case condition

In addition, the simulation results (not plotted here) show that the polarisation curves change slightly (< 5.0%) with different platinum and carbon loadings in the anode

catalyst layer. It can be concluded, the oxygen reduction reaction at the cathode plays a more important role in determining the overall performance of the fuel cell.

4.3.9 Effect of agglomerate radius

The effect of agglomerate radius on the cell performance is shown in Figure 4-16. At lower current densities, the effect of agglomerate radius is not significant because of the slower reaction rate. However, it is clear that the cell performance improves with smaller agglomerates at higher current densities. This improvement is due to two reasons. Firstly, as shown in Eq. (4-28), the ionomer film is thinner with a smaller agglomerate radius. Smaller agglomerates lead to a decrease in the ionomer film thickness, which decreases the oxygen transport resistance through the ionomer film. Secondly, smaller agglomerates increase the effectiveness factor (see Figure 4-17) which is caused by the decreased Thiele's modulus according to Eq. (3-24). Therefore, the oxygen diffusion resistance inside the agglomerate is reduced, which leads to a higher oxygen concentration on the platinum surface.

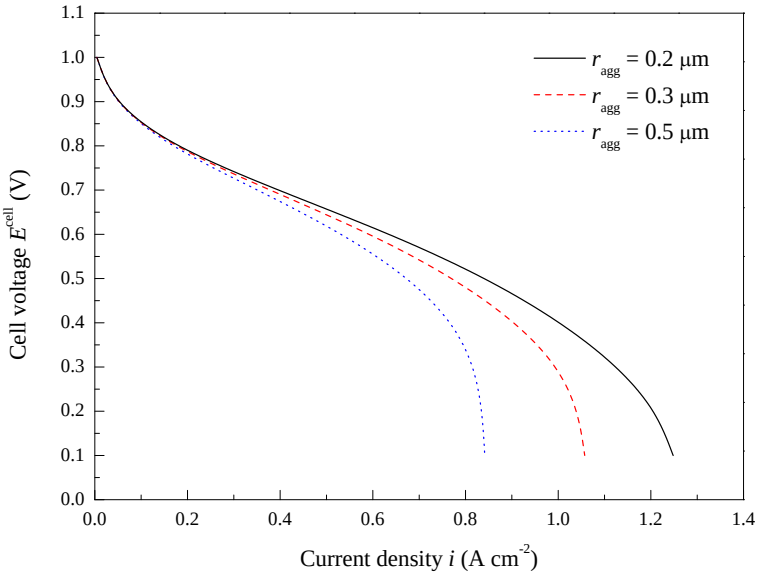

Figure 4-16 Polarisation curves for different agglomerate radius in base case condition

In Figure 4-16, the rapid decrease in current density at lower cell voltage is due to the oxygen diffusion resistance through the ionomer film surrounding the agglomerate. The larger agglomerate radius adopted, a thicker ionomer film is formed and higher oxygen diffusion resistance is obtained. If no ionomer film is generated, the expressions of current density would changes from Eq. (4-16) and Eq. (4-17) to Eq. (4-18) and Eq. (4-19), in which only the effectiveness factor is used to correct the intrinsic Buter-Volmer

kinetic. As shown in Figure 4-3, this overestimates the current density at lower cell voltages. This indicates that the oxygen transport limitation through the ionomer film is the main obstacle for improving the cell performance. Therefore, an optimal ionomer volume fraction is important. Moreover, regardless of the negative effect, such as increased oxygen transport resistance through the smaller pores inside the smaller agglomerate, a smaller agglomerate radius is of great benefit to the cell performance.

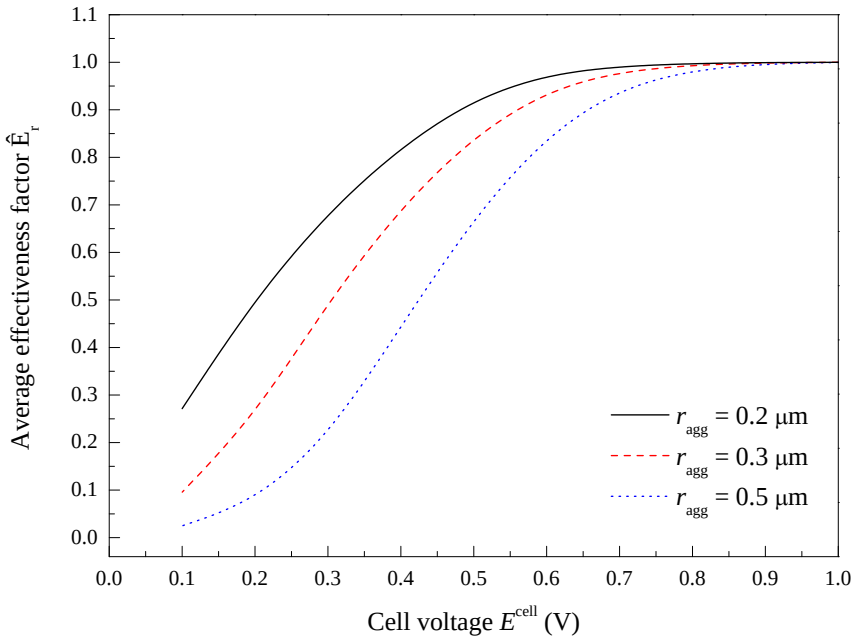

Figure 4-17 Average effectiveness factors for different agglomerate radius in base case condition

4.3.10 Effect of gas inlet pressure

The effect of gas inlet pressures on the cell performance is shown in Figure 4-18. The fuel cell is as expected performs better with higher inlet pressures, for both the anode and cathode. However, the increase in anode inlet pressure leads to a limited improvement of the cell performance, although hydrogen concentration is increased. This is due to the low polarisation losses at the anode.

On the contrary, higher cathode inlet pressure makes a significant improvement in the fuel cell performance. This is because the overall reaction rate is determined by the relative sluggish oxygen reduction reaction at the cathode. The higher oxygen partial pressure increases the dissolved oxygen into the agglomerate, resulting in a greater current density. Moreover, the higher cathode pressure to some extent prevents water migration from the anode, which results in a higher membrane conductivity.

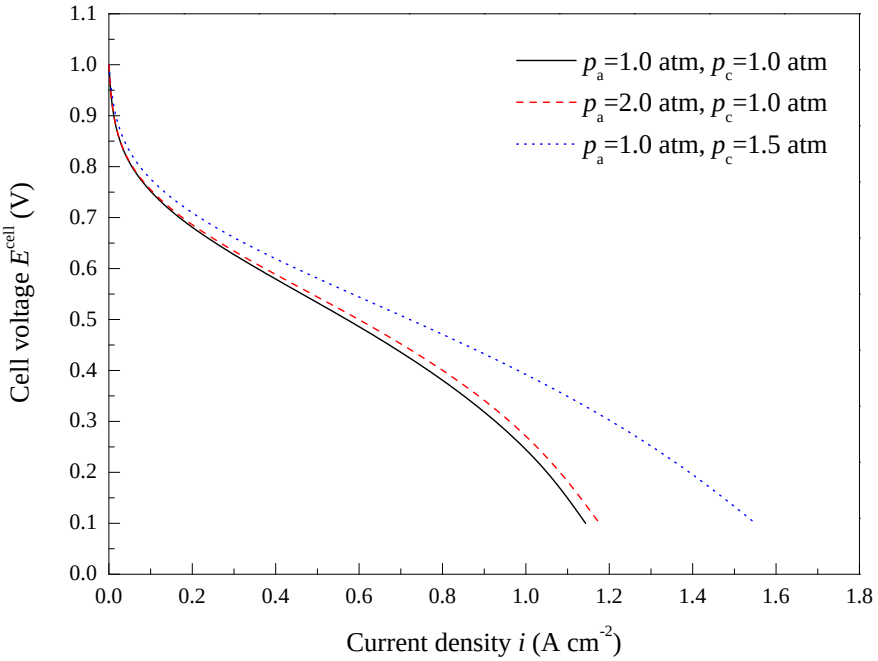

Figure 4-18 Polarisation curves for different inlet pressures compared to base case condition

4.4 Conclusions

A two dimensional, along the channel, steady state, isothermal, single-phase flow model based on an agglomerate catalyst layer structure is developed. Catalyst layer property, including porosity, agglomerate density, ionomer film thickness, and specific area, are quantitatively represented by a mathematical simulation. The presence of the ionomer film surrounding the agglomerate is the main reason for the rapid drop in the current density at lower cell voltages due to the increase in oxygen transport resistance. Higher cathode inlet pressure and platinum loading are of benefit to the cell performance. However, too much carbon loading decreases the current density at lower cell voltages. Both higher platinum and carbon loading decrease the effectiveness factor of the catalyst layer, which leads to a poor utilisation of the catalyst layer. This model gives a theoretical guidance on the effect of operating condition and catalyst layer composition to enhance the fuel cell performance and reduce the cost.

Chapter 5. Two-phase flow isothermal model

This chapter describes a two dimensional, across the channel, two-phase flow, isothermal, steady state model based on a spherical-agglomerate catalyst structure combined with a comprehensive water phase-transfer and transport mechanism. This is used to investigate the effect of catalyst layer parameters and operating conditions on membrane and ionomer swelling and then the performance of the cell. The model provides guidance for optimisation of the dry ionomer volume fraction in the cathode catalyst layer and the relative humidity of the cathode reactant gas.

5.1 Introduction

The performance of PEMFCs is particularly affected by the performance of the cathode catalyst layer, in which the relatively slow oxygen reduction reaction (ORR) occurs [76, 85, 187, 232, 260]. In order to understand the coupled kinetics and mass transport processes in the cathode catalyst layer, numerous researchers have proposed a spherical-agglomerate model as the structure of the catalyst layer of the cathode and concluded that this gives a superior representation of the porous catalyst layer compared with the ultra-thin layer model or pseudo-homogeneous film model [115, 232, 262].

Adequate hydration of the perfluorinated membrane, such as Nafion®, is critical to successful fuel cell operation. During fuel cell operation, the ionic conductivity and the structure of the membrane strongly depend on the membrane water content [187-189, 192]. The polymeric matrix of the membrane expands leading to an increase in the membrane volume when membrane water absorption (water uptake) occurs. Normally a dry Nafion® membrane swells approximately 20% when fully hydrated by water vapour [188, 192]. The membrane penetrates into the gas diffusion layer, combined with the platinum catalyst and ionomer to construct the catalyst layer. Membrane/ionomer swelling has two effects on fuel cell performance. For the membrane, higher swelling increases the membrane ionic conductivity and the water diffusion coefficient, while for the ionomer higher swelling increases the thickness of the iomomer film surrounding the agglomerate and decreases the void space within the catalyst layer, leading to an increase in species transport resistance, specifically the oxygen diffusion [188]. Numerous experimental and numerical studies [184-186] have investigated the

membrane swelling and its effect on the fuel cell performance. However, very few studies account for ionomer swelling.

Water exists as three different phases [184-186]: dissolved water in the membrane/ionomer (membrane/ionomer absorbed water), water vapour and liquid water in the porous media. The main phase transfer mechanisms include: phase transfer between liquid water and water vapour (condensation/evaporation), phase transfer between dissolved water and water vapour (membrane/ionomer absorption or water uptake), and phase transfer between liquid water and dissolved water (membrane/ionomer desorption). Water transport in the membrane plays an important role in determining the water content in the membrane/ionomer [184-188]. During fuel cell operation, water transport through the membrane occurs via three mechanisms: electro-osmotic drag of water molecules carried by protons migrating from anode to cathode, back diffusion driven by the concentration gradient of water, and convection generated by the pressure gradient. By entirely considering the three water transport mechanisms mentioned above, Ge and Yi [234] developed a two dimensional steady state model to describe water transport through the membrane with fuel and oxidant gases in co-flow and counter-flow modes. This so-called combinational water transport model was successfully applied in the literature [190, 237, 272].

The properties of the membrane, gas diffusion layer and catalyst layer play a vital role in water control. The porous electrode must have sufficient porosity to allow oxygen transport and must have sufficient hydrophobic properties to avoid liquid water build-up. Wang *et al.* [108, 191, 240, 241] described the liquid water transport by combining the so-called multi-phase mixture (M^2) approach with the volume of fluid (VOF) method. Nam and Kaviany [114] studied the distribution of water saturation in the porous media and highlighted its tendency in reducing the effective mass diffusivity. Lin *et al.* [242] introduced the agglomerate structure of the catalyst layer into the two-phase flow model and showed that liquid water flooding in the catalyst layer was more severe than that in gas diffusion layer. Consequently, catalyst layer must be considered as an individual domain rather than a segment of gas diffusion layer. The combination of agglomerate structure with the two-phase flow model was improved by Shah *et al.* [188]. In their model, liquid water was assumed to be a thin film surrounding the agglomerate. Wu *et al.* [184] and Yang *et al.* [186] developed a three dimensional water transport model by considering the phase transfer processes between water vapour, dissolved water and liquid water. However, despite the numerous two-phase flow

models available, very few have considered ionomer swelling and its effect on the PEMFC performance.

5.2 Model description

5.2.1 Computational domain and assumption

The three dimensional representation of the PEMFC has been presented in detail in Chapter 4. Different from the along the channel model shown in Figure 4-1(b), a two dimensional across the channel computational domain, plane Y1 in Figure 5-1(a), is selected. This plane is located in the middle of the cell along reactant flow direction, which is shown in detail in Figure 5-1(b). In addition to the geometric parameters in Chapter 4, the shoulder width (H_{Rib}) and the channel width (H_{Ch}) are defined as 0.75 mm and 0.5 mm, respectively. The rest of the geometric parameters and material properties in this model are same as that of the along the channel model in Chapter 4.

In the two-phase flow model, particular model features and assumptions are added as follow:

1. Ideal gas mixture.
2. Reactant crossover is omitted.
3. Spherical agglomerate structure of the catalyst layer.
4. Agglomerates are in turn surrounded by ionomer and liquid water films.
5. The shape of both the swelled membrane and the bulged GDL are half ellipses.
6. Ionomer swelling increases the thickness of the ionomer film rather than the catalyst layer.
7. Liquid water only exists in the secondary pores within cathode, which is generated by water vapour condensation and membrane/ionomer desorption.
8. Water absorbed in membrane/ionomer is in the dissolved phase, which enters the membrane/ionomer from the vapour phase during water uptake and leaves the membrane in the liquid phase when the water content reaches complete saturation. The product water in the cathode catalyst layer is generated in the dissolved phase.

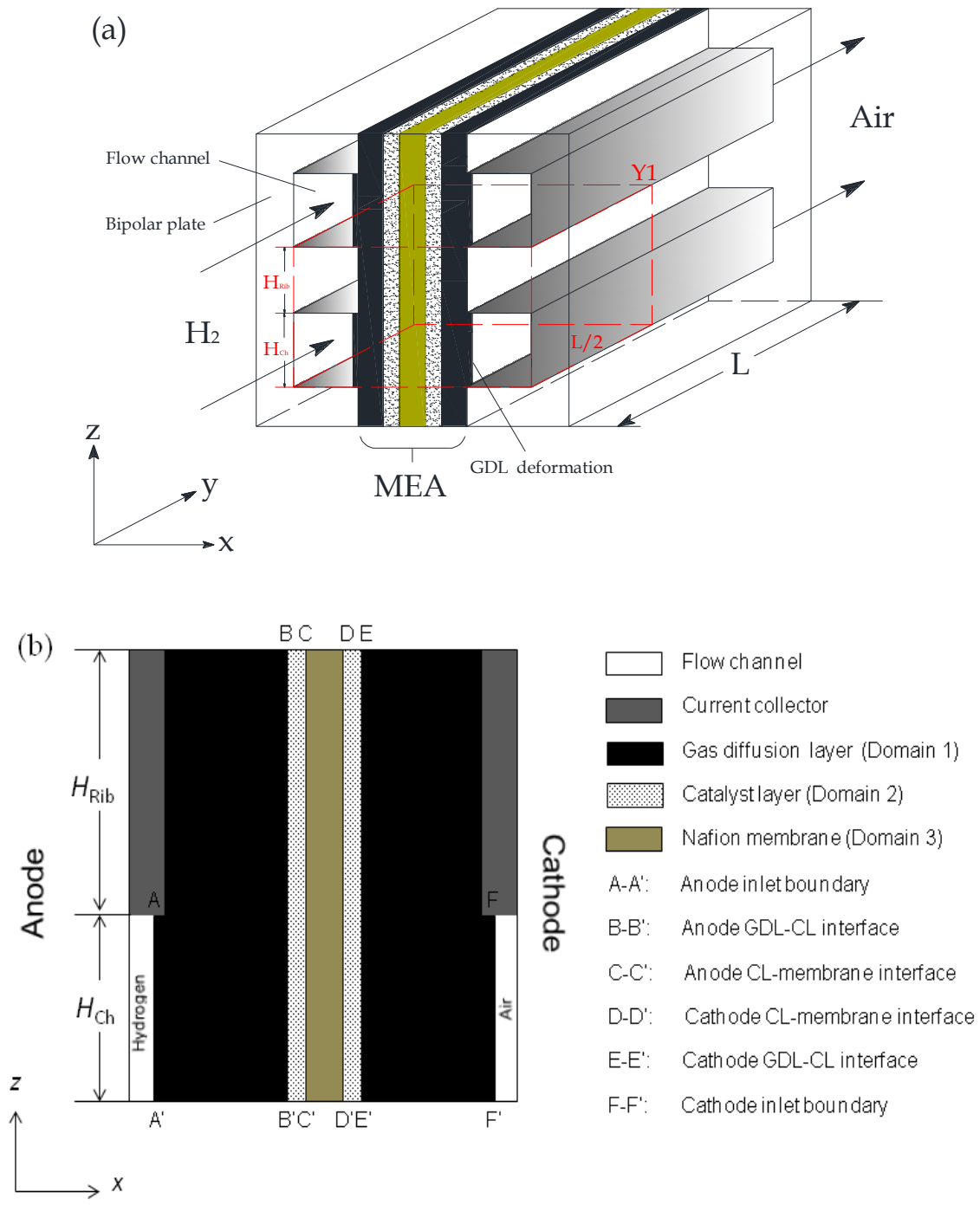

Figure 5-1 Sketch of a typical PEMFC (a) 3D representation (b) 2D computational domain Y1

5.2.2 Governing equations

Having accounted for all assumptions, the governing equations described in Chapter 3 can be specified in Table 5-1 to account for the particular processes occurred in the selected domains. Note that flow channels (Domain 1) are not included in the computational domain.

Table 5-1 Governing equations used in the two-phase flow and isothermal model

Gas diffusion layers (Domain 2)		
Conservation of mass	$-\frac{\rho^g k_p}{\mu^g}\nabla\cdot(\nabla p)=0$	(5-1)
Conservation of species	$\rho^g \mathbf{u}^g\cdot\nabla w_i^g-\nabla\cdot[-\rho^g\sum_{j=1}^{N}(1-s^{'})D_{ij}(\nabla x_j^g-w_j^g)\frac{\nabla p}{p}]=0$	(5-2)
Conservation of charge	$\nabla(-\sigma_s^{eff}\nabla\phi_s)=\nabla(-\sigma_M^{eff}\nabla\phi_M)=0$	(5-3)
Catalyst layers (Domain 3)		
Conservation of mass	$-\frac{\rho^g k_p}{\mu^g}\nabla\cdot(\nabla p)=S_m$	(5-4)
Conservation of species	$\rho^g \mathbf{u}^g\cdot\nabla w_i^g-\nabla\cdot[-\rho^g\sum_{j=1}^{N}(1-s^{'})D_{ij}(\nabla x_j^g-w_j^g)\frac{\nabla p}{p}]=M_i S_i^g$	(5-5)
Conservation of charge	$\nabla(-\sigma_s^{eff}\nabla\phi_s)=Q_s$	(5-6)
	$\nabla(-\sigma_M^{eff}\nabla\phi_M)=Q_M$	(5-7)
Membrane (Domain 4)		
Conservation of charge	$\nabla(-\sigma_M^{eff}\nabla\phi_M)=0$	(5-8)

5.2.3 Electrochemical reactions kinetics

Due to the presence of liquid water film surrounding the agglomerate, the oxygen transport resistance is increased. In order to account for the oxygen diffusion resistance through the ionomer and liquid water films, the cathode volumetric current density based on the agglomerate model is modified as follow:

$$i_{c,agg}=4F\frac{p_{O_2}}{H_{O_2}}\left[\frac{1}{E_{agg,c}k_{agg,c}}+\frac{(r_{agg}+\delta)}{\gamma r_{agg}}\right]^{-1} \tag{5-9}$$

where γ (s^{-1}) is the oxygen diffusion rate through the ionomer/liquid water film to the agglomerate interface and δ (m) is the total thickness of the ionomer and liquid water film. The rest of the parameters used in Eq. (5-9) are those used in Eq. (4-17).

$$\gamma=\frac{\gamma_M\gamma_w}{\gamma_M+\gamma_w},\ \gamma_M=\frac{a_{agg}D_{O_2-M}}{\delta_M},\ \gamma_w=\frac{a_{agg}^{'}D_{O_2-w}}{\delta_w},\ \delta=\delta_M+\delta_w \tag{5-10}$$

in which δ_M (m) and δ_w (m) are the thicknesses of the ionomer film and liquid water film, respectively. D_{O_2-M} (m^2 s^{-1}) and D_{O_2-w} (m^2 s^{-1}) are the diffusion coefficient of oxygen through iomomer and liquid water, respectively. a_{agg} (m^{-1}) is the specific area of the agglomerate without the ionomer film and $a_{agg}^{'}$ (m^{-1}) is the agglomerate with the ionomer film.

5.2.4 Gas transport within catalyst layers

Hydrogen transport in a porous anode is described as the same way by Eq. (4-22) in Section 4.2.5. However, due to the fact that the secondary pores are partially occupied by the liquid water, the effective diffusion coefficient of oxygen diffusing in the secondary pores is corrected as follow:

$$D_{O_2,s}^{eff} = [\varepsilon_s(1-s^{'})]^{1.5} D_{O_2-P} \tag{5-11}$$

where $s^{'}$ is the corrected liquid water saturation, defined as the volume fraction of the secondary pores occupied by the liquid water, and relates to s via:

$$s^{'} = s\frac{\varepsilon_{CL}}{\varepsilon_s} \tag{5-12}$$

where s is the liquid water saturation, defined as the volume fraction of the entire pores occupied by the liquid water.

According to the assumption, no liquid water exist in the primary pores, oxygen diffusion inside agglomerates is therefore described by Eq. (4-23).

5.2.5 Thickness of the liquid water film

The properties of the catalyst layer in the single-phase flow model were described in Section 4.2.5. In the two-phase flow model, the thickness of the liquid water film is included, which can be calculated by Eq. (3-65) in Chapter 3.

$$\delta_w = \sqrt[3]{(r_{agg}+\delta_M)^3 + \frac{s^{'}\varepsilon_{CL}(1-\varepsilon_{CL})r_{agg}^3}{L_{Pt/C}}} - (r_{agg}+\delta_M) \tag{5-13}$$

5.2.6 Liquid water transport

By applying the volume average approach to the continuity equation and then utilising Darcy's law for both the liquid and gas phases [100, 184, 186, 191], the governing equation for the liquid water transport is obtained as shown in Eq. (3-94). At steady state, it can be simplified as follow:

$$\nabla \cdot (\rho_w^l D_c \nabla s - \frac{\rho_w^l k_r^l \mu_w^g}{k_r^g \mu_w^l} \mathbf{u}^g) = M_w S_w^l \tag{5-14}$$

where ρ (kg m^{-3}) is the density, μ (Pa s) is the viscosity, k is the relative permeability, $\mathbf{u}$ (m s^{-1}) is the velocity vector, M (kg mol^{-1}) is the molecular weight, and S (mol m^{-3} s^{-1}) is the source term, respectively. The subscript w is liquid water, and the superscript g and l are gas phase and liquid water, respectively. D_c (m^2 s^{-1}) is the capillary diffusion coefficient, which is calculated using the following equation:

$$D_c = -\frac{k_r^l}{\mu_w^l} \sigma \cos(\theta_c)(\varepsilon k_p)^{1/2} \frac{dJ(s)}{ds} \tag{5-15}$$

in which the surface tension (σ), contact angel (θ_c), electrode porosity (ε) and permeability (k_p) were either described in Table 4-1 in Chapter 4 or in Table 5-2 in this chapter. The rest of the parameters were described in detail in Section 3.3.2.

5.2.7 Dissolved water transport

By accounting for the water phase change and membrane/ionomer swelling, the dissolved water transport at steady state condition can be described by the following equation:

$$\nabla \cdot (n_d \frac{i_M}{F}) - \nabla \cdot (D_{w-M} \nabla c_w^d) - \nabla \cdot (\frac{k_{p,M} c_w^d}{\mu_w} \nabla p) = S_w^d \tag{5-16}$$

in which the electro-osmotic drag coefficient n_d, membrane permeability $k_{p,M}$ (m^2) and water diffusion coefficient through the membrane D_{w-M} (m^2 s^{-1}), which are shown in Table 5-2, are water content dependent parameters. Nafion® membrane/ionomer swells when absorbing water until reaching the saturation level, the concentration of dissolved water depends on the water content of the membrane as follow [188]:

$$c_w^d = \frac{\rho_M}{EW}\frac{\lambda}{1+k_s\lambda} \tag{5-17}$$

when ionomer swelling, the volume fraction of the ionomer in the cathode catalyst layer increases to:

$$L_M = (1+k_s\lambda)L_M^{dry} \tag{5-18}$$

Table 5-2 Transport parameters

Parameters	*Value*	*Reference*
Membrane swelling coefficient, k_s	0.0126	[188]
Molar volume of water, V_W (m^3 mol^{-1})	1.8×10^{-5}	[190]
Molar volume of dry membrane, V_M (m^3 mol^{-1})	5.5×10^{-4}	[190]
Liquid water density, ρ_w^l (kg m^{-3})	988	[186]
Surface tension, σ (N m^{-1})	0.0625	[186, 191, 240]
Contact angel, θ_c (°)	120	[186]
Condensation rate, k_{con} (s^{-1})	100	[100]
Evaporation rate, k_{eva} (atm^{-1} s^{-1})	100	[100]
Electro-osmotic drag coefficient, n_d	$(2.5/22)\lambda$	[186, 187]
Membrane permeability, $k_{p,M}$ (m^2)	$2.86\times10^{-20}\lambda$	[21]

5.2.8 Source terms

The conservation of water in different phases, including water vapour, dissolved water and liquid water, is shown in Table 5-3.

Table 5-3 Conservation of water in different phases

	Anode GDL	Anode CL	Cathode CL	Cathode GDL
Water vapour	$S_w^v = 0$	$S_w^v = -S_{vd}$	$S_w^v = S_w^g - S_{vd}$ -	$S_w^v = -S_{vl}$
Liquid water	$S_w^l = 0$	$S_w^l = 0$	$S_w^l = S_{dl} + S_{vl}$	$S_w^l = S_{vl}$
Dissolved water	$S_w^d = 0$	$S_w^d = S_{vd}$	$S_w^d = S_{vd} - S_{dl}$	$S_w^d = 0$

Note: The unit for every source term is (mol m^{-3} s^{-1})

The source terms for reactant gas S_m in Eq. (5-4) and S_i^g in Eq. (5-5), for liquid water S_w^l in Eq. (5-14) and for dissolved water S_w^d in Eq. (5-16) are given in Table 5-4.

Table 5-4 Source terms

Source terms	*Unit*	*Domain*
$S_m = M_{H_2} S_{H_2}^g + M_{O_2} S_{O_2}^g + M_w S_w^v$	kg m^{-3} s^{-1}	All domain
$S_{H_2}^g = \frac{i_a}{2F}$	mol m^{-3} s^{-1}	Anode CL
$S_{O_2}^g = -\frac{i_c}{4F}$	mol m^{-3} s^{-1}	Cathode CL
$S_w^{rc} = \frac{i_c}{2F}$	mol m^{-3} s^{-1}	Cathode CL
$S_w^{vd} = k_{ads}(c_w^{eq} - c_w^d) \quad c_w^d < c_w^{eq}$	mol m^{-3} s^{-1}	Anode and cathode CLs
$S_w^{dl} = k_{des}(c_w^d - c_w^{eq}) \quad c_w^d \geq c_w^{eq}$	mol m^{-3} s^{-1}	Anode and cathode CLs
$S_w^{vl} = \begin{cases} k_{con}\frac{\varepsilon(1-s)x_w^g}{R_g T}(x_w^g p^g - p_{sat}) & x_w^g p^g \geq p_{sat} \\ k_{eva}\frac{\varepsilon s \rho_w^l}{M_w}(p_{sat} - x_w^g p^g) & x_w^g p^g < p_{sat} \end{cases}$	mol m^{-3} s^{-1}	Cathode CL and GDL

5.2.9 Boundary conditions

The pressures at the GDL-flow channel interfaces of anode (A-A') and cathode (F-F') are defined as p_a (Pa) and p_c (Pa), respectively. The liquid water saturation s, at the cathode GDL-flow channel interface (F-F') is also defined as the Dirichlet boundary with the value of zero, which means no liquid water in the flow channel. The water content on the CL-membrane interfaces of anode (C-C') and cathode (D-D') are defined as the Dirichlet boundaries with their values given by Eq. (3-164). The fraction of the species at the inlets of anode and cathode are calculated by the equations in Table 4-4 of Chapter 4.

5.2.10 Numerical solution

The numerical solution in this study is based on the same principle described in Section 4.2.8 in Chapter 4. The computational geometry in this across the channel model is simpler in comparison with the along the channel model. Therefore, it consists of 8040 elements, less than half of that in the along the channel model. However, by accounting for the effect of liquid water, a self developed two-phase flow module is introduced, which makes the computational process more difficult. The used equations

accounting for the different phenomena are fully coupled and are solved following the schematic shown in Figure 5-2.

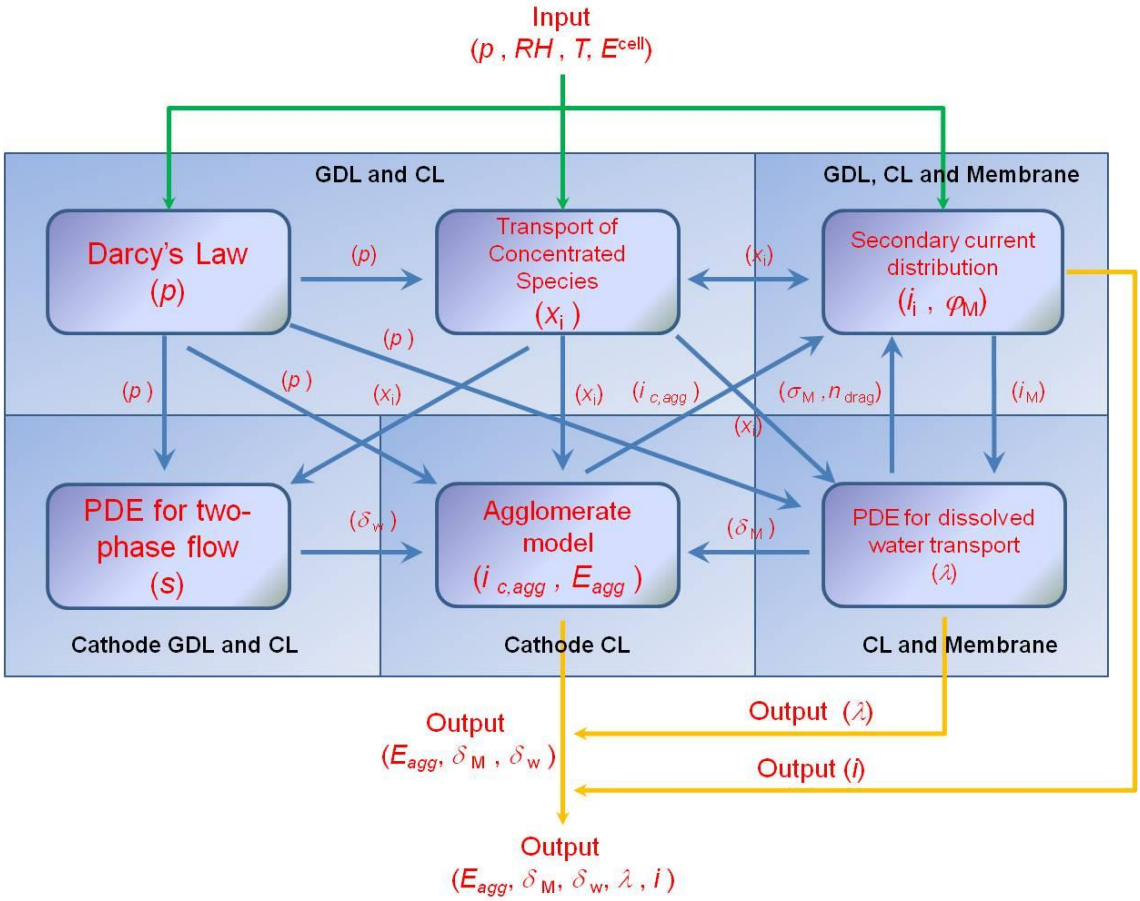

Figure 5-2 Schematic of the computational process

5.3 Results and discussion

5.3.1 Model validation

Figure 5-3 compares experimental data with the results simulated by the single-phase flow model and two-phase flow mode, respectively. In the single-phase flow model, all species are assumed to exist in the gaseous phase. However, in the two-phase flow model, the liquid water generation and transport are taken into account. The experimental data used in this chapter at 60 °C is the same as those in Chapter 4, which is obtained using a single PEM fuel cell with an active area of 1×1 cm^2. The catalyst layers are prepared with the platinum loadings of 0.1 and 0.4 mg cm^{-2} for anode and cathode, respectively. Both the mass ratios of platinum and ionomer are 20% in the catalyst layers of the anode and cathode. The operating condition is temperature at 60 °C, pressure of 1.0 atm, gas humidity of 100%. Based on the same condition, the other

group of experimental data is obtained at 80 °C. The detailed parameters of the cell and operating conditions are listed in Table 5-5.

Table 5-5 Parameters for model validation and base case condition

Symbol	Description (unit)	Validation	Base case
l_{GDL}	GDL thickness (m)	3.0×10^{-4}	3.8×10^{-4}
l_{CL}	CL thickness (m)	1.5×10^{-5}	1.5×10^{-5}
l_M	Membrane thickness (m)	5.5×10^{-5}	8.0×10^{-5}
ε_{GDL}	GDL porosity	40%	40%
m_{Pt}	Platinum loading (mg cm^{-2})	0.40	0.40
f	Platinum mass ratio	20%	40%
L_M^{dry}	Volume fraction of dry membrane	13.3%	30%
T	Operating temperature (°C)	60, 80	70
p	Operating pressure (atm)	1.0	1.0
α_c	Cathode transfer coefficient	0.85 (60 °C) 0.95 (80 °C)	$0.495+2.3\times10^{-3}(T-300)$
r_{agg}	Agglomerate radius (μm)	1.0	0.5
RH	Relative humidity (%)	100%	100%

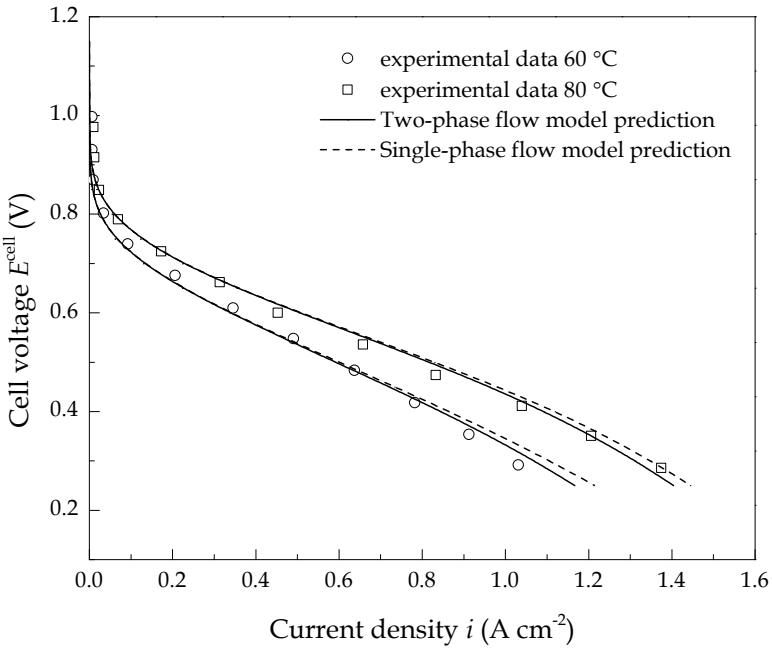

Figure 5-3 Validation of the modelling results to the experimental data at 60 °C and 80 °C ($m_{Pt,a}$ = 0.1 mg cm^{-2}, $m_{Pt,c}$ = 0.4 mg cm^{-2}, f_a = 20%, f_c = 20%, L_S = 6%, l_{CL} = 15 μm, ε_{GDL} = 40%, L_M = 13.3%, T = 60°C, p = 1.0 atm, RH = 100%)

It is apparent from Figure 5-3 that, due to the weak mass transport impact at higher cell voltages (i.e. lower current densities), the two models give very close simulation results in agreement with the experimental data. With increasing current density there is the typical decrease in cell voltage. At higher current densities there is a rapid fall in cell voltage caused by mass transport restrictions. By accounting for the increase in mass transport resistance resulting from membrane and ionomer swelling and considering the void space loss due to liquid water occupation (flooding), the two-phase flow model gives reasonable predictions of the polarisation curve.

Normally, membrane swelling has a significant impact on the species transport as the gas diffusion layer bulges into the channel while ionomer swelling leads to an increase in the volume of ionomer and a decrease in the porosity of the cathode catalyst layer. Considering the membrane and ionomer swelling into the two-phase flow model gives an accurate simulation of the current densities. Similar results can be found in a semi-empirical model developed by Choi and Bae [244].

5.3.2 Liquid water film thickness

In addition to the properties of the catalyst layer discussed in Section 4.3.3 of Chapter 4, the variation in liquid water film thicknesses with the liquid water saturation from zero to 1.0 and the platinum mass ratio from 0.3 to 0.8 are shown in Figure 5-4.

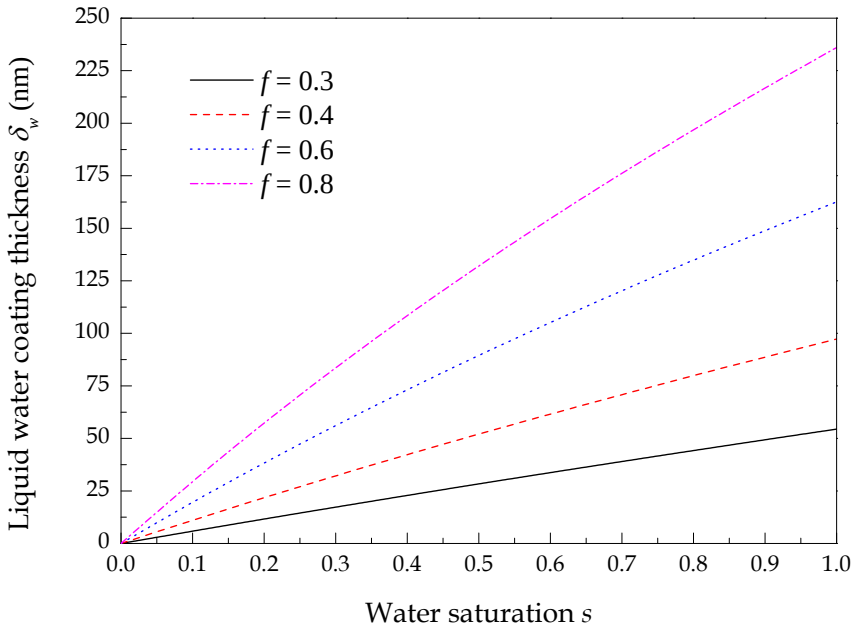

Figure 5-4 Liquid water film thicknesses with different platinum mass ratios in base case condition

The simulation results show that the liquid water film thickness increases as the liquid water saturation and the platinum mass ratio increases. The change in liquid water film thickness can be explained by Eq. (5-13), in which the liquid water film thickness is directly proportional to the liquid water saturation and the porosity of the catalyst layer and is inversely proportional to the agglomerate density. As expected, the increase in the liquid water saturation increases the liquid water film thickness since larger water saturation results in larger portion of the produced water in the liquid phase. For example, the increase in the liquid water saturation from 0.2 to 0.8 increases the liquid water film thickness from 60 nm to 200 nm when the platinum loading and platinum mass ratio are fixed at 0.4 mg cm^{-2} and 0.8, respectively.

As assumed in Section 5.2.1, the liquid water only exists as the liquid water film surrounding the agglomerate. When the agglomerate density decreases, the numbers of agglomerates decrease. Consequently, thicker liquid water films are formed surrounding each individual agglomerates. Due to the fact that oxygen diffusion is faster in liquid water than that in Nafion® ionomer [85, 245], the liquid water has less effect on the overall oxygen diffusion resistance through the liquid water film in comparison with the ionomer film when both of them have the same thickness.

5.3.3 Comparison of the membrane and ionomer swelling

Figure 5-5 shows the effect of membrane and ionomer swelling on the fuel cell performance. The polarisation curves are obtained in four conditions: considering the membrane swelling only, considering the ionomer swelling only, considering both the swellings and neglecting both the swellings. The membrane/ionomer swelling coefficient in Eq. (5-17) is set to zero in the case of neglecting the membrane and ionomer swelling in the model.

It is apparent that, at lower current densities, the four polarisation curves almost overlap each other due to the weak mass transport influence. At higher current densities, by ignoring the membrane and ionomer swellings, the two-phase flow model over estimates the current density at higher current densities where mass transport effect is significant. The relatively higher simulated current densities can be explained by two reasons: firstly, the unchanged porosity of the cathode catalyst layer when the ionomer swelling is not considered; secondly, the constant reactant gas transport resistance when the MEA bulge is not included. It is also clear in Figure 5-5 that the polarisation curve

obtained by considering the membrane swelling only is very close to that considering the ionomer swelling only. This indicates that the effects of ionomer swelling and membrane swelling are of equal importance.

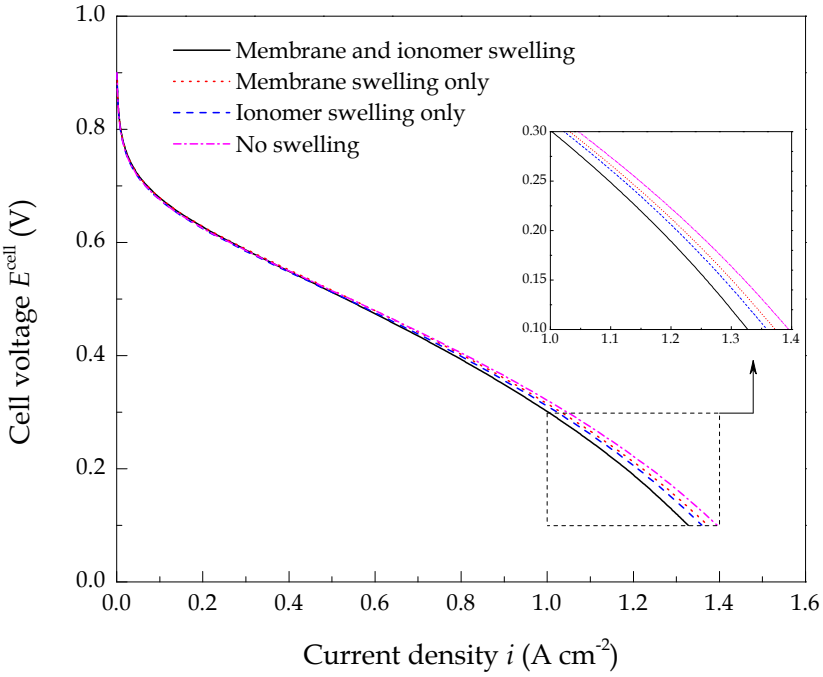

Figure 5-5 Comparison of the effect of membrane and ionomer swelling on fuel cell performance

5.3.4 Membrane and ionomer water content

Figure 5-6 shows the profiles of membrane and ionomer water content as a function of the local current density and position. The influence of electro-osmotic drag is apparent from these results. At lower current density, there is a slight change in water content due to the relatively low amount of drag water and to the fact that the vapour activities at the GDL-CL interfaces of both the anode (B-B') and cathode (E-E') are nearly identical according to Eq. (3-164). As the current density increases, the membrane/ionomer water content becomes more non-uniform since the anode dehydrates and the cathode water content increases. It is apparent in Figure 5-6 that the lowest water content with the value of 3.94 is observed at anode GDL-CL interface (B-B') while the water content at cathode GDL-CL interface (E-E') reaches to saturation at the current density of 0.86 A cm^{-2}, in agreement with the experimental data of Buchi and Scherer [246] and the simulation results of Kulikovsky [247]. In addition, as shown in Figure 5-6, the anode dehydration is more severe and the cathode ionomer water content is higher under the land than under the channel. This is explained by the higher water migration flux driven by the force of electro-osmotic drag under the land.

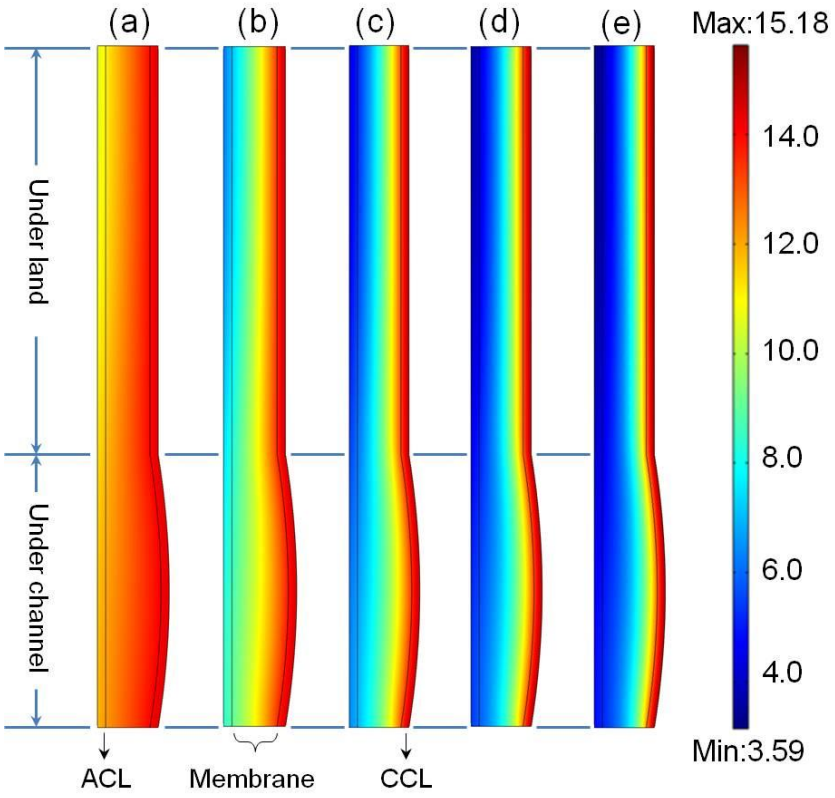

Figure 5-6 Membrane and ionomer water contents at different current densities (a) 0.06 A cm^{-2}; (b) 0.26 A cm^{-2}; (c) 0.53 A cm^{-2}; (d) 0.79 A cm^{-2}; (e) 1.00 A cm^{-2} in base case condition

5.3.5 Ionomer volume fraction in cathode catalyst layer

Figure 5-7 shows the profiles of the ionomer volume fraction within the cathode catalyst layer for the dry ionomer volume fraction of 0.3. The boundaries of $X = 0$ and $X = 1$ refer to the interfaces of CL-membrane (D-D') and CL-GDL (E-E'). The boundaries of $Y = 0$ and $Y = 1$ refer to the lower boundary of the flow channel (D'-E') and the upper boundary of the current collector (D-E) as shown in Figure 5-1(b), respectively. At a cell voltage of 0.3 V, the corresponding current density is 1.0 A cm^{-2}. Similar to the distribution of the ionomer water content, it is shown in Figure 5-7 that the highest ionomer volume fraction (swelling) is observed at the cathode CL-GDL interface (E-E') under the land. The observed higher ionomer volume fraction near the cathode CL-GDL interface in comparison to that of the CL-membrane interface indicates that ionomer water absorption (water uptake) is the main process in determining the ionomer water content rather than electro-osmotic drag (EOD). This is because the EOD effect is pronounced closer to the membrane at the studied current density. However, the higher ionomer swelling gradient from membrane-CL to CL-GDL under the channel in

comparison to that under the land signifies the importance of the EOD on ionomer swelling.

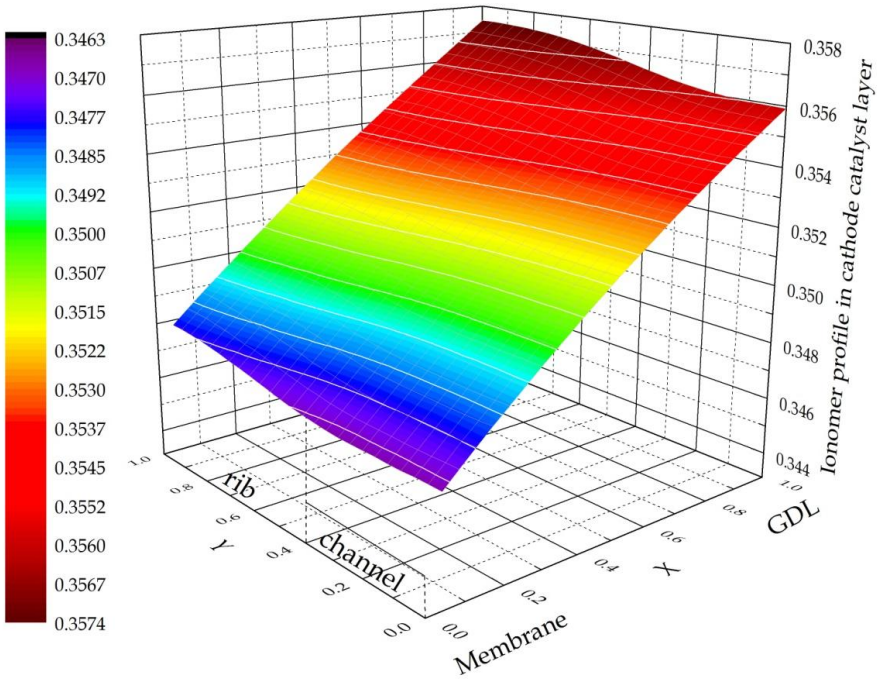

Figure 5-7 Ionomer volume fraction within cathode catalyst layer with dry ionomer volume fraction of 30% in base case condition at the cell voltage of 0.3 V

5.3.6 Liquid water saturation in cathode porous electrode

Figure 5-8 shows the profiles of the liquid water saturation within the cathode porous electrode with two dry ionomer volume fractions. The liquid water, generated via water vapour condensation and ionomer desorption, is prone to occur under the land and close to the cathode CL-membrane interface. The distribution of liquid water in the cathode catalyst layer is consistent with the numerical prediction and neutron radiography data of Wang and Chen [248]. The dry ionomer volume fraction has a small effect on the distribution of liquid water. However, the liquid water saturation increases as the dry ionomer volume fraction decreases. This is explained by the fact that the ionomer in cathode catalyst layer is the carrier of dissolved water. The decrease in the dry ionomer volume fraction reduces the amount of dissolved water, resulting in more liquid water surrounding the agglomerate.

Figure 5-9 shows the average liquid water saturation and the liquid water film thickness within the cathode porous electrode as a function of the local current density and relative humidity. As expected, both the average water saturation and the average

liquid water film thickness increase as the current density increases. As expected, when the cathode gas inlet is fully humidified, liquid water saturation occurs at all current densities.

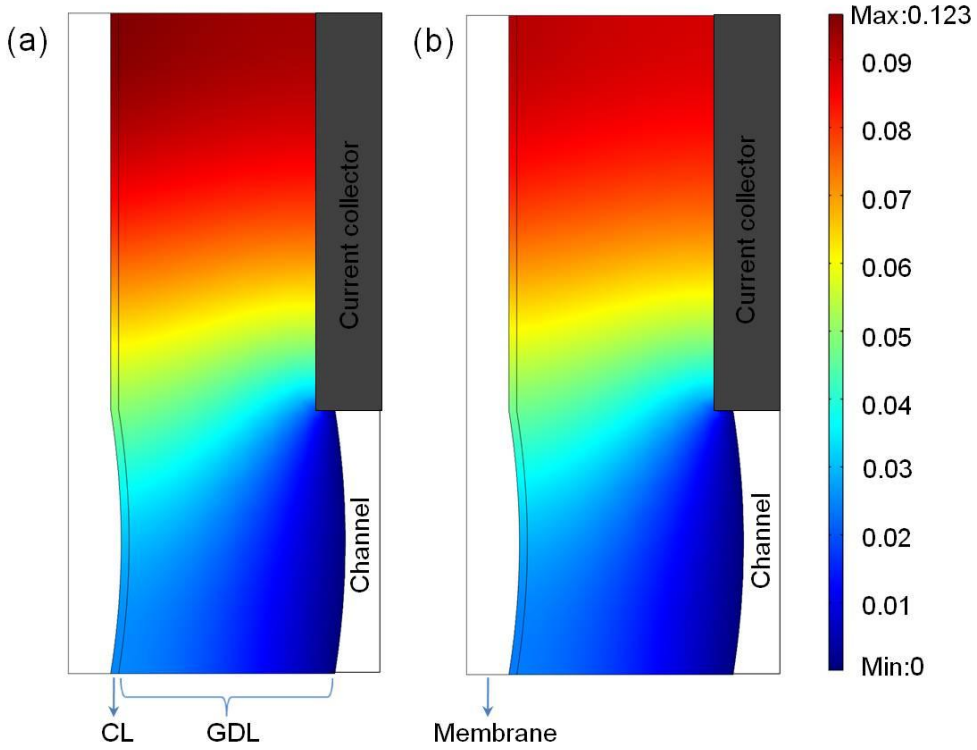

Figure 5-8 Liquid water saturation with dry ionomer volume fraction of 0.2 (a) and 0.4 (b) in base case condition at the cell voltage of 0.3 V

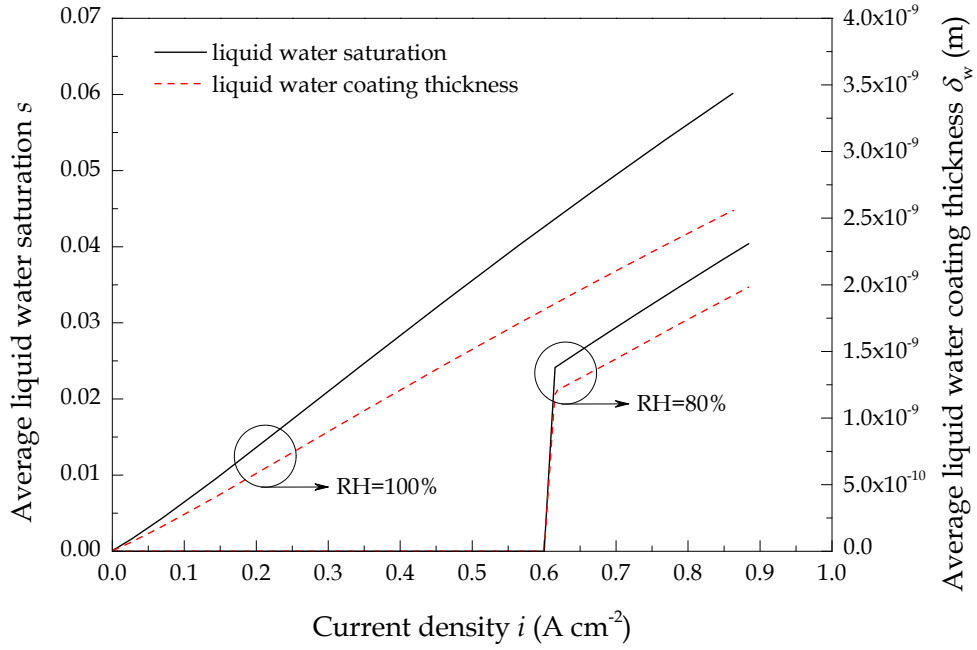

Figure 5-9 Average liquid water saturations and liquid water film thicknesses at different current densities and relative humidity in base case condition

On the contrary, liquid water saturation as shown in Figure 5-9 is only observed at higher current density when the relative humidity of the cathode gas inlet is lower than 100%. In the later case, both the liquid water saturation and the liquid water film thickness are smaller than that of the former case.

5.3.7 Optimal ionomer water content

According to the agglomerate assumption of the catalyst layer, oxygen needs to diffuse through the ionomer and liquid water film before reaching the platinum particle surface (see Figure 5-10).

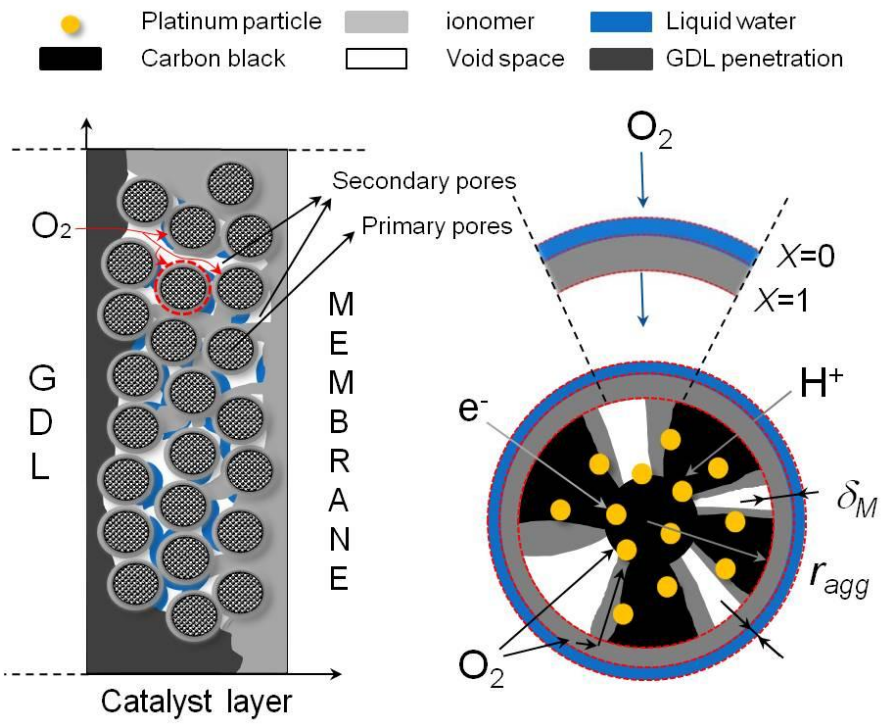

Figure 5-10 Sketch of oxygen diffusion through the ionomer and liquid water film

As shown in Figure 3-7 in Chapter 3, the diffusion coefficient of oxygen through the liquid water is more than ten times bigger than that through the ionomer (above 70 °C), the ionomer film therefore has a more significant effect on the oxygen transport. If no liquid water is generated, the oxygen diffusion flux can be described by the dimensionless Fick's law shown as follow.

$$\vec{N}_{O_2-M} = -\nu c^0_{O_2} \nabla C_{O_2} \tag{5-18}$$

where the parameter ν, is the quotient of oxygen diffusion coefficient and the ionomer film thickness, which represents to the oxygen diffusion rate through the ionomer film.

$$\nu = \frac{D_{O_2-M}}{\delta_M}(m/s) \tag{5-19}$$

The boundary condition for Eq. (5-18) is:

$$\begin{cases} X = 0, & C_{O_2} = 1 \\ X = 1, & \nabla C_{O_2} = 0 \end{cases} \tag{5-20}$$

As shown in Eq. (3-130) and Eq. (3-60), the increase in ionomer water content results in increases in both the oxygen diffusion coefficient and ionomer film thickness. In the following section, the effect of the ionomer water content on parameter ν is investigated to obtain the optimal ionomer water content.

The effect of ionomer water content on parameter ν with different platinum loading, platinum mass ratio and dry ionomer volume fraction is shown in Figure 5-11, in which Figure 5-11(a) shows the effect of ionomer water content on parameter ν with two platinum loadings of 0.2 and 0.4 mg cm^{-2} at fixed platinum mass ratio of 0.6 and dry ionomer volume fraction of 0.3; Figure 5-11(b) shows the effect of ionomer water content on parameter ν with two platinum mass ratios of 0.3 and 0.7 at fixed platinum loading of 0.4 mg cm^{-2} and dry ionomer volume fraction of 0.3; and Figure 5-11(c) shows the effect of ionomer water content on parameter ν with two dry ionomer volume fractions of 0.3 and 0.4 at fixed platinum loading of 0.4 mg cm^{-2} and platinum mass ratio of 0.4, respectively.

For the three conditions above, the thickness of the cathode catalyst layer is fixed at 15 μm. The results in Figure 5-11 show that the optimal water content is higher for smaller platinum loading, larger platinum mass ratio and larger dry ionomer volume fraction. This can be explained by the ionomer film thickness at different platinum loadings, platinum mass ratios and dry ionomer volume fractions. As discussed in Chapter 4, the ionomer film is thicker when smaller platinum loading and larger platinum mass ratio and dry ionomer volume fraction are adopted. The increase in thickness of the thicker ionomer film is smaller than that of the thinner film. For example, the dry ionomer films are 2.31×10^{-7} m and 1.40×10^{-7} m for the platinum loadings of 0.2 and 0.4 mg cm^{-2}, respectively. At the water content of 14, the ionomer film thicknesses increase 74.2% and 89.5%, respectively. In short, the optimal water

content is lower than the fully saturated level of the ionomer. The optimal water content is strongly dependent on the properties of the cathode catalyst layer.

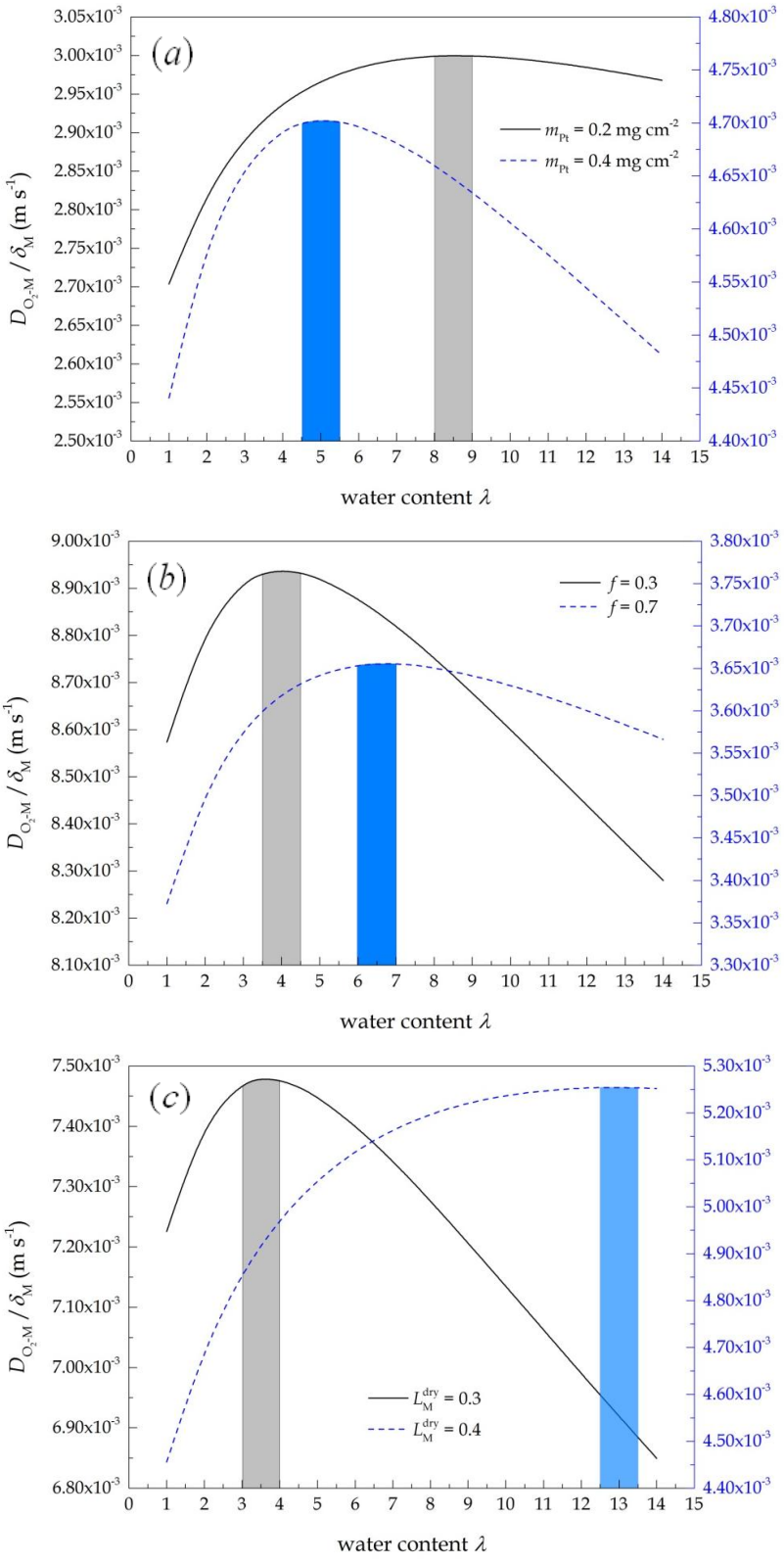

Figure 5-11 Effect of ionomer water content on parameter ν with different platinum loading (a), platinum mass ratio (b) and dry ionomer volume fraction (c)

5.3.8 Orthogonal array testing

The orthogonal array testing is a systematic and statistical way of testing that enables the design of a reasonably small set of test cases that provide maximum test coverage. It is used when the number of design possibilities to the system is relatively small, but too large to allow for exhaustive testing of every possibility to the systems. It is particularly effective in testing the combinations and integrations by considering the interactions between the possibilities. The orthogonal array in this study is applied in fuel cell performance testing, which consists of four design parameters with three levels of each. Platinum loading, platinum mass ratio, dry ionomer volume fraction and catalyst layer thickness are the four parameters and nice testing is carried out. The orthogonal array and testing results are shown in Table 5-6 and Table 5-7, respectively.

Table 5-6 Orthogonal array $L_9(3^4)$

Test case	m_{Pt} (mg cm^{-2})	f	L_M^{dry}	l_{CL} (μm)
1	0.2	0.4	0.2	10
2	0.2	0.6	0.3	15
3	0.2	0.8	0.4	20
4	0.4	0.4	0.3	20
5	0.4	0.6	0.4	10
6	0.4	0.8	0.2	15
7	0.6	0.4	0.4	15
8	0.6	0.6	0.2	20
9	0.6	0.8	0.3	10

Table 5-7 Orthogonal array testing result

Cases	a_{agg} ×10^{-7} (m^{-1})	δ_M ×10^{7} (m)	ε_s	σ^{eff} (S m^{-1})	v ×10^{3} (m s^{-1})	*0.9V*		*0.5V*		*0.3V*	
						i ×10^{4} (A cm^{-2})	δ_w ×10^{13} (m)	i ×10 (A cm^{-2})	δ_w ×10^{11} (m)	i ×10 (A cm^{-2})	δ_w ×10^{10} (m)
1	4.519	1.559	0.373	4.342	7.681	4.712	171.1	4.509	614.0	8.928	117.1
2	4.351	3.99	0.393	5.77	2.982	5.708	286.5	4.565	762.6	8.551	137.9
3	4.713	8.776	0.344	7.063	1.351	8.322	358.6	4.547	815.9	7.439	129.6
4	5.481	1.988	0.262	5.579	5.926	9.618	153.5	5.226	385.9	9.492	68.4
5	5.715	2.998	0.207	6.84	3.987	5.972	83.3	4.458	296.2	8.473	54.5
6	3.507	3.178	0.493	4.581	3.739	4.602	385.0	4.368	1029.8	8.521	193.9
7	7.643	1.882	0.011	6.864	6.325	9.828	4.8	2.052	4.9	4.844	1.2
8	4.104	1.694	0.401	4.372	6.921	7.211	257.2	4.979	673.5	9.392	123.7
9	7.562	1.348	0.019	5.661	8.87	7.89	9.1	2.561	12.5	6.147	2.9

In Table 5-7, the specific area, ionomer film thickness, porosity of the secondary pores, proton conductivity, parameter ν, and the obtained current densities and liquid water film thickness at different cell voltages are investigated. It is clear that the highest current density at the cell voltages of 0.9 V, 0.5 V and 0.3 V are observed in case 7, case 4 and case 4, respectively. The proton conductivity and the specific area of case 7 are the biggest and the second biggest among the nice cases. This indicates that the oxygen reduction kinetic and the proton conductivity are the most important two factors in determining the fuel cell performance at high cell voltages. Both the highest current densities at the cell voltage of 0.5 and 0.3 V are observed in case 4. However, no studied parameters in case 4 are the highest or lowest. The values of all the parameters are in between of the highest and lowest. Case 8 also leads to very high current densities at 0.5 and 0.3 V, which are quite close to the current densities obtained from case 4. All parameters in case 8, except the specific area, are more optimal compared to that in case 4. This indicates that the oxygen reduction kinetics is also very important at low cell voltages. Similarly, all parameters in case 9, except the porosity, are more optimal than that in case 4. However, the obtained current densities are much lower, especially at lower cell voltages. This indicates the importance of the porosity. Therefore, the gas transport is another factor in determining the cell performance at low cell voltages. In medium cell voltages, the fuel cell performance is under a mixed control where the effects of proton conductivity, kinetics and gas transport are of equal importance.

5.3.9 Optimal platinum loading

The polarisation curves and the effectiveness factors of the catalyst layer with various platinum loadings from 0.1 to 0.6 mg cm^{-2} are shown in Figure 5-12 and Figure 5-13, respectively. The platinum mass fraction, dry ionomer volume fraction and catalyst layer thickness are set to 0.6, 0.3 and 15 μm, respectively. It is clear in Figure 5-12 that the increase in platinum loading from 0.1 to 0.4 mg cm^{-2} improves the cell performance. This improvement can be explained by the increase in the specific area and the decrease in the ionomer film thickness. However, the current density increases very slightly when the platinum loading increases from 0.4 to 0.6 mg cm^{-2} due to the decrease in catalyst layer porosity. Consequently, too much platinum loading rather than improves the cell performance can waste expensive platinum.

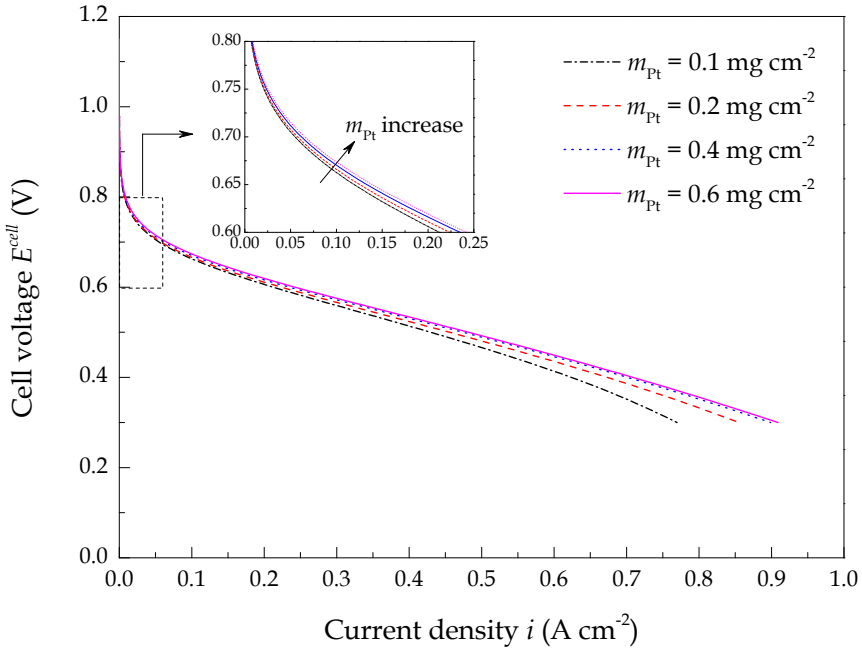

Figure 5-12 Effect of platinum loading on fuel cell performance

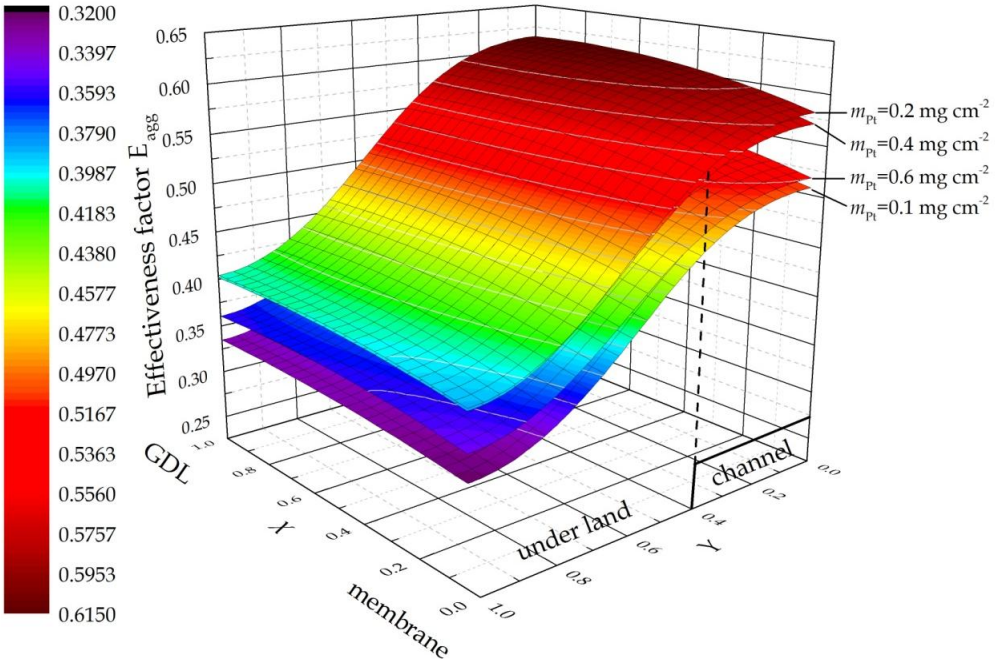

Figure 5-13 Effect of platinum loading on effectiveness factor of cathode catalyst layer

The effectiveness factors of the catalyst layer with various platinum loadings are shown in Figure 5-13. The effectiveness is higher under the channel than that under the land due to the relative high oxygen concentration under the channel. It is clear, the platinum loading of 0.2 mg cm^{-2} leads to the highest effectiveness. The effectiveness factor with the platinum loading of 0.4 mg cm^{-2} almost overlaps that of 0.2 mg cm^{-2}.

The effectiveness decreases as the platinum loading further increases. The effectiveness of platinum loading of 0.1 mg cm^{-2} is the lowest. Consequently, 0.2 - 0.4 mg cm^{-2} are the optimal platinum loading.

5.3.10 Optimal platinum mass ratio

The polarisation curves and the effectiveness factors of the catalyst layer with varying the platinum mass ratio from 0.3 to 0.7 are shown in Figure 5-14 and Figure 5-15, respectively. The platinum loading, dry ionomer volume fraction and catalyst layer thickness are set to 0.4 mg cm^{-2}, 0.3 and 15 μm, respectively. It is apparent in Figure 5-14 that at higher cell voltages, e.g. higher than 0.7 V, lower platinum mass ratio improves the fuel cell performance. However, at medium and lower cell voltages, the cell performance initially increases as the platinum mass ratio increases from 0.3 to 0.5 and decreases as the platinum mass ratio further increases from 0.5 to 0.7.

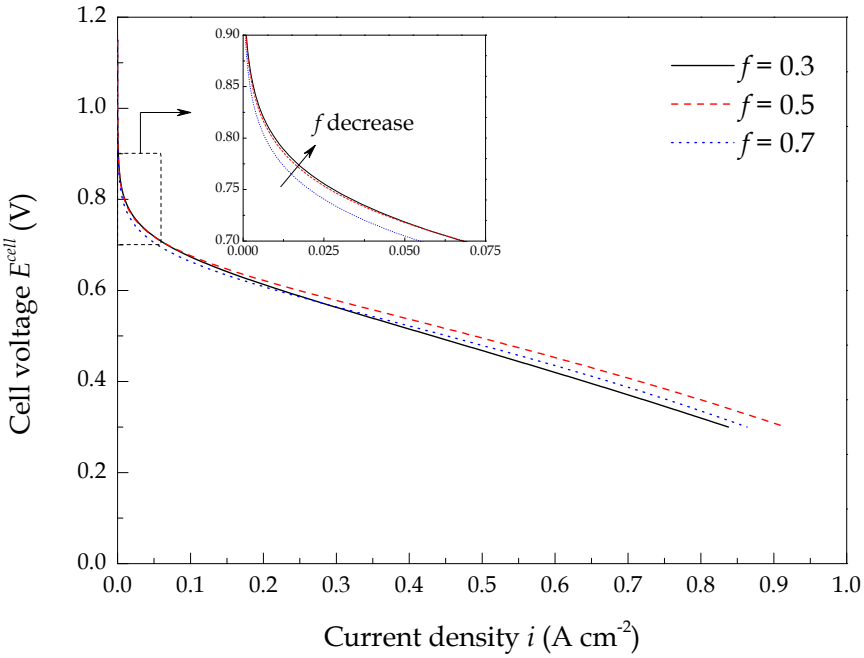

Figure 5-14 Effect of platinum mass ratio on fuel cell performance

As shown in Figure 4-4 and Figure 4-5, the increase in platinum mass ratio increases the porosity and ionomer film thickness. The initial increase in the cell performance resulting from the platinum mass ratio from 0.3 to 0.5 is possibly due to the increase in porosity. As analysed by the orthogonal array testing, catalyst layer porosity is vitally important to the fuel cell performance at higher current densities. However, as the platinum mass ratio further increases from 0.5 to 0.7, the increase in ionomer film

thickness plays a more important role in determining the fuel cell performance. In this condition, the fuel cell performance decreases due to the increased oxygen transport resistance through the thicker ionomer film. Consequently, the optimal platinum mass ratio is around 0.5 in this study. The effectiveness factors of the catalyst layer with various platinum mass ratios are shown in Figure 5-15. It is obvious that the increase in platinum mass ratio increases the effectiveness factor.

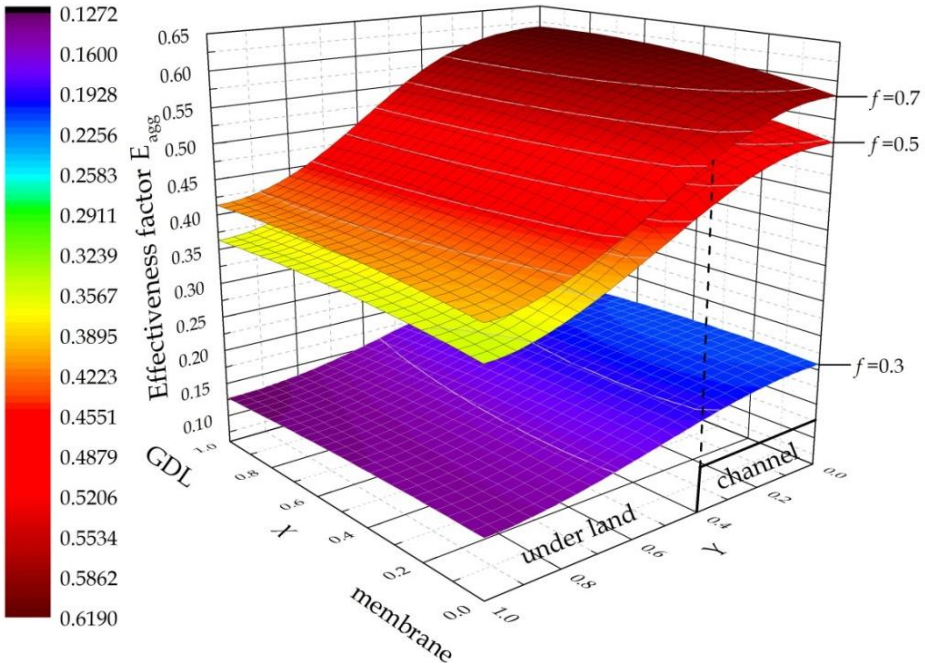

Figure 5-15 Effect of platinum mass ratio on effectiveness factor of cathode catalyst layer

5.3.11 Optimal dry ionomer loading

The polarisation curves and the agglomerate effectiveness factors for various dry ionomer loadings are shown in the Figure 5-16 and Figure 5-17 as follow. Similarly, the platinum loading, platinum mass fraction, and catalyst layer thickness are set to constants with the values of 0.4 mg cm^{-2}, 0.4 and 15μm, respectively. As shown in Figure 5-14, the increase in dry ionomer loading increases the current densities at higher cell voltages whereas it decreases the current densities at lower cell voltages. The improved fuel cell performance at higher cell voltages is because higher ionomer loading increases the proton conductivity and ionomer film thickness. Due to the fact that the electrochemical reaction rate is relative slow at higher cell voltages, the overall rate is therefore mainly control by the proton transport rate. As a result, the increase in ionomer loading is of benefit to the cell performance. However, at medium and low cell voltages, the impact of mass transport becomes significant. The increase in ionmomer

loading decreases the porosity and increases the mass transport resistance. It is clear that the current densities at medium and low cell voltages drop rapidly as the ionomer loading increases to 1.65 mg cm^{-2}. The optimal dry ionomer loading is between 0.2 to 0.3 mg cm^{-2}, which agrees well with the experimental results of Passalacqua *et al.* [249] and Kim *et al.* [250]. Figure 5-17 shows that the agglomerate effectiveness decreases as the ionomer loading increases.

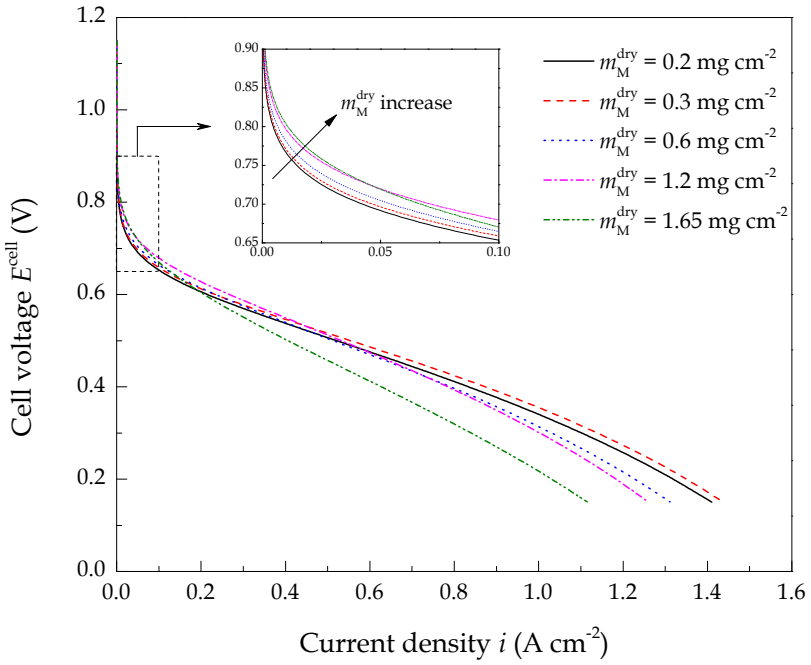

Figure 5-16 Effect of dry ionomer loadings on fuel cell performance

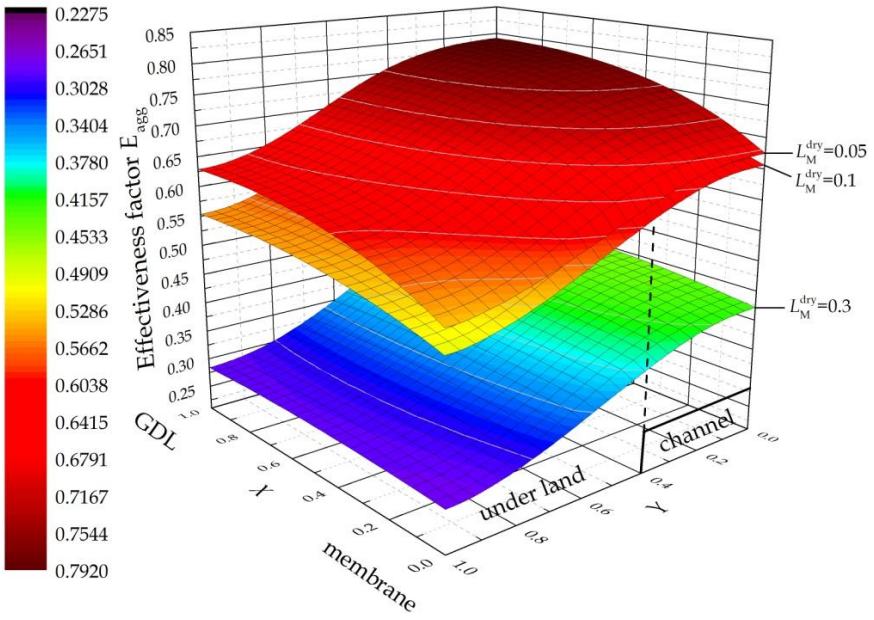

Figure 5-17 Effect of dry ionomer loading on effectiveness factor of cathode catalyst layer

5.3.12 Optimal relative humidity

The polarisation curves for different operating cathode relative humidity are shown in Figure 5-18. It is clear that the effect of the cathode relative humidity on the cell performance can be divided into three segments. With the initial increase in relative humidity, the cell performance decreases at lower current densities and improves at medium current densities and decreases again at higher current densities.

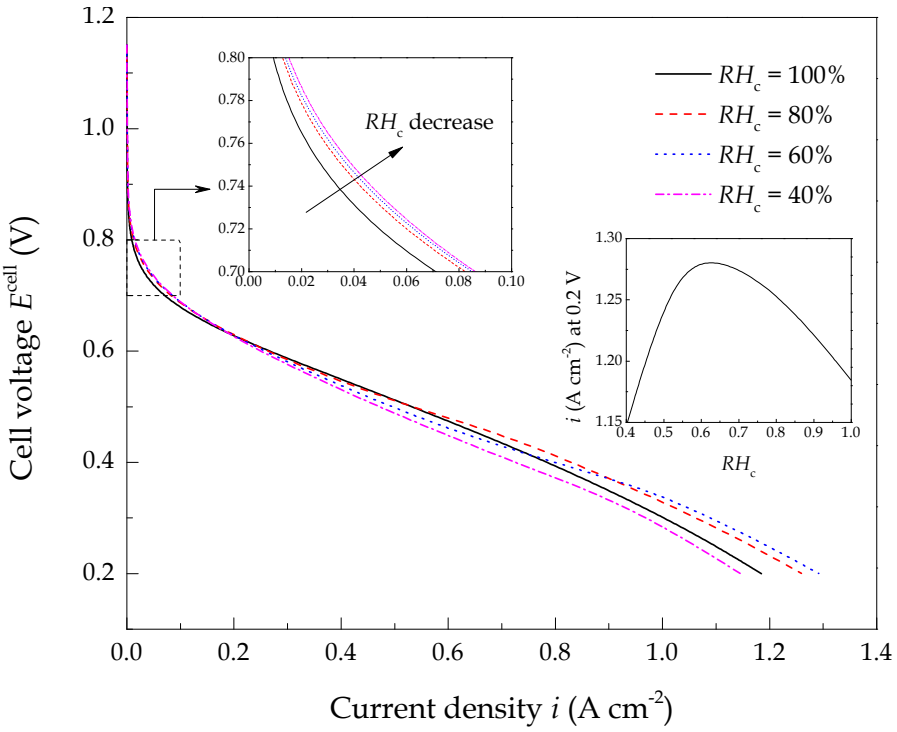

Figure 5-18 Effect of cathode relative humidity on fuel cell performance

At lower current densities, the lower relative humidity benefits the cell performance because a lower relative humidity increases the oxygen fraction of cathode gas inlet and increases the catalyst layer porosity by reducing the ionomer swelling. Even though the oxygen diffusion coefficient through the ionomer is reduced by the lower relative humidity, the negative effect is less remarkable because the mass transport impact is not significant at lower current densities. At medium current densities, the electrode is under mixed control of both the kinetics and mass transport. In this situation, the increase in cathode relative humidity increases the oxygen diffusion rate through the ionomer film and results in an increase in oxygen reduction rate until liquid water is generated at higher current densities. However, the thickness of the ionomer film increases significantly at higher cathode relative humidity. As shown in Table 5-8, the ionomer film thickness increases 26% at the current density of 1.0 A cm^{-2} with the

relative humidity of 60% and 80%, which increases the oxygen mass transport resistance.

Table 5-8 Average ionomer film thicknesses at different current densities and relative humidity in base case condition

RH_c	Dry ionomer	Swelled ionomer at various current densities			
		0.2 A cm^{-2}	0.6 A cm^{-2}	1.0 A cm^{-2}	1.4 A cm^{-2}
80%	133.2 nm	142.9 nm	156.9 nm	168.2 nm	168.2 nm
60%		141.6 nm	144.4 nm	167.8 nm	167.8 nm
40%		139.9 nm	141.8 nm	143.9 nm	------ nm

It is apparent in Figure 5-18 that when the cathode is fed with fully humidified air, the higher cathode relative humidity offsets the improved fuel cell performance at higher current densities due to the increase in oxygen diffusion resistance resulting from the increased thickness of the liquid water film (flooding). This observation is consistent with the experimental results of Yan *et al.* [238] and the simulation results of Nguyen and White [77]. For example, at cathode relative humidity of 80%, the average water saturation is 4.0% and the average thickness of the liquid water film is 2.0 nm at 0.88 A cm^{-2}. Theoretically, the best fuel cell performance is achieved when the ionomer is properly saturated by water with minimum liquid water generation. In this study, the best performance is achieved at a cathode relative humidity between 40% and 60% at the current density of 1.2 A cm^{-2}.

5.4 Conclusions

A two dimensional, across the channel, steady state, isothermal, two-phase flow model based on an agglomerate catalyst layer structure is presented. The water phase transfer between vapour, dissolved and liquid water is addressed in this two-phase flow model leading to a greater accuracy in validating the experimental data compared to the single-phase flow model. The dissolved water transport through the membrane/ionomer is modelled by a combined mechanism in which electro-osmotic drag (EOD), back diffusion and hydraulic permeation are all included. The modelling results show that the non-uniform distribution of the membrane/ionomer water content is caused by the EOD and ionomer water absorption (water uptake). At higher relative humidity and lower current density, ionomer water absorption plays a more important role than EOD. However, at lower relative humidity and higher current density, EOD also plays an

important role in determining the profile of the membrane/ionomer water content. At higher current density, higher membrane/ionomer water contents are observed near the cathode CL-GDL and under the land.

Membrane and ionomer swelling occurs in contact with water, the volume of membrane and ionomer therefore strongly depends on the water content. The modelling results show that the ionomer volume fraction in the cathode catalyst layer approximately increases by 25% when completely saturated. The membrane swelling increases the portion of GDL bulged into flow channel, while the ionomer swelling decreases the catalyst layer porosity and increases the ionomer film thickness. Both the membrane and ionomer swelling lead to an increase in oxygen transport resistance.

The optimal dry ionomer loading (initial ionomer content) is from 0.2 to 0.3 mg cm^{-2} and the optimal cathode relative humidity is around 60% for the best performance of the fuel cell. This model could give a theoretical prediction of how changing the operating conditions and the catalyst layer composition can be used to enhance the fuel cell performance and reduce cost.

Chapter 6. Two-phase flow Non-isothermal model

This chapter describes a two dimensional, across the channel, steady state, two-phase flow, and non-isothermal model based on a spherical agglomerate catalyst structure combined with a comprehensive water phase transfer and transport, namely (1) water vapour condensation and liquid water evaporation, (2) membrane and ionomer water absorption or water uptake, (3) membrane and ionomer desorption, (4) water transport through membrane via electro-osmotic drag, back diffusion and hydraulic permeation. The distribution of water content of membrane and ionomer, temperature and liquid water saturation in the fuel cell and their effects on the performance of the cell under various operating temperatures are investigated. Ionomer swelling is associated with the non-uniform distribution of water in the ionomer. Two approaches, namely (1) applying different operating temperatures on anode and cathode and (2) enlarging the width ratio of the channel/current collector rib, are adopted to improve the fuel cell performance.

6.1 Introduction

As heat is released during the operation of the fuel cells, thermal management is important due to the effect of temperature on various transport, kinetic and phase-transfer parameters [16, 20]. Therefore, numerous mathematical models were developed with the aim of fully understanding the species, momentum and thermal transport by coupling water and thermal transport [77-79, 184-188, 190, 251, 253, 254, 297].

The earliest water and thermal interrelated models were developed by Nguyen and White [77] and Fuller and Newman [78], in which the heat transfer between water evaporation and condensation were coupled with the species transport. Yi and Nguyen [79] improved the previous model [77] by including the convective water transport across the membrane and the temperature distribution in the solid phase, and stated that the counter-flow mode is most effective for heat removal. Djilali and Lu [251] investigated the influence of heat transfer on gas and water transport in fuel cells and concluded that the non-uniform distribution of temperature and pressure have a large impact on the liquid water and vapour fluxes in the porous medias. Ju *et al.* [98] analysed the energy balance in anode catalyst layer, membrane and cathode catalyst layer with the aid of a developed single-phase, non-isothermal model, and confirmed the necessity for non-isothermal modelling of the PEMFCs.

As a new mechanism of heat and water transport, the so-called "heat-pipe effect" in which water evaporates at the hotter catalyst layer, diffuses through the gas diffusion layer, and condenses on the colder plates was first presented by Wang and Wang [252]. The "heat-pipe effect" was emphasised in the one dimensional model developed by Weber and Newman [253], in which the maximum temperature was observed within the cathode catalyst layer and the heat released by the oxygen reduction reaction occupies approximate 80% of the total heat generated. However, due to the simplified treatment of the catalyst layer as an ultra-thin interface between the gas diffusion layer and membrane, these models [77-79, 251-253, 297] show limitation in modelling the catalyst layer. Thus, numerous models adopted a spherical agglomerate structure as the catalyst layer and concluded that the agglomerate model was superior in representing the real porous catalyst layer than the ultra-thin layer model and pseudo-homogeneous film model [115, 183, 215].

Water exists as three different phases: dissolved water in membrane/ionomer, water vapour and liquid water in porous electrodes. In recent years, researchers began to focus on the thermal transport during the water phase transfer between vapour, dissolved water and liquid water [184, 186, 188, 190, 254]. As stated by Yang *et al.* [186], the absorption or release of heat associated with the water phase transfer, corresponds to approximate 20% of the total heat generated within the whole cell and therefore cannot be neglected. Typically, the membrane/ionomer swells when water uptake occurs, which results in an increase in the ionic conductivity of the membrane/ionomer and a decrease in porosity of the electrode [188]. Consequently, water management is another crucial issue in balancing the operation of the fuel cell to achieve optimum performance.

6.2 Model description

6.2.1 Computational domain and assumption

The computational domain is that for the isothermal two-phase flow model represented in Chapter 5. In addition to the assumptions given in Chapter 5, the thickness of the membrane is assumed as a constant in order to simplify the model. It is also assumed that the ionomer film thickness changes with its water content.

6.2.2 Governing equations

The governing equations for the non-isothermal and two-phase flow model in this chapter are summarised in Table 6-1 as follow:

Table 6-1 Governing equations used in the two-phase flow and non-isothermal model

Gas diffusion layers (Domain 2)		
Conservation of mass	$-\frac{\rho^g k_p}{\mu^g}\nabla\cdot(\nabla p)=0$	(6-1)
Conservation of species	$\rho^g \mathbf{u}^g\cdot\nabla w_i^g-\nabla\cdot[-\rho^g\sum_{j=1}^{N}(1-s^{'})D_{ij}(\nabla x_j^g-w_j^g)\frac{\nabla p}{p}+D_i^T\frac{\nabla T}{T}]=0$	(6-2)
Conservation of charge	$\nabla(-\sigma_s^{eff}\nabla\phi_s)=\nabla(-\sigma_M^{eff}\nabla\phi_M)=0$	(6-3)
Conservation of energy	$\nabla\cdot[\sum_{i=g,l}(\varepsilon\rho_i c_{p,i}\mathbf{u}_i)T]-\nabla\cdot(\sum_{i=g,l,s}k_i\nabla T)=S_T$	(6-4)
Catalyst layers (Domain 3)		
Conservation of mass	$-\frac{\rho^g k_p}{\mu^g}\nabla\cdot(\nabla p)=S_m$	(6-5)
Conservation of species	$\rho^g \mathbf{u}^g\cdot\nabla w_i^g-\nabla\cdot[-\rho^g\sum_{j=1}^{N}(1-s^{'})D_{ij}(\nabla x_j^g-w_j^g)\frac{\nabla p}{p}+D_i^T\frac{\nabla T}{T}]=M_i S_i^g$	(6-6)
Conservation of charge	$\nabla(-\sigma_s^{eff}\nabla\phi_s)=Q_s$ $\nabla(-\sigma_M^{eff}\nabla\phi_M)=Q_M$	(6-7) (6-8)
Conservation of energy	$\nabla\cdot[\sum_{i=g,l}(\varepsilon\rho_i c_{p,i}\mathbf{u}_i)T]-\nabla\cdot(\sum_{i=g,l,s}k_i\nabla T)=S_T$	(6-9)
Membrane (Domain 4)		
Conservation of charge	$\nabla(-\sigma_M^{eff}\nabla\phi_M)=0$	(6-10)
Conservation of energy	$\nabla\cdot[\sum_{i=g,l}(\varepsilon\rho_i c_{p,i}\mathbf{u}_i)T]-\nabla\cdot(\sum_{i=g,l,s}k_i\nabla T)=S_T$	(6-11)

In this non-isothermal model, heat generation originating from reaction, Joule heating (ohmic heating) and water phase transfers are all considered in the source term, S_T. It is worth noting that the hydrogen oxidation reaction in the anode is endothermic whereas the oxygen reduction reaction in the cathode is exothermic. In the equations of conservation of energy shown in Table 6-1, the subscript *i* refers to gas mixture, liquid

water and solid phase of the electrode. In addition to the source terms which have been given in Chapter 5, the conservation of heat and heat source terms are listed in Table 6-2 and Table 6-3, respectively.

Table 6-2 Conservation of heat in different computational domains

Anode GDL	Anode CL	Membrane	Cathode CL	Cathode GDL
S_T^{sa}	$S_T^{vd}+S_T^{ra}+S_T^{sa}+S_T^{M}$	S_T^{M}	$S_T^{dl}+S_T^{vl}+S_T^{vd}+S_T^{rc}+S_T^{sc}+S_T^{M}$	$S_T^{vl}+S_T^{sc}$

Note: The unit for each source term is (W m^{-3})

Table 6-3 Source terms of heat

Source terms	Unit	Domain
$S_T^{sa}=\frac{i_a^2}{\sigma_{GDL,a}^{eff}}$	W m^{-3}	Anode GDL
$S_T^{sc}=\frac{i_c^2}{\sigma_{GDL,c}^{eff}}$	W m^{-3}	Cathode GDL
$S_T^{M}=\frac{i_M^2}{\sigma_M^{eff}}$	W m^{-3}	Membrane, Anode and cathode CLs
$S_T^{ra}=-\lvert i_a\rvert[\frac{T\nabla S_a}{2F}]$	W m^{-3}	Anode CL
$S_T^{rc}=\lvert i_c\rvert[\lvert\eta_c\rvert-\frac{T\nabla S_c}{4F}]$	W m^{-3}	Cathode CL
$S_T^{vd}=M_w S_w^{vd}\nabla h_w^{vd}$	W m^{-3}	Anode and cathode CLs
$S_T^{dl}=M_w S_w^{dl}\nabla h_w^{dl}$	W m^{-3}	Cathode CL
$S_T^{vl}=M_w S_w^{vl}\nabla h_w^{vl}$	W m^{-3}	Cathode GDL and CL

6.2.3 Thermal parameters

The effective thermal conductivity and specific heat capacity depend on the volume fractions of the species within a chosen domain. Without a doubt, the cathode catalyst layer is the most complicated domain in which gas mixture, liquid water, ionomer, *Pt/C* catalyst, penetrated GDL are all involved. The detailed expressions for the effective thermal conductivity, specific heat capacity of GDL, CL and membrane/ionomer are listed in Table 6-4. The thermal parameters and temperature dependent heat capacity and thermal conductivity used in this model are given in Table 6-5 and Table 6-6.

Table 6-4 Effective specific heat capacity and thermal conductivity of GDL, CL and membrane

	Gas diffusion layer	*Catalyst layer*	*Membrane*
c_p^{eff}	$\varepsilon_{GDL}c_{p,C} + s\varepsilon_{GDL}c_{p,w}^{l} + (1-s)\varepsilon_{GDL}c_p^g$	$L_{Pt}c_{p,Pt} + (L_C + L_S)c_{p,C} + L_M c_{p,M} + s\varepsilon_{CL}c_{p,w}^{l} + (1-s)\varepsilon_{CL}c_p^g$	$c_{p,M}$
k^{eff}	$\varepsilon_{GDL}k_C + s\varepsilon_{GDL}k_w^{l} + (1-s)\varepsilon_{GDL}k_p^g$	$L_{Pt}k_{Pt} + (L_C + L_S)k_C + L_M k_M + s\varepsilon_{CL}k_w^{l} + (1-s)\varepsilon_{CL}k_p^g$	k_M

Table 6-5 Thermal parameters

Parameters	*Value*	*Reference*
Platinum specific heat capacity, $c_{p,Pt}$ (J kg^{-1} K^{-1})	1.3×10^2	[188]
Carbon specific heat capacity, $c_{p,C}$ (J kg^{-1} K^{-1})	894.4	[188]
Membrane specific heat capacity, $c_{p,M}$ (J kg^{-1} K^{-1})	1090.0	[188]
Liquid water specific heat capacity, $c_{p,w}^{l}$ (J kg^{-1} K^{-1})	4187.0	[188]
Membrane thermal conductivity, k_M (W m^{-1} K^{-1})	0.25	[204]
Entropy of hydrogen oxidation, ∇S_a (J mol^{-1} K^{-1})	161.2	[200]
Entropy of oxygen reduction, ∇S_c (J mol^{-1} K^{-1})	-324.0	[200]
Latent heat of membrane adsorption, ∇h_w^{vd} (J kg^{-1})	3.462×10^6	[185]
Latent heat of membrane desorption, ∇h_w^{dl} (J kg^{-1})	3.462×10^6	[185]
Latent heat of condensation/evaporation, ∇h_w^{vl} (J kg^{-1})	2.308×10^6	[185]

Table 6-6 Temperature dependent heat capacity and thermal conductivity

Parameters	*Expressions*	*Reference*
Hydrogen heat capacity, c_{p,H_2}^g	$1.914\times10^{-6}T^2 - 8.314\times10^{-4}T + 28.890$	fitted [212]
Oxygen heat capacity, c_{p,O_2}^g	$-4.281\times10^{-6}T^2 + 1.371\times10^{-2}T + 25.431$	fitted [212]
Nitrogen heat capacity, c_{p,N_2}^g	$1.788\times10^{-5}T^2 + 2.924\times10^{-3}T + 27.848$	fitted [212]
Water vapour heat capacity, $c_{p,w}^g$	$1.180\times10^{-6}T^2 + 9.621\times10^{-3}T + 30.326$	fitted [212]
Platinum thermal conductivity, k_{Pt}	$-5.037\times10^{-9}T^3 + 2.483\times10^{-5}T^2 - 2.282\times10^{-2}T + 77.80$	[216]
Carbon thermal conductivity, k_C	$1.048\times10^{-6}T^2 - 2.869\times10^{-3}T + 2.979$	[216]
Liquid water thermal conductivity, k_w^{l}	$-1.118\times10^{-5}T^2 + 8.388\times10^{-3}T - 0.9004$	fitted [212]
Hydrogen thermal conductivity, k_{H_2}	$3.777\times10^{-4}T + 7.444\times10^{-2}$	fitted [212]
Oxygen thermal conductivity, k_{O_2}	$6.204\times10^{-5}T + 8.83\times10^{-3}$	fitted [212]
Nitrogen thermal conductivity, k_{N_2}	$5.453\times10^{-5}T + 1.088\times10^{-2}$	fitted [212]
Water vapour thermal conductivity, k_{H_2O}	$1.188\times10^{-4}T - 2.404\times10^{-2}$	fitted [212]

Note: the unit for heat capacity is (J mol K^{-1}) and for thermal conductivity is (W m^{-1} K^{-1})

6.2.4 Boundary conditions

In addition to the boundary conditions shown in Chapter 5, the temperatures at the inlets of anode and cathode are defined as T_a^0 an T_c^0 (K), respectively. Note that the temperatures of the anode and cathode gas inlets are the same as the operating temperatures of the current collectors of anode and cathode, respectively. At a given temperature, the mole fraction of reactants at anode and cathode can be calculated by the following equations:

$$x_{H_2O,a}^0 = \frac{p_w^{sat} RH_a}{p_a}, \quad x_{H_2,a}^0 = 1 - x_{H_2O,a,in} \tag{6-12}$$

$$x_{H_2O,c}^0 = \frac{p_w^{sat} RH_c}{p_c}, \; x_{O_2,c}^0 = 0.21(1 - x_{H_2O,c,in}), \; x_{N_2,c}^0 = 0.21(1 - x_{H_2O,c,in}) \tag{6-13}$$

6.2.5 Numerical solution

The numerical solution in this study is based on the same principle described in Chapter 5. By accounting for the temperature distribution, the fully coupled equations are solved according to the computational process shown schematically in Figure 6-1 as follow:

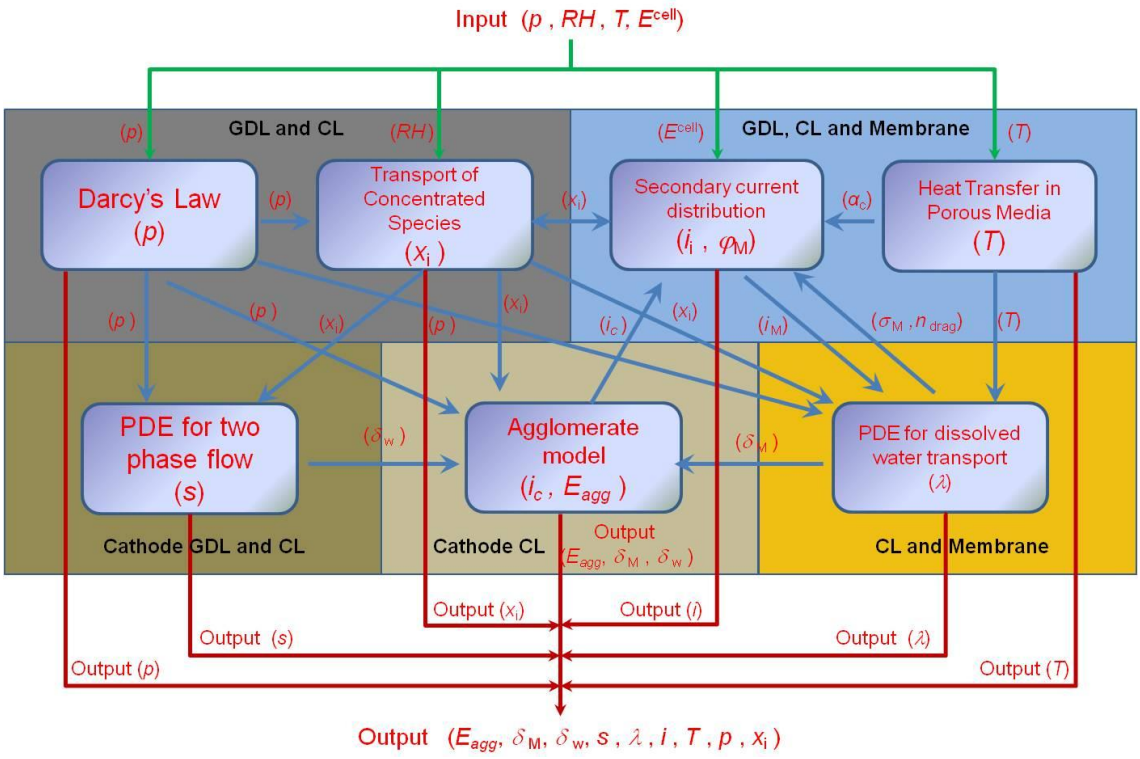

Figure 6-1 Schematic of the computational process

6.3 Results and discussion

6.3.1 Temperature distribution

Though not shown here, the temperature profiles are very similar at three different operating temperatures (60, 70 and 80 °C) at a fixed current density, i.e. at 0.7 A cm^{-2}, the highest temperatures are observed in the cathode catalyst layer under the channel which are approximately 2.3 °C higher than the temperatures at the inlet boundary, which is in agreement of the simulation results of Jung *et al.* [255]. This is because, at a fixed current density, the released heat is almost equivalent at various temperatures as the oxygen reduction reaction (ORR) at the cathode is the main heat source. However, as shown in Figure 6-2, the temperature profiles vary with cell voltages. When the cell voltage is fixed to 0.3 V, the current densities at 60, 70 and 80 °C are 0.73, 0.87 and 0.95 A cm^{-2}, respectively. With increasing operating temperature, the temperature distribution within the cathode catalyst layer becomes more non-uniform. As shown in Figure 6-2, the heat accumulation occurs within the cathode catalyst layer on the region under the channel. The temperature gradients are observed in two directions: one from CL to GDL, and the other from the region under the channel to that under the land. In the two directions, the temperature gradients increase as the operating temperature increases. This is because the ORR in the cathode catalyst layer is exothermic, and the heat released by ORR is the main heat source compared to others. As shown in Table 6-7, the heat released by ORR occupies at least 67% of the total heat at 0.7 A cm^{-2}. According to Eq. (3-31), the reaction rate is accelerated by increasing the temperature. It is worth noting that, more heat is generated in the region under the channel where ORR first occurs. Among the heat sources, the total Joule heat ($S_s^T + S_M^T$) only corresponds to approximately 2% of the total heat due to the high conductivities of the electrode and membrane, therefore it can be neglected. The water phase transfer heat ($S_{vd}^T + S_{dl}^T + S_{vl}^T$) account for approximate 5% of the total heat in which the membrane and ionomer desorption is the main heat source during the phase transfer process.

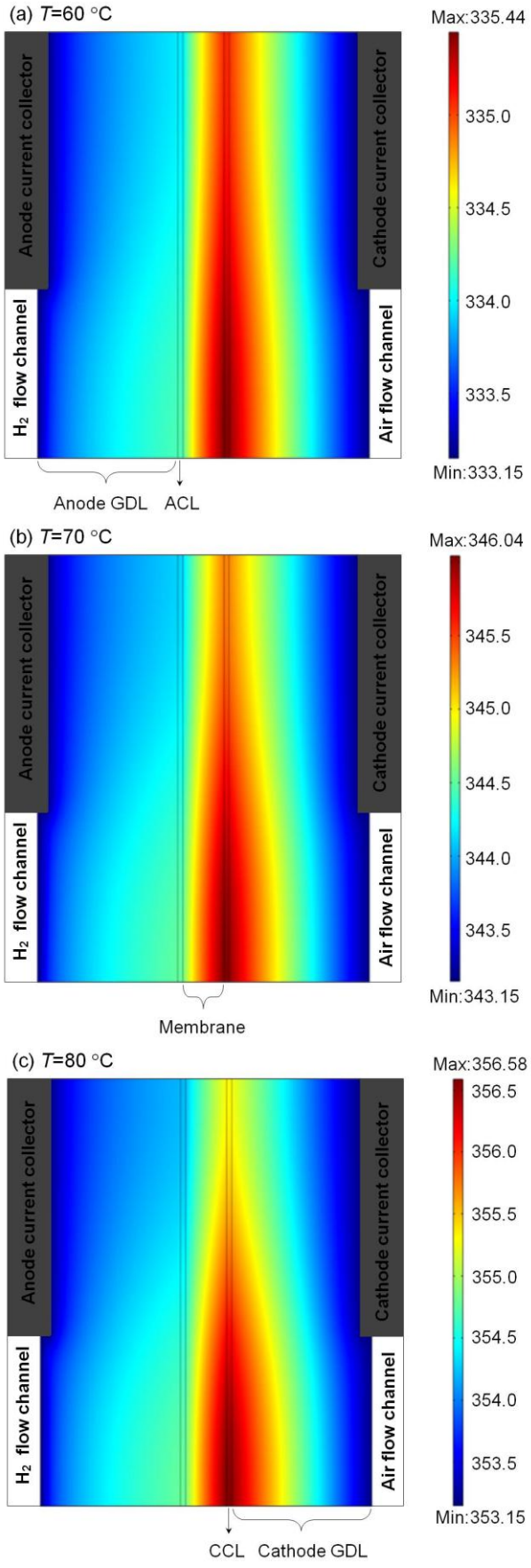

Figure 6-2 Temperature profiles at the cell voltage of 0.3 V and at (a) 60 °C (0.73 A cm^{-2}), (b) 70 °C (0.87 A cm^{-2}) and (c) 80 °C (0.95 A cm^{-2})

6.3.2 Effect of temperature on liquid water saturation

The liquid water saturation profiles at 0.7 A cm^{-2} at different temperatures are shown in Figure 6-3. From the liquid water saturation contours, it can be seen that flooding is more severe and the two-phase flow region is enlarged as the temperature decreases when inlet gases are humidified at a fixed relative humidity, which is consistent with the neutron radiographs tested by Owejan *et al.* [256]. This can be explained by the decrease in the water saturation pressure, which strongly depends on temperature. And this can be also explained with the aid of Table 6-7 in which the total sources for liquid water ($S_{dl}^{w} + S_{vl}^{w}$) increase as the temperature decreases.

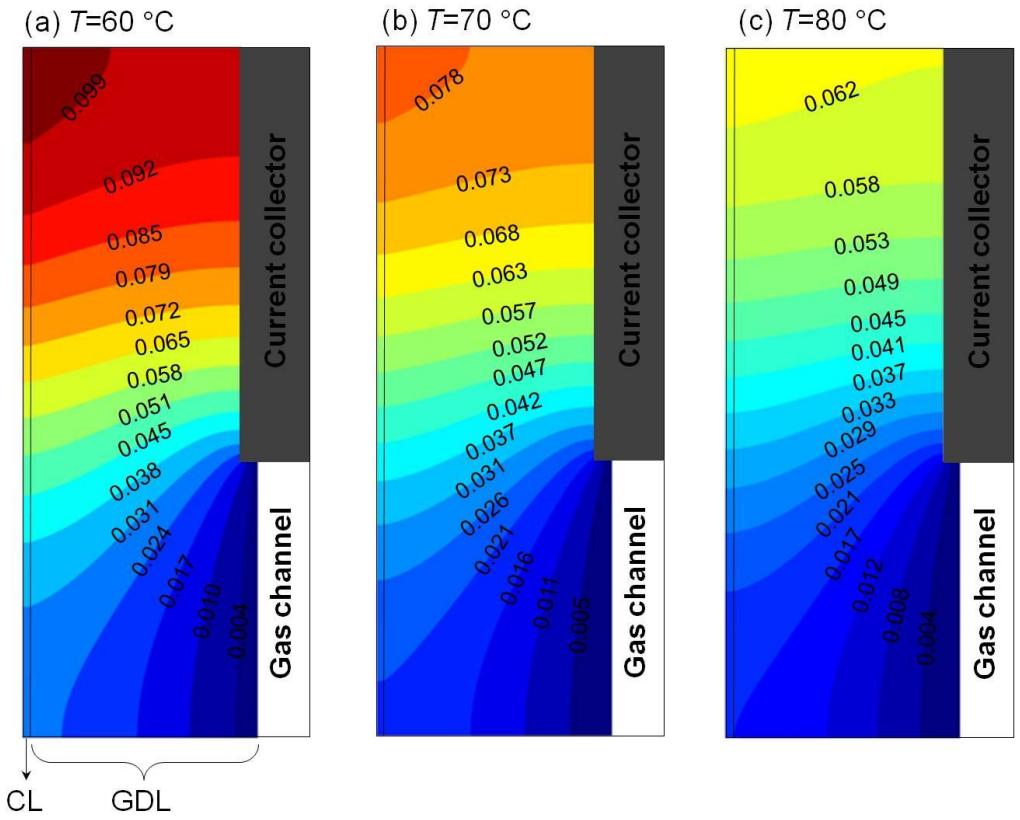

Figure 6-3 Liquid water saturation profiles at 0.7 A cm^{-2} with fully humidified inlet gases at (a) 60 °C (0.32 V), (b) 70 °C (0.39V) and (c) 80 °C (0.42V)

In addition, it is evident from Figure 6-3 that the local saturation is higher in the region close to the CL-membrane interface and under the land, which is consistent with the numerical prediction and neutron radiography data and simulation results of Wang and Chen [248]. As discussed in Chapter 5 and shown in Table 6-7, the liquid water is generated via water vapour condensation and membrane/ionomer desorption, and the membrane/ionomer desorption plays a more important role compared to the water

vapour condensation. The dissolved water under the land firstly reaches to saturation level due to the stronger effect of electro-osmotic drag (EOD) under the land. Consequently, more liquid water is generated under the land than under the channel. In fact, the source term of the liquid water strongly depends on the water production mechanisms: the water generated by ORR exists as vapour, dissolved water or liquid water [185]. In this study, the dissolved water production mechanism is used.

Table 6-7 Dissolved water transport flux, water phase-change and thermal source terms at 0.7 A cm^{-2}

	60 °C (0.32 V)		70 °C (0.39 V)		80 °C (0.42 V)	
Dissolved water transport flux						
F_{EOD} (mol m^{-2} s^{-1})	4.3×10^{-2}	(50.58%)	5.1×10^{-2}	(56.65%)	6.2×10^{-2}	(65.92%)
F_{BD} (mol m^{-2} s^{-1})	4.2×10^{-2}	(49.40%)	3.9×10^{-2}	(43.32%)	3.2×10^{-2}	(34.02%)
F_{HP} (mol m^{-2} s^{-1})	2.1×10^{-5}	(0.02%)	3.0×10^{-5}	(0.03%)	4.9×10^{-5}	(0.05%)
Total flux	8.5×10^{-2}		9.0×10^{-2}		9.4×10^{-2}	
Water phase change sources						
S_{vd}^{w} (mol m^{-3} s^{-1})	2.2×10^{2}	(1.10%)	2.3×10^{2}	(1.17%)	2.4×10^{2}	(1.2%)
S_{dl}^{w} (mol m^{-3} s^{-1})	7.9×10^{2}	(3.94%)	3.8×10^{2}	(1.93%)	1.9×10^{2}	(1.23%)
S_{vl}^{w} (mol m^{-3} s^{-1})	54.2	(0.27%)	52.9	(0.27%)	50.97	(0.98%)
S_{ORR}^{w} (mol m^{-3} s^{-1})	1.9×10^{4}	(94.70%)	1.9×10^{4}	(96.63%)	1.9×10^{4}	(97.53%)
Total phase-change sources	2.01×10^{4}		1.97×10^{4}		1.95×10^{4}	
Thermal sources						
S_{vd}^{T} (W m^{-3})	1.3×10^{7}	(1.67%)	1.4×10^{7}	(1.95%)	1.5×10^{7}	(2.15%)
S_{dl}^{T} (W m^{-3})	4.9×10^{7}	(6.30%)	2.4×10^{7}	(3.34%)	1.2×10^{7}	(1.72%)
S_{vl}^{T} (W m^{-3})	2.3×10^{6}	(0.33%)	2.2×10^{6}	(0.31%)	2.1×10^{6}	(0.30%)
S_{HOR}^{T} (W m^{-3})	-1.8×10^{8}	(23.15%)	-1.5×10^{8}	(20.85%)	-1.4×10^{8}	(20.10%)
S_{ORR}^{T} (W m^{-3})	5.2×10^{8}	(66.89%)	5.2×10^{8}	(72.27%)	5.2×10^{8}	(74.66%)
S_{s}^{T} (W m^{-3})	7.7×10^{5}	(0.10%)	7.8×10^{5}	(0.11%)	7.9×10^{5}	(0.11%)
S_{M}^{T} (W m^{-3})	1.2×10^{7}	(1.54%)	8.5×10^{6}	(1.18%)	6.6×10^{6}	(0.95%)
Total thermal source	7.77×10^{8}		7.19×10^{8}		6.96×10^{8}	

Note: the values in brackets are the percentage each item corresponded to the total

6.3.3 Effect of temperature on membrane/ionomer water content

Figure 6-4(a) to Figure 6-4(c) show the profiles of membrane/ionomer water content at a fixed current density of 0.7 A cm^{-2} while varying the operating temperature from 60 °C to 80 °C, while Figure 6-4(d) is added to compare the membrane/ionomer water content profiles at a fixed temperature of 80 °C with the current densities of 0.2 A cm^{-2}.

It is clear that due to the effect of electro-osmotic drag (EOD), the water content of the membrane and iomomer is lower at the anode and higher at the cathode. Thus, the membrane is prone to dry out at the anode and to be saturated at the cathode. As shown in Figure 6-4(a) to Figure 6-4(c), the influence of temperature on the water content is apparent. The relatively higher water content is observed at higher temperature. This can be explained by the increase in the water carrying capacity (WCC) of the reactant gases according to Eq. (6-12) and Eq. (6-13) as the temperature increases. Moreover, as shown in Table 6-7, the net water diffusion flux (F_{EOD} - F_{BD} - F_{HP}) increases as the temperature increases at a fixed current density, which means more water migrates to cathode. However, the increase in temperature enhances the amount of water carried by the anode gases. Calculated by Eq. (6-12), when the inlet gases are fully humidified, the molar fractions of water are 0.196 at 60 °C and 0.468 at 80 °C. Although the increase in temperature reinforces the net water diffusion flux through the membrane, the increase in WCC of the anode gas compensates for the loss of water at the anode side of the membrane leading to a relatively higher membrane water content. In addition, as shown in Table 6-7, the water diffusion flux driven by the hydraulic permeation can be neglected as it is three orders of magnitude less than the water diffusion fluxes driven by the EOD and back diffusion.

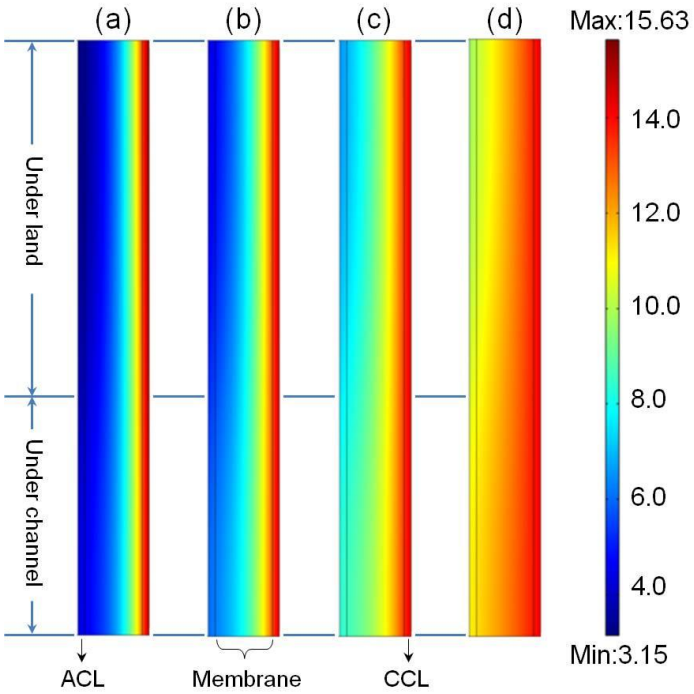

Figure 6-4 Membrane/ionomer water content profiles at (a) 60 °C, 0.7 A cm^{-2} (0.32 V), (b) 70 °C, 0.7 A cm^{-2} (0.39 V), (c) 80 °C, 0.7 A cm^{-2} (0.42 V) and (d) 80 °C, 0.2 A cm^{-2} (0.61 V) with fully humidified inlet gases

The water contents at a fixed temperature with various current densities are shown in Figure 6-4(c) and Figure 6-4(d). At lower current density, a relative small change in water content is observed due to the lower amount of drag. When the current density increases, the water content becomes more non-uniform since the anode dehydrates and the cathode water content increases. It is clear in Figure 6-4 that the minimum water content, with the value of 3.15, is observed at the anode side of the membrane (ionomer in the anode CL) while the water content reaches the equilibrium level at the cathode side of the membrane, which agrees with the experimental data of Buchi and Scherer [246]. Moreover, anode dehydration is more severe under the land than that under the channel, which can be explained by the higher water migration flux driven by the EOD.

6.3.4 Effect of temperature on fuel cell performance

The predicted polarisation curves obtained using the isothermal and non-isothermal models for the operating temperature from 60 to 80 °C are shown in Figure 6-5. At 60 and 70 °C, the cell performance is expected to improve as the operating temperature increases and the predicted current densities are higher obtained using the non-isothermal model than that of the isothermal model. This can be explained by the increase in the cathode exchange current density (Eq. 3-109) and transfer coefficient (Eq. 3-107) and the decrease in liquid water saturation resulting from the temperature increase in the MEA, the cathode catalyst layer in particular. However, at 80 °C, the current density predicted using the non-isothermal model is lower than that of the isothermal model, which is consistence to the simulation result of Abdollahzadeh *et al.* [257]. This can be explained by the decrease in the oxygen mole fraction as the temperature increases. Without considering the temperature increase in the MEA, the oxygen mole fraction is 11.2% at 80 °C with fully humidified gas. Then it decreases to 9.7% when approximate 3.4 °C increase in temperature is taken into account. The insufficient oxygen limits the cell performance at higher current densities when the relative humidity is 100%. It can be concluded that lower cathode relative humidity is required when fuel cells are operated at higher temperatures, e.g. higher than 80 °C.

It is also clear that the increase in temperature from 60 to 70 °C leads to a greater improvement on the cell performance than that from 70 to 80 °C. At a fixed cell voltage of 0.3V, as the temperature increases from 60 to 70 and 80 °C, the ionic conductivity of the membrane increases from 4.88 to 6.08 and 8.14 S m^{-1}, and the liquid water

saturation decreases from 0.057 to 0.054 and 0.047, respectively. Compared with the increase in temperature from 60 to 70 °C, the temperature change from 70 to 80 °C makes a greater contribution towards increasing membrane conductivity and reducing oxygen transport resistance. However, the oxygen fraction of the cathode inlet gases decreases from 16.9% at 60 °C to 14.5% at 70 °C, and to 11.2% at 80 °C. The depletion of oxygen results in a limitation of the cathode performance since the cathode volumetric current density increases from 377.5 A cm^{-3} at 60°C to 450.7 A cm^{-3} at 70°C, and to 490.8 A cm^{-3} at 80 °C. It is clear the increase in cathode volumetric current density is much smaller as the temperature changes from 70 to 80 °C than that change from 60 to 70 °C. Consequently, only increasing the operating temperature is prone to lead to the oxygen starvation on the cathode, which is a limitation to the improvement of the cell performance, unless the relative humidity of the cathode inlet gas is reduced simultaneously.

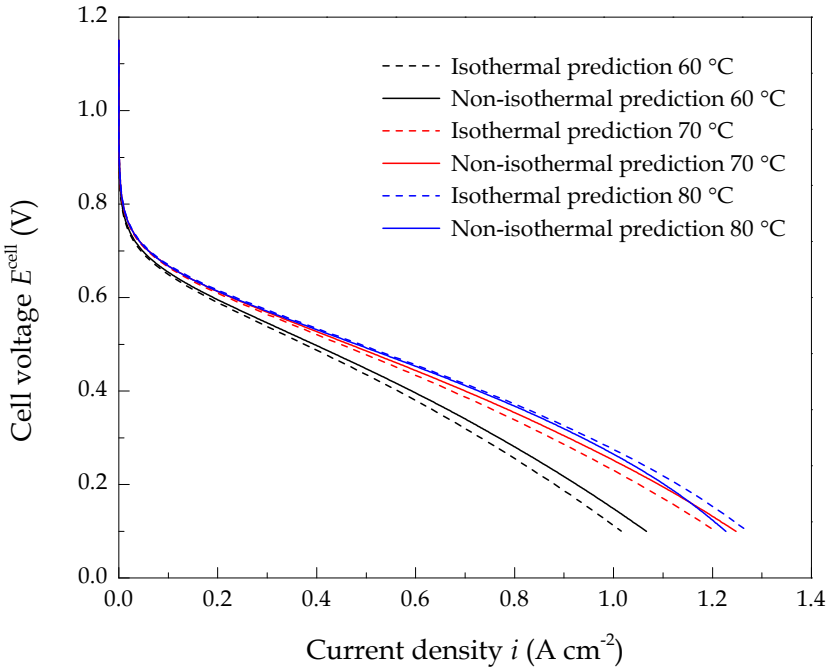

Figure 6-5 Polarisation curves at three operating temperatures with fully humidified inlet gases

6.4 Optimise the temperature distribution and improve the cell performance

Although numerous researchers studied the effect of temperature on fuel cell performance [79, 186, 188, 253], few of them applied different temperatures on the anode and cathode, respectively. The effects of channel geometry and the widths of channel and shoulder were studied by Ahmed and Sung [258, 259] and Wang *et al.*

[260]. Based on the analysis above, two parameters were varied to optimise the temperature distribution and improve the fuel cell performance in this section. This entailed increasing the operating temperature on the anode and the width ratio of the channel/rib, respectively.

6.4.1 Increasing the operating temperature on the anode

Due to the fact that higher inlet temperature increases the water carrying capacity (WCC) of the inlet gases, three anode temperatures and two cathode temperatures are applied to the current model to investigate the temperature effect on the polarisation curves. Note that heat conduction through the bipolar plates is not allowed as the single cell is assumed to being perfectly insulated. Figure 6-6 shows the polarisation curves with varying temperature on anode and cathode from 70 °C to 90 °C. It is clear that the increase in anode temperature increases the cell performance at higher current densities whereas it decreases the cell performance at lower current densities. However, the increase in cathode temperature is of benefit to the cell performance at lower current densities and makes a very slight change on the cell performance at higher current densities. When the inlet gases are fully humidified, the water mole fraction of the inlet gases increases from 19.6% at 60°C to 30.8% at 70 °C, and to 46.8% at 80 °C. According to Eq. (3-164), Eq. (3-165), Eq. (6-12) and Eq. (6-13), the membrane/ionomer water content is finally determined by the relative humidity of the reactant gas on the boundary of CL-GDL.

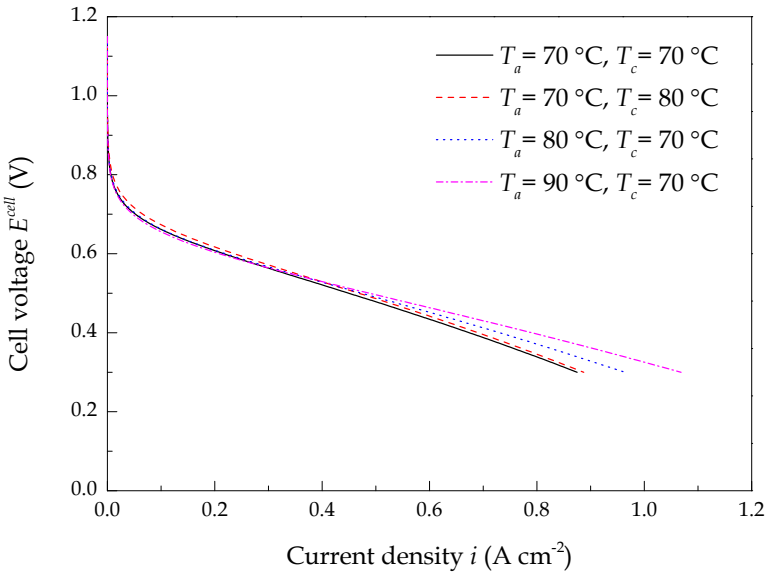

Figure 6-6 Polarisation curves at different anode and cathode temperatures with fully humidified inlet gases

As shown in Figure 6-4, the minimum membrane/ionomer water content is observed on the anode side of the membrane (ionomer in the anode CL). By increasing the anode temperature from 70 °C to 90 °C, the minimum membrane/ionomer water content increases from 3.9 to 5.8 at the cell voltage of 0.3 V, which results in an increase in the average ionic conductivity of the membrane from 6.1 S m^{-1} to 7.3 S m^{-1}. The increase in the ionic conductivity of the membrane is the main reason for the improvement of the cell performance at higher current densities. At lower current densities, the ionic conductivities of the membrane are almost the same for different temperatures on anode and cathode, i.e. at 0.8 V, when the cathode temperature is fixed at 70 °C, the ionic conductivities of the membrane are 11.1 S m^{-1} at the anode temperature of 70 °C and 11.2 S m^{-1} at the anode temperature of 90 °C, respectively. In this situation, the membrane conductivity is not the most important factor in determining the cell performance. The decrease in fuel cell performance at lower current densities can be explained by the decrease in hydrogen mole fraction resulting from the increase in the water carrying capacity (WCC) as the anode temperature increases. As shown in Figure 6-6, only increasing the cathode temperature makes very limited improvement in the current density at lower cell voltage because the average oxygen mole fraction in cathode catalyst layer decreases from 6.6% to 4.3% as the cathode temperature increases from 70 °C to 80 °C. Even when the ORR rate is increased, the lack of oxygen remains a barrier to improving the performance of the cell. However, the increase in the cathode temperature improves the cell performance at higher cell voltage which can be explained by the increased ORR rate as the cathode temperature increases.

The temperature profiles at two different anode and cathode temperatures are shown in Figure 6-7. In the first condition, the anode and cathode temperatures are set to 70, 80 °C, respectively. In the second condition, the anode and cathode temperatures are set to 80, 70 °C, respectively. It is clear that the temperature profiles of the two conditions are not the same even with the same temperature difference of 10 °C. The heat accumulation is observed at cathode when the higher temperature (80 °C) is applied at the cathode, which is due to the exothermic ORR occurring within the cathode catalyst layer. In this condition, heat transport from the cathode to anode results in an average membrane temperature increase of 9.2 °C. For the other condition, when the lower temperature (70 °C) is applied at the cathode, no heat accumulation occurs at the anode, which is because of the endothermic HOR within the anode catalyst layer as shown in

Table 6-5. It is believed that a certain amount of heat is absorbed by the HOR during the transport process from the anode to cathode, which leads to a decrease in temperature within the anode catalyst layer. Therefore, the average increase in temperature of the membrane is 4.9 °C, which is much smaller than that of the first condition.

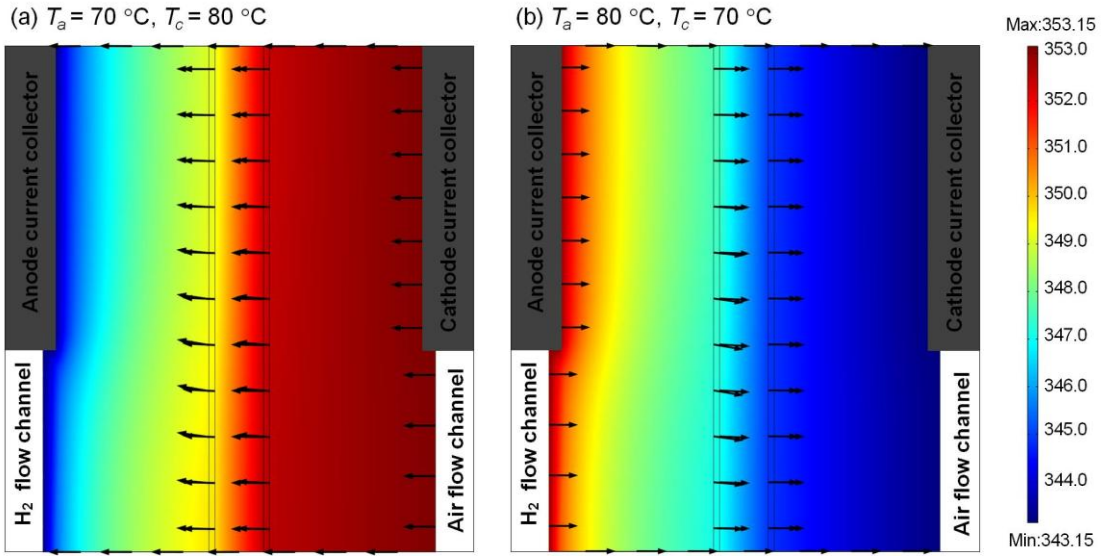

Figure 6-7 Temperature profiles at two conditions: (a) T_a = 70 °C, T_c = 80 °C, (b) T_a = 80 °C, T_c = 70 °C with fully humidified inlet gases

6.4.2 Increasing the width ratio of the channel/rib

The polarisation curves corresponding with different width ratios of the channel/rib from 0.4 to 0.8 are shown in Figure 6-8. It is clear that the increase in the width ratio of the channel/rib improves the cell performance during the full range of cell voltages, which can be explained by the increase in the reaction area of the oxygen with the cathode catalyst layer and the increase in the amount of water at both the anode and cathode.

By increasing the width ratio of the channel/rib from 0.4 to 0.6 and 0.8, the average membrane/ionomer water content increases from 6.1 to 6.4 and 6.7 at 0.3 V, respectively. However, the cell performance is improved slightly when the width ratio of the channel/rib increases from 0.6 to 0.8, which is due to the limitation of the ORR rate. Under this condition, although the oxygen mole fraction within the cathode catalyst layer increases from 6.6% to 8.3% and 9.5%, the average cathode volumetric current density increases from 450.74 to 494.82 and 506.44 A cm^{-3} as the width ratio of the channel/rib increases from 0.4 to 0.6 and 0.8, respectively. It is clear that the

increase in the cathode volumetric current density varies slightly as the width ratio of the channel/rib increases from 0.6 to 0.8. Consequently, it is believed that the sluggish ORR at the cathode is the main obstacle to the improvement of the cell performance. The temperature profiles of two different width ratios of channel/rib at 0.3 V are shown in Figure 6-9. By comparing with Figure 6-2, it is clear that the temperature gradient from the region under the channel to that under the land is reduced by increasing the width ratio of channel/rib, which is beneficial to preventing hot spots within the cathode catalyst layer and membrane.

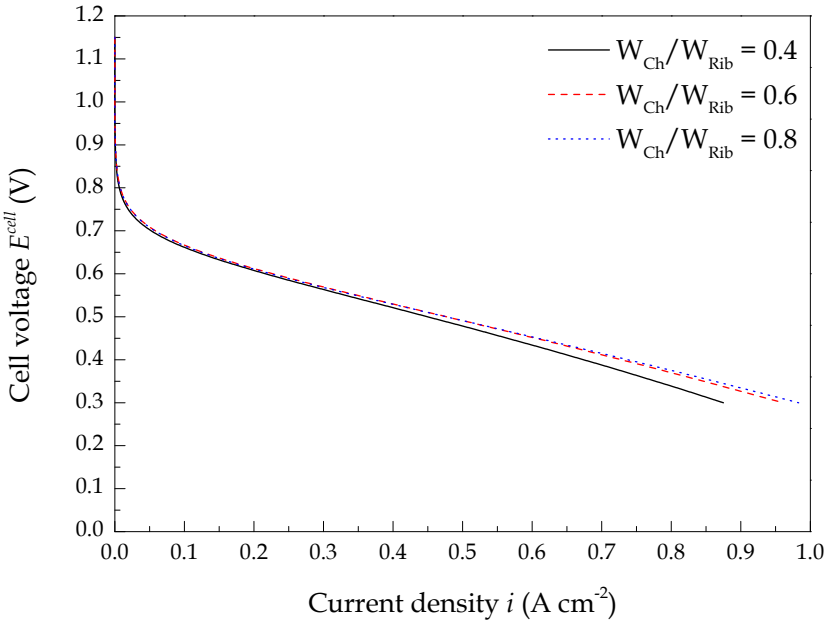

Figure 6-8 Polarisation curves with different width ratios of channel/rib and fully humidified inlet gases

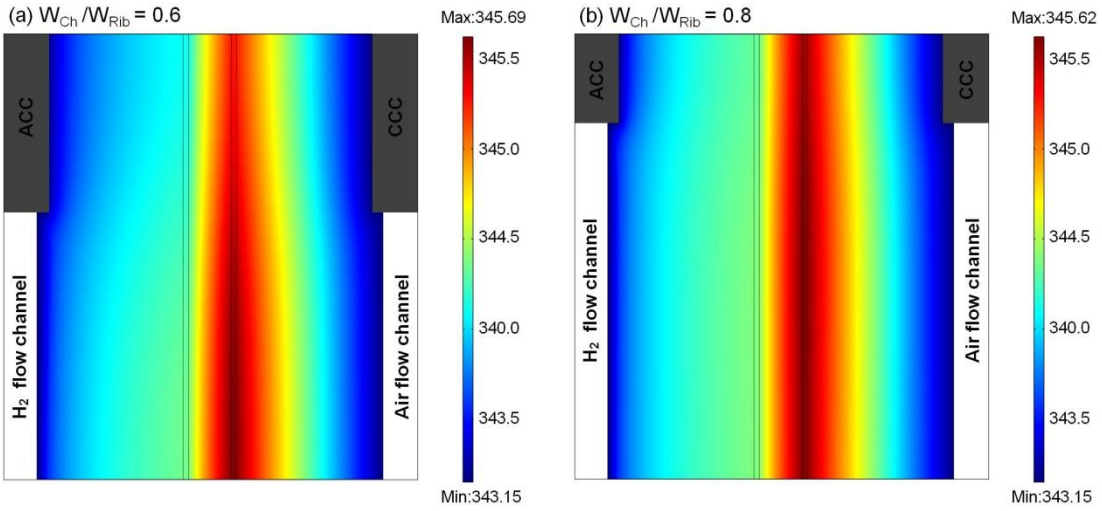

Figure 6-9 Temperature profiles with two different width ratios of channel/rib and fully humidified inlet gases

6.5 Conclusions

A two dimensional, across the channel, steady-state model for a proton exchange membrane fuel cell is developed in which the non-isothermal model for temperature distribution, the two-phase flow model for liquid water saturation and the agglomerate model for oxygen reduction reaction are fully coupled. The properties of the catalyst layer, such as porosity, volume fractions of platinum, carbon and ionomer, as well as the thicknesses of the ionomer and liquid water coatings are calculated. The water phase-transfer between vapour, dissolved water and liquid water and the associated heat generation and absorption are addressed in the non-isothermal, two-phase flow model which shows greater accuracy in validating the experimental data in comparison with the single-phase flow model. The dissolved water transport through the membrane is described by the combinational mechanism, in which the driving forces of electro-osmotic drag, back diffusion and hydraulic permeation are all considered. Nafion® ionomer swells in contact with water vapour, leading to an increase in the ionomer coating thickness and a decrease in catalyst layer porosity. Such effects resulting from ionomer swelling is included. In addition, the oxygen diffusivity and solubility through Nafion® ionomer are related to both temperature and ionomer water content, which could give a more accurate description on oxygen transport properties inside the cathode catalyst layer.

The increase in operating temperature at a fixed current density improves the cell performance by increasing the membrane/ionomer water content and reducing the liquid water saturation. Applying higher temperatures on the cathode increases the ORR kinetics, thus improves the cell performance at lower current density. However, higher temperatures on the cathode also decrease the oxygen mole fraction when the cathode gases are fed at fully humidity, which probably leads to an oxygen starvation that then limits the cell performance, unless the relative humidity of the cathode inlet gas is reduced simultaneously. As a new thermal management strategy, applying higher temperatures on the anode increases the water carrying capacity (WCC) of the anode gas which improves the cell performance at higher current densities.

The amount of water and heat generated by the ORR inside the CCL occupy a majority of total amount of water and heat generation and consumption. For example, at a fixed current density of 0.7 A cm^{-2}, ORR corresponds to at least 94% and 67% of total amount of water and heat, respectively. In accounting for the factors influencing water

transport through the membrane, the hydraulic permeation can be neglected as it is three orders of magnitude less than the EOD and back diffusion. The modelling results indicate that heat accumulates within the CCL in the region under the channel, resulting in an approximate 3.0 °C increase in temperature at the cell voltage of 0.3 V. Applying higher temperatures on the anode and lower temperatures on the cathode is capable of optimising the temperature distribution within the MEA. Moreover, enlarging the width ratio of channel/rib improves the cell performance. However, the improvement is limited by the sluggish ORR.

The model developed can give a theoretical guidance on optimisation of channel width and operating temperature for the purpose of cell performance improvement.

Chapter 7. Cathode catalyst layer optimisation

In this chapter, five design parameter of the cathode catalyst layer, namely platinum loading (m_{Pt}), platinum mass ratio (f), ionomer volume fraction (L_M), catalyst layer thickness (l_{CL}) and agglomerate radius (r_{agg}) are optimised by a multiple surrogate model and their sensitivities are analysed by a Monte Carlo method based approach. Two optimisation strategies, maximising the current density at a fixed cell voltage and during a specific cell voltage range, are implemented for the optima prediction.

7.1 Introduction

Although significant improvements on PEMFC performance have been achieved over the last ten years, the high cost associated with platinum catalyst is one of the major barriers hampering the commercial use of PEMFCs. Since platinum is dispersed within carbon black and combines with electrolyte to construct the catalyst layer, the performance depends on how effectively the platinum is dispersed, i.e. the effectiveness of the catalyst layer [215]. Accordingly, the function of different component within the catalyst layer requires the existence of triple phase boundaries (TPB) [176], where the content of ionomer (for proton transfer), void space (for gas transport) and platinum dispersed carbon (for catalysis and electron transfer) interacted [21, 177, 239, 261, 262]. As a result, optimisation of the composition and structure of the electrode is important.

Traditionally, the optimum composition and structure of the catalyst layer is conducted through experiments [177, 239, 261, 262], which are expensive and time-consuming. Computer simulations facilitate the exploration of alternative designs and reduce the resource and time for producing expensive prototypes. Numerical simulations also help the design and optimisation of a fuel cell, there has been many studies in this area [47, 115, 263-269]. For instance, Wu *et al.* [145] investigated the optimal operating conditions of hydrogen polymer electrolyte fuel cells based on the radial basis function (RBF) surrogate model. Tirnovan *et al.* [263, 264] applied a moving least squares (MLS) model for the PEMFC, and proved that the method was suitable for predicting and describing the fuel cell behaviour in all points of the approximation domain. Zervas *et al.* [265] utilised radial basis function (RBF) neural network architecture for optimizing the operation of fuel cells systems. Wahdame *et al.* [266] reviewed design of experiment (DoE) techniques for fuel cell characterisation and

development. Miao and Cheng *et al.* [267, 270] presented an approach to improve the performance of the power density of a PEMFC based on artificial neural network (ANN) metamodel.

The design optimisation of PEMFC is challenging due to several factors: (a) fuel cell simulation is still lengthy and complicated, (b) there are many design variables to be considered, (c) design variables are interdependent, (d) multiple design objectives are desired simultaneously and multiple design constraints need to be satisfied, (e) conventional sensitivity-based optimisation method is not suitable for the local sensitivity issues. In addition, most of the aforementioned research adopted maximising the current density at a specific voltage as the optimisation objective. However, PEMFCs do not usually work at a fixed voltage, the voltage condition always has a certain variation as the environments surrounding it and other factors, such as operating temperature [271], always change. For this reason, the present study concerns both optimisation of the PEMFC at specific voltages and within specific voltage ranges.

To solve these problems, a surrogate model technique is introduced in this chapter, which could formulate an explicit relationship between the objective/constraint functions and design variables in terms of a few computer simulations and thus it can calculate the local sensitivity quickly and efficiently. An optimisation algorithm is implemented to search for the global optimum designs and a global sensitivity analysis based on Monte Carlo (MC) method is carried out to examine the influence of design variables on the fuel cell performance.

7.2 Mathematical model

The mathematical model developed in Chapter 4 is used to describe the mass balance and transport, reactant diffusion and reaction, water transport through the membrane, charge conservation and current distribution coupled in the PEMFCs. Water phase transfer, two-phase flow, and non-isothermal operation are not included in this model. In order to account for the liquid water generation at high current density, we assume that liquid water fills the primary pores inside the agglomerate only. The same assumption can be found from the work of Marr *et al.* [85].

Another highlighted feature of this model is the effective diffusion coefficient. In order to account for gas diffusion in anisotropic porous electrodes, the effective

diffusion coefficient is corrected by the percolation theory presented by Nam and Kaviany [114] instead of the Bruggeman's factor as follow:

$$f(\varepsilon) = \varepsilon\left(\frac{\varepsilon - \varepsilon_{pc}}{1-\varepsilon_{pc}}\right)^{\chi} \qquad \chi = \begin{cases} 0.521 & in-plane \\ 0.785 & through-plane \end{cases} \tag{7-1}$$

where ε_{pc} is the percolation critical value of the porosity. $\varepsilon_{pc} = 0.11$ reported by Pharoah *et al.* [272]. As assumed previously, the primary pores can be completely filled by liquid water. Then oxygen diffuses through the secondary pores to the outer boundary of the ionomer film. The effective diffusion coefficient of oxygen diffusion in catalyst layer is:

$$D_{O_2,CL}^{eff} = f(\varepsilon_s) D_{O_2-P}^{0} \tag{7-2}$$

The effective diffusion coefficient of oxygen within agglomerate is

$$D_{O_2,agg}^{eff} = f(\varepsilon_{agg,M}) D_{O_2-M}^{0} + f(\varepsilon_{agg,p}) D_{O_2-W}^{0} \tag{7-3}$$

$D_{O_2-M}^{0}$, $D_{O_2-W}^{0}$ and $D_{O_2-P}^{0}$ (m^2 s^{-1}), which have been explained in Chapter 3, are the intrinsic diffusion coefficients of oxygen through ionomer film, liquid water and void space, respectively.

The boundary conditions and computational process are as same as that of the two dimensional, along the channel, single phase, isothermal model represented in Chapter 4.

7.3 Model verification and validation

7.3.1 Mesh independence

Theoretically, the calculating errors in the solution related to the grid must disappear for an increasingly fine mesh. In this study, the current density at a certain cell voltage (0.7V) is taken as the parameter to evaluate six grids (see Table 7-1) and determine the influence of the number of nodes on the solution. It is clear in Figure 7-1 that the current density reaches an asymptotic value while the calculating time increases as the number of nodes increases. Having considering both the calculation time and accuracy in this work, Grid D is selected as it is considered to be sufficiently reliable to ensure mesh independence with acceptable calculating time.

Table 7-1 Characters of mesh sizes

Mesh characteristics	Number of nodes
Grid A	6894
Grid B	31490
Grid C	110290
Grid D	262055
Grid E	434290
Grid F	648265

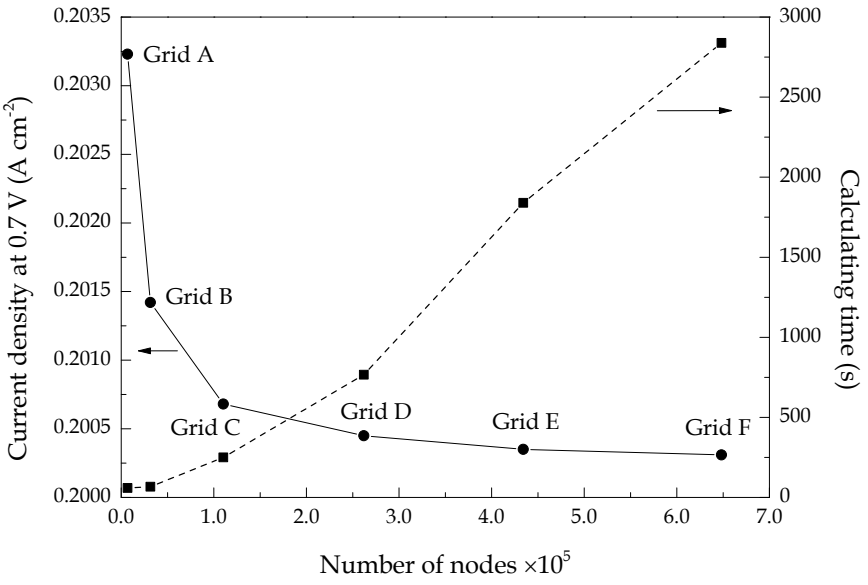

Figure 7-1 Influence of mesh characteristics on current density

7.3.2 Model validation

The modelling results are validated by the experimental data in Figure 4-3 of Chapter 4, in which the predicted polarisation curves agree well with the experimental data. Thus the numerical model is proven to be sufficiently accurate.

7.4 Global sensitivity analysis and design optimisation

Global sensitivity analysis (GSA) and design optimisation are increasingly recognised as useful tools for the analysis and design of PEMFCs. The former is able to determine the influence of design variables on a PEMFC. The latter could help identify the optimum design under different conditions. However, a global sensitivity analysis and/or design optimisation of a fuel cell is still a challenging endeavour because the

relations between design variables and design objectives/constraints are often not explicitly known. A function of a certain design can generally be found from a large number of time-consuming numerical calculations. To do this, explicitly known approximations of objective/constraint functions in terms of a few sampling data obtained from computer simulations can be used, which is called a surrogate model (also called metamodel technique).

The optimisation in this chapter adopts a widespread used surrogate model- Kriging (KRG) model- to evaluate the approximation models of the objective functions. The approximation models are then used to visualise the input-output relationship, assess the effect of each design variable and predict the optimum design of the cathode catalyst layer.

7.4.1 Kriging Surrogate models

Kriging model was originally developed for mining and geostatistical application involving spatially and temporally correlated data [273, 274]. Kriging model postulates a combination of a global model combined with departures:

$$y(\tilde{x}) = f(\tilde{x}) + Z(\tilde{x}) \tag{7-4}$$

where $y(\tilde{x})$ is the unknown function of interest, $f(\tilde{x})$ is a known polynomial, and $Z(\tilde{x})$ is assumed as a Gaussian random process with mean zero and variance σ^2 as well as a non-zero covariance to create local deviations so that Kriging model interpolates the sampled data points. The covariance matrix of $Z(\tilde{x})$ is formulated as

$$Cov[Z(\tilde{x}^i), Z(\tilde{x}^j)] = \sigma^2 \mathbf{R} \quad \mathbf{R} = [R(\tilde{x}^i, \tilde{x}^j)] \tag{7-5}$$

where $\mathbf{R}$ is the symmetric correlation matrix with ones along the diagonal, and $R(\tilde{x}^i, \tilde{x}^j)$ is the correlation function between any two sampled data points $\tilde{x}^i$ and $\tilde{x}^j$. The correlation function could be exponential, Gaussian, cubic or other kinds of functions. In this work, the Gaussian correlation function is assumed:

$$R(\tilde{x}^i, \tilde{x}^j) = \exp\left(-\sum_{k=1}^{n_{dv}} \theta_k \left| \tilde{x}_k^i - \tilde{x}_k^j \right|^2 \right) \tag{7-6}$$

where n_{dv} is the number of design variables, θ_k are the unknown correlation parameters used to fit the model, and $\left|\tilde{x}_k^i - \tilde{x}_k^j\right|$ is the distance between the k-th components of sample points $\tilde{x}^i$ and $\tilde{x}^j$. Once the correlation function has been selected, the estimate, $\hat{y}$, of the response $y(\tilde{x})$ at untried values of $\tilde{x}$ are given as:

$$\hat{y} = \hat{\beta} + \mathbf{r}^{\mathbf{T}}(\tilde{\mathbf{x}})\mathbf{R}^{-1}(\mathbf{y} - \mathbf{f}\hat{\beta}) \tag{7-7}$$

where $\mathbf{y}$ is the column vector of length n_s which contains the sample values of the response, and $\mathbf{f}$ is an column vector of length n_s which is filled with ones when $f(\tilde{x})$ is taken as constant. $\mathbf{r}^{\mathbf{T}}(\mathbf{x})$ is the correlation vector between a untried $\tilde{x}$ and the sampled data points:

$$\mathbf{r}^{\mathbf{T}}(\tilde{\mathbf{x}}) = [R(\tilde{x}, \tilde{x}^1), R(\tilde{x}, \tilde{x}^2), ..., R(\tilde{x}, \tilde{x}^{n_s})]^{\mathbf{T}} \tag{7-8}$$

and $\hat{\beta}$ is estimated as

$$\hat{\beta} = (\mathbf{f}^{\mathbf{T}}\mathbf{R}^{-1}\mathbf{f})^{-1}\mathbf{f}^{\mathbf{T}}\mathbf{R}^{-1}\mathbf{y} \tag{7-9}$$

The estimate of variance of the sample data from the global model is

$$\hat{\sigma}^2 = \frac{(\mathbf{y} - \mathbf{f}\hat{\beta})^{\mathbf{T}}\mathbf{R}^{-1}(\mathbf{y} - \mathbf{f}\hat{\beta})}{n_s} \tag{7-10}$$

where $f(\tilde{x})$ is assumed to be the constant $\hat{\beta}$. The maximum likelihood estimates (i.e., "best guesses") for θ_k in Eq. (7-6) used to fit the model can be found by solving the following maximisation problem over the interval $\theta_k > 0$:

$$\max . \left(-\frac{n_s \ln(\hat{\sigma}^2) + \ln|\mathbf{R}|}{2} \right) \tag{7-11}$$

where both $\hat{\sigma}^2$ and $|\mathbf{R}|$ are the functions of θ_k.

7.4.2 Sobol' Global sensitivity analysis

There are two kinds of sensitivities, one is called local sensitivity and the other is global sensitivity. Local sensitivity is equivalent to the partial derivative, which is

usually used to locally estimate the sensitivity of an objective to a specific design variable. On the contrary, global sensitivity characterises the overall behaviour of a specific design variable on a system or model. GSA can increase the understanding of the relationships between design variables and design objective and classify the individual variable influence, hence help researcher to pay more attention on the design variables with large influence, and remove design variables with less influence. Among many kinds of GSA methods, Sobol' method [275, 276] is used to do it in this work. The Sobol' method is a variance-based Monte Carlo method that allows the computation of both the sensitivity indices of individual parameters, S_i , and the interactions between these parameters through the ratio of each sensitivity index to the corresponding total sensitivity index, S_i^{tot} . Specifically, considering an integrable function, $f(\tilde{\mathbf{x}})$, which can be written in the form:

$$f(\tilde{\mathbf{x}}) = f_0 + \sum_{s=1}^{n} \sum_{i_1<\ldots<i_s}^{n} f_{i_1\ldots i_s}\left(\tilde{x}_{i_1},\ldots,\tilde{x}_{i_s}\right) \tag{7-12}$$

where $1 \le i_1 < \cdots < i_s \le n$, $f_{i_1\ldots i_s}\left(\tilde{x}_{i_1},\ldots,\tilde{x}_{i_s}\right)$ is a function of a unique subset of variables from $\tilde{\mathbf{x}}$. The components $f_i(\tilde{x}_i)$ are called the first order terms, $f_{ij}(\tilde{x}_i,\tilde{x}_j)$ are the second order terms and so on. The total number of summands in Eq. (7-12) is $2n$. Eq. (7-12) is also called the ANOVA representation of $f(\tilde{\mathbf{x}})$ if

$$\int_0^1 f_{i_1\cdots i_s}\left(\tilde{x}_{i_1},\cdots,\tilde{x}_{i_s}\right) d\tilde{x}_k = 0 \quad for\ k = i_1,\cdots,i_s \tag{7-13}$$

It follows from condition Eq. (7-13) that the members in Eq. (7-12) are orthogonal and can be expressed as integrals of $f(\tilde{\mathbf{x}})$. Assume now that $f(\tilde{\mathbf{x}})$ is square integrable, then all the $f_{i_1\ldots i_s}$ in Eq. (7-13) are square integrable as well. Squaring Eq. (7-13) and integrating over the n-dimensional unit hypercube, the following equation can be obtained:

$$\tilde{D} = \int f^2(\tilde{\mathbf{x}}) d\tilde{\mathbf{x}} - {f_0}^2 = \sum_{s=1}^{n} \sum_{i_1<\cdots<i_s}^{n} \int {f^2}_{i_1\cdots i_s} d\tilde{x}_{i_1} \ldots d\tilde{x}_{i_s} = \sum_{s=1}^{n} \sum_{i_1<\ldots<i_s}^{n} \int \tilde{D}_{i_1\cdots i_s} \tag{7-14}$$

where $\tilde{D}_{i_1\cdots i_s}$ is the partial variance in the model response brought about by simultaneous changes in factors i_1 to i_s and D is the total variance of $f(\tilde{x})$. Then the global sensitivity indices of each variable can be calculated in terms of following equation:

$$S_{i_1\cdots i_s}=\frac{\widetilde{D}_{i_1\cdots i_s}}{\widetilde{D}} \tag{7-15}$$

This method can be extended to evaluate the global sensitivity indices of an arbitrary set of m variables. Let *y* denote the set of m variables ($1\le m\le n-1$), and *Z* denote the set of *n-m* complementary variables, thus $\widetilde{x}=(y,z)$, let $K=(k_1,\cdots,k_m)$. The variance corresponding to the subset y can be defined as

$$\widetilde{D}_y=\sum_{s=1}^{m}\sum_{(i_1<\cdots<i_s)\in K}^{m}\int\widetilde{D}_{i_1\cdots i_s} \tag{7-16}$$

The sum in Eq. (7-16) is extended over all groups ($i_1,\cdots,i_s$) where all the $i_1,\cdots,i_s$ belongs to *K*. Similarly, the variance D_z can be obtained. Then the total variance corresponding to the subset *y* is

$$\widetilde{D}_y^{tot}=\widetilde{D}-\widetilde{D}_z \tag{7-17}$$

Note that $\widetilde{D}_y^{tot}$ is also a sum of $S_{i_1\cdots i_s}$, but it is extended over all group ($i_1,\cdots,i_s$) where at least one $i_l\in K$. Here $1\le s\le n$. Therefore the individual sensitivity indices (or main sensitivity indices) and the total sensitivity indices can be calculated as follows:

$$S_y=\frac{\widetilde{D}_y}{\widetilde{D}} \tag{7-18}$$

$$S_y^{tot}=\frac{\widetilde{D}_y^{tot}}{\widetilde{D}} \tag{7-19}$$

It is obvious that $S_y^{tot}=1-S_z$ and always $0\le S_y\le S_y^{tot}\le 1$. Then a Monte Carlo method can be conducted to calculate the sensitivity indices.

7.5 Optimisation formulation

The performance of a PEMFC is often characterised by its polarisation behaviour, i.e. voltage versus current density. For design optimisation of a specific PEMFC, the objective is usually set to maximise the current density at given cell voltages and other constraint conditions. That is, a fixed voltage is usually assumed beforehand, and current density at this voltage is maximised by using optimisation methods. However, a PEMFC does not always work at one fixed voltage but usually works within a varying

range of cell voltage based on different environment and work conditions. This variation of the cell voltage means that the optimal design obtained based on one fixed cell voltage is not necessarily the best design for other voltages. Consequently, the so-called optimal design cannot produce the best performance when the voltage changes in the fluctuation range. To avoid this problem, a new objective function considering the average performance of a PEMFC within a given range of cell voltage is added. There are two optimisation strategies, strategy A and B, corresponding formulations in this work, which are presented as follows.

Strategy A: the common formulation at fixed cell voltage:

$$\begin{cases} find \quad \tilde{\mathbf{x}}_i(m_{Pt}, f, L_M, l_{CL}, r_{agg}) \\ \begin{cases} max. \quad i_i \left(at \ \ fixed \ \ E_i\right) \\ s.t. \begin{cases} \varepsilon_{pc} \le \varepsilon_{CL} \le 1.0 \\ 0 < L_{Pt/C} < 1.0 \\ \tilde{\mathbf{x}}_{LB} \le \tilde{\mathbf{x}}_i \le \tilde{\mathbf{x}}_{UB} \end{cases} \end{cases} \end{cases} \tag{7-20}$$

where i_i is the current density at a fixed cell voltage E_i, and integral i varies from 1 to 9, corresponding to the cell voltage from 0.2V to 1.15V (OCP at base-case conditions), respectively. There are five design variables, m_{Pt} (mg cm^{-2}) is the platinum loading, f is the platinum mass ratio, L_M is the ionomer volume fraction in cathode catalyst layer, l_{CL} (m) is the catalyst layer thickness, r_{agg} (m) is the agglomerate radius, the bound of each variable is listed in Table 7-2. In addition, other two parameters ε_{CL} and $L_{Pt/C}$ are both constrained in the range of ε_{pc}~100% and 0 ~100%, respectively.

Strategy B: the new one for a specific range of cell voltage:

$$\begin{cases} find \quad \tilde{\mathbf{x}}_{ij}(m_{Pt}, f, L_M, l_{CL}, r_{agg}) \\ \begin{cases} max. \quad \bar{i}_{ij} \left(from \ E_i \ to \ E_j\right) \\ s.t. \begin{cases} \varepsilon_{pc} \le \varepsilon_{CL} \le 1.0 \\ 0 < L_{Pt/C} < 1.0 \\ \tilde{\mathbf{x}}_{LB} \le \tilde{\mathbf{x}}_i \le \tilde{\mathbf{x}}_{UB} \end{cases} \end{cases} \end{cases} \tag{7-21}$$

where $\bar{i}_{ij}$ is the average current density for the cell voltage from E_i to E_j, integral i is smaller than integral j, $\tilde{\mathbf{x}}_{ij}$ is the vector of the optimal design variables.

In strategies A and B, the objectives are to find the optimal design $\tilde{\mathbf{x}}_i$ which is capable of maximising the current dentsities at a fixed cell voltage or during a specific cell voltage range subjected to the following constrains: (1) the catalyst layer porosity between the percolation critical value and 1; (2) the volume fraction of *Pt/C* between 0 and 1; 3). the design variables between the lower boundary and upper boundary.

Table 7-2 Lower and upper bound of design variables for the optimisation

Design parameters	Description (Unit)	Lower bound	Upper bound
m_{Pt}	Platinum loading (mg cm^{-2})	0.1	1.0
f	Platinum mass ratio to *Pt/C*	0.2	0.8
L_M	Electrolyte volume fraction	0.05	0.5
l_{CL}	Catalyst layer thickness (μm)	5.0	30.0
r_{agg}	Agglomerate radius (μm)	0.1	1.0

7.6 Implementation of the optimisation process

The proposed simulation-based optimisation approach consists of the following 7 steps as shown in Figure 7-2.

1. Optimisation problem, including design variables, ranges of variables, design objectives and design constraints, are defined.
2. A sampling strategy is determined and a series of sampling points are generated in the design domain, numerical simulations are carried out at these sampling points and corresponding response values are collected.
3. Constructing the surrogate models (KRG) based on the sample data. Note that the KRG model cannot be explicitly obtained as the second term in the right hand of Eq. (7-4) varies significantly for different estimated design.
4. Checking the accuracy of the surrogate models, if the accuracy satisfies the required criterion, then it goes to the next step, otherwise, more sampling data should be added in terms of sequential sampling strategies [277] and new surrogate models with more accuracy are constructed.
5. Combining optimisation algorithm with the surrogate models to search the optimum design under specific working condition.

6. Validating the optimisation results, the validation result can generally be satisfied if the sampling data generated above is sufficient enough and the right surrogate model is employed. However, this step remains necessary to guarantee the optimum designs have the best performance. In case of error between the predicted optimal design and validation design, new infill sampling data like those in the fourth step should be added and a new loop will stop until the validation results satisfy the desired criterion.

7. Carrying out GSAs in terms of the surrogate models to investigate the effects of design variables.

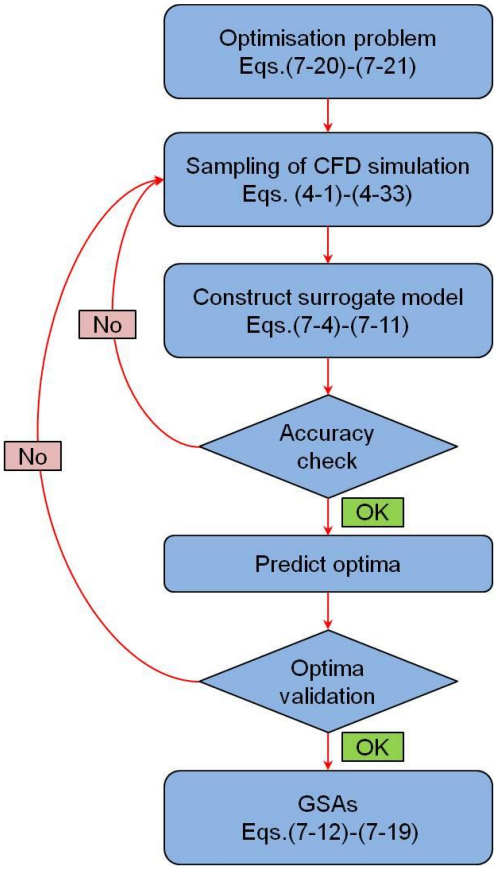

Figure 7-2 Flowchart of the optimisation process

7.7 Optimisation at a fixed cell voltage

The optimisation problem in Strategy A (Eq. 7-20) is solved in this section for three different cell voltages: low (0.2 V), medium (0.5 V) and high (0.8 V) which corresponds to a high, medium and low current densities. For each of these cases, the effect of structural parameters, including platinum loading, platinum mass ratio, catalyst layer thickness, ionomer volume fraction and agglomerate radius, on fuel cell performance is studied. In addition, as mentioned above, the optimal design obtained is

taken into the agglomerate model as a new design to validate the optimisation results. In this model, coordinates *X* and *Y* refer to diffusion and flow direction, respectively.

7.7.1 Base design

The parameters of base design are presented in Table 7-3. For this initial design, the volume fractions of solid phase (ε_S), ionomer (L_M) and void space (ε_{CL}) of the cathode catalyst layer are 63.5%, 20.0% and 16.5% respectively. In this situation, the current density at 0.8, 0.5 and 0.2 V are 0.05, 0.46 and 0.52 A cm^{-2}, respectively. The optimal composition of catalyst layer is then obtained by solving the optimisation problems in Eq. (7-20) and Eq. (7-21). Then the polarisation curve, oxygen mole fraction, cathode overpotential and cathode volumetric current density for the base design in contrast to the optimal design are shown in figures from Figure 7-3 to Figure 7-5.

Table 7-3 Physical parameters for base-case conditions

Electrode parameters	*Value*
Platinum loading, m_{Pt} (mg cm^{-2})	0.4
Platinum mass ratio, f	0.2
Ionomer volume fraction, L_M	0.2
Catalyst layer thickness, l_{CL} (μm)	15.0
Agglomerate radius, r_{agg} (μm)	0.2
Operating conditions	*Value*
Operating temperature, T (K)	343
Anode pressure, p_a (atm)	1.0
Cathode pressure, p_c (atm)	1.0
Relative humidity, RH (%)	100
Anode stoichiometric flow ratio, ξ_a	1.2
Cathode stoichiometric flow ratio, ξ_c	2.0

Five design variables, platinum loading, platinum mass ratio, ionomer volume fraction, catalyst layer thickness and agglomerate radius are abbreviated as

$\{m_{Pt}, f, L_M, l_{CL}, r_{agg}\}$. At base design, the ionomer film thickness (δ_M) and agglomerate specific area (a_{agg}) are 1.55×10^{-8} m and 4.22×10^{7} m^{-1}, respectively.

7.7.2 Optimisation at low cell voltage

Figure 7-3 shows the polarisation curve, cathode overpotential, cathode volumetric current density and oxygen mole fraction for the base design and the optimal design at 0.2 V. The simulation results, based on the agglomerate model, agree very well with the optimisation results, with a maximum error of approximately 0.3% at lower current density. It is clear in Figure 7-3(a), at 0.2 V, the current density increases from 0.52 to 1.95 A cm^{-2} for the optimal design $\{m_{Pt}, f, L_M, l_{CL}, r_{agg}\}$={1.0, 80.0%, 7.0%, 5.0, 0.1}. For these values, ε_S, L_M and ε_{CL} are 40.1%, 7.0% and 52.9%, respectively. Moreover, the optimal design simultaneously decrease δ_M to 3.16×10^{-10} m and a_{agg} to 3.41×10^{7} m^{-1}. The increase in current density upon optimal design is due to the decrease in the ionomer film thickness and the increases in catalyst layer porosity. This is because the dramatic fall in current density at lower cell voltages is mainly due to the oxygen transport limitation through the ionomer film [85, 115] and within the void space of the porous electrode [21].

It is clear in Figure 7-3(b) that the absolute value of cathode average overpotential decreases from 0.89 to 0.55 V, resulting in an improvement in cell performance according to Eq. (4-21). The maximum absolute value of cathode overpotential is observed at the cathode outlet adjacent to the membrane where the biggest oxygen transport resistance exists. The overpotential on the cathode is negative, which results in the second term of Eq. (3-13) much smaller then is reasonable to omit. According to Eq. (3-13), the increase in the absolute value of cathode overpotential enhances the oxygen reduction reaction (ORR), leading to a relative higher cathode volumetric current density since overpotential is the driving force for the reaction rate. However, according to Eq. (4-21), higher overpotential decreases the current density of the cell. Consequently, optimal overpotential is required for the best performance of the cell. As shown in Figure 7-3(c), for optimal design, the cathode volumetric current density increases everywhere, but is less uniform, in the cathode catalyst layer. The biggest increase occurs at the CL-membrane interface near the cathode inlet where both the oxygen concentration and proton conductivity are relatively higher. The average cathode volumetric current density increases from 282.80 to 3892.87 A cm^{-3}. The

increase in current density can also be explained by the decrease in oxygen mole fraction as shown in Figure 7-3(d). The decrease in oxygen mole fraction and the increase in its gradient indicate a faster consumption of oxygen by applying the optimised parameters.

However, the optimal design performance is poorer than the base design at lower current densities, although it exhibits enhanced performance at higher current density which is because of the decrease in agglomerate specific area and then the decrease in ORR rate according to Eq. (3-31).

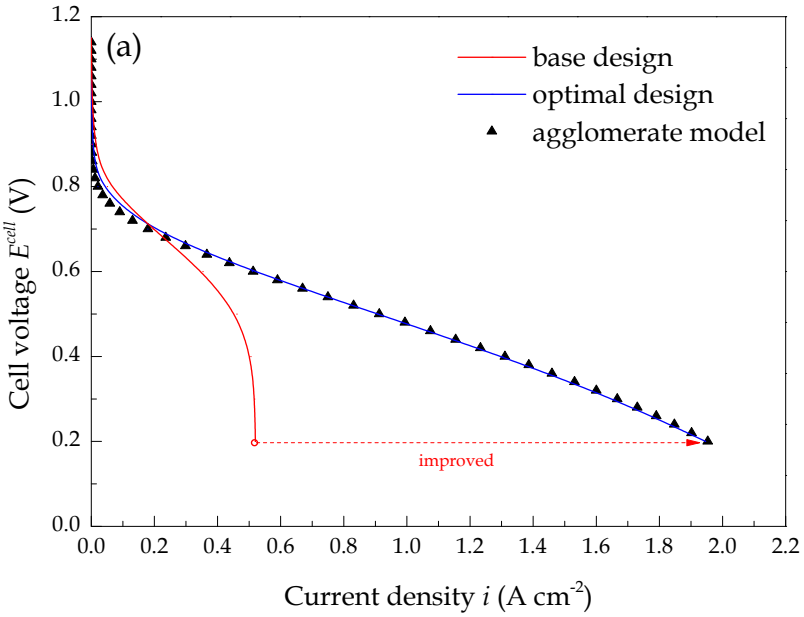

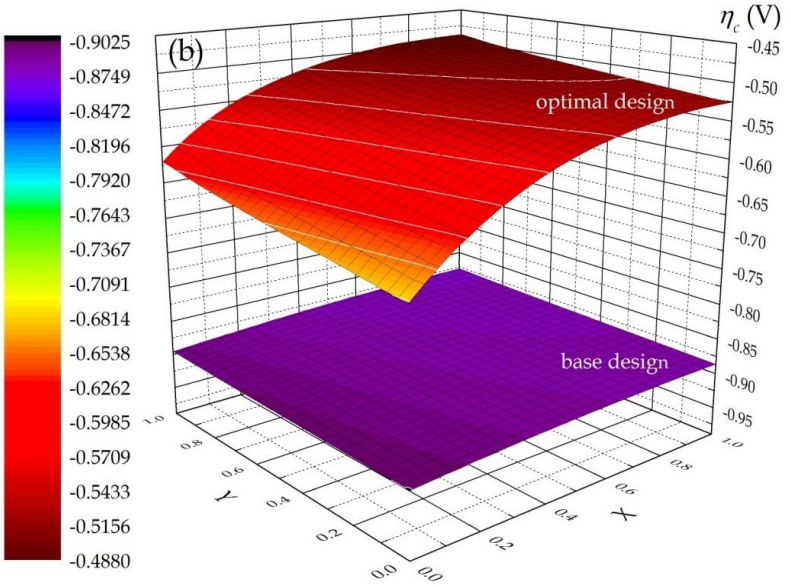

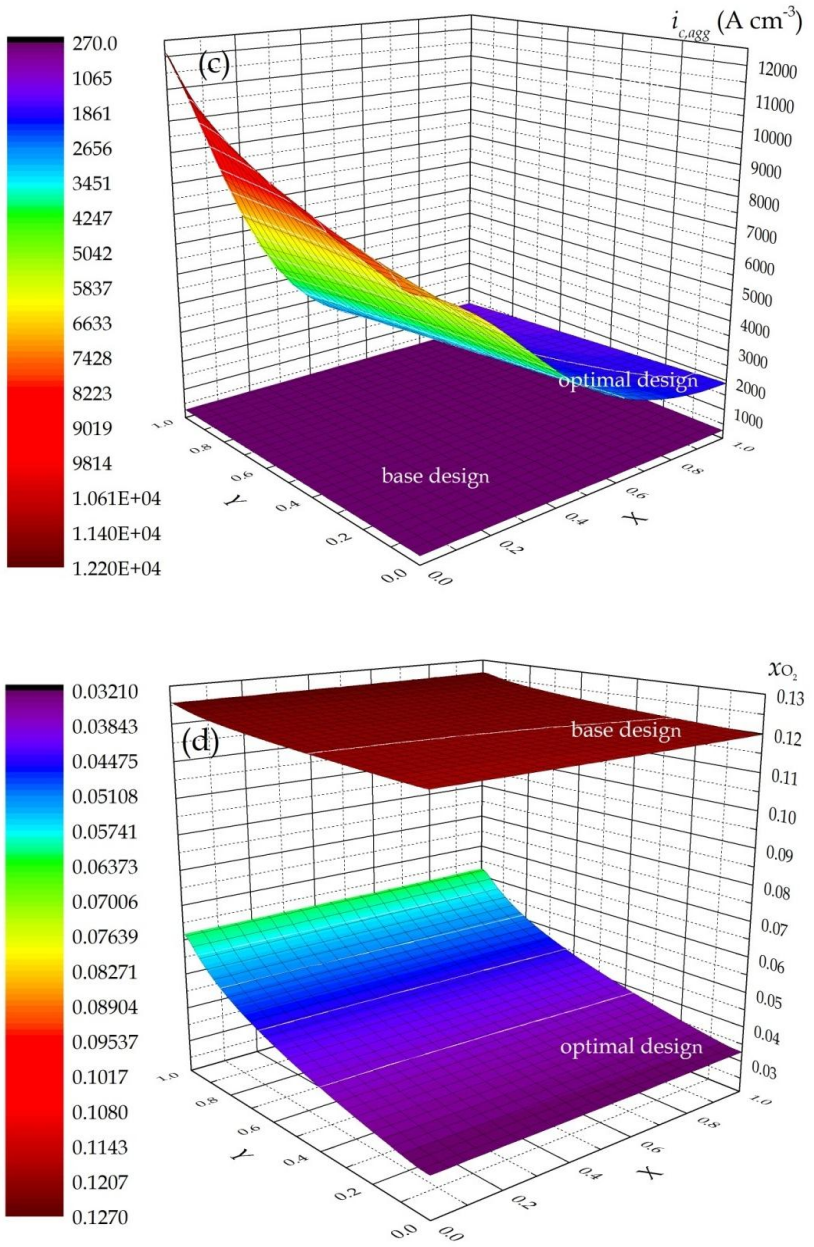

Figure 7-3 Polarisation curve (a), cathode overpotential (b), cathode volumetric current density (c) and oxygen mole fraction (d) for base design and optimal design at the cell voltage of 0.2 V

7.7.3 Optimisation at medium cell voltage

Figure 7-4 shows the polarisation curve, cathode overpotential, cathode volumetric current density and oxygen mole fraction for the base design and the optimal design at 0.5 V. The simulation results based on the agglomerate model agree well with the optimisation result, an approximate 4.5% maximum error is observed at the cell voltage of 0.2 V. Apparently, as shown in Figure 7-4(a), the current density increases from 0.46 to 1.02 A cm^{-2} for the optimal design $\{m_{Pt}, f, L_M, l_{CL}, r_{agg}\}$={1.0, 31.5%, 11.5%, 30.0,

0.1}. At this condition, ε_S, L_M and ε_{CL} are 44.8%, 11.5% and 43.7%, respectively. Simultaneously, the optimal design decreases δ_M to 2.89×10^{-9} m and a_{agg} to 3.92×10^{7} m^{-1}. Note that, by optimising, these two parameters are both greater than that obtained at 0.2 V. As stated previously, at a lower cell voltage (0.2 V), the overall rate control process of the ORR is the oxygen transport rate through the ionomer film. When the cell voltage increases, the electrochemical kinetics play more important role in determining the overall rate. Consequently, both the increases in the volume fraction of solid and void space give a higher current density at medium cell voltages. By optimising, the volume fractions of solid and void space are approximate 45.0%, which results in the best performance of the cell.

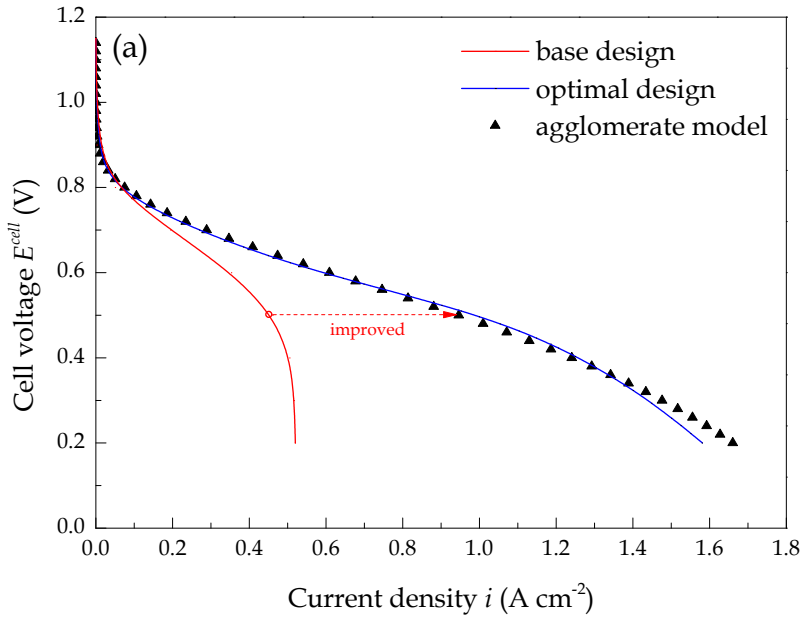

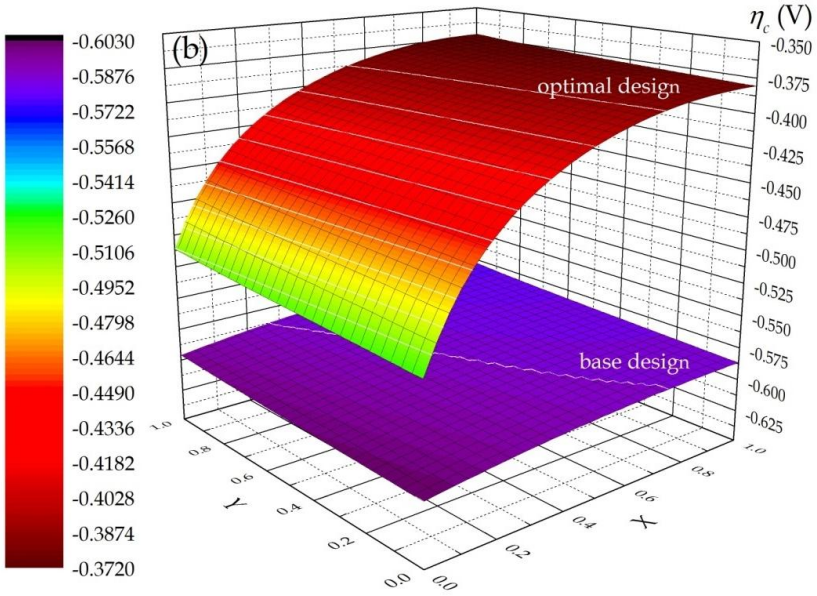

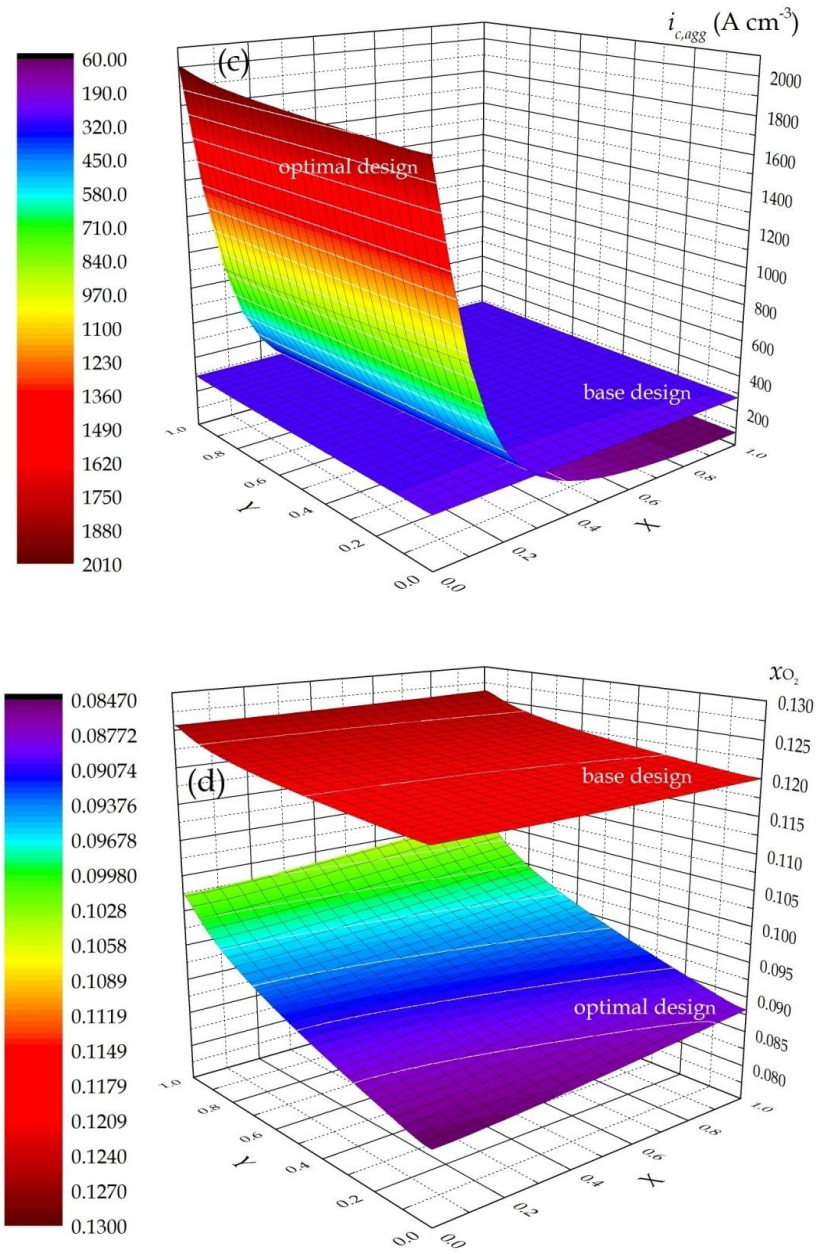

Figure 7-4 Polarisation curve (a), cathode overpotential (b), cathode volumetric current density (c) and oxygen mole fraction (d) for base design and optimal design at the cell voltage of 0.5 V

The cathode overpotential for the base design and optimal design are shown in Figure 7-4(b). After optimising, the absolute value of average cathode overpotential decreases from 0.59 to 0.41 V, which leads to an improved cell performance according to Eq. (4-21). The cathode volumetric current density is shown in Figure 7-4(c). Although the average volumetric current density increases from 280.91 to 312.97 A cm^{-3} by optimisation, the volumetric current density near the CL-GDL decreases. The complicated distribution of volumetric current density can be explained by the combination of the ORR kinetics (the first term in Eq. (3-13)) and oxygen transport resistance (the second term in Eq. (3-13)). Near the CL-membrane, although the optimal

design causes a decrease in the rate coefficient of ORR by reducing the overpotential according to Eq. (3-13), the volumetric current density increases due to the decrease in ionomer film thickness according to Eq. (3-31). However, the decrease in ionomer film thickness cannot compensate the decrease in rate coefficient of the ORR near the CL-GDL, resulting in a decrease in volumetric current density. It can be concluded that, at medium cell voltages the overall rate is controlled by both the ORR kinetics and oxygen transport. The decrease in oxygen mole fraction and the increase in its gradient are observed in Figure 7-4(d). The increase in the gradient of oxygen mole fraction and overpotential increase the cathode current density by enhancing the mass and charge transport [278].

7.7.4 Optimisation at high cell voltage

Figure 7-5 shows the polarisation curve, cathode overpotential, cathode volumetric current density and oxygen mole fraction for the base design and the optimal design at 0.8 V. The simulation results based on the agglomerate model agree well with the optimisation result where a maximum error of approximate 1.0% is observed at higher cell voltages. It is clear in Figure 7-5(a) that the current density increases from 0.05 to 0.13 A cm^{-2} at the cell voltage of 0.8 V with the optimal design $\{m_{Pt}, f, L_M, l_{CL}, r_{agg}\}$ ={1.0, 35.6%, 50.0%, 30.0, 0.1}. In this situation, ε_S, L_M and ε_{CL} are 38.0%, 50.0% and 12.0%, respectively. Unlike the situation at 0.2 and 0.5 V, the optimal design increases δ_M to 3.08×10^{-8} m and a_{agg} to 6.53×10^{7} m^{-1}.

It is expected that fuel cell performance is limited by ORR kinetics rather than oxygen transport at higher cell voltages [21, 85, 115]. In this case, the main target of the optimisation is to increase the electrochemical kinetics and this is achieved by the increase in the specific area and decrease in porosity. Note that the optimal volume fraction of the electrolyte reaches to the upper bound, 50.0%, indicating that the proton migration rate is also important in determining the overall rate at higher cell voltages. It is clear in Figure 7-5(b) that the absolute value of average cathode overpotential decreases from 0.346 V to 0.335 V at the cell voltage of 0.8 V. Compared to that of low and medium cell voltages, the change in overpotential is smaller due to the slower kinetics at high cell voltages. As shown in Figure 7-5(c), the average volumetric current density only increases from 40.11 to 42.30 A cm^{-3} A cm^{-3} after optimisation. However, the gradient in oxygen mole fraction shown in Figure 7-5(d) increases more significant

than that of 0.2 V and 0.5 V. This is due to the decrease in catalyst layer porosity. At high cell voltages, the electrochemical kinetics is the main limitation to the overall reaction rate while the influence of oxygen diffusion rate within the pores of the porous electrode reduced.

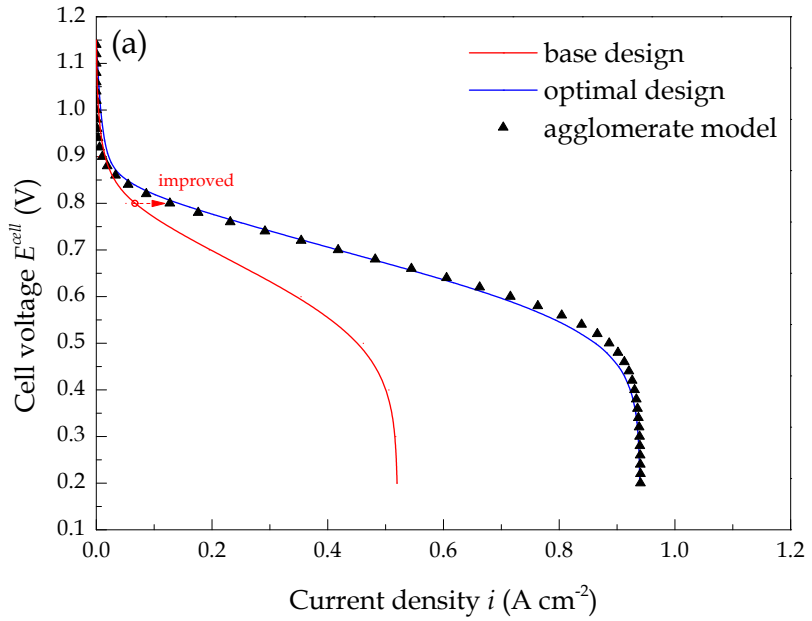

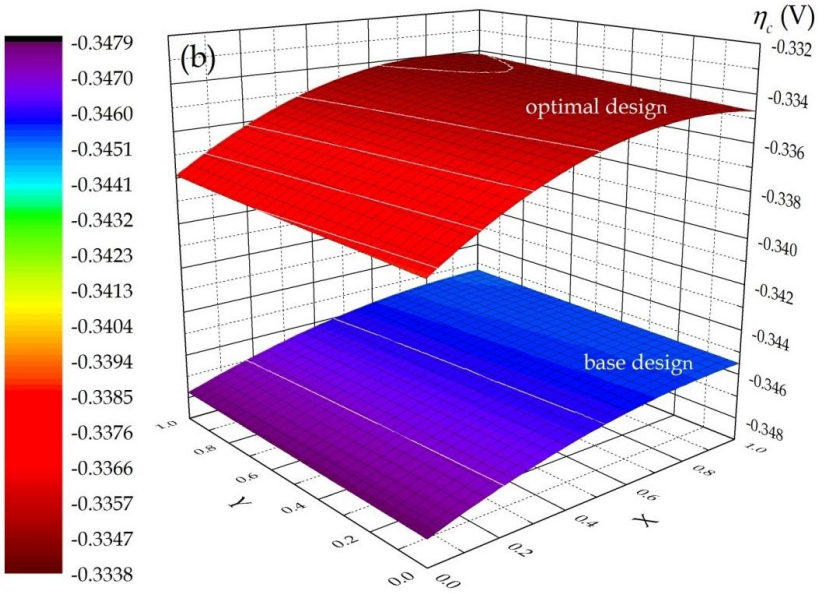

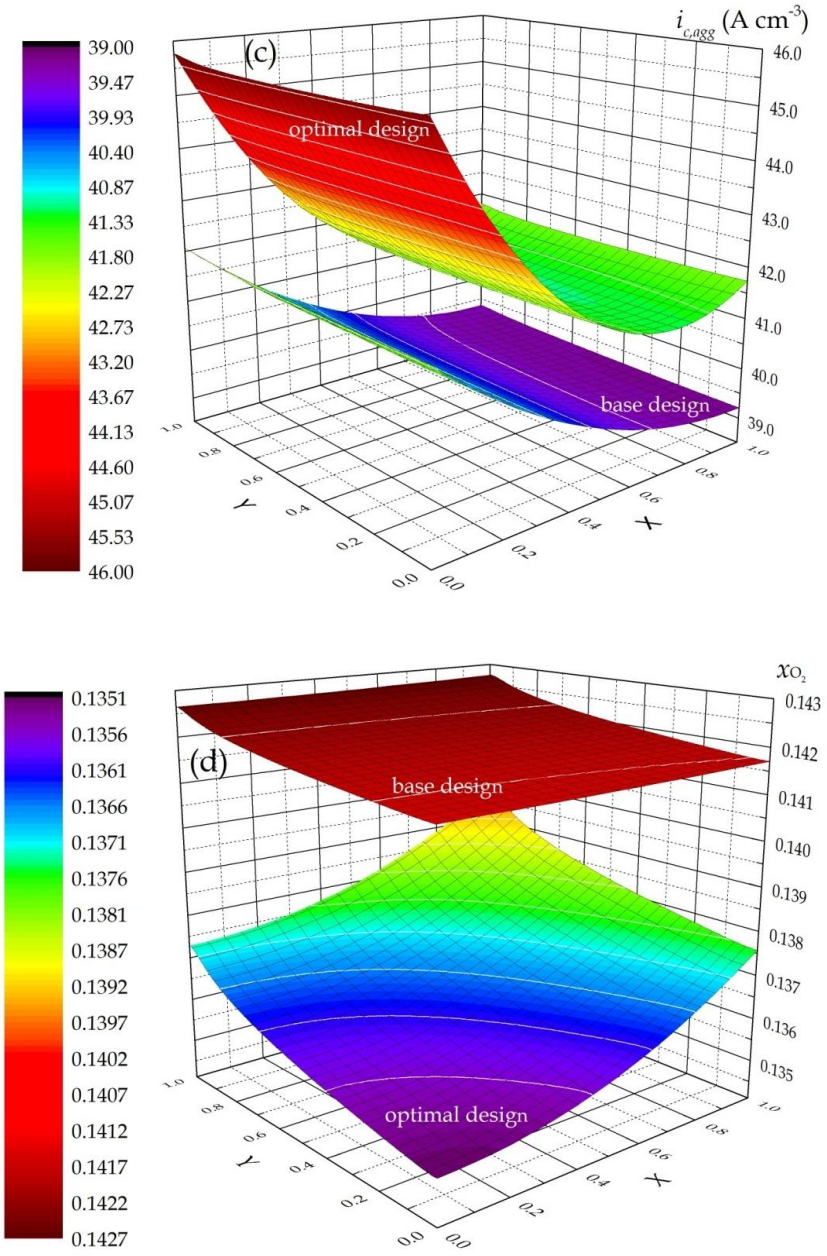

Figure 7-5 Polarisation curve (a), cathode overpotential (b), cathode volumetric current density (c) and oxygen mole fraction (d) for base design and optimal design at the cell voltage of 0.8 V

In addition, the proton conductivity of the catalyst layer is another important issue in deterring the overall reaction rate. At the cell voltage of 0.8 V, the optimal design leads to an increase in effective proton conductivity of catalyst layer (from 1.82 to 3.96 S m^{-1}). However, the optimal designs at 0.2 and 0.5 V result in decreases (from 1.86 to 0.23 at 0.2 V and from 1.86 to 0.44 at 0.5V) in effective proton conductivity of the catalyst layer. It can be concluded that, at high cell voltages, ORR kinetics and proton conductivity of the catalyst layer both control the overall reaction rate. Consequently, the cell performance can be improved by increasing the volume fraction of solid phase

when keeping ionomer volume fraction at a sufficient level. The parameters for base design and optimal designs for different cell voltages are summarised in Table 7-4.

Table 7-4 Parameters for base design and optimal designs at different cell voltages

Parameters	Base design	Optimal design at different cell voltages		
		0.2 V	0.5 V	0.8 V
ε_S	63.5%	40.1%	44.8%	38.0%
L_M	20.0%	7.0%	11.5%	50.0%
ε_{CL}	16.5%	52.9%	43.7%	12.0%
δ_M (m)	1.55×10^{-8}	3.16×10^{-10}	2.89×10^{-9}	3.08×10^{-8}
a_{agg} (m^{-1})	4.22×10^{7}	3.41×10^{7}	3.92×10^{7}	6.53×10^{7}
σ_{CL} (S m^{-1})	1.82	0.23	0.44	3.96

7.8 Optimisation during a specific cell voltage range

The power density curves for the base design and optimal design at three cell voltages are shown in Figure 7-6(a). It is apparent that the optimal cell voltages are observed to the highest power density at different conditions, i.e. the optimal cell voltages are 0.54 V for base design, 0.36 V for optimal design for 0.2 V. As mentioned in Section 7.4, fuel cell is often operated during a range of cell voltage close to the optimal value. Consequently, the optimisation problem in Strategy B (Eq. 7-21) is solved in this section for two ranges of cell voltage range: 0.3-0.6V, 0.5-0.7V. In addition, the range of 0.6-0.9 V is added to compare. For each of these cases, the parameters in Table 7-3 are applied as the base design during the design optimisation process.

Figure 7-6(b)-(d) show the polarisation curves for the base case and optimal design during the cell voltage range of 0.3-0.6 V, 0.5-0.7 V and 0.6-0.9 V, respectively. The shaded areas refer to the improved output of the cell upon optimisation. It is clear that each optimal design corresponding to the specific range of cell voltage improves the cell performance. The optimal design are $\{m_{Pt}, f, L_M, l_{CL}, r_{agg}\}$={1.0, 34.35%, 8.44%, 28.92, 0.1} for 0.3-0.6 V, {0.959, 34.27%, 49.46%, 30.0, 0.1} for 0.5-0.7 V and {0.957, 34.59%, 50.0%, 30.0, 0.1} for 0.6-0.9 V, respectively.

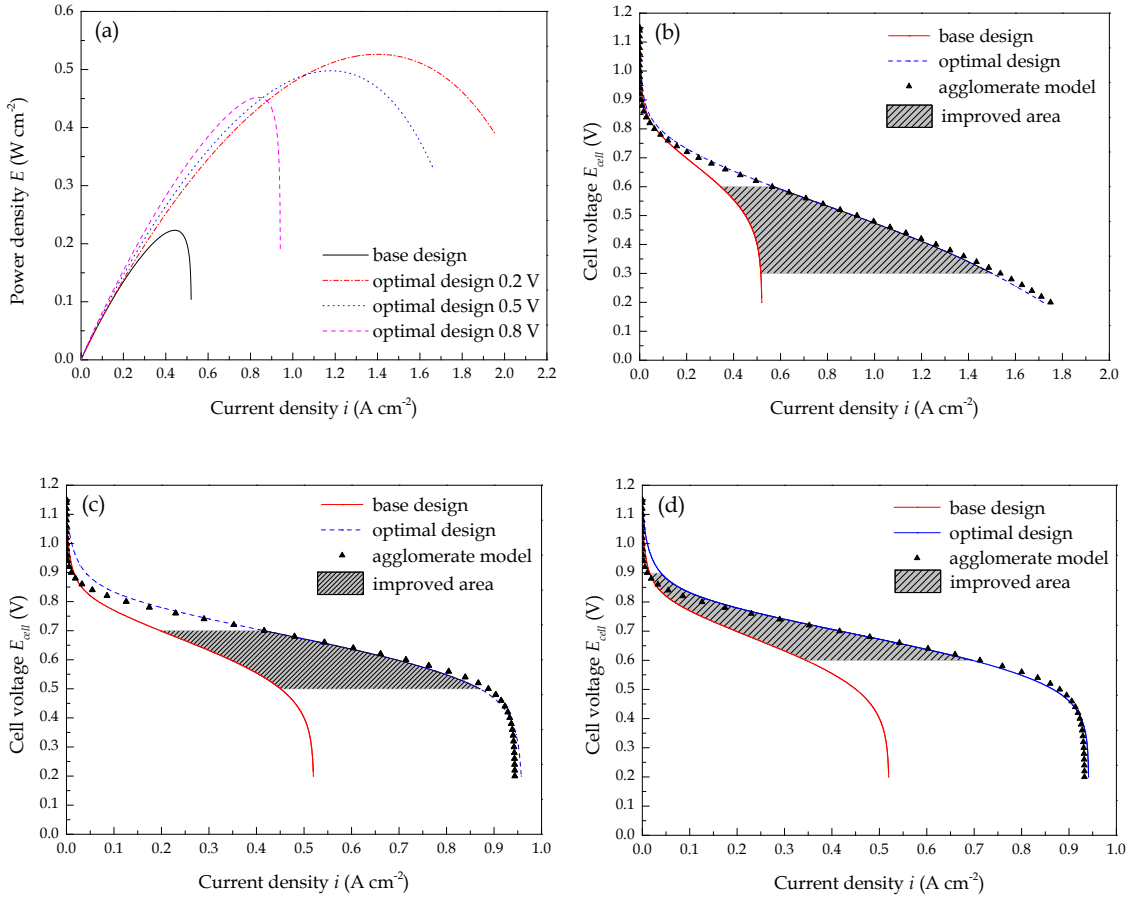

Figure 7-6 Power density curves (a) and polarisation curves during the cell voltage range of 0.3-0.6 V (b), 0.5-0.7 V (c) and 0.6-0.9 V (d) for the base design and optimal design

For these values, as shown in Table 7-5, ε_S, L_M and ε_{CL} are 41.3%, 8.5% and 50.2% for 0.3-0.6 V, 38.5%, 49.5% and 12.0% for 0.5-0.7 V and 38.0%, 50.0% and 12.0% for 0.6-0.9 V, respectively. In addition, the optimal designs change δ_M and a_{agg} to 1.13×10^{-9} m and 3.63×10^{7} m^{-1} for 0.3-0.6 V, 3.02×10^{-8} m and 6.41×10^{7} m^{-1} for 0.5-0.7 V and 3.08×10^{-8} m and 6.44×10^{7} m^{-1} for 0.6-0.9V, respectively. The obtained mean current densities during the selected cell voltages and the relative errors between the optimisation results and the simulation results are 1.06 A cm^{-2} and 1.16% for 0.3-0.6V, 0.68 A cm^{-2} and 0.28% for 0.5-0.7 V, and 0.32 A cm^{-2} and 0.51% for 0.6-0.9V, respectively.

It is obvious in Table 7-6 that the obtained parameters are very close for optimal designs for 0.5-0.7 V and 0.6-0.9V. It is also observed that the improvement in fuel cell output requires higher platinum loading and lower ionomer volume fraction during lower voltage range and it requires lower platinum loading and higher ionomer volume fraction during higher voltage range. The improvement in cell performance during

lower voltage range can be mainly explained by two reasons: the decrease in oxygen diffusion resistance through the ionomer film surrounding the agglomerate and the increase in the porosity of the catalyst layer. And the improvement in cell performance during higher voltage range can be explained by the increased specific area and proton conductivity.

Table 7-5 Parameters for base design and optimal designs for different cell voltage ranges

Parameters	Base design	Optimal design at different cell voltage ranges		
		0.3 – 0.6 V	0.5 – 0.7 V	0.6 – 0.9 V
ε_S	63.5%	41.3%	38.5%	38.0%
L_M	20.0%	8.5%	49.5%	50.0%
ε_{CL}	16.5%	50.2%	12.0%	12.0%
δ_M (m)	1.55×10^{-8}	1.13×10^{-9}	3.02×10^{-8}	3.08×10^{-8}
a_{agg} (m^{-1})	4.22×10^{7}	3.63×10^{7}	6.41×10^{7}	6.44×10^{7}
i_{mean} (A cm^{-2})	0.29	1.06	0.68	0.32

Table 7-6 Key parameters to optimal design at different cell voltages

Cell voltages	Optimal volume fraction of the component in catalyst layer					Other parameters		
E^{cell} (V)	$L_{Pt/C}$	L_M	ε_{CL}		L_S	δ_M (nm)	a_{agg} (m^{-1})	N_{agg} (m^{-3})
			ε_p	ε_s				
0.2	37.10%	7.00%	35.42%	17.48%	3.00%	0.316	3.407×10^{7}	1.880×10^{20}
0.5	41.82%	11.50%	27.57%	16.11%	3.00%	2.894	3.924×10^{7}	1.773×10^{20}
0.8	35.00%	50.00%	4.06%	7.95%	3.00%	30.828	6.525×10^{7}	9.494×10^{19}
0.3 - 0.6	38.33%	8.40%	32.88%	17.35%	3.00%	1.129	3.628×10^{7}	1.839×10^{20}
0.5 - 0.7	35.55%	49.50%	4.12%	7.87%	3.00%	30.186	6.408×10^{7}	9.644×10^{19}
0.6 - 0.9	35.00%	50.00%	4.06%	7.94%	3.00%	30.826	6.436×10^{7}	9.495×10^{19}

It is also clear in Table 7-6 that the optimal volume fraction of the secondary pores at lower cell voltages is approximate 20% and the optimal ionomer volume fraction is approximate 50% when cell voltage is higher than 0.5 V, which agree with the previous work by Bernardi *et al.* [21] and Sun *et al.* [115].

7.9 Global sensitivity analysis

The good agreement of the results obtained from the surrogate model and agglomerate model indicates that the approximate model obtained with the Kriging surrogate model is sufficiently accurate. Therefore, it can be used for the GSAs of these design variables. In this work, the Sobol' indices are computed based on the surrogate models to obviate the problem of expensive computation. A total of 50,000 Monte Carlo (MC) simulations are conducted for one indices calculation. Figure 7-7 shows the individual and total sensitivity indices for each design variable at different cell voltages.

As shown in Figure 7-7, the significance of variables is determined by ranking the total sensitivity indices over the 50,000 MC simulations, as the total sensitivity indices takes into account not only the contribution of the individual effect of a design variable but also the contribution of interactions between variables. Assuming the minimum error to be 2.0%, then it can be concluded that the catalyst layer thickness has no measurable effect on the fuel cell performance at most voltage condition except at 0.8V. It is also found that three variables, i.e., platinum loading, platinum mass ratio, and ionomer volume fraction, play very significant roles on the performance at low and medium voltages, but the effect of ionomer volume fraction decreases sharply at high voltage. Ionomer volume fraction plays most important role at the lower cell voltages due to its significant effect on the ionomer film thickness and then the oxygen diffusion resistance. At higher cell voltages, the importance of platinum loading and platinum mass ratio increase as ORR kinetics becomes to the rate control process. The importance of ionomer volume fraction decreases at higher cell voltages, but it is still important due to its strong effect on the proton conductivity. Platinum loading has an important effect at every cell voltage because it greatly affects the volume fraction solid phase and specific area of agglomerates according to Eq. (3-39) and Eq. (3-68).

Note that the rankings of individual and total sensitivities are same at low and medium cell voltages, but different at high cell voltages. In specific, catalyst layer thickness is negligible at low and medium cell voltages, but no variable can be neglect at high cell voltages. The GSAs of the 5 variables can be used to reduce the size of the problem in subsequent research, neglecting the design variables with unimportant impact. For instance, just use the top 4 relatively important variables in subsequent work and freeze the relatively unimportant variable (catalyst layer thickness) at their nominal values.

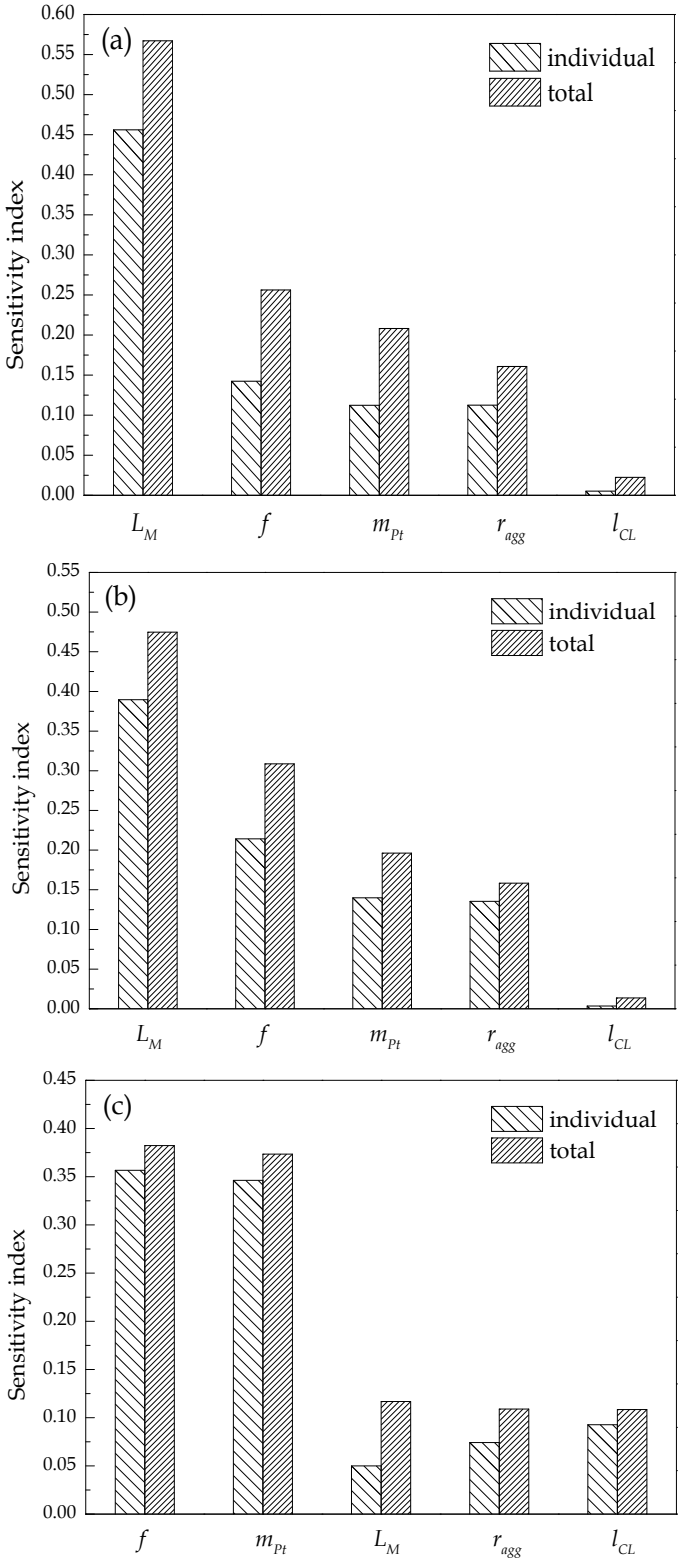

Figure 7-7 Sensitivity indices of the five variables at 0.2V (a), 0.5V (b) and 0.8V (c)

7.10 Final remarks

At three fixed voltages, the optimal value of platinum loading is its upper bound, 1.0 mg cm^{-2}, and the agglomerate radius is its lower bound, 0.1 μm. This is because,

according to Eq. (3-39), the approximate ten times bigger in density of platinum than that of carbon results in a more significant effect on volume fraction of *Pt/C* when changing platinum loading. Moreover, the specific area of agglomerate is proportional to platinum loading according to Eq. (3-69). Consequently, as stated in the work of Secanell *et al.* [47], the maximum platinum loading is required to ensure the maximum value of specific area of agglomerate at every cell voltage. Due to the relationship between agglomerate radius and ionomer film thickness according to Eq. (3-60), the minimum agglomerate radius should be adopted in order to maintain the lowest mass transport resistance of oxygen diffusion through the electrolyte coating. In addition, the number of agglomerate per unit (agglomerate density) increases by applying smaller agglomerate radius according to Eq. (3-50).

As discussed in Section 7.8, the thickness of catalyst layer has least important effect on the cell performance. According to Eq. (3-42), the increase in porosity is resulted from the thicker catalyst layer. Consequently, the optimal catalyst layer thickness is almost at the upper bound value, 30 μm except for the cell voltage of 0.2 V. This is because the increase in porosity is resulted from the increase in platinum mass ratio at 0.2 V. It is clear in Figure 7-7 that the effect of platinum mass ratio is more obvious than catalyst layer thickness. According to Eq. (3-66), the increase in platinum mass ratio leads to the decrease in reaction surface area per unit platinum mass, then the decrease in specific area of agglomerate. Moreover, the optimal platinum loading obtained at its upper bound is because of the omission of the effectiveness factor and the cost of platinum in the current optimisation target.

7.11 Conclusions

A design method to obtain the optimal parameters for PEMFC cathodes containing a two dimensional, steady state and an isothermal model, finite element method (FEM) analysis and surrogate model based optimisation has been presented. An improved cathode numerical approach, considering the volume fraction of all components, is conducted to simulate and investigate the effect of cathode platinum loading, platinum mass ratio, ionomer volume fraction, catalyst layer thickness and agglomerate radius on the polarisation curves of PEMFC. Reactant flow in flow channels, species transport in porous media and water transport through the membrane are included in the numerical model. A surrogate model-based optimisation method is adopted to build the approximate model of the cell response with respect to 5 design variables and to predict

the optimal design based on two optimisation strategies. The first strategy maximises the current densities at fixed cell voltages commonly used in previous work, and the second strategy is modified from the first strategy to maximise the current densities within a specific range of cell voltages. The final surrogate model-based GSAs provide an insight into the effect of each design variable on the PEMFC performance, and help reduce the design dimensions in the subsequent work. It is found that, porosity is important to the performance of PEMFCs operated at lower cell voltages, ionomer volume fraction is important to the performance of fuel cells operated at higher cell voltages and platinum loading is important at a full range of cell voltage.

Chapter 8. Steady state and time dependent models for DMFC anode

The one dimensional, isothermal, steady state and time dependent models for the kinetics of methanol oxidation based on the dual-site mechanism in a porous Pt-Ru anode of DMFC are presented in this chapter. The coverage ratios of various intermediate species, e.g. CH_3OH_{ads}, CO_{ads}, OH_{ads}, on the surface of Pt and Ru with various temperatures and methanol concentrations are represented and the rate control steps at different overpotentials are determined. The dimensionless secondary partial differential equations (PDEs) are developed to plot the distributions of the dimensionless methanol concentration and overpotential inside the porous anode catalyst layer. The macro (apparent) current density is also obtained from the PDEs. The influence of operating conditions, such as temperature and methanol concentration, and electrode parameters, such as catalyst layer thickness, specific area, effective species diffusivity and conductivity, on the anode performance is studied.

8.1 Introduction

In comparison with hydrogen fuel cells, direct methanol fuel cells (DMFCs) have significant advantages such as higher efficiency, easier design and operation, simple storage and refilling of liquid fuel. However, DMFCs show serious disadvantages such as lower current density, larger polarisation and lower limiting currents resulting from the more complex kinetics of methanol oxidation in the anode of DMFCs than that for hydrogen fuel cells [29, 43]. The adsorption coverage of the intermediates on the active sites, which is involved in the kinetics of methanol oxidation, plays a crucial role in controlling the behaviour of DMFCs [111, 279-282]. Moreover, the micro structure of the electrode also determines the performance of DMFCs to a certain extent [283, 284].

Even though the mechanism of methanol electro-oxidation on the surface of Pt-Ru catalyst is not fully understood, researchers have come to a common understanding that simple Butler-Volmer kinetics are unable to represent the intrinsic methanol oxidation kinetics. Therefore, a dual site mechanism on Pt-Ru catalyst surfaces has been accepted [27, 43, 282, 284-287]. Consequently, it is important to introduce the appropriate dual site mechanism into the model aimed to investigate the macro kinetics of methanol oxidation. The earliest comprehensive model for methanol oxidation was developed by Meyers and Newman [279], in which the thermodynamics, mass transport and electrode

kinetics are coupled. Kauranen and Skou [156] studied the methanol oxidation catalysed by pure platinum and indicated that the limiting current density is due to the saturation of OH on the surface of platinum. In order to analysis the effect of porous electrode structure on the anode performance of DMFCs, the agglomerate model was coupled with the methanol oxidation kinetics by Nordlund and Lindbergh [162]. Argyropoulos, Shivhare and Scott *et al.* [167, 288, 289] investigated the methanol oxidation reaction occurred on Pt-Ru catalyst based on the surface coverage of platinum and ruthenium, respectively. They found that the limiting current density is caused by the saturation of methanol on the surface of platinum and OH on the surface of ruthenium.

8.2 Model description

8.2.1 Computational domain and assumption

The schematic view of a typical DMFC unit is shown in Figure 8-1, in which the porous anode catalyst layer is the computational domain in this study. Methanol is fed into the anode channel and diffuses through the gas diffusion layer to the active Pt-Ru particle located in the catalyst layer. The specifications and parameters of the anode catalyst layer are shown in Table 8-1.

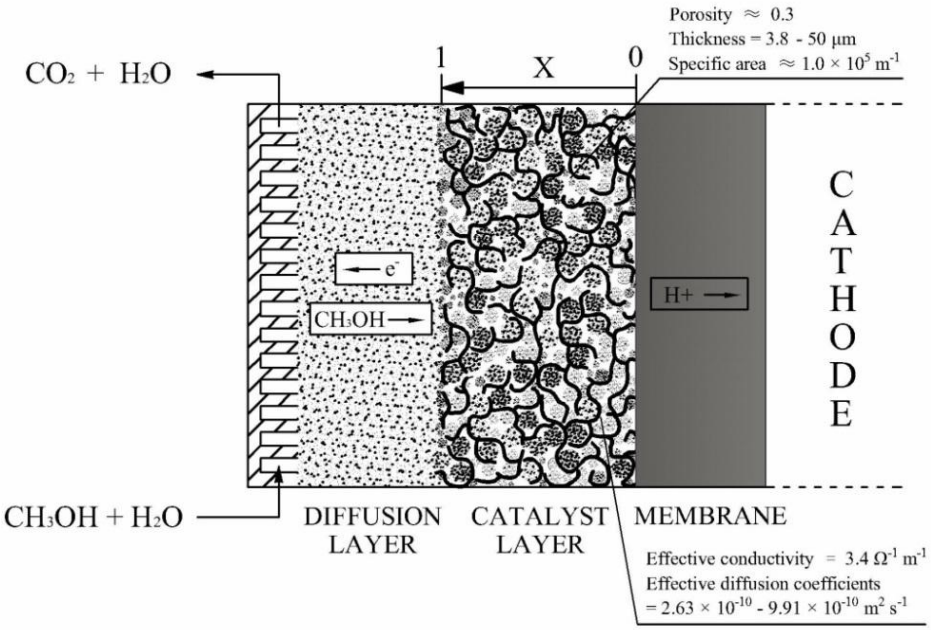

Figure 8-1 Schematic view of the DMFC unit and the computational domain

The assumptions adopted in the present model are as follows:

1. Methanol concentration is defined as constant, which is equal to the methanol bulk concentration, at the CL-GDL interface (X=0) along the Y-direction.
2. Carbon dioxide bubbles are assumed to be formed beyond the catalyst layer, because it is possible to control the nucleation of carbon dioxide in the GDL or portion of the catalyst layer by choosing appropriate operating condition [290, 291].
3. The porous catalyst layer is assumed to be isothermal, isotropic and homogeneous.

Table 8-1 Electrode parameters used in the model

Electrode parameters	*References*
Catalyst layer thickness l (m)	
3.8×10^{-6}	[279]
5.0×10^{-6}	[294]
1.0×10^{-5}	[167]
2.3×10^{-5}	[162]
5.0×10^{-5}	[286]
Special area of anode a (m^{-1})	
3.75×10^{4}	[167]
118317	[290]
1.0×10^{5}	[291]
Porosity of anode ε	
0.3	[286]
Diffusion coefficients D_0 ($m^2\ s^{-1}$)	
$2.8\times10^{-9}\exp[2436(1/353-1/T)]$	[286, 288]
Effective conductivity σ_s^{eff} ($\Omega^{-1}\ m^{-1}$)	
3.4	[284, 290]

8.2.2 Intrinsic methanol oxidation kinetics

According to the widely accepted dual-site kinetics for methanol absorption and electrochemical oxidation on the surface of Pt-Ru catalyst, the methanol oxidation mechanism can be described by the four elemental steps shown as follow:

$$CH_3OH \underset{k_1'}{\overset{k_1}{\leftrightarrow}} CH_3OH_{ads} \tag{8-1}$$

$$CH_3OH \xrightarrow{k_2} CO_{ads} + 4H^+ + 4e^- \tag{8-2}$$

$$H_2O \underset{k'_{3,1}}{\overset{k_{3,1}}{\leftrightarrow}} OH_{ads,Ru} + H^+ + e^- \tag{8-3a}$$

$$H_2O \underset{k'_{3,2}}{\overset{k_{3,2}}{\leftrightarrow}} OH_{ads,Pt} + H^+ + e^- \tag{8-3b}$$

$$CO_{ads} + (OH_{ads,Pt} + OH_{ads,Ru}) \underset{k'_4}{\overset{k_4}{\rightarrow}} CO_2 + H^+ + e^- \tag{8-4}$$

According to the dual sites mechanism [288, 289], steps (8-1), (8-2) and (8-3b) occur on platinum sites (Pt) only and step (8-3a) occurs on ruthenium sites (Ru) only whereas step (4) occurs on the both the Pt and Ru sites. Generally, it is believed that the reaction of CO_{ads} to CO_2 occurs on Ru while Pt serves as an active surface of adsorption and dehydrogenation of methanol [279, 280, 286]. As a result, the rate controlling step is described by Eq. (8-4), which in turn depends on elemental steps (8-1), (8-2), (8-3a) and (8-3b) for the formation of the adsorbed intermediates. Thus, the rate expression of the overall reaction can be written as:

$$r_4 = k_4\theta_{OH,Pt}\theta_{CO,Pt}\exp(\beta\eta) + k_4\theta_{OH,Ru}\theta_{CO,Pt}\exp(\beta\eta) \tag{8-5}$$

where $\beta = (1-\beta_3)F/R_gT = (1-\beta_4)F/R_gT$.

The rates of changes of surface coverage of different intermediates with respect to time are:

$$\frac{d\theta_M}{dt} = k_1 c_M(1-\theta_{OH,Pt}-\theta_{CO,Pt}-\theta_M) - k'_1\theta_M - k_2\theta_M\exp(\frac{\alpha_2 F\eta}{R_gT}) \tag{8-6}$$

$$\begin{aligned}\frac{d\theta_{CO,Pt}}{dt} &= k_2\theta_M\exp(\frac{\alpha_2 F\eta}{R_gT}) - k_4\theta_{OH,Pt}\theta_{CO,Pt}\exp(\frac{(1-\beta_4)F\eta}{R_gT}) \\ &\quad - k_4\theta_{OH,Ru}\theta_{CO,Pt}\exp(\frac{(1-\beta_4)F\eta}{R_gT})\end{aligned} \tag{8-7}$$

$$\begin{aligned}\frac{d\theta_{OH,Ru}}{dt} &= k_{3,1}a_w(1-\theta_{OH,Ru})\exp(\frac{(1-\beta_3)F\eta}{R_gT}) - k'_{3,1}\theta_{OH,Ru}\theta_{CO,Pt}\exp(\frac{-\beta_3 F\eta}{R_gT}) \\ &\quad - k_4\theta_{OH,Ru}\theta_{CO,Pt}\exp(\frac{(1-\beta_4)F\eta}{R_gT})\end{aligned} \tag{8-8}$$

$$\begin{aligned}\frac{d\theta_{OH,Pt}}{dt} &= k_{3,2}a_w(1-\theta_{OH,Pt}-\theta_{CO,Pt}-\theta_M)\exp(\frac{(1-\beta_3)F\eta}{R_gT}) \\ &\quad - k'_{3,2}\theta_{OH,Pt}\theta_{CO,Pt}\exp(\frac{-\beta_3 F\eta}{R_gT}) - k_4\theta_{OH,Pt}\theta_{CO,Pt}\exp(\frac{(1-\beta_4)F\eta}{R_gT})\end{aligned} \tag{8-9}$$

Numerous papers indicate that OH_{ads} is preferentially formed on the surface of Ru rather than Pt [279, 284, 286, 292, 293] and $\theta_{OH,Pt}$ is almost zero when the overpotential is lower than 0.5 V (versus standard hydrogen electrode (SHE)). As a result, it is reasonable to assume adsorption of hydroxyl ions on Pt could be neglected ($\theta_{OH,Pt} = 0$). Thus, if the water activity can be defined as unity ($a_w = 1$), Eq. (8-5) is simplified to:

$$r_4 = k_4 \theta_{OH,Ru} \theta_{CO,Pt} \exp(\beta\eta) \tag{8-10}$$

where, the coverage ratio $\theta_{OH,Ru}$ and $\theta_{CO,Pt}$ can be obtained by solving Eqns. (8-6) to (8-9). Therefore, the intrinsic current density is derived using Faraday's law as follow:

$$i = nFr_4 = i_0 \theta_{OH,Ru} \theta_{CO,Pt} \exp(\beta\eta) \tag{8-11}$$

where, the exchange current density $i_0 = nFk_4$. The kinetics parameters used in this model is listed in Table 8-2.

Table 8-2 Kinetics parameters used in this model [288]

Kinetics parameters	*303 K*	*333 K*	*363 K*
k_1 (m s^{-1})	8.7×10^{-7}	4.2×10^{-6}	1.0×10^{-5}
$k_1^{'}$ (mol m^{-2} s^{-1})	4.0×10^{-4}	1.5×10^{-3}	2.6×10^{-3}
k_2 (mol m^{-2} s^{-1})	3.5×10^{-9}	9.5×10^{-8}	8.0×10^{-7}
$k_{3,1}$ (mol m^{-2} s^{-1})	4.0×10^{-5}	5.0×10^{-5}	6.0×10^{-5}
$k_{3,1}^{'}$ (mol m^{-2} s^{-1})	3.0×10^{-5}	1.8×10^{-5}	1.4×10^{-5}
k_4 (mol m^{-2} s^{-1})	5.3×10^{-2}	5.9×10^{-2}	6.2×10^{-2}
α_{H_2O}		1.0	
α_2		0.79	
β_3 (V^{1})		0.5	
β_4 (V^{1})		0.5	

8.2.3 Macro methanol oxidation kinetics

The macro kinetics of the methanol oxidation reaction is obtained by introducing the impact of mass and charge transport into the intrinsic kinetics.

Mass transport balance

Mass transport of methanol in porous catalyst layer can be described by Fick's first law as follow:

$$N_M = -D_e \nabla c_M \tag{8-12}$$

where N_M (mol m^{-2} s^{-1}) is the methanol flux, D_e (m^2 s^{-1}) is the effective diffusion coefficient, and c_M (mol m^{-3}) is the methanol concentration. Due to the fact the methanol transport process in an elemental volume of the catalyst layer is driven by diffusion only, the divergence of N_M can be written as:

$$\nabla N_M = -D_e \nabla^2 c_M \tag{8-13}$$

According to the mass balance [281-284], the divergence of methanol flux equals to the methanol oxidation reaction rate, leading to:

$$\nabla N_M = R = -a_{CL} r_4 \tag{8-14}$$

where a_{CL} (m^{-1}) is the specific area of the catalyst layer. For a one dimensional slab porous catalyst layer, combing Eq. (8-10), Eq. (8-13) and Eq. (8-14) gives:

$$\frac{d^2 c_M}{dx^2} = \frac{a_{CL}}{D_e} k_4 \theta_{\mathrm{OH,Ru}} \theta_{\mathrm{CO,Pt}} \exp(\beta\eta) \tag{8-15}$$

The boundary conditions for Eq. (8-15) are:

$$\begin{aligned} x = 0, \quad & \frac{dc_M}{dx} = 0 \quad \text{(at CL - membrane interface)} \\ x = l, \quad & c_M = c_M^0 \quad \text{(at GDL - CL interface)} \end{aligned} \tag{8-16}$$

where c_M^0 (mol m^{-3}) is the bulk concentration of methanol, Eq. (8-15) is used to describe the effect of concentration gradient on anode polarisation.

Charge transport balance

Charge transport in the porous catalyst layer can be described by Ohm's law as follow:

$$i = -\sigma_s^{eff} \nabla \phi^l \tag{8-17}$$

where i (A m^{-2}) is the current density, σ_s^{eff} (Ω^{-1} m^{-1}) is the effective conductivity, and ϕ^l (V) is the potential of the electrolyte. The divergence of i can be written as:

$$\nabla i = -\sigma_s^{eff} \nabla^2 \phi^l \tag{8-18}$$

According to the mass balance [281-284],

$$\nabla i = a_{CL} i \tag{8-19}$$

The overpotential, η (V) is written as $\eta = \phi^s - \phi^l - \phi^0$ [162, 282-284]. Both the potential of the solid phase (ϕ^s) and equilibrium potential (ϕ^0) could be considered as constant. For a one dimensional slab porous catalyst layer, combing Eq. (8-11), Eq. (8-18) and Eq. (8-19) leads to a nonlinear Poisson equation which is used to describe the potential field of the porous catalyst layer as follow:

$$\frac{d^2\eta}{dx^2} = \frac{a_{CL} nF}{\sigma_s^{eff}} k_4 \theta_{\mathrm{OH,Ru}} \theta_{\mathrm{CO,Pt}} \exp(\beta\eta) \tag{8-20}$$

The boundary conditions for Eq. (8-20) are:

$$\begin{aligned} x = 0, \quad & \frac{d\eta}{dx} = 0 \quad && \text{(at CL - membrane interface)} \\ x = l, \quad & \eta = \eta^0 && \text{(at GDL - CL interface)} \end{aligned} \tag{8-21}$$

where η^0 (V) is the initial overpotential applied at the GDL-CL boundary, Eq. (8-21) is used to describe the effect of ionic resistance on anode polarisation.

Generalisation of the model equations

By defining dimensionless variables $C_M = c_M / c_M^0$, $\Psi = \eta / \eta^0$ and $X = x/l$, Eq. (8-15) and Eq. (8-20) can be generalised as follow:

$$\frac{d^2 C_M}{dX^2} = \varsigma \cdot \theta_{\mathrm{OH,Ru}} \theta_{\mathrm{CO,Pt}} \exp(\Phi^0 \Psi) \tag{8-22}$$

$$\frac{d^2 \Psi}{dX^2} = \nu^2 \cdot \theta_{\mathrm{OH,Ru}} \theta_{\mathrm{CO,Pt}} \exp(\Phi^0 \Psi) \tag{8-23}$$

with the boundary conditions:

$$\begin{aligned} X = 0, \quad & \frac{dC_M}{dX} = 0, \quad && \frac{d\Psi}{dX} = 0 \\ X = 1, \quad & C_M = 1, \quad && \Psi = 1 \end{aligned} \tag{8-24}$$

where $\Phi^0 = \beta\eta^0$ is the dimensionless overpotential, and the dimensionless modulus $\varsigma = \frac{a_{CL} i_0 l^2}{nFD_e c_M^0}$, $\nu^2 = \frac{a_{CL} i_0 l^2}{\sigma_s^{eff} \eta^0}$, $\zeta = \nu^2 \Phi^0 = \frac{a_{CL} i_0 l^2 \beta}{\sigma_s^{eff}}$.

The dimensionless modulus, ς in Eq. (8-22) is used to characterise the mass transport resistances of the porous catalyst layer while the dimensionless modulus, ζ in Eq. (8-23)

is used to characterise the charge transport resistance of the catalyst layer when applying different overpotential at the GDL-CL boundary.

Current density and effectiveness factor

According to Ohm's law, the local current density can be described by concentration and charge flux as:

$$i_{loc} = -nFD_e \frac{dc_M}{dx} = -\sigma_s^{eff} \frac{d\eta}{dx} \tag{8-25}$$

The dimensionless current density is therefore defined as:

$$I_{loc} = -nF \frac{1}{\varsigma} \frac{dC_M}{dX} = -\frac{1}{\nu^2} \frac{d\Psi}{dX} \tag{8-26}$$

Eq. (8-25) and Eq. (8-26) are used to describe the current density distribution in the anode catalyst layer. Then the relationship between i_{loc} and I_{loc} can be obtained by the expression of the dimensionless modulus ς and ζ as follow:

$$i_{loc} = a_{CL} i_0 l \cdot I_{loc} \tag{8-27}$$

Therefore, the total current density, i.e. the apparent (macro-) current density of a porous catalyst layer with a thickness of l is derived as:

$$i_T = a_{CL} i_0 l \cdot I_T = -\sigma_s^{eff} \left(\frac{d\eta}{dx}\right)_{x=l} = -\frac{\sigma_s^{eff} \eta^0}{l} \left(\frac{d\Psi}{dX}\right)_{X=1} \tag{8-28}$$

where the relationship of $\eta^0 - i_T$ is used to represent the apparent (macro-) polarisation curve of the porous anode catalyst layer. In Eq. (8-28), $\Phi^0 = \beta\eta^0$. As a result, the relationship of $\Phi^0 - I_T$ is used to describe the dimensionless polarisation curve. The corresponding apparent (macro-) reaction rate can be written as:

$$R = \frac{i_T}{nF} = \frac{a_{CL} i_0 l}{nF} \cdot I_T = -D_e \left(\frac{dc_M}{dx}\right)_{x=l} = -\frac{D_e c_M^0}{l} \left(\frac{dC_M}{dX}\right)_{X=1} \tag{8-29}$$

The effectiveness factor is introduced to evaluate the impact of physical parameters, such as thickness and specific surface area of the catalyst layer, effective diffusion coefficient and effective conductivity of the anode, on the apparent current density, which is defined as the quotient of the obtained apparent density and the intrinsic current density shown by the following equation:

$$E_r = \frac{i_T}{a_{CL} li} \tag{8-30}$$

where the intrinsic current density i, which depends on the bulk methanol concentration (c_M^0) and initial overpotential on GDL-CL boundary (η^0), is calculated by solving coupled equations form Eq. (8-6) to Eq. (8-11).

Substituting Eq. (8-11) into Eq. (8-30) leads to:

$$E_r = \frac{i_T}{a_{CL} l i_0 \theta_{\mathrm{OH,Ru}} \theta_{\mathrm{CO,Pt}} \exp(\beta \eta^0)} = \frac{I_T}{\theta_{\mathrm{OH,Ru}} \theta_{\mathrm{CO,Pt}} \exp(\Phi^0)} \tag{8-31}$$

Hence, the expressions of $E_r - i_T$ and $E_r - I_T$ are used to evaluate the effectiveness of the Pt-Ru anode catalyst layer.

8.2.4 Numerical solution

This intrinsic and macro kinetics models in this chapter are established and solved in the PDE module of COMSOL Multiphysics 4.2. The surface coverage of intermediates such as methanol, CO and OH and the time dependent current density are obtained by solving Eq. (8-6) to Eq. (8-11), which are solved by the time dependent solver of COMSOL during the time range of 0 to 2000 seconds with an interval of 1 second. Then the distributions of the dimensionless methanol concentration and overpotential are described by Eq. (8-22) and Eq. (8-23). Finally, the effectiveness factor, which is represented by Eq. (8-31), is calculated.

Note that the dimensionless methanol concentration and overpotential described by Eq. (8-22) and Eq. (8-23) are coupled. The numerical solution is based on the finite element method (FEM). The one dimensional model consists of 1285 elements, the distance between each element is known as the step. At each step ΔX_i, a subroutine used to calculate the surface coverage of $\theta_{\mathrm{OH,Ru}}(X_i)$ and $\theta_{\mathrm{CO,Pt}}(X_i)$ is inserted. Therefore, all values of $C_M(X_i)$ and $\Psi(X_i)$ are obtained. The calculation process is undertaken step by step along the nodes from $X_i = 0$ to $X_i = 1$. At the boundary of $X_i = 1$, the polarisation curves and effectiveness factor can be obtained according to Eq. (8-22), Eq. (8-23) and Eq. (8-31).

8.3 Result and discussion

8.3.1 Model validation

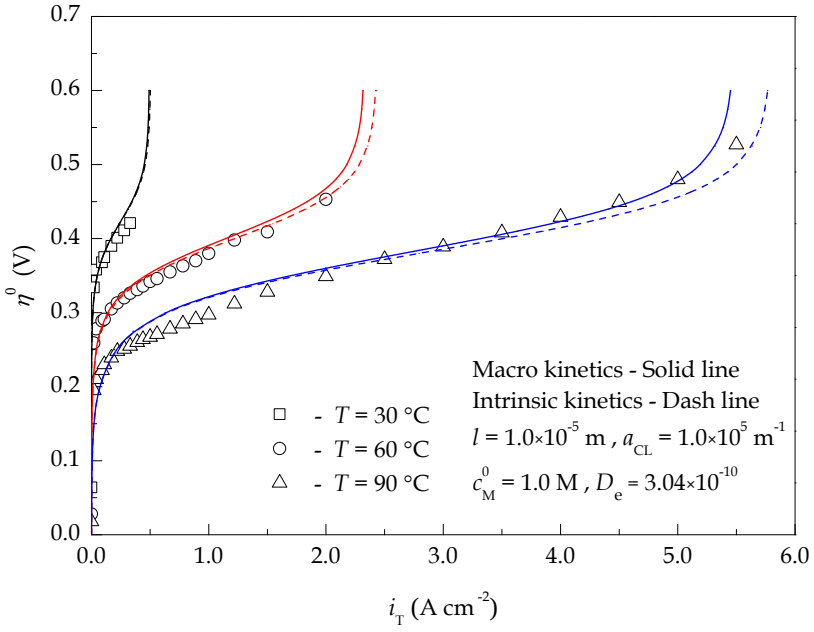

Figure 8-2 Model validation and comparison of intrinsic and macro kinetics

Figure 8-2 shows the simulated intrinsic and macro polarisation curves in comparison with the experimental data, respectively. The experimental data is reported by Shivhare *et al.* [288, 289] and was obtained using a small scale laboratory DMFC with an active electrode area of 9 cm^{-2}. During operation, aqueous methanol solutions and nitrogen were fed to the anode and cathode above stoichiometry, respectively. The anode potential was measured vs. a dynamic hydrogen reference electrode. The intrinsic polarisation curves, which only depend on the bulk methanol concentration c_M^0 and the initial applied overpotential η^0, are calculated by Eq. (8-11). The intrinsic polarisation curves are consistent with the macro polarisation curves calculated by Eq. (8-28), in which the thickness of the catalyst layer is set to $l \to 0$ in the computation process. It is apparent from Figure 8-2 that, due to weak mass transport impact, the simulated intrinsic and macro polarisation curves almost overlap each other at lower current densities in agreement with the experimental data. At a fixed overpotential, the simulated current density based on the intrinsic kinetics is higher than that of the macro kinetics, especially at higher current densities. This can be explained by the influence of methanol and charge transport inside the porous electrode.

8.3.2 Distributions of dimensionless methanol concentration and overpotential

The distributions of dimensionless methanol concentration C_M and dimensionless overpotential Ψ are shown in Figure 8-3a. X axis refers to the dimensionless distance through the anode catalyst layer from the CL-membrane interface (X=0) to the GDL-CL interface (X=1). It is clear that, due to the existence of the mass and charge transport resistance, both C_M and Ψ decrease along methanol diffusion direction as the overpotential Φ^0 increases. The dimensionless methanol concentration decreases more significant in comparison with the dimensionless overpotential. This can be explained by the relative high effective conductivity of the electrode. The distribution of dimensionless overpotential is shown in detail in Figure 8-3b. Although the change of dimensionless overpotential is not obvious, it has a strong effect on the anode performance because overpotential is the driven force of the electrochemical reaction. Surprisingly, the dimensionless overpotential initially decreases to minimum value then increases as the overpotential increases. This is due to the change of rate determining step at higher overpotential, which will be discussed in detail in the following sections.

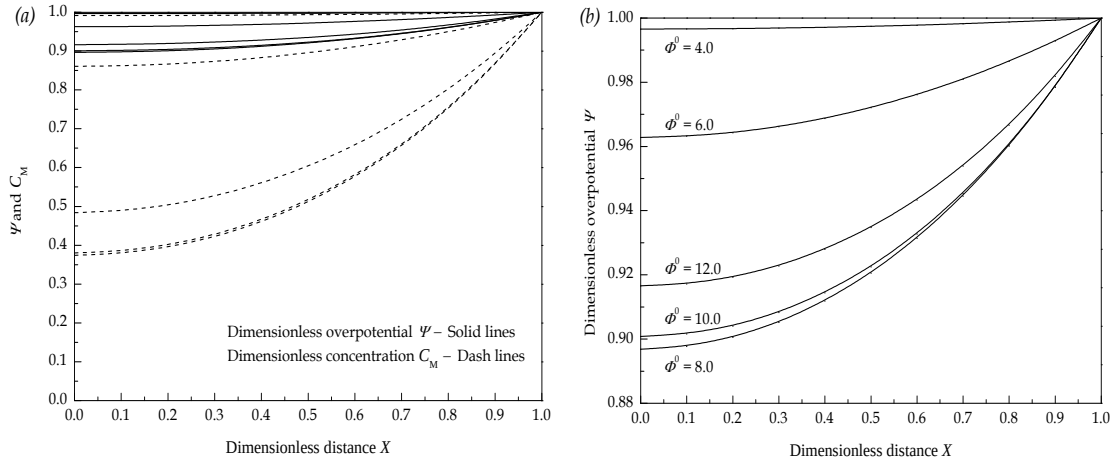

Figure 8-3 Distributions of dimensionless methanol concentration and overpotential

8.3.3 Coverage ratios of intermediates on active sites

Depending on the expressions of the intrinsic and macro kinetics, Eq. (8-11) and Eq. (8-28), the simulated current density is proportional to both the coverage ratios of OH adsorbed on Ru ($\theta_{OH,Ru}$) and CO adsorbed on Pt ($\theta_{CO,Pt}$). Moreover, $\theta_{OH,Ru}$ and $\theta_{CO,Pt}$ are mutually coupled with the coverage ratio of CH_3OH_{ads} absorbed on Pt (θ_M). According to Eq. (8-6) to Eq. (8-9), all coverage ratios are functions of methanol concentration, operating temperature and overpotential. In the following section, the effect of methanol

concentration, operating temperature and overpotential on θ_M, $\theta_{OH,Ru}$, $\theta_{CO,Pt}$ are discussed.

Figure 8-4 shows variations of surface coverage ratios with various overpotentials calculated using the kinetics parameters at 30 °C, 60 °C and 90 °C with 1.0 M (mol dm^{-3}) of methanol. The values for θ_M and $\theta_{OH,Ru}$ are shown on the left *y*-axis while values for $\theta_{CO,Pt}$ are shown on the right *y*-axis with a scale of 10^{-5}. As the overpotential increases, $\theta_{OH,Ru}$ rapidly increases to near 1, undergoes a slight decrease and, approaches 1 again. This indicates that the electrochemical formation of OH on Ru (step 8-3a) may not become a rate limit step. θ_M initially does not change with an increase in overpotential (maintains a value approximately that of the adsorption equilibrium) but undergoes a sharp decrease as the overpotential increases, finally maintaining a small constant value near zero. However, with increasing overpotential, $\theta_{CO,Pt}$ first shows a sharp increase and then undergoes a sharp decrease, ultimately maintaining very small values.

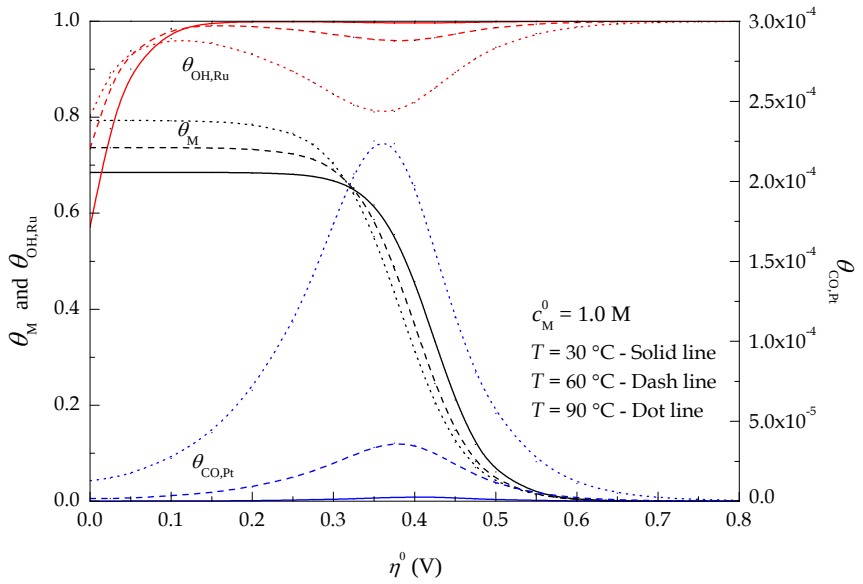

Figure 8-4 Variations of coverage ratios with overpotential at different temperatures

It is also clear in Figure 8-4 that the influence of operating temperature on the coverage ratios of intermediates is important. As shown in Figure 8-5, the activation energies, determined from the Arrhenius plots of the rate constants in Table 8-2 with inverse temperature, of methanol adsorption (step 8-1) and CH_3OH_{ads} dehydrogenation (step 8-2) are approximately 40 kJ mol^{-1} and 80 kJ mol^{-1}, respectively. Looking back to Figure 8-4, the greatest influence of temperature on the coverage ratios is observed with

the overpotential from 0.3 V to 0.5 V, and it is apparent that $\theta_{CO,Pt}$ is more sensitive to temperature than the other two coverage ratios.

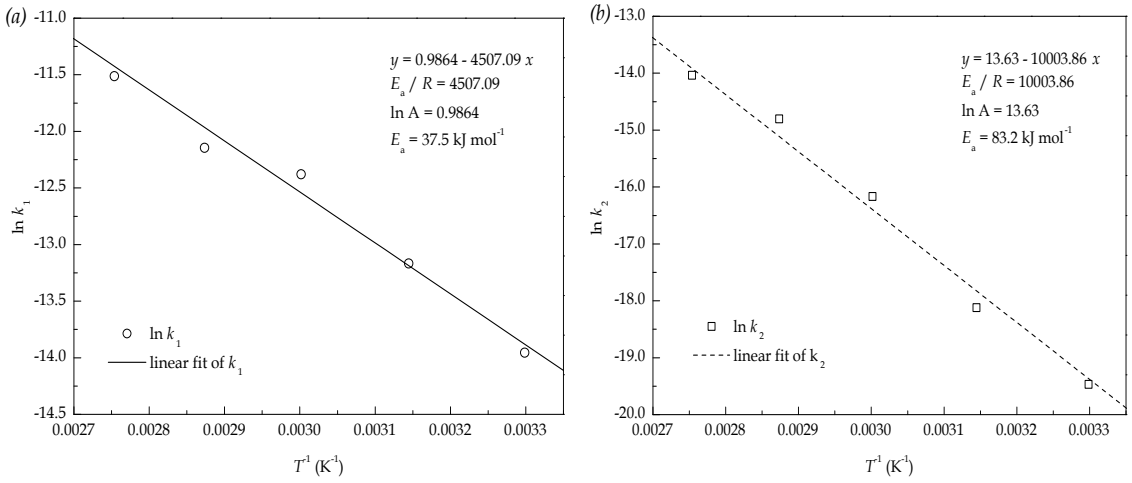

Figure 8-5 Activation energy of methanol adsorption (a) and CH_3OH_{ads} dehydrogenation (b)

Figure 8-6 shows the variation in coverage ratios with different overpotentials and methanol concentrations at the operating temperature of 60 °C. θ_M and $\theta_{CO,Pt}$ are much sensitive to methanol concentration than $\theta_{OH,Ru}$. And θ_M is more sensitive, and $\theta_{OH,Ru}$ and $\theta_{CO,Pt}$ are less sensitive to methanol concentration than to temperature.

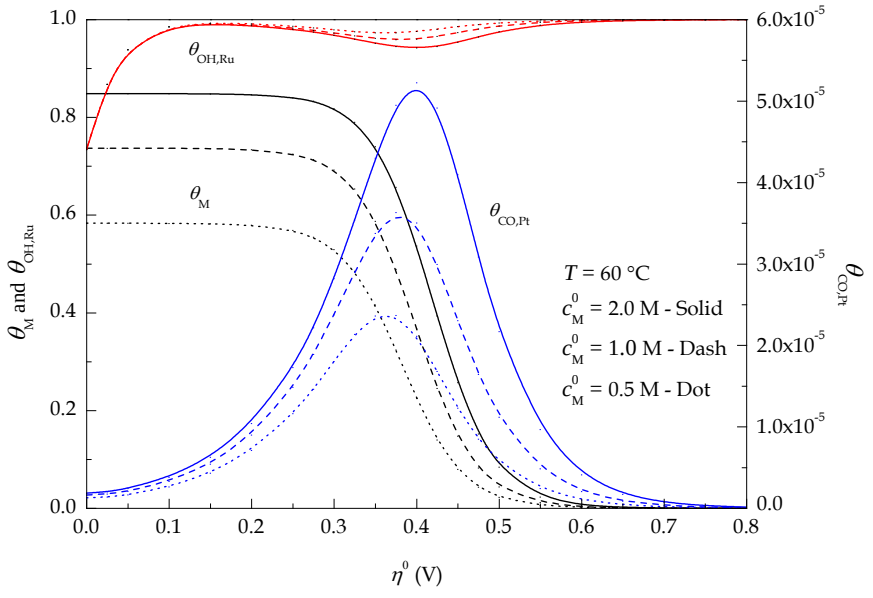

Figure 8-6 Variations of coverage ratios with overpotential at different methanol concentrations

The influence of different operating temperatures and methanol concentrations on the transient surface coverage ratio of methanol (θ_M) is shown in Figure 8-7. Elemental step (8-1) happens on the surface of Pt and thus results in the typical change of θ_M from zero

to saturation. In Figure 8-7, it is clear that θ_M takes a longer period of time to approach saturation at lower operating temperature and methanol (see the dot lines). On the contrary, θ_M reaches the saturation level faster when higher operating temperature and methanol concentration are applied (see the solid lines). Figure 8-7 also indicates that the operating temperature has a greater influence on θ_M in comparison with methanol concentration.

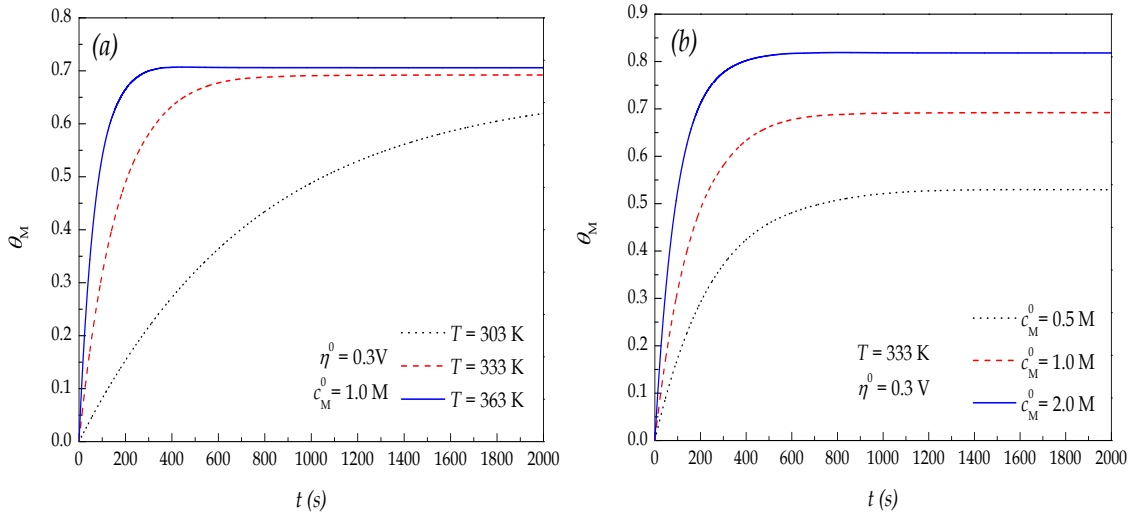

Figure 8-7 Transient coverage ratio of methanol on Pt with different operating temperature (a) and methanol concentration (b)

The influence of different operating temperatures and methanol concentrations on the transient surface coverage ratio of CO on Pt ($\theta_{CO,Pt}$) is shown in Figure 8-8. Note that $\theta_{CO,Pt}$ is approximately four to eight orders of magnitude smaller than θ_M shown in Figure 8-5 and Figure 8-6. Depending on the methanol oxidation mechanism, CH_3OH_{ads} dehydrogenation (step 8-2) is occurred on Pt, leading to a coverage ratio of CH_3OH_{ads} on the surface of platinum. CH_3OH_{ads} dehydrogenation is the subsequent reaction of methanol adsorption (step 8-1). Therefore, $\theta_{CO,Pt}$ is also affected by θ_M. The reaction rate of CH_3OH_{ads} dehydrogenation will be controlled by methanol adsorption when methanol adsorption is slower than CH_3OH_{ads} dehydrogenation on Pt. As shown in Figure 8-8, the effect of temperature is more significant than methanol concentration.

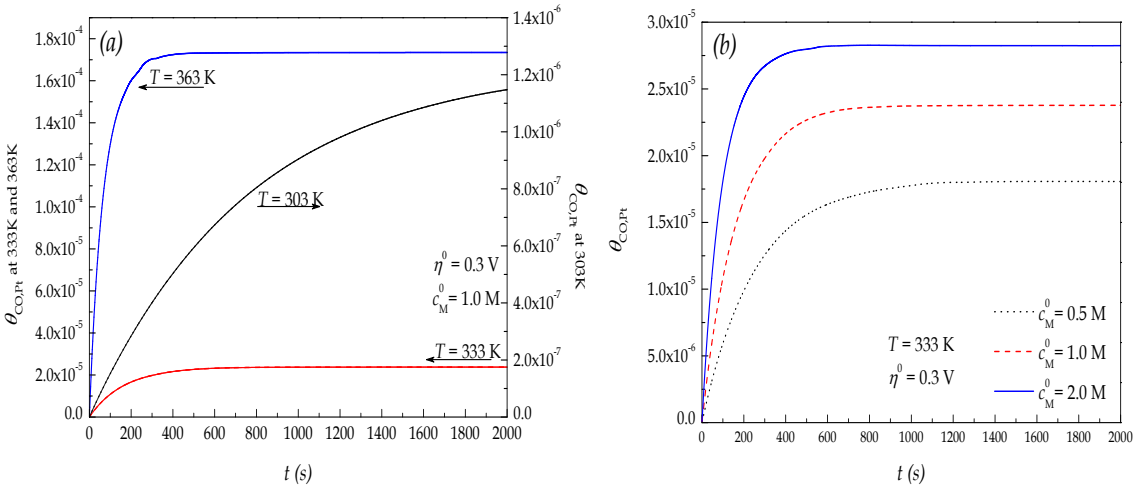

Figure 8-8 Transient coverage ratio of CO on Pt with different operating temperature (a) and methanol concentration (b)

8.3.4 Time dependent current density and rate determining step

Figure 8-9 shows the transient variation in current density at different operating conditions. Typically, the steady state is approached within 200-400 seconds. The time for the transient current density to approach a steady state decreases as the operating temperature and methanol concentration increase. The effect of operating temperature on the current density is more significant than the methanol concentration. Moreover, the plotted curves in Figure 8-9 and Figure 8-8 show great similarities in respect of shape and the time variation. It can be conclude that the obtained current density is mainly determined by CH_3OH_{ads} dehydrogenation (step 8-2) although $\theta_{CO,Pt}$ is some four to eight orders of magnitude smaller than θ_M.

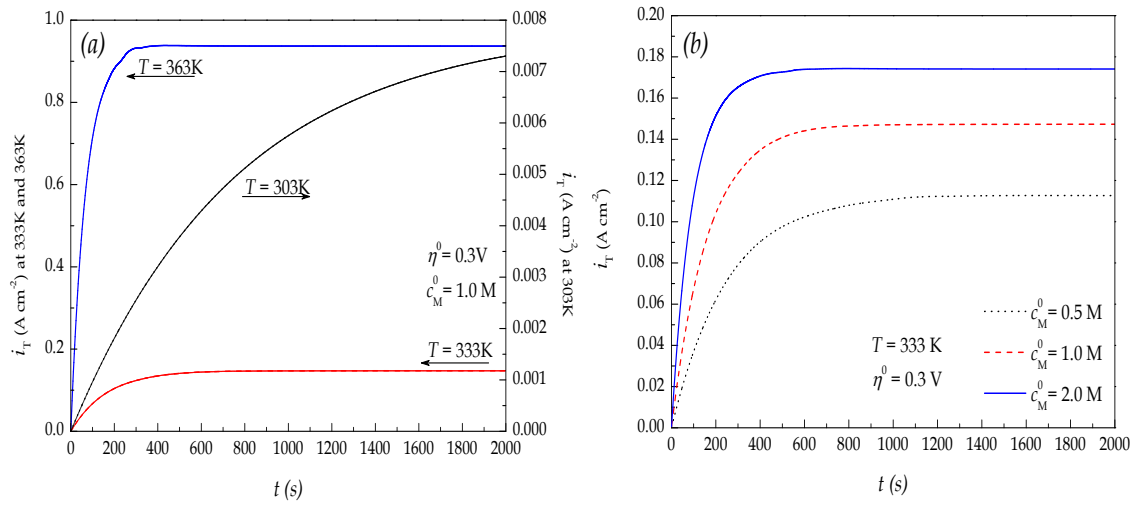

Figure 8-9 Transient current density with various operating temperature (a) and methanol concentration (b)

As stated in Eq. (8-11), the current density is a function of the product of $\theta_{CO,Pt}$ and $\theta_{OH,Ru}$. As shown in Figure 8-4 and Figure 8-5 that the element step (8-3a), which is occurred on the surface of Ru, is extremely fast and lead to a very high saturation (very close to unity) of $\theta_{OH,Ru}$ on the surface of Ru. Therefore, the current density would have no relationship to $\theta_{OH,Ru}$ if it can be considered as constant (the value is one). We may reasonably conclude that step (8-3a) is not the rate determining step and the whole speed of the electrochemical reaction is determined by CH_3OH_{ads} dehydrogenation (step 8-2). In addition, methanol adsorption (step 8-1) might be the rate determining step because it provides the reactant to step (8-2), especially at higher overpotential, i.e. higher than 0.6 V.

8.3.5 Macro polarisation curves and effectiveness

As shown in Eq. (8-28), the macro polarisation curve is used to describe the variation in the applied surface overpotential η^0 (V) and the integral total current density i_T (A cm^{-2}) while the dimensionless macro polarisation curve is used to describe the relationship between the applied dimensionless overpotential Φ^0 and the obtained dimensionless current density I_T .

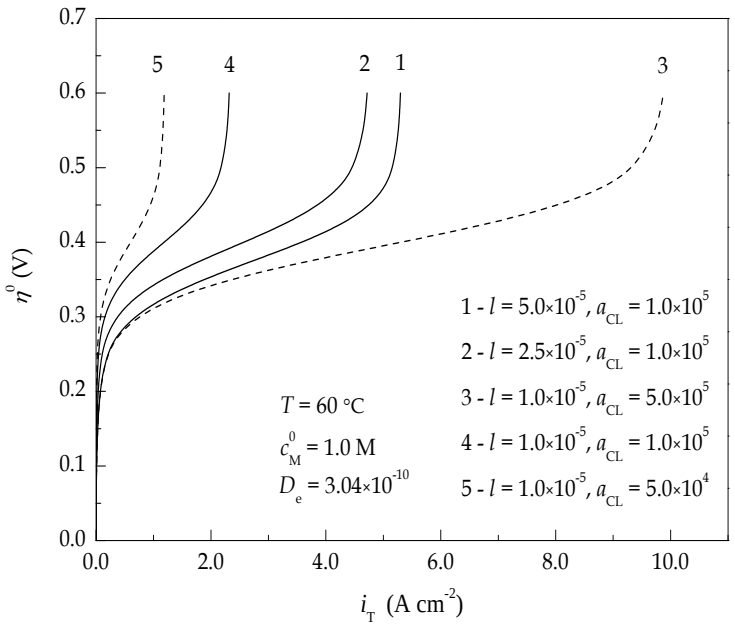

Figure 8-10 Macro polarisation curves with different catalyst layer thickness and specific area

Figure 8-10 shows the polarisation curves (η^0 - i_T) corresponding to the electrode parameters arranged into five groups in which 3 levels of catalyst layer thickness, 2 levels of catalyst layer specific area and 1 level of effective diffusion coefficient are

included. All the macro polarisation curves undergo an approximate exponential rise in current density with increasing overpotential and eventually approaching a maximum current density. This maximum current density is an "adsorption limiting current density" rather than the limiting current density resulting from mass transport. The parameters used for the curve numbered 4 are very close to those used in reference [288, 291].

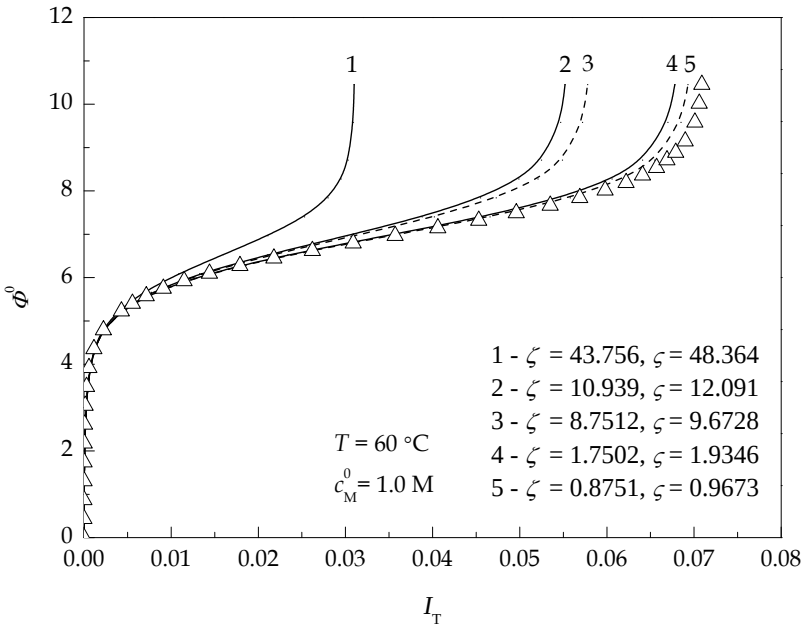

Figure 8-11 Dimensionless macro polarisation curves with different catalyst layer thicknesses and specific areas

Figure 8-11 shows the dimensionless macro polarisation curves (Φ^0 - I_T) corresponding to the same parameters used in Figure 8-10. The dimensionless parameters ς and ζ are calculated using the parameters in Table 8-1. The dimensionless current density I_T is proportional to the averaged current density per unit of inner surface area over the porous catalyst layer, the Φ^0 - I_T curve therefore shows the effects of mass and charge transport on the anode performance of DMFC. The curve represented by symbol △ is the dimensionless intrinsic polarisation curve independent of electrode parameters, which can be calculated by the macro model equation with $l \to 0$ i.e. $l = 10^{-8}$ m. In this condition, both the dimensionless parameters ς and ζ are very close to zero in the numerical process. It is clear in Figure 8-11 that the decrease in ς and ζ (from curve number 1 to 5) leads to higher current densities due to the decrease in mass and charge transport impact through the catalyst layer. The polarisation curve 1 is obtained by relative high ς and ζ (approximately 40-50) and curve 5 is obtained

with ς and ζ smaller than 1.0. As mentioned above, ς and ζ are used to characterise the mass and charge transport resistance through the catalyst layer, in case of the smaller transport resistance, the obtained current density is consequently much higher in case 5 than that in case 1. In addition, the electrode parameters used for curve 4 are close to those in references [288, 291], which indicates that the experiments in reference [288, 291] are carried out under approximate intrinsic condition.

The effects of mass and charge transport can be characterised by the effectiveness E_r of the porous anode. The E_r - I_Γ curves, calculated corresponding to the parameters used in Figure 8-10, are shown in Figure 8-12. Theoretically, the effectiveness factor is a function of both the effectiveness diffusivity and effective conductivity, which are related to the porosity of the porous media according to Bruggeman equation [162, 286]. In order to account for the effect of effective diffusion coefficient, the curves of the dimensionless effectiveness factor are divided into 3 groups by 3 levels of catalyst layer thickness l (m). In each group, 3 levels of effective diffusion coefficient D_e (m^2 s^{-1}) are included. As shown in Figure 8-12, the effectiveness is higher for thinner catalyst layer with higher effective diffusion coefficient due to the decreasing impact of mass transport. In the case of thinner catalyst layer and higher diffusivity, the mass transport through the pores of the catalyst layer becomes less significant, higher effectiveness factor is therefore achieved. The end point of each curve represents the dimensionless adsorption limiting current density.

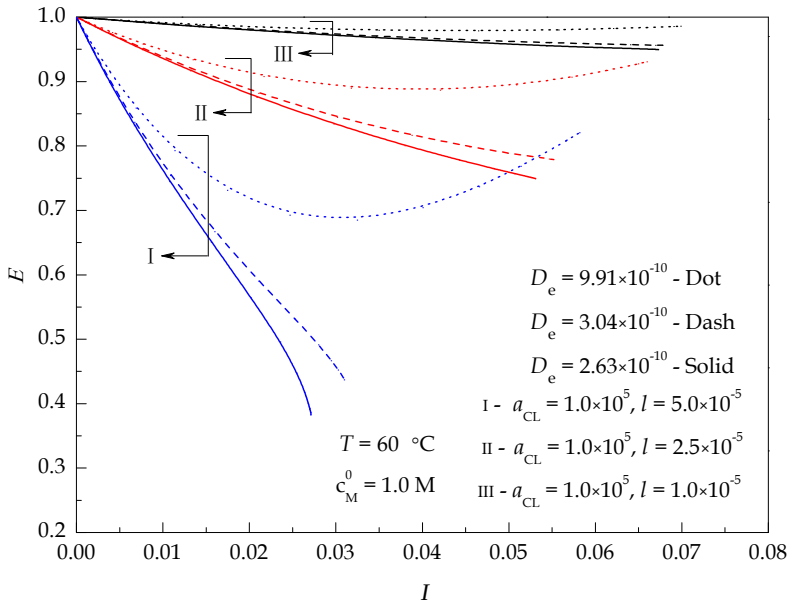

Figure 8-12 Effectiveness factor with different catalyst layer thicknesses and effective diffusion coefficients

Generally, effectiveness factor decreases as the macro current density increases. However, for a thicker catalyst layer as well as a larger D_e, the effectiveness factor goes through a minimum with current density, which is caused by the effects of both mass and charge transport. With unceasingly increasing current density, the effect of charge transport resistance gradually disappears due to the change of the rate determining step from CH_3OH_{ads} dehydrogenation (step 8-2) to methanol adsorption (step 8-1). The improved mass transport due to larger D_e indicates an increase in utilisation of the inner area of the catalyst layer, leading to an increase in the effectiveness factor as the current density increases. In this condition, more portion of the catalyst layer would be operated at or close to the limiting current until the adsorption limiting current density is achieved.

8.4 Conclusions

The steady state and time dependent macro kinetic model for methanol oxidation in a porous Pt-Ru anode is developed. The anode performance strongly depends on the kinetics parameters based on the dual-site mechanism as well as electrode parameters such as catalyst layer thickness, specific area, and porosity.

The intrinsic kinetics of methanol oxidation only relates to the flux of charge on the surface of porous electrode, i.e. the current density being independent of any physical parameter. However, the macro kinetics relates to the divergence of current density in the volume of the porous electrode. The macro kinetics requires a set of second order differential equations to describe the coupled mass and charge transport processes and chemical reaction in a three dimensional volume. By using the finite element method (FEM) with a subroutine for solving a set of non-linear algebraic equations in each step, the distributions of concentration and overpotential, as well as the surface coverage ratio of the intermediates, effectiveness factor and macro polarisation curves are obtained.

Comparing the predicted polarisation curves with experimental data, the theoretical analysis on the performance of the porous anode can be carried out to understand the macro kinetics and to find out ways to improve the performance of the electrode. Analysing the coverage ratios of the intermediates demonstrates that the change in coverage ratio of OH on Ru ($\theta_{OH,Ru}$) is very fast, with values close to 1.0 in the full range of overpotential. The element step (8-3a) is therefore not the rate determining step. The surface coverage ratio of CO on Pt ($\theta_{CO,Pt}$) determined the current density at lower

overpotential, i.e. lower than 0.5V. Consequently, CH_3OH_{ads} dehydrogenation (step 8-2) can be considered as the rate determining step at lower overpotential. The rate determining step changed to methanol adsorption (step 8-1) when the overpotential increased to above 0.6V. The apparent current densities are very small and almost approach zero at low overpotential for all cases since the electrolysis rate of CH_3OH_{ads} adsorbed on Pt is too small. Therefore, improving the catalyst activity is one of the important issues for reducing the electrode polarisation near "open-circuit". Due to the fact that the rate determining step will be changed from CH_3OH_{ads} dehydrogenation (step 8-2) to methanol adsorption (step 8-1) at higher overpotential, accelerating the adsorption rate of methanol on the surface of the catalyst is another important issue.

8.5 Final marks

DMFCs are a subcategory of PEMFCs, in which hydrogen is replaced by methanol solution at the anode as the fuel. Therefore, the mathematical models developed for PEMFCs can be applied to DMFCs by changing the kinetic expressions on the anode. The kinetic anode model for methanol oxidation in DMFCs developed in this chapter is expected to combine with the oxygen reduction model developed for PEMFCs. As a consequence, a complete and detailed model for a typical DMFC could be developed. The agglomerate kinetics based oxygen reduction reaction (ORR) and two-phase flow model developed from Chapter 4 to Chapter 6 for the cathode behavior of a PEMFC can be incorporated with the methanl oxidation reaction (MOR) kinetics developed in this chapter for a full representation of a DMFC unit. By considering the methanol cross over through the membrane, a comprehensive model for a DMFC operated at various conditions can be obtained.

Chapter 9. Conclusions and Future work

9.1 Conclusions

This thesis contributes to a better understanding of the physical and electrochemical processes within a PEM fuel cell, especially the water formation, phase change and transport. The developed models are believed to be useful tools to analyse the transport and electrochemical reaction processes involved in the fuel cell operation and predict the cell performance.

The mathematical models developed in this thesis are typically mechanistic, i.e. all physical and chemical phenomena in the fuel cell are described by algebraic and differential equations based on the properties of the species and processes. Three outstanding features are presented namely (1). Agglomerate assumption is applied for catalyst layer simulation. The properties of the catalyst layer, e.g. porosity, agglomerate density, specific area, ionomer and liquid water film thicknesses, can be algebraically calculated. (2). A combinational water phase transfer and transport mechanism is applied to describe the water phase transfer between water vapour, dissolved water and liquid water and the water transport through the membrane/ionomer under the driving forces of electro-osmotic drag (EOD), back diffusion and hydraulic permeation. (3). The majority of parameters used are treated as functions of temperature, pressure and/or water content. As a result of these features the model is capable of performing several tests at a variety of operating conditions and analysing the parameters which are hard to be obtained by experiment.

An along the channel, single-phase flow and isothermal model based on an agglomerate catalyst layer structure is developed. The increase in oxygen mass transport resistance through the ionomer film surrounding the agglomerate is proved to be critical for the rapid decrease in the predicted current density at high current. Higher platinum loading and carbon loading improve the cell performance at low current. However, the effectiveness factor is decreased, leading to a poor utilisation of the platinum particles near the membrane. Too much platinum and carbon loadings rather than improve the cell performance at high current densities can waste expensive catalyst.

An across the channel, two-phase flow and isothermal model based on an agglomerate catalyst layer structure is presented. The water phase transfer between water vapour, dissolved water and liquid water is addressed and the dissolved water transport through the membrane/ionomer according to a combinational mechanism is included. The membrane and ionomer swellings associating with the non-uniform water distribution are taken into account. By accounting for the increase in mass transport resistance resulting from membrane and ionomer swelling and considering the void space loss due to liquid water occupation (flooding), the two-phase flow model gives a greater accuracy in validating the experimental data in comparison with the single-phase flow model. The non-uniform distribution of the membrane and ionomer water content is a consequence of the electro-osmotic drag (EOD) and water absorption (water uptake) of the membrane and ionomer. At low current density and high relative humidity, the membrane/ionomer water absorption is the main mechanism in determining the membrane/ionomer water content. However, the effect of EOD is pronounced with low relative humidity and high current density, especially the portion of the catalyst layer close to the membrane.

Higher membrane/ionomer water content is predicted near the cathode CL-GDL boundary along the air flow direction on the region under the bipolar current collector. The membrane swelling increases the portion of GDL bulged into flow channel while the ionomer swelling decreases the catalyst layer porosity and increases the ionomer film thickness. For the purpose of the best fuel cell performance, the optimal dry ionomer loading (initial ionomer content) is from 0.2 to 0.3 mg cm^{-2} and the optimal cathode relative humidity is around 60%.

A fully coupled across the channel, two-phase flow and non-isothermal model is developed. The cell performance is improved by the heat accumulation in the MEA due to the increases in some important electrochemical parameters and the decrease in liquid water saturation in the electrode. At a fixed current density, the increase in operating temperature increases the water carrying capacity (WCC) which is of benefit to the membrane/ionomer water content and cell performance. Applying higher temperatures on the anode could improve the cell performance at high current densities. Applying higher temperatures on the cathode increases the ORR kinetics. However, it decreases the oxygen mole fraction at a fixed relative humidity, which probably leads to an oxygen depletion that then limits the cell performance. Heat accumulates inside the cathode catalyst layer on the region under the channel. Applying higher temperatures on

the anode and lower temperatures on the cathode optimise the temperature distribution in the MEA and avoid hot spots within the cathode catalyst layer and membrane. Enlarging the width ratio of the channel/rib also improve the cell performance. However, the improvement is limited by the sluggish ORR.

Five key parameters of the cathode catalyst layer, namely platinum loading, platinum mass ratio, ionomer volume fraction, catalyst layer thickness and agglomerate radius, are investigated and optimised by a multiple surrogate model and their sensitivities are analysed by a Monte Carlo method based approach. Maximising the current densities at a fixed cell voltage and during a specific cell voltage range are the two optimisation strategies implemented for the optima prediction. For the purpose of improving the cell performance, the catalyst layer porosity is important at high current densities while the ionomer volume fraction is important at low current densities. The platinum loading is important during a full range of current densities.

Both the steady state and time dependent macro kinetic model for methanol oxidation in a porous Pt-Ru anode of a DMFC is developed. The anode performance strongly depends on the intrinsic kinetics based on the dual-site mechanism as well as the electrode parameters, such as thickness, specific area and porosity of the electrode. Analysing the coverage ratios of the intermediates demonstrates that the methanol dehydrogenation reaction is the rate determining step at lower overpotential and it changes to the methanol adsorption as the overpotential increases, e.g. higher than 0.6 V. As a result, improving the catalyst activity for methanol dehydrogenation reaction and accelerating the methanol adsorption rate on the catalyst surface are considered as the two important issues for performance improvement.

9.2 Recommendations for future works

In order to improve the modelling reliability and compatibility, further works have to be done on several aspects.

1. Species crossover, such as, hydrogen, oxygen and nitrogen transport through the membrane have to be considered. Even through the amount of species crossover is small, it has significant effect on the PEMFCs degradation.

2. The steady state models for water generation, phase change and transport have to be extended to the dynamic models, which is capable of predicting the time-dependent behaviour of water and coupling the degradation processes of the PEMFCs.
3. For the purposes of fully representing and better understanding the physical and electrochemical behaviours in the practical fuel cells, the current two dimensional models have to be extended to three dimensional models.
4. Catalyst degradation, carbon corrosion and membrane degradation by chemical process to predict loss of fuel cell performance with time could be performed over a three dimensional domain.
5. Different three dimensional flow fields, such as interdigitated, serpentine and pin-type, have to be developed.
6. In DMFCs, both the oxygen reduction reaction at the cathode and methanol crossover through the membrane have to be considered into the kinetic anode model developed.
7. The mathematical model developed for the low temperature PEMFC should be extended to study the fuel cells with high temperature proton exchange membrane (HTPEM) and alkaline membrane.

References

1. Lund, H., *Renewable energy strategies for sustainable development*. Energy, 2007. **32**: p. 912-919.
2. Das, D. and T.N. Veziroglu, *Hydrogen production by biological processes: a survey of literature.* International Journal of Hydrogen Energy, 2001. **26**: p. 13-28.
3. Edwards, P.P., V.L. Kuznetsov, W.I.F. David and N.P. Brando, *Hydrogen and fuel cells: Towards a sustainable energy future*. Energy Policy, 2008. **36**: p. 4356-4362.
4. Conte, M., A. Iacobazzi, M. Ronchetti and R. Vellone, *Hydrogen economy for a sustainable development: State-of-the-art and technological perspectives.* Journal of Power Sources, 2001. **100**: p. 171-187.
5. Dincer I., *Renewable energy and sustainable development: a crucial review*. Renewable and Sustainable Energy Review, 2000, **4**: p.157-175.
6. Network, R.E.P. *Renewables Global Status Report*. 2013; Available from: http://www.ren21.net/REN21Activities/GlobalStatusReport.aspx. (accessed Jan 2014).
7. Edwards, P.P., V.L. Kuznetsov and W.I.F. David, *Hydrogen energy.* Philosophical Transactions of the Royal Society A: Mathematical, Physical and Engineering Sciences, 2007. **365**: p. 1043-1056.
8. Marban, G. and T. Valdes-Solis, *Towards the hydrogen economy?* International Journal of Hydrogen Energy, 2007. **32**: p. 1625-1637.
9. Network, *Renewables Global Status Report*. 2005; Available from: http://www.ren21.net/REN21Activities/GlobalStatusReport.aspx (accessed Jan 2014).
10. Lund, H. and P.A. Ostergaard, *Electric grid and heat planning scenarios with centralised and distributed sources of conventional, CHP and wind generation.* Energy, 2000. **25**: p. 299-312.
11. Dunn, S., *Hydrogen futures: Toward a sustainable energy system*. International Journal of Hydrogen Energy, 2002. **27**: p. 235-264.

12. Bossel, U., *The birth of the fuel cell 1835-1845*. Oberrohrdorf, Switzerland: European Fuel Cell Forum, 2000.

13. Grove, W.R., *On voltaic series and the combination of gases by platinum*. London and Edinburgh Philosophical Magazine and Journal of Science, 1839. **14**: p. 127-130.

14. Grove, W.R., *On a gaseous voltaic battery*. London and Edinburgh Philosophical Magazine and Journal of Science, 1842. **21**: p. 417-420.

15. Nadal, M. and F. Barbir, *Development of a hybrid fuel cell/battery powered electric vehicle.* International Journal of Hydrogen Energy, 1996. **21**: p. 497-505.

16. Weber, A.Z., S. Balasubramanian and P.K. Das. *Proton Exchange Membrane Fuel Cells.* in K. Sundmacher (editor), *Advances in Chemical Engineering Fuel Cell Engineering*, USA: Elsevier Inc; 2012. **41**: p. 66-143.

17. Barbir, F., *PEM fuel cells: theory and practice - 2nd Edition*. 2005, Oxford: Academic.

18. O'Hayre, R., S. Cha, W. Colella and F.B. Prinz, *Fuel cell fundamentals*. 2006, Hoboken, NJ: John Wiley & Sons, INC.

19. Appleby, A.J. and E.B. Yeager, *Solid polymer electrolyte fuel cells (SPEFCs).* Energy, 1986. **11**: p. 137-52.

20. Wang, Y., K.S. Chen, J. Mishler, S.C. Cho and X.C. Adroher, *A review of polymer electrolyte membrane fuel cells: Thechology, applications, and needs on fundamental research.* Applied Energy, 2011. **88**: p. 981-1007.

21. Bernardi, D.M. and M.W. Verbrugge. *A mathematical model of the solid-polymer-electrolyte fuel cell.* Journal of Electrochemical Society, 1992. **139**: p. 2477-2491.

22. Stone, C. and Morrison A.E., *From curiosity to "power to change the world".* Solid State Ionics, 2002. **152-153**: p.1-13.

23. Network, Fuel cell today patent review (2011 and 2012), Available from: www.fuelcelltoday.com/analysis.patents (accessed Jan 2014).

24. Gittleman C., D. Masten and S. Jorgensen. Automotive fuel cell R&D needs. in: DOE fuel cell pre-solicitation workshop. Department of Energy, Lakewood, Colorado, 2010.

25. Network, Intelligent energy launches Upp (TM) - Portable power for your connected devices (2013). Available from: www.intellignet-energy/consumer-electronics (accessed Jan 2014).

26. Scott, K. and A.K. Shukla, *Direct methanol fuel cells: fundamentals, problems and perspectives*. in R.E. White (editor), *Modern aspects of electrochemistry*, New York: Springer; 2007. **40**: p. 127-228.

27. Garcia, B.L. and J.W. Weidner, Review of direct methanol fuel cells. in R.E. White (editor), *Modern aspects of electrochemistry*, New York: Springer; 2007. **40**: p. 229-284.

28. Zhang, J. and Y. Wang, *Modeling the effects of methanol crossover on the DMFC*. Fuel Cells, 2004. **4**: p. 90-95.

29. Gottesfeld, S., *Fuel cell techno-personal milestones 1984-2006.* Journal of Power Sources, 2007. **171**: p. 37-45.

30. Scott, K. and L. Xing, *Direct Methanol Fuel Cells*. in K. Sundmacher (editor), *Advances in Chemical Engineering Fuel Cell Engineering*, USA: Elsevier Inc; 2012. **41**: p. 145-195.

31. Murgia, G., L. Pisani, A.K. Shukla and K. Scott, Journal of Electrochemical Society, 2003. **150**: p. A1231-A1245.

32. Li, X. and A. Faghri, *Review and advances of direct methanol fuel cells (DMFCs) part I: Design, fabrication, and testing with high concentration methanol solutions.* Journal of Power Sources, 2013. **226**: p. 223-240.

33. Yomogita H., Sony Unveils Ultra small Hybrid Fuel Cell (2008). Available from: http://techon.nikkeibp.co.jp/english/NEWS EN/20080502/151303/. (accessed Jan 2014).

34. Network, Toshiba launches direct methanol fuel cell in Japan as external power source for Mobile Electronic Devices (2009). Available from: http://www.toshiba.com/taec/news/press_releases/2009/dmfc_09_580.jsp (accessed Jan 2014).

35. Network, OorjaPac Model III Product Sheet (2011). Available from: http://oorjafuelcells.com/services/oorjapac-model-iii/ (accessed Jan 2014).

36. Guran, V., H. Liu and S. Kakac, *Two-dimensional model for proton exchange membrane fuel cells.* AIChE Journal, 1998, **44**: p. 2410-2422.

37. Hottinen, T. and O. Himanen, *PEMFC temperature distribution caused by inhomogeneous compression of GDL*. Electrochemistry Communications, 2007, **9**: p. 1047-1052.

38. Yan, W.M., C.Y. Soong, F. Chen and H.S. Chu, *Effect of flow distributor geometry and diffusion layer porosity on reactant gas transport and performance of proton exchange membrane fuel cells*. Journal of Power Source, 2004, **125**: p. 27-39.

39. Secanell, M, J. Wishart and P. Dobson, *Computational design and optimisation of fuel cells and fuel cell systems: A review*. Journal of Power Sources, 2011. **196**: p. 3690-3704.

40. Mehta, V. and J.S. Cooper, *Review and analysis of PEM fuel cell design and manufacturing*. Journal of Power Sources, 2003. **114**: p. 32-53.

41. Sharma, S. and B.G. Pollet, *Support materials for PEMFC and DMFC electrocatalysts- A review*. Journal of Power Sources, 2012. **208**: p. 96-119.

42. Aiyejina, A. and M.K.S Sastry, *PEMFC flow channel geometry optimization: A review*. Journal of Fuel Cell Science and Technology, 2012. **9**: p. 011011-1-011011-24.

43. Scott, K. and A.K. Shukla, *Direct Methanol Fuel Cells: Fundamentals, problems and perspectives*. in R.E. White (editor), *Modern aspects of electrochemistry*, New York: Springer; 2007. **40**: p. 127-218.

44. Song, D., Q. Wang, Z. Liu, T. Navessin, M. Eikerling and S. Holdcroft, *Numerical optimisation study of the catalyst layer of PEM fuel cell cathode*. Journal of Power Sources, 2004. **126**: p. 104-111.

45. Song, D., Q. Wang, Z. Liu, T. Navessin and S. Holdcroft, *Numerical study of PEM fuel cell cathode with non-uniform catalyst layer*. Electrochimica Acta, 2004. **50**: p. 731-737.

46. Secanell, M., R. Songprakorp, A. Suleman and N. Djilali, *Multi-objective optimisation of a polymer electrolyte fuel cell membrane electrode assembly*. Energy & Environmental Science. 2008, **1**: p. 378-388.

47. Secanell, M., R. Sonprakorp, N. Djilali and A. Suleman, *Optimisation of a proton exchange membrane fuel cell membrane electrode assembly*. Structural and Multidisciplinary Optimisation. 2010, **40**: p. 563-583.

48. Jeon, D.H., K.N. Kim, S.M. Baek and J.H. Nam, *The effect of relative humidity of the cathode on the performance and uniformity of PEM fuel cells*. International Journal of Hydrogen Energy, 2011. **36**: p. 12499-12511.

49. Kim, Y.B., *Study on the effect of humidity and stoichimetry on the water saturation of PEM fuel cells*. International Journal of Energy Research, 2012. **36**: p. 509-522.

50. Liu, H., P. Li and K. Wang, *Optimization of PEM fuel cell flow channel dimensions- Mathematic modelling analysis and experimental verification.* International Journal of Hydrogen Energy, 2013. **38**: p. 9835-9846.

51. Nguyen, T.V., *A gas distributor design for proton exchange membrane fuel cells*. Journal of Electrochemical Society, 1996. **143**: p. L103-L105.

52. Kazim, A., H.T. Liu and P. Forges, *Modelling of performance of PEM fuel cells with conventional and interdigitated flow fields*. Journal of Applied Electrochemistry, 1999. **29**: p. 1409-1416.

53. Sousa, T., M. Mamlouk, K. Scott and C.M. Rangel, *Three dimensional model of a high temperature PEMFC. Study of the flow field effect on performance.* Fuel Cells, 2012. **12**: p. 566-576.

54. Akhtar, N., A. Qureshi, J. Scholta, C. Hartnig, M. Messerschmidt and W. Lehnert, *Investigation of water droplet kinetics and optimisation of channel geometry for PEM fuel cell cathodes*. International Journal of Hydrogen Energy, 2009. **34**: p. 3104-3111.

55. Salah, Y.B., Y. Tabe and T. Chikahisa, *Gas channel optimisation for PEM fuel cell using the lattice Boltzmann method*. Energy Procedia, 2012. **28**: p. 125-133.

56. Ji, M. and Z. Wei, *A Review of Water Management in Polymer Electrolyte Membrane Fuel Cells.* Energies, 2009. **2**: p. 1057-1106.

57. Nguyen, T.V. and M.W. Knobbe, *A liquid water management strategy for PEM fuel cell stacks.* Journal of Power Sources, 2003. **114**: p. 70-79.

58. Canut, J.M.L., R.M. Abouatallah and D.A. Harrington, *Detection of membrane drying, fuel cell flooding, and anode catalyst poisoning on PEMFC stacks by electrochemical impedance spectroscopy*. Journal of Electrochemical Society, 2006. **153**: p. A857-A864.

59. Hickner, M.A., C.H. Fujimoto and C.J. Cornelius, *Transport in sulfonated poly(phenylene)s: Proton conductivity, permeability, and the state of water*. Polymer, 2006. **47**: p. 4238-4244.

60. Stumper, J., M. Lohr and S. Hamada, *Diagnostic tools for liquid water in PEM fuel cells.* Journal of Power Sources, 2005. **143**: p. 150-157.

61. Barbir, F., H. Gorgun and X. Wang, *Relationship between pressure drop and cell resistance as a diagnostic tool for PEM fuel cells*. Journal of Power Sources, 2005. **141**: p. 96-101.

62. Natarajan, D. and T.V. Nguyen, *Current distribution in PEM fuel cells. Part I: Oxygen and fuel flow rate effects*. AIChE Journal, 2005. **51**: p. 2587-2598.

63. Meng, H. and C.Y. Wang, *New model of two-phase flow and flooding dynamics in polymer electrolyte fuel cells*. Journal of Electrochemical Society, 2005. **152**: p. A1733-A1741.

64. Janssen, G.J.M. and M.L.J. Overvelde, *Water transport in the proton-exchange-membrane fuel cell: measurements of the effective drag coefficient*. Journal of Power Sources, 2001. **101**: p. 117-125.

65. Sridhar, P., *Humidification studies on polymer electrolyte membrane fuel cell*. Journal of Power Sources, 2001. **101**: p. 72-78.

66. Wang, Y. and C.Y. Wang, *Dynamics of polymer electrolyte fuel cells undergoing load changes.* Electrochimica Acta, 2006. **51**: p. 3924-3933.

67. Li, C.C. and P.G. Pickup, *Dependence of electrode overpotentials in PEM fuel cells on the placement of the reference electrode.* Electrochemical and Solid-State Letters, 2006. **9**: p. A249-A251.

68. Okada, T., *Theory for water management in membranes for polymer electrolyte fuel cells: Part I. The effect of impurity ions at the anode side on the membrane performances*. Journal of Electroanalytical Chemistry, 1999. **465**: p. 1-17.

69. Knights, S.D., K.M. Colbow, J. St-Pierre and D.P. Wilkinson, *Aging mechanisms and lifetime of PEFC and DMFC*. Journal of Power Sources, 2004. **127**: p. 127-134.

70. Sinha, P.K. and C.Y. Wang, *Probing effects of GDL microstructure on liquid water transport by pore network modeling*. ECS Transactions, 2006. **3**: p. 387-396.

71. Kumbur, E.C., K.V. Sharp and M.M. Mench, *Validated Leverett approach for multiphase flow in PEFC diffusion media: III. temperature effect and unified approach*. Journal of Electrochemical Society, 2007. **154**: p. B1315-B1324.

72. Natarajan, D. and T.V. Nguyen, *A two-dimensional, two-phase, multicomponent, transient model for the cathode of a proton exchange membrane fuel cell using conventional gas distributors*. Journal of Electrochemical Society, 2001. **148**: p. A1324-A1335.

73. Berg, P., K. Promislow, J. St-Pierre, J. Stumper and B. Wetton, Water management in PEM fuel cells. Journal of Electrochemical Society, 2004. **151**: p. A341-A353.

74. Springer, T.E., T.A. Zawodzinski and S. Gottesfeld, *Polymer electrolyte fuel cell model*. Journal of Electrochemical Society, 1991. **138**: p. 2334-2342.

75. Springer, T.E., M.S. Wilson and S. Gottesfeld, *Modeling and experimental diagnostics in polymer electrolyte fuel cells*. Journal of Electrochemical Society, 1993. **4**: p. 3513-3526.

76. Bernardi, D.M. and M.W. Verbrugge, *Mathematical model of a gas diffusion electrode bonded to a polymer electrolyte*. AIChE Journal, 1991. **37**: p. 1151-1163.

77. Nguyen, T.V. and R. E. White, *A water and heat management model for proton-exchange-membrane fuel cells*. Journal of Electrochemical Society, 1993. **140**: p. 2178-2186.

78. Fuller, T.F. and J. Newman, *Water and thermal management in solid-polymer-electrolyte fuel cells*. Journal of Electrochemical Society, 1993. **140**: p. 1218-1225.

79. Yi, J.S. and T.V. Nguyen, *An along-the-channel model for proton exchange membrane fuel cells*. Journal of Electrochemical Society, 1998, **145**: p. 1149-1159.

80. Yi, J.S. and T.V. Nguyen, *Multicomponent transport in porous electrodes of proton exchange membrane fuel cells using the interdigitated gas distributors*. Journal of Electrochemical Society, 1999. **146**: p. 38-45.

81. Gloaguen, F. and R. Durand, *Simulations of PEFC cathodes: an effectiveness factor approach*. Journal of Applied Electrochemistry, 1997. **27**: p. 1029-1035.

82. Bultel, Y., P. Ozil and R. Durand, *Modelling the mode of operation of PEMFC electrodes at the particle level: influence of ohmic drop within the active layer on electrode performance*. Journal of Applied Electrochemistry, 1998. **28**: p. 269-276.

83. Bultel, Y., P. Ozil and R. Durand, *Modified thin film and agglomerate models for active layers of P.E. fuel cells*. Electrochimica Acta, 1998. **43**: p. 1077-1087.

84. Bultel, Y., P. Ozil and R. Durand, *Modelling of mass transfer within the PEM fuel cell active layer: limitations at the particle level.* Journal of Applied Electrochemistry, 1999. **29**: p. 1025-1033.

85. Marr, C. and X. Li, *Composition and performance modelling of catalyst layer in a proton exchange membrane fuel cell*. Journal of Power Sources, 1999. **77**: p. 17-27.

86. Spernjak, D., A.K. Prasad and S.G. Advani, *Experimental investigation of liquid water formation and transport in a transparent single-serpentine PEM fuel cell*. Journal of Power Sources, 2007. **170**: p. 334-344.

87. Tuber, K., D. Pocza and C. Hebling, *Visualization of water buildup in the cathode of a transparent PEM fuel cell*. Journal of Power Sources, 2003. **124**: p. 403-414.

88. Dutta, S., S. Shimpalee and J.W. Van-Zee, *Three-dimensional numerical simulation of straight channel PEM fuel cells.* Journal of Applied Electrochemistry, 2000. **30**: p. 135-146.

89. Dutta, S., S. Shimpalee and J. W. Van-Zee, *Numerical prediction of mass-exchange between cathode and anode channels in a PEM fuel cell*. International Journal of Heat and Mass Transfer, 2001. **44**: p. 2029-2042.

90. Zhou, T. and H. Liu, *A general three-dimensional model for proton exchange membrane fuel cells.* International Journal of Transport Phenomena, 2001. **3**: p. 177-198.

91. Berning, T., D.M. Lu and N. Djilali, *Three-dimensional computational analysis of transport phenomena in a PEM fuel cell.* Journal of Power Sources, 2002. **106**: p. 284-294.

92. Mazumder, S. and J.V. Cole, *Rigorous 3-D mathematical modeling of PEM fuel cells: I model predictions without liquid water transport*. Journal of Electrochemical Society, 2003. **150**: p. A1503-A1509.

93. Lee, W.K., S. Shimpalee and J.W. Van-Zee, *Verifying predictions of water and current distributions in a serpentine flow field polymer electrolyte membrane fuel cell.* Journal of Electrochemical Society, 2003. **150**: p. A341-A348.

94. Um S. and C.Y. Wang, *Three-dimensional analysis of transport and electrochemical reactions in polymer electrolyte fuel cells*. Journal of Power Sources, 2004. **125**: p. 40-51.

95. Wang, Y. and C.Y. Wang, *Transient analysis of polymer electrolyte fuel cells*. Electrochimica Acta, 2005. **50**: p. 1307-1315.

96. Liu, Z., Z. Mao, C. Wang, W. Zhuge and Y. Zhang, *Numerical simulation of a mini PEMFC stack*. Journal of Power Sources, 2006. **160**: p. 1111-1121.

97. Shimpalee, S., S. Greenway, D. Spuckler and J.W. Van-Zee. *Predicting water and current distributions in a commercial-size PEMFC*. Journal of Power Sources, 2004. **135**: p. 79-87.

98. Ju, H., H. Meng and C.Y. Wang, *A single-phase, non-isothermal model for PEM fuel cells.* International Journal of Heat and Mass Transfer, 2005. **48**: p. 1303-1315.

99. Wang, Y. and C.Y. Wang, *Ultra large-scale simulation of polymer electrolyte fuel cells.* Journal of Power Sources, 2006. **153**: p. 130-135.

100. He, W., J.S. Yi and T.V. Nguyen, *Two-phase flow model of the cathode of PEM fuel cells using interdigitated flow fields*. AIChE Journal, 2000. **46**: p. 2053-2064.

101. Lin, G. and T.V. Nguyen, *A two-dimensional two-phase model of a PEM fuel cell*. Journal of the Electrochemical Society, 2006. **153**: p. A372-A382.

102. Natarajan, D. and T.V. Nguyen, *Three-dimensional effects of liquid water flooding in the cathode of a PEM fuel cell.* Journal of Power Sources, 2003. **115**: p. 66-80.

103. Ye, Q. and T.V. Nguyen, *Three-dimensional simulation of liquid water distribution in a PEMFC with experimentally measured capillary functions*. Journal of the Electrochemical Society, 2007. **154**: p. B1242-B1251.

104. Sui, P.C., S. Kumar and N. Djilali, *Advanced computational tools for PEM fuel cell design: Part I. Development and base case simulations*. Journal of Power Sources, 2008. **180**: p. 410-422.

105. Sui, P.C., S. Kumar and N. Djilali, *Advanced computational tools for PEM fuel cell design: Part II. Detailed experimental validation and parametric study*. Journal of Power Sources, 2008. **180**: p. 423-432.

106. Berning, T. and N. Djilali, *A 3D, multiphase, multicomponent model of the cathode and anode of a PEM fuel cell.* Journal of Electrochemical Society, 2003. **150**: p. A1589-A1598.

107. Mazumder, S. and J.V. Cole, *Rigorous 3-D mathematical modeling of PEM fuel cells:II. model predictions with liquid water transport*. Journal of Electrochemical Society, 2003. **150**: p. A1510-A1517.

108. Basu, S., J. Li and C.Y. Wang, *Two-phase flow and maldistribution in gas channels of a polymer electrolyte fuel cell.* Journal of Power Sources, 2009. **187**: p. 431-443.

109. Wang, Y., S. Basu and C.Y. Wang, *Modeling two-phase flow in PEM fuel cell channels*. Journal of Power Sources, 2008. **179**: p. 603-617.

110. Quan, P., B. Zhou, A. Sobiesiak and Z. Liu, *Water behaviour in serpentine micro-channel for proton exchange membrane fuel cell cathode*. Journal of Power Sources, 2005. **152**: p. 131-145.

111. Newman, J., *Electrochemical Systems*. 3th edition, 2004, New Jersey: Prentice-Hall.

112. Weber, Z. and J. Newman, *Transport in polymer-electrolyte membranes. I. Pyhyssical Model*. Journal of Electrochemical society, 2003. **150**: p. A1108-A1115.

113. Pintauro, P.N. and D.N. Bennion, *Mass transport of electrolytes in membrane I: development of mathematical transport model*. Industrial and Engineering Chemistry Fundamentals, 1984. **23**: p. 230-234.

114. Nam, J.H. and M. Kaviany, *Effective diffusion and water-saturation distribution in single- and two-layer PEMFC diffusion medium*. International Journal of Heat and Mass Transfer, 2003. **46**: p. 4595-4611.

115. Sun, W., B.A. Peppley and K. Karan, *An improved two-dimensional agglomerate cathode model to study the influence of catalyst layer structural parameters*. Electrochimica Acta, 2005. **50**: p. 3359-3374.

116. Das, P.K., X. Li and Z.S. Liu, *A three-dimensional agglomerate model for the cathode catalyst layer of PEM fuel cells.* Journal of Power Sources, 2008. **179**: p. 186-199.

117. Park, J.W., K. Jiao and X. Li, *Numerical investigation on liquid water removal from the porous gas diffusion layer by reactant flow*. Applied Energy, 2010. **87**: p. 2180-2186.

118. Wang, L.-P. and B. Afsharpoya, *Modeling fluid flow in fuel cells using the lattice-Boltzmann approach*. Mathematics and Computer in Simulation, 2006. **72**: p. 242-248.

119. Park, J., M. Matsubara and X. Li, *Application of lattice Boltzmann method to a micro-scale flow simulation in the porous electrode of a PEM fuel cell*. Journal of Power Sources, 2007. **173**: p. 404-414.

120. Delavar, M.A., M. Farhadi and K. Sedighi, *Numerical simulation of direct methanol fuel cells using lattice Boltzmann method*. International Journal of Hydrogen Energy, 2010. **35**: p. 9306-9317.

121. Gao, Y., X.X. Zhang, P. Rama, Y. Liu, R. Chen, H. Ostadi and K. Jiang, *Modeling fluid flow in the gas diffusion layers in PEMFC using the multiple relaxation-time Lattice Boltzmann method*. Fuel Cells, 2012. **12**: p. 365-381.

122. Jeng, K.T., S.F. Lee, G.F. Tsai and C.H. Wang, *Oxygen mass transfer in PEM fuel cell gas diffusion layers*. Journal of Power Sources, 2004, **138**: p. 41-50.

123. Wood, D.L., J.S. Yi and T.V. Nguyen, *Effect of direct liquid water injection and interdigitated flow field on the performance of proton exchange membrane fuel cell.* Electrochimica Acta, 1998. **43**: p. 3795-3809.

124. Guo, N., M.C. Leu and U.O. Koylu, *Network based optimization model for pin-type flow field of polymer electrolyte membrane fuel cell*. International Journal of Hydrogen Energy, 2013. **38**: p. 6750-6761.

125. Hakenjos, H. Muenter, U. Wittstadt and C. Hebling, *A PEM fuel cell for combined measurement of current and temperature distribution, and flow field flooding*. Journal of Power Sources, 2004. **131**: p. 213-216.

126. Zhang, F.Y., X.G. Yang and C.Y. Wang, *Liquid water removal from a polymer electrolyte fuel cell*. Journal of Electrochemical Society, 2006. **153**: p. A225-A232.

127. Hussaini, I.S. and C.Y. Wang, *Visualization and quantification of cathode channel flooding in PEM fuel cells*. Journal of Power Sources, 2009. **187**: p. 444-451.

128. Minard, K., V. Viswanathan, P. Majors, L. Wang and P. Rieke, *Magnetic resonance imaging (MRI) of PEM dehydration and gas manifold flooding during continuous fuel cell operation*. Journal of Power Sources, 2006. **161**: p. 856-863.

129. Satija, R., D. Jacobson, M. Arif and S. Werner, *In situ neutron imaging technique for evaluation of water management systems in operating PEM fuel cells*. Journal of Power Sources, 2004. **129**: p. 238-245.

130. Nam, J.H., K.J. Lee, G.S. Hwang, C.J. Kim and M. Kaviany, *Microporous layer for water morphology control in PEMFC*. International Journal of Heat and Mass Transfer, 2009. **52**: p. 2779-2791.

131. Bazylak, A., D. Sinton, Z.S. Liu and N. Djilali, *Effect of compression on liquid water transport and microstructure of PEMFC gas diffusion layers*. Journal of Power Sources, 2007. **163**: p. 784-792.

132. Bazylak, A., D. Sinton and N. Djilali, *Dynamic water transport and droplet emergence in PEMFC gas diffusion layers*. Journal of Power Sources, 2008. **176**: p. 240-246.

133. Arora, J.S. and Q. Wang, *Review of formulations for structural and mechanical system optimisation*. Structural and Mulidisciplinary Optimization, 2005. **30**: p. 251-272.

134. Evgrafov, A., M. Patriksson and J. Petersson, *Stochastic structural topology optimisation: existence of solution and sensitivity analyses*. Journal of Applied Mathematics and Mechanics, 2003. **83**: p. 479-492.

135. Secanell, M. and A. Suleman, *Numerical evaluation of optimisation algorithms for low-Reynolds-number aerodynamic shape optimisation*. AIAA Journal, 2005. **43**: p. 2262-2267.

136. Bendsoe, M. and O. Sigmund, Topology Optimisation, 2nd edition, Springer-Verlag, 2003.

137. Grujicic, M. and K.M. Chittajallu, *Design and optimisation of polymer electrolyte membrane (PEM) fuel cells*. Applied Surface Science, 2004. **227**: p. 56-72.

138. Lin, H.-H., C.-H. Cheng, C.-Y. Soong, F. Chen and W.-M. Yan, *Optimisation of key parameters in the proton exchange membrane fuel cell*. Journal of Power Sources, 2006. **162**: p. 246-254.

139. Secanell, M., K. Karan, A. Suleman and N. Djilali, *Multi-variable optimization of PEMFC cathodes using an agglomerate model*. Electrochimica Acta, 2007. **52**: p. 6318-6337.

140. Kazim, A., P. Forges and H.T. Liu, *Effects of cathode operating conditions on performance of a PEM fuel cell with interdigitated flow field*. International Journal of Energy Research, 2003. **27**: p. 401-414.

141. Kim, S., S. Shimpalee and J.W. Van-Zee, *The effect of stoichiomerty on dynamic behaviour of a proton exchange membrane fuel cell (PEMFC) during load change*. Journal of Power Sources, 2004. **135**: p. 110-121.

142. Amirinejad, M., S. Rowshanzamir and M.H. Eikani, *Effect of operating parameters on performance of a proton exchange membrane fuel cell*. Journal of Power Sources, 2006. **161**: p. 872-875.

143. Wishart, J., Z. Dong and M. Secanell, *Optimisation of a PEM fuel cell system based on empirical data and a generalised electrochemical semi-empirical model.* Journal of Power Sources, 2006. **161**: p. 1041-1055.

144. Mawardi, A., F. Yang and R. Pitchumani, *Optimisation of the operating parameters of a proton exchange membrane fuel cell for maximum power density*. Journal of Fuel Cell Science and Technology, 2005. **2**: p. 121-135.

145. Wu, J., Q. Liu and H. Fang, *Toward the optimisation of operating conditions for hydrogen polymer electrolyte fuel cells*. Journal of Power Sources, 2006. **156**: p. 388-399.

146. Zhang, W. and C.-W. Wu, *Effect of clamping load on the performance of proton exchange membrane fuel cell stack and its optimisation design: A review of modelling and experimental research.* Journal of Fuel Cell Science and Technology, 2014. **11**: p. 021012-1 - 021012-11.

147. Zhou, P., C.W. Wu and G.J. Ma, *Numerical study on the compression effect of Gas Diffusion Layer on PEMFC Performance*, Journal of Power Sources, 2007. **170**: p. 93-100.

148. Mohamed, I. and N. Jenkins, *Proton exchange membrane (PEM) fuel cell stack configuration using genetic algorithms*. Journal of Power Sources, 2004. **131**: p. 142-146.

149. Zhou, Y., Y. Luo, S. Yu and K. Jiao, *Modelling of cold start processes and performance optimisation for proton exchange membrane fuel cell stacks.* Journal of Power Sources, 2014. **247**: p. 738-748.

150. Scott, K., W. Taama, J. Cruickshank, *Performance and modeling of a direct methanol solid polymer electrolyte fuel cell*. Journal of Power Sources, 1997. **65**: p. 159-171.

151. Cruickshank, J. and K. Scott, *The degree and effect of methanol crossover in the direct methanol fuel cell*. Journal of Power Sources, 1998. **70**: p. 40-47.

152. Sundmacher, K. and K. Scott, *Direct methanol polymer electrolyte fuel cell: analysis of charge and mass transfer in the vapor-liquid-solid system*. Chemical Engineering Science, 1999. **54**: p. 2927-2936.

153. Kulikovsky, A.A., *The voltage-current curve of a direct methanol fuel cell: "exact" and fitting equations*. Electrochemistry Communications, 2002. **4**: p. 939-946.

154. Kulikovsky, A.A., *Analytical model of the anode side of DMFC: the effect of non-Tafel kinetics on cell performance*. Electrochemistry Communications, 2003. **5**: p. 530-538.

155. Kulikovsky, A.A., *A method for analysis of DMFC performance curves*. Electrochemistry Communications, 2003. **5**: p. 1030-1036.

156. Kauranen, P.S. and E. Skou, *Mixed methanol oxidation/oxygen reduction currents on a carbon supported Pt catalyst*. Journal of Electroanalytical Chemistry, 1996. **408**: p. 189-198.

157. Sundmacher, K., T. Schultz, S. Zhou, K. Scott, M. Ginkel and E.D. Gilles, *Dynamics of the direct methanol fuel cell (DMFC): experiments and model-based analysis*. Chemical Engineering Science, 2001. **56**: p. 333-341.

158. Simoglou, A., P. Argyropoulos, E.B. Martin, K. Scott, A.J. Morris, W.M. Taama, *Dynamic modeling of the voltage response of direct methanol fuel cells and stacks Part I: model development and validation*. Chemical Engineering Science, 2001. **56**: p. 6761-6772.

159. Simoglou A., P. Argyropoulos, E.B. Martin, K. Scott, A.J. Morris, W.M. Taama, *Dynamic modeling of the voltage response of direct methanol fuel cells and stacks Part II: feasibility study of model-based scale-up and scale-down*. Chemical Engineering Science, 2001. **56**: p. 6773-6779.

160. Argyropoulos, P., K. Scott, A.K. Shukla, C. Jackson, *A semi-empirical model of the direct methanol fuel cell performance Part I. Model development and verification*. Journal of Power Sources, 2003, **123**: p. 190-199.

161. Dohle, H. and K. Wippermann, *Experimental evaluation and semi-empirical modeling of U/I characteristics and methanol permeation of a direct methanol fuel cell*. Journal of Power Sources, 2004. **135**: p. 152-164.

162. Nordlund, J. and G. Lindbergh, *A model for the porous direct methanol fuel cells anode*. Journal of Electrochemical Society, 2002. **149**: p. A1107-A1113.

163. Freelink, T., W. Visschev, J.A.R. van Veen, *Measurement of the Ru Surface Content of Electrocodeposited Pt-Ru Electrodes with the Electrochemical Quartz Crystal Microbalance: Implications for Methanol and CO Electrooxidation*. Langmuir, 1996. **12**: p. 3702-3708.

164. Meyers, J.P. and J. Newmann, *Simulation of the Direct Methanol Fuel Cell I. Thermodynamic Framework for a Multicomponent Membrane*. Journal of Electrochemical Society, 2002. **149**: p. A710-A717.

165. Meyers, J.P. and J. Newmann, *Simulation of the Direct Methanol Fuel Cell II. Design and Optimization*. Journal of Electrochemical Society, 2002. **149**: p. A729-A735.

166. Gasteiger, H.A., N. Markovic, P.N. Ross Jr., E.J. Cairns, *Temperature-Dependent Methanol Electro-Oxidation on Well-Characterized Pt-Ru Alloys*. Journal of Electrochemical Society, 1995. **141**: p. 1795-1803.

167. Scott, K. and P. Argyropoulos, *A one dimensional model of a methanol fuel cell anode*. Journal of Power Sources, 2004. **137**: p. 228-238.

168. Valdez, T.I., S.R. Narayanan, H. Frank and W. Chun, Annual Battery Conference on Application and Advances. Long Beach, USA. 1997.

169. Argyropoulos, P., K. Scott and W.M. Taama, *Dynamic response of the direct methanol fuel cell under variable load conditions*. Journal of Power Sources, 2000. **87**: p. 153-161.

170. Argyropoulos, P., K. Scott and W. M. Taama, *An investigation of scale-up on the response of the direct methanol fuel cell under variable load conditions*. Journal of Applied Electrochemistry, 2001. **31**: p. 13-24.

171. Schultz, T., S. Zhou and K. Sundmacher, *Current Status of and Recent Developments in the Direct Methanol Fuel Cell.* Chemical Engineering and Technology, 2001. **24**: p. 1223-1233.

172. Schultz, T., *Experimental and Model-based Analysis of the Steady State and Dynamic Operating Behaviour of the Direct Methanol Fuel Cell*. Ph D Thesis, Otto-von-Guericke University, Magdeburg, Germany, 2003.

173. Gerteisen, D., *Transient and steady-state analysis of catalyst poisoning and mixed potential formation in direct methanol fuel cells*. Journal of Power Sources, 2011. **195**: p. 6719-6731.

174. Chippar, P., J. Ko, H. Ju, *A global transient, one-dimensional, two-phase model for direct methanol fuel cells (DMFCs) Part II: Analysis of the time-dependent thermal behaviour of DMFCs*. Energy, 2010. **35**: p. 2301-2308.

175. Guarnieri, M., V.D. Noto and F. Moro, *A Dynamic Circuit Model of a Small Direct Methanol Fuel Cell for Portable Electronic Devices*. IEEE Transactions on Industrial Electronics, 2010. **57**: p. 1865-1873.

176. O'Hayre R., D.M. Barnett, F.B. Prinz, *The triple phase boundary - A mathematical model and experimental investigations for fuel cells.* Journal of Electrochemistry Society, 2005. **152**: p. A439-A444.

177. Xie, Z., T. Navessin, K. Shi, R. Chow, Q. Wang, D. Song, B. Andreaus, M. Eikerling, Z. Liu and S. Holdcroft, *Functionally graded cathode catalyst layer for polymer electrolyte fuel cells II. Experimental study of the effect of Nafion distribution*. Journal of Electrochemical Society, 2005. **152**: p. A1171-A1179.

178. Karan, K., *Assessment of transport-limited catalyst utilization for engineering of ultra-low Pt loading polymer electrolyte fuel cell anode*. Electrochemistry Communications, 2007. **9**: p. 747-753.

179. Thomas, J.M. and W.J. Thomas, *Introduction to the principles of heterogeneous catalysis*. 1967, London; New York: Academic Press.

180. Morais, R.F., P. Sautet, D. Loffreda and A.A. Franco, *A multiscale theoretical methodology for the calculation of electrochemical observables from ab initio data: Application to the oxygen reduction reaction in a Pt (1 1 1)-based polymer electrolyte membrane fuel cell.* Electrochimica Acta, 2011. **56**: p. 10842-10856.

181. Xing, L., X. Song, K. Scott, V. Pickert, W. Cao, *Multi-variable optimisation of PEMFC cathodes based on surrogate modelling*. International Journal of Hydrogen Energy, 2013. **38**: p. 14295-14313.

182. Khajeh-Hosseini-Dalasm N., M.J. Kermani, D.G. Moghaddam and J.M. Stockie, *A parametric study of cathode catalyst layer structural parameters on the performance of a PEM fuel cell*. International Journal of Hydrogen Energy, 2013. **35**: p. 2417-2427.

183. Khajeh-Hosseini-Dalasm N., M. Fesanghary, K. Kushinobu and K. Okazaki, *A study of the agglomerate catalyst layer for the cathode side of a proton exchange membrane fuel cell: Modeling and optimization.* Electrochimica Acta, 2012. **60**: p. 55-65.

184. Wu, H., P. Berg and X. Li, *Modelling of PEMFC Transients with Finite-Rate Phase-Transfer Processes*. Journal of Electrochemistry Society, 2010. **157**: p. B1-B12.

185. Wu, H., P. Berg and X. Li, *Steady and unsteady 3D non-isothermal modelling of PEM fuel cells with the effect of non-equlibrium phase transfer*. Applied Energy, 2010. **87**: p. 2778-2784.

186. Yang, X.G., Q. Ye and P. Cheng, *Matching of water and temperature fields in proton exchange membrane fuel cells with non-uniform distributions*. International Journal of Hydrogen Energy, 2011. **36**: p. 12524-12537.

187. Springer, T.E., T.A. Zawodzinski and S. Gottesfeld, *Polymer Electrolyte Fuel Cell Model*. Journal of Electrochemistry Society, 1991. **138**: p. 2234-2242.

188. Shah, A.A., G.S. Kim, P.C. Sui and D. Harvey, *Transient non-isothermal model of a polymer electrolyte fuel cell*. Journal of Power Sources, 2007. **163**: p. 793-806.

189. Weber, A.Z. and J. Newman, *Transport in polymer-electrolyte membranes I. Physical model*. Journal of Electrochemistry Society, 2003. **150**: p. A1008-A1015.

190. Ge, S.H., X.G. Li, B.L. Yi and I.M. Hsing, *Absorption, Desorption, and Transport of Water in Polymer Electrolyte Membrane for Fuel Cells*. Journal of Electrochemistry Society, 2005. **152**: p. A1149-A1157.

191. Pasaogullari, U. and C.Y. Wang, *Two-phase transport and the role of micro-porous layer in polymer electrolyte fuel cells*. Electrochimica Acta, 2004. **49**: p. 4359-4369.

192. Weber A.Z. and J. Newman, *Transport in polymer-electrolyte membranes II. Mathematical model*. Journal of Electrochemistry Society, 2004. **151**: p. A311-A325.

193. Uchiyama, T., M. Kato and T. Yoshida, *Buckling deformation of polymer electrolyte membrane and membrane electrode assembly under humidity cycles*. Journal of Power Sources, 2012. **206**: p. 37-46.

194. Kusoglu, A., A.M. Karlsson, M.H. Santare, S. Cleghorn and W.B. Johnson, *Mechanical behaviour of fuel cell membranes under humidity cycles and effect of swelling anisotropy on the fatigue stresses*. Journal of Power Sources, 2007. **170**: p. 345-358.

195. Silberstein, M.N. and M.C. Boyce, *Hydro-thermal mechanical behaviour of Nafion during constrained swelling*. Journal of Power Sources, 2011. **196**: p. 3452-3460.

196. Bird, R.B., W.E. Stewart, and E.N. Lightfoot, *Transport phenomena*. 2nd edition. 2002, New York: John Wiley.

197. Brinkman, H.C., *A calculation of the viscous force exerted by a flowing fluid on a dense swarm of particles*. Applied Scientific Research, 1949. **1**: p. 27-34.

198. Curtiss, C.F. and R. Byron Bird, *Multicomponent diffusion*. Industrial and Engineering Chemistry Research, 1999. **38**: p. 2515-2522.

199. COMSOL, *Chemical Engineering Module User's Guide*. 2011.

200. Lampinen, M.J. and M. Fomino, *Analysis of free energy and entropy changes for half-cell reactions*. Journal of the Electrochemical Society, 1993. **140**: p. 3537-3546.

201. Cheddie, D. and N. Munroe, Three dimensional modeling of high temperature PEM fuel cells. Journal of Power Sources, 2006. **160**: p. 215-223.

202. Sousa, T., Mamlouk, M. and Scott, K., An isothermal model of a Laboratory Intermediate Temperature Fuel Cell using PBI doped Phosphoric Acid Membranes. Chemical Engineering Science, 2010. **65**: p. 2513-2530.

203. Parthasarathy, A., S. Srinivasan, A.J. Appleby and C.R. Martin, *Temperature dependence of the electrode kinetics of oxygen reduction at platinum/Nafion interface- A microelectrode investigation*. Journal of Electrochemistry Society, 1992. **139**: p. 2530-2537.

204. Scharifker, B.R., P. Zelenay, and J.O.M. Bockris, *Kinetic of oxygen reduction in molten phosphoric acid at high temperatures*. Journal of the Electrochemical Society, 1987. **134**: p. 2714-2725.

205. Vogel, W., J. Lundquist, P. Ross, and P. Stonehart, *Reaction Pathways and Poisons - II The rate controlling step for electrochemical oxidation of hydrogen on Pt in acid and poisoning of reaction by CO*. Electrochimica Acta, 1974. **20**: p. 79-93.

206. Liu, Z., J.S. Wainright, M.H. Litt, and R.F. Savinell, *Study of the oxygen reduction reaction (ORR) at Pt interfaced with phosphoric acid doped polybenzimidazole at elevated temperature and low relative humidity*. Electrochimica Acta, 2006. **51**: p. 3914-3923.

207. Birgersson, E., M. Noponen, and M. Vynnycky, *Analysis of a two-phase non-isothermal model for a PEFC*. Journal of the Electrochemical Society, 2005. **152**: p. A1021-A1034.

208. Liu, Z., Z. Mao and C. Wang, *A two dimensional partial flooding model for PEMFC*. Journal of Power Sources, 2006. **158**: p. 1229-1239.

209. Suzuki, T., K. Kudo and Y. Morimoto, *Model for investigation of oxygen transport limitation in a polymer electrolyte fuel cell*. Journal of Power Sources, 2013. **222**: p. 379-389.

210. Takamura, Y., E. Nakashima, H. Yamada, A. Tasaka and M. Inaba, *Effects of temperature and relative humidity on oxygen permeation in Nafion® and sulfonated poly (Arylene Ether Sulfone)*. ECS Transaction, 2008. **16**: p. 881-889.

211. Nonoyama, N., S. Okazaki, A.Z. Weber, Y. Ikogiand and T. Yoshida, *Analysis of oxygen-transport diffusion resistance in proton-exchange-membrane fuel cells*. Journal of the Electrochemical Society, 2011. **158**: p. B416-B423.

212. Reid, R.C., J.M. Prausnitz and B.E. Poling, *The properties of gases and liquids*. 4th edition. 1987, New York: McGraw-Hill.

213. Jaouen, F., G. Lindbergh and G. Sundholm, *Investigation of Mass-Transport Limitation in the Solid Polymer Fuel Cell Cathode*. Journal of the Electrochemical Society, 2002. **149**: p. A437-A447.

214. Jaouen, F., G. Lindbergh and K. Wiezell, *Transient Techniques for Investigating Mass-Transport Limitations in Gas Diffusion Electrodes*. Journal of the Electrochemical Society, 2003. **150**: p. A1711-A1717.

215. Kamarajugadda, S. and S. Mazumder, *Numerical investigation of the effect of cathode catalyst layer structure and compositon on polymer electrolye membrane fuel cell performance*. Journal of Power Sources, 2008. **183**: p. 629-642.

216. Sousa, T., M. Mamlouk and K. Scott, *A non-isothermal model of a laboratory intermediate temperature fuel cell using PBI doped phosphoric acid membranes*. Fuel Cells, 2010. **10**: p. 993-1012.

217. Zhou, T. and H. Liu, *Effects of the electrical resistances of the GDL in a PEM fuel cell*. Journal of Power Sources, 2006. **161**: p. 444-453.

218. Pantea, D., H. Darmstadt, S. Kaliaguine, and C. Roy, *Electrical conductivity of conductive carbon blacks: Influence of surface chemistry and topology*. Applied Surface Science, 2003. **217**: p. 181-193.

219. Powell, R.W. and R.P. Tye, *The promise of platinum as a high temperature thermal conductivity reference material*. British Journal of Applied Physics, 163. **14**: p. 662-666.

220. Wilke, C.R., A Viscosity Equation for Gas Mixture. The Journal of Chemical Physics, 1950. **18**: p. 517-519.

221. Poling, B.E., J.M. Prausnitz and J.P. O'Connell, *Properties of Gases and Liquids*. 5th edition. 2001, New York: Mc Graw-Hill Education.

222. Haynes, W.M., editor, *CRC handbook of chemistry and physics*. 94th edition (Internet version 2014).CRC Press/Taylor and Francis, Boca Raton, FL.

223. Pierson, H.O., *Handbook of carbon, graphite, diamond, and fullerenes properties, processing, and applications*. Materials science and process technology series. Electronic materials and process technology. 1993, Park Ridge, N.J.: Noyes Publications.

224. Weng, D., J.S. Wainright, U. Landau, and R.F. Savinell, *Electro-osmotic drag coefficient of water and methanol in polymer electrolytes at elevated temperatures*. Journal of the Electrochemical Society, 1996. **143**: p. 1260-1263.

225. Ismail M.S., D. Borman, T. Damjanovic, D.B. Ingham, M. Pourkashanian, *On the through-plane permeability of microporous layer-coated gas diffusion layers used in proton exchange membrane fuel cells.* International Journal of Hydrogen Energy, 2011. **36**: p. 10392-103402.

226. Ismail, M.S., K.J. Hughes, D.B. Ingham, L. Ma, M. Pourkashanian, *Effects of anisotropic permeability and electrical conductivity of gas diffusion layers on the performance of proton exchange membrane fuel cells.* Applied Energy, 2012. **95**: p. 50-63.

227. Yaws, C.L., *Handbook of transport property data: viscosity, thermal conductivity, and diffusion coefficients of liquid and gases*. 1995, Houston: Gulf Pub. Co.

228. Kestin, J., M. Sokolov and W.A. Wakeham, *Viscosity of liquid water in the range -8 ℃ to 150 ℃*. Journal of Physical and Chemical Reference Data, 1978. **7**: p. 941-948.

229. Djilali, N, *Computational modeling of polymer electrolyte membrane (PEM) fuel cells: Challenges and opportunities*. Energy, 2007. **32**: p. 269-280.

230. Carton, J.G. and A.G. Olabi, *Wind/hydrogen hybrid systems: Opportunity for Ireland's wind resource to provide consistent sustainable energy supply*. Energy, 2010. **35**: p. 4536-4544.

231. Springer, T.E., T.A. Zawodzinski and S. Gottesfeld, *Polymer Electrolyte Fuel Cell Model*, Journal of Electrochemistry Society, 1991. **138**: p. 2234-2342.

232. Broka, K. and P. Ekdunge, *Modelling the PEM fuel cell cathode*. Journal of Applied Electrochemistry, 1997. **27**: p. 281-289.

233. Thepkaew, J., A. Therdthianwong and S. Therdthianwong, *Key parameters of active layers affecting proton exchange membrane fuel cell performance*. Energy, 2008. **33**: p. 1794-1800.

234. Ge, S.H. and B.L. Yi, *A mathematical model for PEMFC in different flow modes*. Journal of Power Sources, 2003. **124**: p. 1-11.

235. Murgia, G., L. Pisani, M. Valentini and B.D. Aguanno, *Electrochemistry and Mass Transport in Polymer Electrolyte Membrane Fuel Cells. I. Model*. J. Journal of Electrochemistry Society, 2002. **149**: p. A31-A38.

236. Costamagna, P., *Transport phenomena in polymeric membrane fuel cells*. Chemical Engineering Science, 2001. **56**: p. 323-332.

237. Hertwig, K., L. Martens and R. Karwoth, *Mathematical modelling and simulation of polymer electrolyte membrane fuel cells. Part I: Model structures and solving an isothermal one-cell model*. Fuel Cells, 2002. **2**: p. 61-77.

238. Yan, Q., H. Toghiani and H. Causey, *Steady state and dynamic performance of proton exchange membrane fuel cells (PEMFCs) under various operating conditions and load changes*. Journal of Power Sources, 2006. **161**: p. 492-502.

239. Suzuki, A., U. Sen, T. Hattori, R. Miura, R. Nagumo, H. Tsuboi, N. Hatakeyama, A. Endou, H. Takaba, M.C. Willims and A. Miyamoto, *Ionomer content in the catalyst layer of polymer electrolyte membrane fuel cell (PEMFC): Effect on diffusion and performance*. International Journal of Hydrogen Energy, 2011. **36**: p. 2221-2229.

240. Wang, Z.H., C.Y. Wang and K.S. Chen, *Two-phase flow and transport in the air cathode of proton exchange membrane fuel cells*. Journal of Power Sources, 2001. **64**: p. 40-50.

241. Pasaogullari, U. and C.Y. Wang, *Two-phase modelling and flooding prediction of polymer electrolyte fuel cells*. Journal of Electrochemistry Society, 2005. **152**: p. A380-A390.

242. Lin, G.Y., W.S. He and T.V. Nguyen, *Modeling liquid water effects in the gas diffusion and catalyst layers of the cathode of a PEM fuel cell*. Journal of Electrochemistry Society, 2004. **151**: p. A1999-A2006.

243. Wang, L., A. Husar, T. Zhou and H.T. Liu, *A parameter study of PEM fuel cell performances*. International Journal of Hydrogen Energy, 2003. **28**: p. 1263-1272.

244. Choi, J.E. and Y.C. Bae, *Swelling effect of a polymer electrolyte membrane on the development of a semi-empirical cell voltage model*. Journal of Applied Electrochemistry, 2009. **39**: p. 1419-1425.

245. Xing L., M. Mamlouk and K. Scott, *A two dimensional agglomerate model for a proton exchange membrane fuel cell*. Energy, 2013. **61**: p. 196-210.

246. Buchi, F.N. and G.G. Scherer, *Investigation of the transversal water profile in Nafion membranes in polymer electrolyte fuel cells*. Journal of Electrochemistry Society, 2001. **148**: p. A183-A188.

247. Kulikovsky, A.A., *Quasi-3D modelling of water transport in polymer electrolyte fuel cells*. Journal of Electrochemistry Society, 2003. **150**: p. A1432-A1439.

248. Wang, Y. and K.S. Chen, *Through-plane water distribution in a polymer electrolyte fuel cell: comparison of numerical prediction with neutron radiography data*. Journal of Electrochemistry Society, 2010. **157**: p. B1878-B1886.

249. Passalacqua, E., F. Lufrano, G. Squadrito, A. Patti and L. Giorgi, *Nafion content in the catalyst layer of polymer electrolyte fuel cells: effects on structure and performance*. Electrochimica Acta, 2001. **46**: p. 799-805.

250. Kim, K.H., K.Y. Lee, H.J. Kim, E. Cho, S.Y. Lee, T.H. Lim, S.P. Yoon, I.C. Hwang, J.H. Jang, *The effects of Nafion® ionomer content in PEMFC MEAs prepared by a catalyst-coated membrane (CCM) spraying method*. International Journal of Hydrogen Energy, 2010. **35**: p. 2119-2126.

251. Djilali, N. and D. Lu, *Influence of heat transfer on gas and water transport*. Internation Journal of Thermal Science, 2002. **41**: p. 29-40.

252. Wang, Y. and C.Y. Wang, *A nonisothermal, Two-Phase Model for Polymer Electrolyte Fuel Cells*. Journal of Electrochemistry Society, 2006. **153**: p. A1193-A1200.

253. Weber, A.Z. and J. Newman, *Coupled Thermal and Water Management in Polymer Electrolyte Fuel Cells*. Journal of Electrochemistry Society, 2006. **153**: p. A2205-A2214.

254. Khajeh-Hosseini-Dalasm, N., K. Fushinobu and K. Okazaki, *Phase change in the cathode side of a proton exchange membrane fuel cell*. Journal of Power Sources. 2010. **195**: p. 7003-7010.

255. Jung, C.Y., H.S. Shim, S.M. Koo, S.H. Lee, and S.C. Yi, *Investigations of the temperature distribution in proton exchange membrane fuel cells*. Applied Energy, 2012. **93**: p. 733-741.

256. Owejan, J.P., J.J. Gagliardo, J.M. Sergi, S.G. Kandlikar and T.A. Trabold, *Water management studies in PEM fuel cells, Part I: Fuel cell design and in situ water distributions*. International Journal of Hydrogen Energy, 2009. **34**: p. 3436-3444.

257. Abdollahzadeh, M., J.C. Pascoa, A.A. Ranjbar and Q. Esmaili, *Analysis of PEM (Polymer Electrolyte Membrane) fuel cell cathode two-dimensional modeling*. Energy, 2014. **68**: p. 478-494.

258. Ahmed, D.H. and H.J. Sung, *Effects of channel geometrical configuration and shoulder width on PEMFC performance at high current density*. Journal of Power Sources, 2006. **162**: p. 327-339.

259. Ahmed, D.H. and H.J. Sung, *Design of a deflected membrane electrode assembly for PEMFCs*. International Journal of Heat and Mass Transfer, 2008. **51**: p. 5443-5453.

260. Wang, X.D., G. Lu, Y.Y. Duan and D.J. Lee, *Numerical analysis on performance of polymer electrolyte membrane fuel cells with various cathode flow channel geometries*. International Journal of Hydrogen Energy, 2012. **37**: p. 15778-15786.

261. Wu, X. and K. Scott, *The effects of ionomer content on PEM water electrolyser membrane assembly performance*. International Journal of Hydrogen Energy, 2010. **35**: p. 12029-12037.

262. Hwang, D.S., C.S. Park, S.C. Yi, Y.M. Lee, *Optimal catalyst layer structure of polymer electrolyte membrane fuel cell*. International Journal of Hydrogen Energy, 2011. **36**: p. 9876-9885.

263. Tirnovan, R., S. Giurgea, A. Miraoui and M. Cirrincione, *Surrogate model for proton exchange membrane fuel cell (PEMFC)*. Journal of Power Sources, 2008. **175**: p. 773-778.

264. Tirnovan, R., S. Giurgea, A. Miraoui and M. Cirrincione, *Proton exchange membrane fuel cell modelling based on a mixed moving least squares technique*.

International Journal of Hydrogen Energy, 2008. **33**: p. 6232-6238.

265. Zervas, P.L., A. Tatsis, H. Sarimveis and N.C.G. Markatos, *Development of a novel computational tool for optimizing the operation of fuel cells systems: Application for phosphoric acid fuel cells*. Journal of Power Sources, 2008. **185**: p. 345-355.

266. Wahdame, B., D. Candusso, X. François, F. Harel, J.M. Kauffmann and G. Coquery, *Design of experiment techniques for fuel cell characterisation and development*. International Journal of Hydrogen Energy, 2009. **34**: p. 967-980.

267. Miao, J.M., S.J. Cheng and S.J. Wu, *Metamodel based design optimisation approach in promoting the performance of proton exchange membrane fuel cells*. International Journal of Hydrogen Energy, 2011. **36**: p. 15283-15294.

268. Shokuhi-Rad A., A. Jamali, M. Naghashzadegan, N. Nariman-zadeh and A. Hajiloo, *Optimum Pareto design of non-linear predictive control with multi-design variables for PEM fuel cell*. International Journal of Hydrogen Energy, 2012. **37**: p. 11244-11254.

269. Peksen, M., L. Blum and D. Stolten, *Optimisation of a solid oxide fuel cell reformer using surrogate modelling, design of experiments and computational fluid dynamics*. International Journal of Hydrogen Energy, 2012. **37**: p. 12540-12547.

270. Cheng, S.J., J.M. Miao and S.J. Wu, *Use of metamodeling optimal approach promotes the performance of proton exchange membrane fuel cell (PEMFC)*. Applied Energy, 2013. **105**: p. 161-169.

271. Riascos, L.A. and D.D. Pereira, *Limit Operating Temperature in Polymer Electrolyte Membrane Fuel Cells*. Journal of Electrochemistry Society, 2009. **156**: p. B1051-B1058.

272. Pharoah, J.G., K. Karan and W. Sun, *On effective transport coefficient in PEM fuel cell electrodes: Anisotropy of the porous transport layers*. Journal of Power Sources, 2006. **161**: p.214-224.

273. Matheron, G., *Principles of geostatistics*. Economic Geology, 1963. 58: p. 1246-1266.

274. Sacks, J., W.J. Welch, T.J. Mitchell and H.P. Wynn, *Design and analysis of computer experiments*. Statistical Science, 1989. **4**: p. 409-423.

275. Sobol's, I.M., *Global sensitivity indices for nonlinear mathematical models and their Monte Carlo estimates*. Mathematics and Computers in Simulation, 2001. **55**: p. 271-280.

276. Sobol's I.M. and S.S. Kucherenko, *On global sensitivity analysis of quasi-Monte Carlo algorithms*. Monte Carlo Methods and Applications, 2005. **1**: p. 1-9.

277. Jin, R., W. Chen and A. Sudjianto, *On sequential sampling for global metamodeling in engineering design*. Proceedings of DETC, 2002. **2**: p. 539-548.

278. Sun, Y.P., L. Xing and K. Scott, *Analysis of the kinetics of methanol oxidation in a porous Pt-Ru anode*. Journal of Power Sources, 2010. **195**: p. 1-10.

279. Meyers, J.P. and J. Newman, *Simulation of the direct methanol fuel cell: II. Modeling and data analysis of transport and kinetic phenomena*. Journal of Electrochemical Society, 2002. **149**. p. A718-A728.

280. Newman, J. and C.W. Tobias, Theoretical analysis of current distribution in porous electrodes. Journal of Electrochemical Society, 1962. **109**. p. 1183-1191.

281. Scott, K. and Y.-P. Sun, *Approximate analytical solutions for models of three-dimensional electrodes by Adomian's decomposition methode*. in C.G. Vayenas (editor), *Modern aspects of electrochemistry*, New York: Springer; 2007. **41**: p. 127-218.

282. Sun, Y.-P. and K. Scott, *The influence of mass transfer on a porous fuel cell electrode*. Fuel Cells, 2004. **4**: p. 30-38.

283. Sun, Y.-P. and K. Scott, *An analysis of the influence of mass transfer on porous electrode performance*. Chemical Engineering Journal, 2004. **102**: p. 83-91.

284. Sun, Y.-P. and L. Xing, *Modeling of macro kinetics of methanol oxidation in porous Pt-Ru anode for DMFC*. CIESC Journal, 2009. **60**: p. 55-68.

285. Gasteiger, H.A., N. Markovic, P.N. Ross Jr and E.J. Cairns, *Methanol electrooxidation on well-characterized Pt-Ru alloys*. Journal of Physical Chemistry, 1993. **97**: p. 12020-12029.

286. Kauranen, P.S., E. Skou and J. Munk, *Kinetics of methanol oxidation on carbon-supported Pt and Pt + Ru catalysts*. Journal of Electrochemical Society, 1996. **404**. p. 1-13.

287. Nordlund, J. and G. Lindbergh. *Temperature-dependent kinetics of the anode in*

the DMFC. Journal of Electrochemical Society, 2004. **151**. p. A1357-A1362.

288. Shivhare, M.R., R.G. Allen, K. Scott, A.J. Morris and E.B. Martin, *A kinetic model for the direct methanol fuel cell anode based on surface coverage*. Journal of Electroanalytical Chemistry, 2006. **595**: p. 145-151.

289. Shivhare, M.R., C.L. Jackson, K. Scott and E.B. Martin, *Simplified model for the direct methanol fuel cell anode*. Journal of Power Sources, 2007. **173**: p. 240-248.

290. Scott, K., W.M. Taama, S. Kramer, P. Argyropoulos and K. Sundmacher, *Limiting current behaviour of the direct methanol fuel cell*. Electrochimica Acta, 1999. **45**: p. 945-957.

291. Scott, K., P. Argyropoulos and K. Sundmacher, *Model for the liquid feed direct methanol fuel cell*. Journal of Electrochemical Society, 1999. **477**. p. 97-110.

292. Tian, N., Z.-Y. Zhou, S.-G. Sun, Y. Ding and L.-W. Zhong, *Synthesis of tetrahexahedral platinum nanocrystals with high-index facets and high electro-oxidation activity*. Science, 2007. **316**: p. 732-735.

293. Wang, Q., G.Q. Sun, L. Cao, L.H. Jiang, G.X. Wang, S.L. Wang, S.H. Yang, and Q. Xin, *High performance direct ethanol fuel cell with double-layered anode catalyst layer*. Journal of Power Sources, 2008. **177**: p. 142-147.

294. Shao, Z.-G., W.F. Lin, F. Zhu, P.A. Christensen, M. Li and H. Zhang, *Novel electrode structure for DMFC operated with liquid methanol*. Electrochemistry Communications, 2006. **8**: p. 5-8.

Appendix A: Conservation equations

Conservation of mass

The mass balance within a volume element can be described by the following equation:

$$\left\{\begin{matrix} rate\ of \\ mass \\ accumulation \end{matrix}\right\} = \left\{\begin{matrix} rate\ of \\ mass \\ inlet \end{matrix}\right\} - \left\{\begin{matrix} rate\ of \\ mass \\ outlet \end{matrix}\right\} + \left\{\begin{matrix} rate\ of \\ mass\ production \\ or\ consumption \end{matrix}\right\} \qquad \text{(A-1)}$$

Applying Eq. (A-1) on the fluid continuously flowing in a porous media following the methodology developed by Bird *et al.* [196]:

$$\frac{\partial(\varepsilon\rho)}{\partial t} + \nabla\cdot(\rho\mathbf{u}) = Q_c \qquad \text{(A-2)}$$

where ε is the porosity of the porous media, ρ (kg m^{-3}) is the density of the fluid, t (s) is the time, $\mathbf{u}$ (m s^{-1}) is the velocity vector, Q_c (kg m^{-3} s^{-1}) is the general fluid sources, and ∇ is the nabla operator.

Note that the porosity equals unity if the flow media is non-porous. The vector $\rho\mathbf{u}$ (kg m^{-2} s^{-1}) is the mass flux, and its divergence $\nabla\cdot(\rho\mathbf{u})$ (kg m^{-3} s^{-1}) is the mass flux net rate per unit of volume. Consequently, Eq. (A-2) means that the rate increase in density within a small volume element is equal to the mass flux net rate divided by its volume. This equation is valid for all the flowing and diffusion processes, such as fluid flow, mass transport and electrochemical reactions, occurred inside the fuel cell.

Eq. (A-2) can be expanded for a multi-component mixture consisting of n species by applying the law of conservation of mass for each species i (i = 1,2,3,…n):

$$\frac{\partial(\varepsilon\rho_i)}{\partial t} + \nabla\cdot(\rho_i\mathbf{u} + \mathbf{j}_i) = Q_{c,i} \qquad \text{(A-3)}$$

where $\mathbf{j}_i$ (kg m^{-2} s^{-1}) is the mass flux vector of species i. This equation describes the change of density of species i with time. The addition of all n equations results in Eq. (A-2), where

$$\sum_{i=1}^{n}\rho_i\mathbf{u} = \rho\mathbf{u}, \quad \sum_{i=1}^{n}\mathbf{j}_i = 0, \quad \sum_{i=1}^{n}Q_{c,i} = 0 \qquad \text{(A-4)}$$

Conservation of momentum

The momentum balance within a volume element can be described by the following equation:

$$\begin{Bmatrix} rate\ of \\ momentum \\ accumulation \end{Bmatrix} = \begin{Bmatrix} rate\ of \\ momentum \\ in \end{Bmatrix} - \begin{Bmatrix} rate\ of \\ momentum \\ out \end{Bmatrix} + \begin{Bmatrix} sum\ of\ forces \\ acting\ on \\ system \end{Bmatrix} \quad \text{(A-5)}$$

The momentum flow through the volume element can by described by two mechanisms: convection and molecular transfer. By considering the fact that the fluid flows through all faces of the volume element, Eq. (A-5) can be written as follow [196]:

$$\frac{\partial(\rho \mathbf{u})}{\partial t} = -\nabla \cdot (\rho \mathbf{u}\mathbf{u}) - \nabla \cdot p - \nabla \cdot \boldsymbol{\tau} + \rho \mathbf{g} \quad \text{(A-6)}$$

where ∇p (Pa m^{-1}) is the pressure gradient, $\boldsymbol{\tau}$ (kg m^{-1} s^{-2}) is the shear stress tensor, and $\mathbf{g}$ (m s^{-2}) is the gravitational acceleration vector.

The term on the left hand side of Eq. (A-6) means the rate of momentum increase per unit of volume while on the right hand side of Eq. (A-6) the first term is the rate of momentum gain by convection per unit of volume, the second term is the pressure force on element per unit of volume, the third term describes the rate of momentum gain by viscous transfer per unit of volume, and the last term is the gravitational force on the element per unit of volume. This equation, which is valid for any continuous medium, is the general form of the motion equation. If the behaviour of the fluids obeys Newton's law of viscosity, in which the shear force per unit of area is proportional to the negative of the local velocity gradient, the shear stress tensor is therefore being expressed as [196]:

$$\boldsymbol{\tau} = \mu[\nabla \mathbf{u} + (\nabla \mathbf{u})^T - \frac{2}{3}(\nabla \cdot \mathbf{u})\mathbf{I}] \quad \text{(A-7)}$$

where $\mathbf{I}$ is the identity matrix, $\begin{bmatrix} 1 & 0 & 0 \\ 0 & 1 & 0 \\ 0 & 0 & 1 \end{bmatrix}$.

In order to describe the momentum balance in the porous media, the Brinkman equation [197] is used. This equation was developed based on Darcy's law by Brinkman in 1949. An additional term was added into Darcy's law accounting for the viscous transport in

the momentum balance. And both the pressure and flow velocity vector were treated as independent variables in the Brinkman equation shown as follow:

$$(\frac{\rho}{\varepsilon})\frac{\partial \mathbf{u}}{\partial t} = -\mathbf{u}\frac{\mu^{eff}}{K} - \nabla \cdot p - \nabla \cdot \boldsymbol{\tau} + \rho \mathbf{g} \tag{A-8}$$

where K (m^2) and ε are the permeability and porosity of the porous media, respectively. μ^{eff} (Pa s) is the effective viscosity of the fluid. The shear stress tensor is similar to that in Eq. (A-7) but the porosity of the porous media is included:

$$\boldsymbol{\tau} = \frac{\mu}{\varepsilon}[\nabla \mathbf{u} + (\nabla \mathbf{u})^T - \frac{2}{3}(\nabla \cdot \mathbf{u})\mathbf{I}] \tag{A-9}$$

For a multi-component mixture the motion equation is very similar to the equations developed for single fluid represented by Eq. (A-6) and Eq. (A-8). The difference is that the last term, $\rho \mathbf{g}$ is replaced by $\sum \rho_i \mathbf{g}_i$, which accounts for the fact that each species may be affected by different external force per unit of mass. Simultaneously, a unit tensor $\boldsymbol{\delta}$ is introduced to the pressure term shown as follow:

$$\frac{\partial(\rho \mathbf{u})}{\partial t} = -\nabla \cdot (\rho \mathbf{u}\mathbf{u}) - \nabla \cdot (p\boldsymbol{\delta}) - \nabla \cdot \boldsymbol{\tau} + \sum_{i=1}^{n} \rho_i \mathbf{g}_i, \qquad i = 1,2,3,.....,n \tag{A-10}$$

$$(\frac{\rho}{\varepsilon})\frac{\partial \mathbf{u}}{\partial t} = -\mathbf{u}\frac{\mu^{eff}}{K} - \nabla \cdot (p\boldsymbol{\delta}) - \nabla \cdot \boldsymbol{\tau} + \sum_{i=1}^{n} \rho_i \mathbf{g}_i, \qquad i = 1,2,3,.....,n \tag{A-11}$$

Note that the flow velocity in equations from Eq. (A-6) to Eq. (A-11) is the superficial averaged velocity, which is defined as the volume rate of flow through a unit cross-sectional area including both pores and solid matrix. This definition makes the velocity field continuous across the boundaries between the porous and free flow regions. The flow therefore can be described by the same velocity in the entire domain.

Conservation of species

The mass balance of species *i* in a multi-component mixture can be obtained by applying the law of conservation of mass on species *i* to the volume element, through which a multi-component mixture. For species *i*, the mass balance is described as follow:

$$\begin{Bmatrix} rate\ of\ mass \\ accumulation \end{Bmatrix} = \begin{Bmatrix} rate\ of \\ mass\ in \end{Bmatrix} - \begin{Bmatrix} rate\ of \\ mass\ out \end{Bmatrix} + \begin{Bmatrix} rate\ of\ production \\ or\ consumption \end{Bmatrix} \tag{A-12}$$

By considering the species transport through convection and diffusion, Eq. (A-12) could be written as follow:

$$\frac{\partial(\rho_i w_i)}{\partial t} = -\rho_i \mathbf{u}\nabla \cdot w_i - \nabla \cdot \mathbf{j}_i + r_i \tag{A-13}$$

where w_i, $\mathbf{j}_i$ (kg m^{-2} s^{-1}) and r_i (kg m^{-3} s^{-1}) are the mass fraction, mass flux vector and source or sink term of species *i*, respectively.

Eq. (A-13) describes the change of mass fraction of species *i* with respect to time in a fixed volume element. On the right hand side of this equation, the first term represents the mass change resulting from convection, the second term represents the mass change due to diffusion, and the third term is the chemical reaction dependent mass change.

Bird *et al.* [196] states that four driving forces have to be considered for the mass flux vector in a multi-component system. Thus the mass flux vector of species *i* is written as:

$$\mathbf{j}_i = \mathbf{j}_i^x + \mathbf{j}_i^p + \mathbf{j}_i^g + \mathbf{j}_i^T \tag{A-14}$$

Each term on the right hand side represent the contribution of ordinary diffusion ($\mathbf{j}_i^x$), pressure diffusion ($\mathbf{j}_i^p$), forced diffusion ($\mathbf{j}_i^g$) and thermal diffusion ($\mathbf{j}_i^T$), respectively.

According to the approach proposed by Curtiss and Bird [198], the mass flux vector can be rearranged as follow:

$$\mathbf{j}_i = -D_i^T \nabla \ln T - \rho_i \sum_{j=1}^{v} D_{ij}^{eff} \mathbf{d}_j, \; i = 1,2,3,.....,n \tag{A-15}$$

where D_i^T (m^2 s^{-1}) is the thermal diffusion coefficient, T (K) is the temperature, D_{ij} (m^2 s^{-1}) is the Fick diffusion coefficient matrix for species *i* diffusing through species *j* in the multi-component mixture, and $\mathbf{d}_j$ (m^{-1}) is the driving force for diffusion through concentration, pressure and external forces. If gravity is the only external force, $\mathbf{d}_j$ can be expressed as [199]:

$$\mathbf{d}_j = \nabla x_j + (x_j - w_j)\frac{\nabla p}{p} \tag{A-16}$$

The mole fraction of species *j* (x_j) and its gradient (∇x_j) can be related to the mass fraction of species *j* (w_j) by the following equation:

$$x_j = \frac{w_j}{M_j} M_n \tag{A-17}$$

$$\nabla x_j = \frac{M_n^2}{M_j}\sum_{\substack{j=1\\k\neq j}}^{n}\left[\frac{1}{M_j} + w_k\left(\frac{1}{M_k} + \frac{1}{M_j}\right)\right]\nabla w_k \tag{A-18}$$

where M_n (kg mol^{-1}) is the mean molecular weight of the mixture.

In a porous media, the Fick's diffusion coefficient matrix needs to be corrected by the porosity and tortuosity of the porous media. Bruggman correction [17] shown as follow is the most common relationship used.

$$D_{ij}^{eff} = D_{ij}\varepsilon^{\tau} \tag{A-19}$$

Normally, $\tau = 1.5$ is selected.

The source term for species conservation is associated with the chemical reaction. The source term for species *i* is zero unless species *i* is involved in the chemical reactions. As discussed in Section 3.1.1, the reaction rate is negative in the anode catalyst layer and positive in the cathode catalyst layer. Consequently, the source terms for hydrogen, oxygen, nitrogen and water vapour are given as follow:

$$r_{H_2} = i_a\frac{M_{H_2}}{2F},\quad r_{O_2} = -i_c\frac{M_{O_2}}{4F},\quad r_{N_2} = 0,\quad r_{H_2O} = i_c\frac{M_{H_2O}}{2F} \tag{A-20}$$

where i_a and i_c (A m^{-3}) are the volumetric current densities for the anode and cathode, respectively. It is important to note that the source terms for hydrogen and oxygen are negative due to the chemical reaction consumption, while the source term for water vapour is positive because water is the production. As nitrogen is not involved in the chemical reaction, the source term for nitrogen is zero.

Conservation of energy

By applying the same principle, which is used to develop the equation of motion, on energy, the law of conservation of energy for the fluid contained in the volume element can be written as follow:

$$\begin{Bmatrix}\text{rate of}\\ \text{internal and}\\ \text{kinetic energy}\\ \text{accumulation}\end{Bmatrix} = \begin{Bmatrix}\text{rate of}\\ \text{internal and}\\ \text{kinetic energy}\\ \text{in by convection}\end{Bmatrix} - \begin{Bmatrix}\text{rate of}\\ \text{internal and}\\ \text{kinetic energy}\\ \text{out by convection}\end{Bmatrix} + \begin{Bmatrix}\text{net rate of}\\ \text{heat addition}\\ \text{by conduction}\end{Bmatrix} + \begin{Bmatrix}\text{net rate of}\\ \text{work done by}\\ \text{system on}\\ \text{surroundings}\end{Bmatrix} \tag{A-21}$$

In Eq. (A-21) the kinetic energy is associated with the fluid motion, and the internal energy is related to the random translational and internal motion of the molecules. The equation of energy for a multi-component mixture is given by using the methodology developed by Bird *et al.* [196]:

$$\frac{\partial}{\partial t}\rho(U+\frac{1}{2}u^2) = -\nabla\cdot[\rho(U+\frac{1}{2}u^2)\mathbf{u}] - \nabla\cdot\mathbf{q} - \nabla\cdot(\boldsymbol{\tau}\cdot\mathbf{u}) + \nabla\cdot(p\boldsymbol{\delta}\cdot\mathbf{u}) + \sum_{i=1}^{n}(\rho_i\mathbf{u}\cdot\mathbf{g}_i) + Q_e \tag{A-22}$$

where U (J kg^{-1}) is the internal energy per unit of mass of fluid in the volume element, Q_e (J m^{-3} s^{-1}) is the heat source term, and $\mathbf{q}$ (J m^{-2} s^{-1}) is the heat flux vector.

The term on the left hand side of Eq. (A-22) is the rate of energy gained per unit of volume, while on the right hand side of Eq. (A-22), the first term is the rate of energy input per unit of volume by convection; the second term is the rate of energy input per unit of volume by thermal conduction; the third term is the rate of work done on the fluid per unit of volume by viscous forces; the fourth term is the rate of work done on the fluid per unit of volume by pressure forces; the fifth term is the rate of work done on the fluid per unit of volume by gravitational forces; and the last term is the heat source which accounts for heat generation and consumption due to chemical reactions and Joule heating.

According to Fourier's law, the heat flux vector is expressed in terms of temperature gradients as follow:

$$\mathbf{q} = -k\nabla T \tag{A-23}$$

This equation represents the energy transport by heat conduction, which is used to describe the molecular transport of heat in isotropic media. Expanding Eq. (A-23) to a multi-component mixture gives:

$$\mathbf{q} = -k_i\nabla T + \sum_{i=1}^{n}\frac{H_i}{M_i}\mathbf{j}_i, \quad i = 1,2,3,.....,n \tag{A-24}$$

where k_i (W m^{-1} K^{-1}) and H_i (J mol^{-1}) are the thermal conductivity and partial molar enthalpy of species *i*. The second term on the right hand side represents the heat transport by species diffusion.

Combing the equations of motion and continuity with the equation of energy, the equation of thermal energy can be obtained as follow [196]:

$$\rho(\frac{\partial U}{\partial t}+\mathbf{u}\cdot\nabla U)=-\nabla\cdot\mathbf{q}-p\nabla\cdot\mathbf{u}-\boldsymbol{\tau}\nabla\cdot\mathbf{u}+Q_e \tag{A-25}$$

The term on the left hand side of the equation above represents the rate of internal energy gained per unit of volume; the first term on the right hand is the rate of internal energy input per unit of volume by conduction; the second term on the right hand is the reversible rate of internal energy increase per unit of volume by compression; the third term on the right hand is the irreversible rate of internal energy increase per unit of volume by viscous dissipation; and the fourth term on the right hand is the heat source.

Instead of internal energy, Eq. (A-25) can be written in terms of the temperature and heat capacity of the fluid, which becomes more convenient for calculating the temperature profiles. At a constant pressure, the internal energy can be related to the temperature and heat capacity via the following equation:

$$\frac{\partial U}{\partial t}=-p\frac{\partial V}{\partial t}+c_p\frac{\partial T}{\partial t} \tag{A-26}$$

where V (m^3 kg^{-1}) is the volume per unit of mass, and c_p (J mol^{-1} K^{-1}) is the averaged heat capacity of the multi-component mixture at a constant pressure, which can be calculated by the heat capacity and mole fraction of the species of the multi-component mixture:

$$c_p=\sum_{i=1}^{n}c_{p,i}x_i\ ,\ i=1,2,3,.....,n \tag{A-27}$$

With the aid of the equation of continuity $\rho(dV/dt)=\nabla\cdot\mathbf{v}$, then multiplying both sides of Eq. (A-26) by the averaged density (could be calculated follow the method shown in Eq. (A-27)) of the multi-component mixture and combing Eq. (A-25) gives:

$$\rho c_p\frac{\partial T}{\partial t}+\rho c_p\mathbf{u}\cdot\nabla T=-\nabla\cdot\mathbf{q}-\boldsymbol{\tau}\nabla\cdot\mathbf{u}+Q_e \tag{A-28}$$

Due to the fact that the second term on the right hand side of the equation above ($\boldsymbol{\tau}\nabla\cdot\mathbf{v}$) is only significant in high speed flow system in which the velocity gradient is large [196], it is reasonable to neglect this term on the purpose of simplification. By simply substituting Eq. (A-23) into Eq. (A-28), a secondary order partial differential equation for temperature profiles can be obtained as follow:

$$\rho c_p \frac{\partial T}{\partial t} + \rho c_p \mathbf{u} \cdot \nabla T - \nabla \cdot (k \nabla T) = Q_e \tag{A-29}$$

For a multi-phase heat transfer process occurred in the porous media, Eq. (A-29) becomes to:

$$\frac{\partial}{\partial t}[\sum_{i=g,l,s}(\varepsilon \rho_i c_{p,i})T] + \nabla \cdot [\sum_{i=g,l}(\varepsilon \rho_i c_{p,i} \mathbf{u}_i)T] - \nabla \cdot (\sum_{i=g,l,s} k_i \nabla T) = Q_e \tag{A-30}$$

where ε is the porosity of the porous media, the subscript *g*, *l*, and *s* refer to phases of gas, liquid and solid, respectively.

It is important to note that the solid phase is not included in the second term on the left hand side of the equation above. This is because the solid phase (porous electrode) does not move. The source term Q_e (J m^{-3} s^{-1}) is responsible for the heat generation and sink due to chemical reaction, latent heat due to phase change, and Joule heating. The heat generation in terms of Joule heating is expressed by the following equation:

$$q_{Joule} = \sigma \phi^2 \tag{A-31}$$

where σ (S m^{-1}) is the ionic conductivity, ϕ (V) is the potential.

For a fuel cell unit, Joule heating is taken into account in the gas diffusion layer, catalyst layer and membrane. Especially for the catalyst layer where hydrogen or methanol oxidation reaction and oxygen reduction reaction occurred, Joule heating is much significant, which can be calculated by the entropy changes of the reactant and the activation overpotential for each electrode. For a hydrogen fuel cell, Joule heating on both the anode and cathode is expressed as [200]:

$$q^a_{reaction} = -|i_a|(\frac{T\Delta S_a}{2F}) \tag{A-32}$$

$$q^c_{reaction} = -|i_c|(|\eta_c| - \frac{T\Delta S_c}{4F}) \tag{A-33}$$

where ΔS_a and ΔS_c (J mol^{-1} K^{-1}) are the entropy change for the reaction on anode and cathode, respectively. From the study of Lampinen and Fomino [200], the HOR on anode is endothermic whereas the ORR is exothermic. The entropy change is 161.2 J mol^{-1} K^{-1} for HOR and -324.0 J mol^{-1} K^{-1} for ORR.

Conservation of charge

It is assumed that a finite volume dV (m^3) carries an amount of charge dG_v (C). The charge density g_v (C m^{-3}) is:

$$g_v = \frac{dG_v}{dV} \tag{A-34}$$

Then the total charge of the volume V is expressed as follow:

$$\int dG_v = \int dV g_v \tag{A-35}$$

The change of total charge in time generates current flow in and/or out of the surface dS (m^2) surrounding the volume dV. The expression of conservation of charge is therefore:

$$\frac{d}{dt}\int dV g_v = -\oint dS \cdot \mathbf{i} \tag{A-36}$$

where $\mathbf{i}$ (A m^{-2}) is the current density vector. By using the Gauss divergence theorem, which states that the outward flux of a vector field through a closed surface is equal to the volume integral of the divergence over the region inside the surface, and assuming that the volume V did not change with time, Eq. (A-36) can be rewritten as:

$$\frac{d}{dt}\int dV g_v = -\nabla \cdot \mathbf{i} \tag{A-37}$$

Assuming the charge density at any location does not change with time and adding a source term Q_i (A m^{-3}), Eq. (A-36) can be simplified as follow:

$$\nabla \cdot \mathbf{i} = Q_i \tag{A-38}$$

If no external source applied, Q_i is equal to the volume current density i_v (A m^{-3}). At stationary condition, the current density does not depend on time.

$$\nabla \cdot \mathbf{i} = 0 \tag{A-39}$$

The current density vector $\mathbf{i}$ can be related to the electric filed $\mathbf{E}$ (V m^{-1}) and conductivity σ (S m^{-1}) by Ohm's law as:

$$\mathbf{i} = \sigma \mathbf{E} \tag{A-40}$$

At a specific point within the electric field, the voltage is equal to the negative gradient of the potential shown as follow:

$$\mathbf{E} = -\nabla \phi \tag{A-41}$$

Substituting Eq. (A-40) and Eq. (A-41) into Eq. (A-38) gives:

$$\nabla \cdot \mathbf{i} = \nabla(-\sigma \nabla \phi) = Q_i \tag{A-42}$$

Applying Eq. (A-42) on the solid (electrode) and electrolyte (membrane and ionomer) phases, respectively, two sub-equations are obtained [201]:

$$\nabla \cdot \mathbf{i}_s = \nabla(-\sigma_s^{eff} \nabla \phi_s) = Q_s \tag{A-43}$$

$$\nabla \cdot \mathbf{i}_M = \nabla(-\sigma_M^{eff} \nabla \phi_M) = Q_M \tag{A-44}$$

where σ_s^{eff} and σ_M^{eff} (S m^{-1}) are the effective electrical conductivity for the solid phase and electrolyte conductivity for the membrane and ionomer, respectively. For any volume of the computational domain the electronic and the ionic currents generated are equal, leading to:

$$\nabla \cdot \mathbf{i}_s + \nabla \cdot \mathbf{i}_M = 0 \tag{A-45}$$

In a porous media, the source terms Q_s and Q_M can be expressed in terms of the volumetric current for the electrode and electrolyte, respectively. The total current generated in the anode must be equal to the total current consumed in the cathode. In the situation of no external resource the conservation of charge requires that:

$$Q_s = -Q_M \tag{A-46}$$

$$\int_{V_{CL,a}} i_a dV = -\int_{V_{CL,c}} i_c dV \tag{A-47}$$

The average volumetric current density i_{avg} (A m^{-3}) is expressed as:

$$i_{avg} = \frac{1}{V_{CL,a}} \int_{V_{CL,a}} i_a dV = -\frac{1}{V_{CL,c}} \int_{V_{CL,c}} i_c dV \tag{A-48}$$

where $V_{CL,a}$ and $V_{CL,c}$ (m^3) are the volume of the catalyst layer of anode and cathode, respectively. The surface overpotential, the driving force for the transfer current density in an electrochemical reaction, is defined as [17]:

$$\eta = \phi_s - \phi_M - E^{eq} \tag{A-49}$$

where E^{eq} (V) is the equilibrium potential, which is zero on the anode and is equal to the theoretical cell potential at a given temperature and pressure on the cathode side calculated by the Nernst equation.

Appendix B: List of Publications

Book contribution

- Scott, K. and L. Xing. *Direct methanol fuel cell*. in K. Sundmacher (editor), *Advances in Chemical Engineering Fuel Cell Engineering*, USA: Elsevier Inc; 2012. p. 150-200.

Scientific journals

- Xing L., M. Mamlouk and K. Scott. *A two dimensional agglomerate model for a proton exchange membrane fuel cell*. Energy 2013. **61**: p. 196-210.
- Xing L., X. Song, K. Scott, V. Pickert and W. Cao. Multi-variable optimisation of PEMFC cathodes based on surrogate modelling. International Journal of Hydrogen Energy 2013. **38**: p. 14295-14313.
- Ji B., V. Pickert, W. Cao and L. Xing. *Onboard condition monitoring of solder fatigue in IGBT power modules*. Proceedings- 2013 9th IEEE International Symposium on Diagnostics for Electric Machines, Power Electronics and Drives, SDEMPED 2013, art. no. 6645690, p. 9-15.
- Xing L., K. Scott and Y.-P. Sun. *Transient response and steady-state analysis of the anode of direct methanol fuel cells based on dual-site kinetics*. International Journal of Electrochemistry 2011, Article ID 853261, 14 pages.
- Xing, L., M. Mamlouk, R. Kuma and K. Scott. *Numerical investigation of the optimal Nafion® ionomer content in cathode catalyst layer: A two-phase flow agglomerate approach*. International Journal of Hydrogen Energy 2014. **39**: p. 9087-9104.
- Xing, L., R. Kumar, T. Alaje, M. Mamlouk and K. Scott. *A two-phase flow and non-isothermal agglomerate model for a proton exchange membrane (PEM) fuel cell*. Submitted to Energy, current status: minor revision under review.
- Xing, L., P.K. Das, X. Song, M. Mamlouk and K. Scott. *Numerical analysis of the optimum membrane/ionomer water content of PEMFCs: The interaction of Nafion® ionomer content and cathode relative humidity*. Submitted to Applied Energy, current status: under review.

Oral presentations

- Xing, L., M. Mamlouk and K. Scott. *Modelling and experimental study of water transport in PEMFCs*. Supergen Annual Meeting, Loughborough University, UK, November, 2010.
- Xing, L., M. Mamlouk and K. Scott. *A two-dimensional agglomerate model for PEMFCs*. Supergen Annual Meeting, Birmingham University, UK, November, 2011.
- Xing, L., M. Mamlouk and K. Scott. *A two-dimensional model for water transport of PEMFCs*. 9th Symposium on Fuel Cell and Battery Modelling and Experimental Validation (ModVal 9), Campus Sursee, Switzerland, April, 2012.
- Xing, L., M. Mamlouk and K. Scott. *A parametric study of the cathode catalyst layer composition based on a two-dimensional two-phase flow agglomerate model*. Fifth European Fuel Cell Technology & Applications Conference - Piero Lunghi Conference, Rome, Italy, December, 2013.

Poster presentations

- Xing, L. and K. Scott. *Modelling the anode behaviour of DMFCs*. IAB Poster Session, Newcastle upon Tyne, UK, December, 2011.